UNIVERSITY OF SOUTHAMPTON
School of Electronics and Computer Science

Compressed Sensing Aided Design Aspects of Indoor Attocells

by

Hongming Zhang
BEng, MSc

May 2017

SUPERVISORS: Professor Lie-Liang Yang and Professor Lajos Hanzo
Southampton Wireless
School of Electronics and Computer Science
University of Southampton
Southampton SO17 1BJ
United Kingdom

Dedicated to my family

UNIVERSITY OF SOUTHAMPTON

ABSTRACT

School of Electronics and Computer Science
Faculty of Physical Science and Engineering

Doctor of Philosophy

Compressed Sensing Aided Design Aspects of Indoor Attocells

by Hongming Zhang

Compressed Sensing (CS) is invoked for indoor attocells utilising Power Line Communication (PLC) and Visible Light Communication (VLC), in order to strike a compelling tradeoff between the performance attained and the complexity imposed. We commence by detailing our motivation as well as by introducing PLCs and VLCs. Then, we specify the related technical issues to be addressed and outline the general framework of our CS-assisted system design.

Firstly, we propose a Compressed Impairment Sensing (CIS)-assisted Interleaved-Double-FFT (IDFFT) system for broadband PLC, in order to mitigate the deleterious effects of asynchronous impulsive noise. A Frequency-Domain (FD) equaliser is employed for achieving a beneficial multipath diversity gain, which is amalgamated with a Two-Dimensional (2D) interleaver conceived for efficiently dispersing the asynchronous impulsive bursts encountered. As a result, the attainable system performance of the IDFFT system becomes better than that of the classic Orthogonal Frequency-Division Multiplexing (OFDM) system. As a further improvement, some of the disabled sub-bands, which are due to either high level of attenuation or narrowband interference, are exploited as pilot symbols in our IDFFT system for supporting the operation of CIS. We demonstrate that the sparse impairment vector can be readily estimated by our 2D-interleaving aided CS solution. Moreover, we propose a computationally efficient search algorithm capable of approaching the performance of the optimal pilot design. Finally, based on the turbo principle, we propose a joint CIS estimation and symbol detection algorithm for our IDFFT system. Explicitly, the CIS estimator iteratively exchanges ever more reliable information with the symbol detector upon each new iteration, hence resulting in an improved system performance. More particularly, our CIS estimator invokes a greedy algorithm, where locally optimal choices are made at each iteration. The performance of our CIS-assisted IDFFT system is investigated by simulations, where the various aspects of the design-tradeoffs are studied. We demonstrate that our CIS-assisted detector is capable of efficiently mitigating the deleterious effects of asynchronous impulsive noise at a low complexity.

Secondly, we propose a Linear Precoding assisted Index Modulation (LPIM) scheme and a Compressed Sensing assisted Index Modulation (CSIM) scheme for beneficial bit-to-symbol mapping in OFDM systems. These mapping schemes are represented by a pair of codebooks. We commence by analysing the system performance in the context of achievable Spectral Efficiency (SE), Energy Efficiency (EE), diversity gain and coding gain. Moreover, the detailed codebook design criteria are outlined and discussed. Then, our LPIM codebook is designed based on the maximum diversity gain and the maximum coding gain criteria. By contrast, our CSIM codebook is designed based on the maximum diversity gain and the maximum achievable rate criteria. Both analytical and simulation results are provided for characterising the attainable performance of LPIM and CSIM, demonstrating that LPIM is capable of attaining an attractive coding gain, whilst CSIM is capable of striking a compelling tradeoff between the attainable coding gain and the maximum achievable rate. Additionally, we also demonstrate that in comparison to the conventional Subcarrier Index Modulation (SIM) scheme, our CSIM is capable of achieving a higher SE as well as an increased EE. However, the complexity of Maximum-Likelihood (ML) detection of both the LPIM and the CSIM symbols may be excessive, hence we propose a low-complexity Generalised Iterative Residual Check Detector (GIRCD). Similar to the CIS estimator, our GIRCD is also based on the basic principle of greedy algorithms. Finally, simulation results are provided for demonstrating that the GIRCD is capable of striking a beneficial tradeoff between the Bit Error Ratio (BER) performance and complexity.

Finally, our CSIM scheme is applied to Direct Current biased Optical OFDM (DCO-OFDM) for VLC relying on Intensity-Modulation and Direct Detection (IM/DD), in order to improve the maximum achievable rate of the optical system. Both analytical and simulation results are provided for characterising the attainable performance of the CSIM-assisted DCO-OFDM system, showing that for the same maximum achievable rate as well as the same sensitivity to nonlinear distortions, the BER performance of the DCO-OFDM using CSIM is better than that of the DCO-OFDM using Quadrature Amplitude Modulation (QAM). In particular, we demonstrate that about 24% improvement of the maximum achievable rate expressed in bits-per-second-per-Hertz can be achieved by our CSIM scheme using Quadrature Phase-Shift Keying (QPSK), in comparison to the conventional QPSK scheme dispensing with our CSIM arrangement. As a further improvement, a piecewise Companding Transform (CT) is conceived for our O-OFDM system, forming the CTO-OFDM arrangement for the sake of mitigating the nonlinear distortions induced by the limited linear dynamic range of Light Emitting Diodes (LEDs). We first investigate the general principles and design criteria of the piecewise CTO-OFDM scheme and conceive three prototype designs. Furthermore, we investigate the nonlinear effects of both hard clipping and CT on our O-OFDM systems by both analytical and simulation results. Our investigations show that CTO-OFDM constitutes a promising signalling scheme for VLCs, as a benefit of its high bandwidth efficiency, high reliability, high implementational flexibility, as well as robustness to nonlinear distortions.

Declaration of Authorship

I, **Hongming Zhang**, declare that the report entitled **Compressed Sensing Aided Design Aspects of Indoor Attocells** and the work presented in it are my own and has been generated by me as the result of my own original research. I confirm that:

- This work was done wholly or mainly while in candidature for a research degree at this University;
- Where any part of this thesis has previously been submitted for a degree or any other qualification at this University or any other institution, this has been clearly stated;
- Where I have consulted the published work of others, this is always clearly attributed;
- Where I have quoted from the work of others, the source is always given. With the exception of such quotations, this thesis is entirely my own work;
- I have acknowledged all main sources of help;
- Where the thesis is based on work done by myself jointly with others, I have made clear exactly what was done by others and what I have contributed myself;
- Parts of this work have been published.

Signed: .... Date: ....

Acknowledgements

I would like to express my appreciation and thanks to my supervisors Prof. Lie-Liang Yang and Prof. Lajos Hanzo for their tremendous guidance and constructive comments. I also wish to thank to Prof. Sheng Chen, Dr. Soon Xin Ng, Dr. Rob Maunder, Dr. Mohammed El-Hajjar and Dr. Rong Zhang for their criticism and suggestions about my research work. Meanwhile, I am grateful to the other members in the Southampton wireless group for their kind suggestions. I wish to express my gratitude to all the staffs of the Hartley Library at University of Southampton for providing a nice, quiet and friendly environment during my PhD studies.

Finally, I am grateful to my parents for their financial support of my PhD studies. Special thanks to them for their endless love.

List of Publications

Journal Papers

1. **Hongming Zhang**, L.-L. Yang and L. Hanzo, “Performance analysis of orthogonal frequency division multiplexing systems in dispersive indoor power line channels inflicting asynchronous impulsive noise”, *IET Communications*, vol. 10, pp.453-461, 2016.

2. **Hongming Zhang**, L.-L. Yang and L. Hanzo, “Compressed Impairment Sensing-Assisted and Interleaved-Double-FFT-Aided Modulation Improves Broadband Power Line Communications Subjected to Asynchronous Impulsive Noise”, *IEEE Access*, vol. 4, pp.81-96, 2016.

3. **Hongming Zhang**, L.-L. Yang and L. Hanzo, “Compressed Sensing Improves the Performance of Subcarrier Index-Modulation Assisted OFDM”, *IEEE Access*, vol. 4, pp.7859-7873, 2016.

4. **Hongming Zhang**, L.-L. Yang and L. Hanzo, “Piecewise Companding Transform Assisted Optical-OFDM Systems for Indoor Visible Light Communications”, *IEEE Access*, vol. 5, pp.295-311, 2017.

5. **Hongming Zhang**, L.-L. Yang and L. Hanzo, “Joint Compressed Impairment Sensing and Symbol Detection for Broadband Power Line Communications”, to be submitted.

6. **Hongming Zhang**, L.-L. Yang and L. Hanzo, “Compressed Sensing Assisted Index Modulation”, to be submitted.

7. **Hongming Zhang**, L.-L. Yang and L. Hanzo, “Compressed Sensing Aided Optical OFDM for Visible Light Communications”, to be submitted.

8. T. Bai, **Hongming Zhang**, R. Zhang, A. Rawi, J. Zhang, L.-L. Yang and L. Hanzo,

"Discrete Multi-Tone Digital Subscriber Loop Performance in the Face of Impulsive Noise", to be submitted.

Conference Papers

1. **Hongming Zhang** and L.-L. Yang and L. Hanzo, "LDPC-Coded Index-Modulation Aided OFDM for In-Vehicle Power Line Communications", *2016 IEEE 83rd Vehicular Technology Conference (VTC Spring)*, May 2016, pp.1-5.

Basic Notations

$\mathbb{B}$	the bit set containing $\{0, 1\}$
$\mathbb{Z}$	the ring of integers
$\mathbb{Z}[j]$	the ring of Gaussian integers, which is defined as $\mathbb{Z}[j] \triangleq \{a + jb : a, b \in \mathbb{Z}\}$
$\mathbb{Z}[\omega]$	the ring of Eisenstein integers, which is defined as $\mathbb{Z}[\omega] \triangleq \{a + \omega b : a, b \in \mathbb{Z}\}$ with $\omega = \exp(j2\pi/3)$
$\mathbb{Q}$	the rational field
$\mathbb{R}$	the real field
$\mathbb{C}$	the complex field
$\mathbb{Q}(\alpha_P)$	the cyclotomic field with α_P being a primitive Pth root of unity in $\mathbb{C}$
$\boldsymbol{x}$ and $\boldsymbol{X}$	vector in boldface lower-case and matrix in boldface upper-case, respectively
$\boldsymbol{x}_{\mathrm{T}}$ and $\boldsymbol{x}_{\mathrm{F}}$	time-domain (TD) and frequency-domain (FD) vectors in boldface lower-case, respectively
$\boldsymbol{x}(l)$ and $x(m, l)$	lth block of symbols and mth symbol of lth block, respectively
X and x	Random variables and their realisations in upper-case and lower-case letters, respectively

List of Variables

Latin Letters

a_q	the qth candidate in the alphabet of a QAM/PSK scheme
b_i	the ith bit used for symbol mapping
d	the time duration
e	the base of the natural logarithm
f	frequency

f_{B}	bandwidth
g	the group index
j	is a primitive fourth root of unity, where $j = \sqrt{-1}$
k	sparsity level of a vector
m	the dimensional size of a vector containing measurements in compressed sensing
s_i	the ith state
t	time
t_{stop}	the stopping time of an algorithm
v_{p}	the phase velocity
$\boldsymbol{A}$	the measurement matrix in compressed sensing
E_b^{Rx}	received energy per bit in Joule-per-bit
G	the total number of groups of symbols
$\boldsymbol{H}_{\mathrm{cir}}$	a circulant matrix
$\boldsymbol{I}_m$	the $(m \times m)$-element identity matrix
L	the total number of bits conveyed within a symbol block
L_M	the number of OFDM blocks
L_{cp}	the length of a cyclic prefix
L_{h}	the taps of a multipath channel
$L_{\Pi_{\mathrm{s}}}$	the size of an interleaver Π_{s}
L_{SF}	the spreading factor of an interleaver

M	the IFFT/FFT size in an OFDM system
M_d	the number of data symbols in an OFDM block
N	the dimensional size of a sparse vector
N_0	the PSD for complex AWGN
P_{ab}	the transition probability from state s_a to state s_b
P_T	the total power consumed by a transmitter
P_Tx	the total power of the transmitted signal
Q	the constellation size of a QAM/PSK shceme
T_s	the OFDM block duration
T_coh	the channel coherence time
$\boldsymbol{U}$	a linear precoding matrix
V_C	the coding gain
V_D	the diversity gain
$\boldsymbol{W}$	the equalisation matrix

Greek Letters

α_P	a primitive Pth root of unity
γ_0	the average SNR per bit
γ_s	the average SNR per symbol
$\bar{\gamma}_\mathrm{d}$	the average SINR per data symbol

δ_{Π}	the minimum coding product of an interleaved
$\delta_{\mathcal{E}}$	the squared minimum produce distance
$\varepsilon_{\mathrm{TH}}$	the threshold
$\varepsilon_{\min}$	the lower bound clipping level
$\varepsilon_{\max}$	the upper bound clipping level
ε_X and ε_S	the cutoff levels of a compander
ε_o	the break-points of a compander
η_{SE}	the spectral efficiency
η_{EE}	the energy efficiency
θ	the angle
λ_i	the ith nonzero eigenvalues of a matrix
μ	the symbol mapping rule
$\mu_{\boldsymbol{A}}$	the mutual coherence of a matrix $\boldsymbol{A}$
π	a constant value defined as the ratio of a circle's circumference to its diameter
Λ_{P}	the ratio of the impulsive noise power to the background noise power
Λ_{T}	the ratio of the average duration time and the average inter-burst arrival time
Π_{s}	a symbol interleaver
$\boldsymbol{\Upsilon}_{\mathcal{I}}$	the mapping matrix whose columns are extracted from an identity matrix according to an index set $\mathcal{I}$
Φ_{s_0} and Φ_{s_1}	the PSDs of background noise and impulsive noise, respectively
Ω_0 and Ω_1	the average inter-burst arrival time and the average duration time of asynchronous impulsive bursts

List of Sets

$\mathcal{A}$	the alphabet of a QAM/PSK scheme
$\mathcal{B}$	the bounded set of a noise vector
$\mathcal{E}$	a set contains error vectors
$\boldsymbol{\mathcal{F}}_M$ and $\boldsymbol{\mathcal{F}}_M^H$	the $(M \times M)$-element DFT and IDFT matrices, respectively
$\mathcal{I}_{\mathrm{d}}$	an index set for data symbols in a compressed sensing assisted system
$\mathcal{I}_{\mathrm{p}}$	an index set for pilots
$\mathcal{M}_{\mathrm{d}}$	an index set for data symbols in OFDM system
$\mathcal{P}$	a set of row indices for the design of measurement matrix in compressed sensing
$\mathcal{S}$	an index set for states
$\mathcal{T}$	an index set for nonzero elements of a sparse vector
$\mathcal{V}$	a symbol codebook
$\mathcal{Z}$	a set contains index modulated symbols
$\mathbb{B}^L$	the set of L elements in the bit space containing $\{0, 1\}$
$\mathbb{Z}_+^N$	a set of real integers containing $\{1, 2, \ldots, N\}$
$\mathbb{R}^{M \times L}$	the set of $(M \times L)$-element matrices in the real field
$\mathbb{C}^{M \times L}$	the set of $(M \times L)$-element matrices in the complex field

Mathematical Operators and Functions

$(\cdot)^T$ and $(\cdot)^*$	the transpose and the conjugate, respectively
$(\cdot)^H$ and $(\cdot)^{-1}$	the conjugate transpose and the inverse, respectively
$f(x)$	the output of a function f given a input x
$\int\limits_a^b f(x)\mathrm{d}x$	the definite integral of a function $f(x)$ over the interval $[a, b]$
$p_X(x)$	the probability density function of a random variable $X = x$
$g_X(x)$	the probability sub-density function of a random variable $X = x$
$P_X(x)$	the cumulative distribution function of a random variable $X \leq x$
$Q(x)$	the Q-function defined as $Q(x) = \int\limits_x^\infty e^(- u^2/2)/\sqrt{2\pi}\mathrm{d}u$
$Q_1(0, x)$	the special case of the first order Marcum Q-function defined as $Q_1(0, x) = e^{-x^2/2}$
$\mathbb{E}[\cdot]$	the expectation operator
$\mathcal{O}[\cdot]$	the big O of operator
$\mathcal{F}\{\cdot\}$ and $\mathcal{F}^{-1}\{\cdot\}$	the Fourier transform and the inverser Fourier transform, respectively
$\mathrm{diag}(\boldsymbol{x})$	a diagonal matrix with diagonal entries given in $\boldsymbol{x}$
$\mathrm{rank}(\boldsymbol{X})$	the rank of a matrix $\boldsymbol{X}$
$\det \boldsymbol{X}$	the determinant of a matrix $\boldsymbol{X}$
$tr(\boldsymbol{X})$	the trace of a matrix $\boldsymbol{X}$
$\Re\{x\}$ and $\Im\{x\}$	the real and the imaginary parts of a complex-valued variable x
$\lvert\mathcal{A}\rvert$	the cardinality of the set $\mathcal{A}$
$Supp(\boldsymbol{x})$	the support of a vector $\boldsymbol{x}$, which is defined as $Supp(\boldsymbol{x}) \triangleq \{i : x(i) \neq 0\}$

Abbreviations

2D	Two-Dimensional.
2G	Second-Generation.
5G	Fifth-Generation.
ACO-OFDM	Asymmetric Clipping based Optical OFDM.
ADO-OFDM	Asymmetric clipping and Direct-current-bias based Optical OFDM.
APM	Amplitude-Phase Modulated.
AWGN	Additive White Gaussian Noise.
BB-PLC	BroadBand Power Line Communication.
BLUE	Best Linear Unbiased Estimator.
BP	Basis Pursuit.
BPDN	Basis Pursuit De-Noising.
CCDF	Complementary Cumulative Distribution Function.
CDF	Cumulative Distribution Function.
CIOD	Coordinate Interleaved Orthogonal Design.
CIR	Channel Impulse Response.
CIS	Compressed Impairment Sensing.
CO-OFDM	Clipping-based Optical OFDM.
CoSaMP	Compressive Sampling Matching Pursuit.
CP	Cyclic Prefix.
CPsDF	Constant Probability sub-Distribution Function.
CS	Compressed Sensing.
CSI	Channel State Information.
CSIM	Compressed Sensing assisted Index Modulation.
CSIR	Channel State Information at the Receiver side.
CT	Companding Transform.
CTF	Channel Transfer Function.
D2D	Device-to-Device.
DAC	Digital-to-Analog Conversion.

DCO-OFDM	Direct Current biased Optical OFDM.
DFT	Discrete Fourier Transform.
EE	Energy Efficiency.
EMC	ElectroMagnetic Compatibility.
ETF	Equiangular Tight Frame.
FD	Frequency-Domain.
FDCHTFs	Frequency-Domain CHannel Transfer Factors.
FEC	Forward Error Correction.
FFT	Fast Fourier Transform.
GHz	GigaHertz.
GIRCD	Generalised Iterative Residual Check Detector.
HetNets	Heterogeneous Networks.
HSMM	Hidden Semi-Markov Model.
i.i.d.	Independent and Identically Distributed.
ICI	Inter-Carrier Interference.
IDFFT	Interleaved-Double-FFT.
IDFT	Inverse Discrete Fourier Transform.
IEEE	Institute of Electrical and Electronics Engineer.
IFDMA	Interleaved Frequency Division Multiple Access.
IFFT	Inverse Fast Fourier Transform.
IHT	Iterative Hard Thresholding.
IRCD	Iterative Residual Check Detector.
ISI	Inter-Symbol Interference.
ISM	Industrial, Scientific and Medical.
ITU	International Telecommunication Union.
JML	Joint Maximum-Likelihood.
JMLD	Joint Maximum-Likelihood Detector.
LASSO	Least Absolute Shrinkage and Selection Operator.
LCP-OFDM	Linear Constellation Precoded OFDM.
LED	Light Emitting Diode.
LHS	Left-Hand-Side.
LiFi	Light-Fidelity.
LLR	Log-Likelihood Ratio.
LPIM	Linear Precoding assisted Index Modulation.
LPsDF	Linear Probability sub-Distribution Function.
LS	Least Square.

MAP	Maximum *A Posterior*.
MAR	Maximum Achievable Rate.
MIMO	Multiple-Input-Multiple-Output.
MIP	Mutual Incoherence Property.
ML	Maximum-Likelihood.
MMSE	Minimum Mean Square Error.
MP	Matching Pursuit.
MPD	Minimum Product Distance.
MWBE	Maximum-Welch-Bound-Equality.
NB-PLC	NarrowBand Power Line Communication.
NLOS	Non-Line Of Sight.
NLPsDF	Non-Linear Probability sub-Distribution Function.
O-OFDM	Optical Orthogonal Frequency-Division Multiplexing.
OFDM	Orthogonal Frequency-Division Multiplexing.
OLS	Ordinary Least Square.
OMP	Orthogonal Matching Pursuit.
OOK	On-Off Key.
PD	PhotoDetector.
PDF	Probability Density Function.
PEP	Pairwise Error Probability.
PLC	Power Line Communication.
PMF	Probability Mass Function.
PSD	Power Spectral Density.
PsDF	Probability sub-Distribution Function.
PSK	Phase-Shift Keying.
QAM	Quadrature Amplitude Modulation.
QoS	Quality-of-Service.
QPSK	Quadrature Phase-Shift Keying.
RF	Radio Frequency.
RHS	Right-Hand-Side.
RIP	Restricted Isometry Property.
ROP	Restricted Orthogonality Property.
SC-FDMA	Single-Carrier Frequency-Division Multiple Access.
SE	Spectral Efficiency.
SIM	Subcarrier Index Modulation.
SINR	Signal-to-Interference-plus-Noise power Ratio.
SM	Spatial Modulation.
SNR	Signal-to-background Noise power Ratio.

TD	Time-Domain.
TPC	Transmit Pre-Coding.
TV	TeleVision.
VLC	Visible Light Communication.

Contents

Chapter 1

Introduction

1.1 Motivation

Over the past three decades, a 1000-fold bit rate improvement was achieved. At the time of writing, wireless communications is capable of providing high-data-rate services to users across the globe [1]. In the next decade, a further substantial increase of mobile data traffic is predicted by the market study of [2]. The exponential growth of teletraffic forces vendors and operators to further improve the performance of wireless networks. Generally, the network capacity can be improved by designing advanced coding and signal processing techniques, as well as by expanding the available bandwidth, as shown in the red and blue frames of Fig. 1.1, respectively.

As a benefit of the substantial research efforts inspired by Shannon's pioneering paper [3], the attainable link-capacity of wireless Radio Frequency (RF) techniques is approaching the Shannon limit, as shown in [1, 4, 5] and the references therein. Hence, only a limited link-capacity gain can be achieved by further developments of coding and/or signal processing techniques for the traditional cellular network. For this reason, more and more attention has been paid to expanding access to the hitherto unused parts of the electromagnetic spectrum. Typically, the exploitation of electromagnetic spectrum can be expanded by using smaller cells as well as by exploiting the unlicensed spectrum, as illustrated in Fig. 1.1. On one hand, reusing the RF spectrum relies on the fact that the RF waves are attenuated by the path-loss. Hence, the same frequency band can be reused after a sufficiently long distance, which has been routinely exploited by cellular networks, see Chapter 15 of [6] for details. On the other hand, the use of unlicensed spectrum is based on the opportunistic consideration that the unlicensed frequency bands can be used for data transmission in a certain area without suffering from excessive in-band interference or crosstalk. A

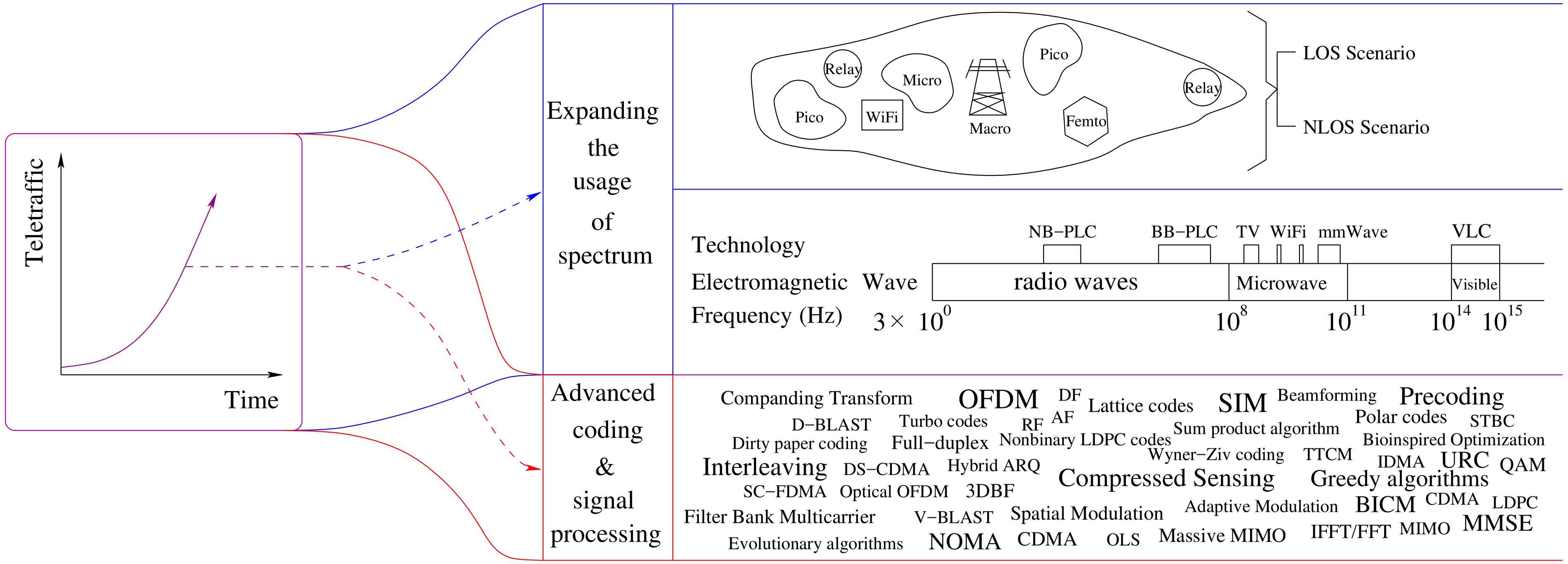

Figure 1.1: Efficient techniques of accommodating the dramatic growth of teletraffic.

well-known example is WiFi, where the 2.4 GigaHertz (GHz) Industrial, Scientific and Medical (ISM) frequency band is configured to transmit data in local area networks, see [7] for details. Both methods exploit the fact that reliable data transmission can be achieved, when the in-band interference is under a certain level. A similar idea will be adopted in Chapter 2 of this treatise.

Relying on reusing the RF spectrum within an ever-denser geographic area accompanied by the technological evolution of digital cellular network all the way from the Second-Generation (2G) to the Fifth-Generation (5G) systems, a significant improvement in network capacity has been achieved. A recent development associated with the cell-size reduction led to the creation of Heterogeneous Networks (HetNets) [8, 9]. As shown in Fig. 1.1, in a HetNet, small microcells, picocells, femtocells, attocells, relays and distributed antenna systems are overlaid on top of the macrocells. In comparison to expensive tower-mounted base stations, small cells rely on low-cost access points imposing low power consumption. Both the licensed and unlicensed spectrum are used in HetNets. Furthermore, as pointed out in [10], future HetNets may also include 'cloud' base stations for providing a centralised server platform for sophisticated central signal processing. As a benefit of their flexibility, HetNets are capable of adjusting their spatial reuse; hence supporting both a wide coverage area, seamless connectivity and a high Quality-of-Service (QoS).

The above-mentioned techniques are capable of reducing network congestion, even in Non-Line Of Sight (NLOS) indoor environments, such as homes, offices, shopping centres, underground stations, and so forth. This is important, because as shown in [11], over 50 percent of voice calls and 70 percent of data traffic are originated from indoor environments. However, operators can hardly provide high data rates and a high QoS for indoor users at a competitive price due to the high outdoor-to-indoor penetration losses. This may lead to coverage dead zones for macrocell vendors. In order to eliminate coverage dead zones, the above-mentioned WiFi, femtocells as well as cognitive radios exploiting the TeleVision (TV) white space can be employed. Specifically, in the femtocell network, femtocell access points, which are home base stations characterised by low cost and low power, are installed for supporting high data rates and a high QoS for indoor users. Hence, in comparison to microcells and picocells, whose installation is carried out by operators, the femtocell deployment is directly arranged by the subscribers. Although it seems that femtocells resemble WiFi, their standards and licensed spectrum allocations are different. The most appealing aspect of the femtocell network is that it is capable of providing both a high data rate as well as a high QoS for users in a cost efficient way. Nonetheless, there are also technical challenges, such as those associated with interference coordination,

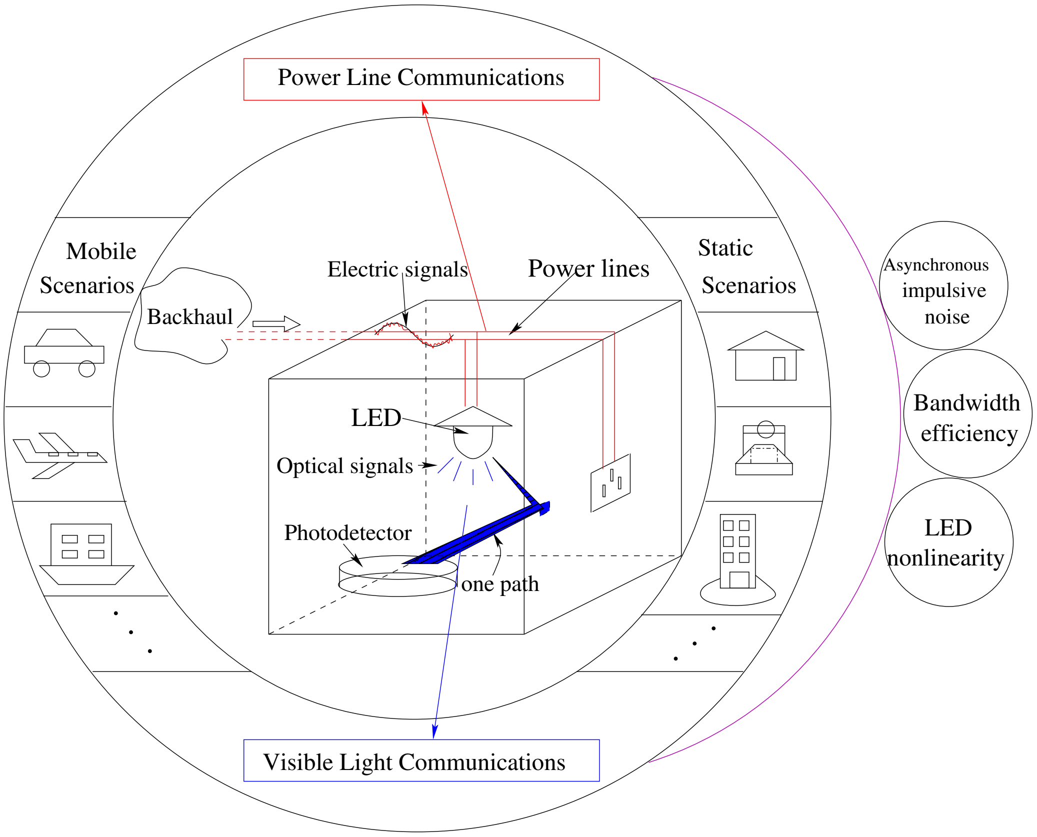

Figure 1.2: Integration of power line communications (PLCs) and visible light communications (VLCs).

cell association and biasing, handover and self-organisation issues, as detailed in [12].

1.2 An Introduction to indoor attocells

A compelling technique, which is capable of tackling some of the above issues, is the indoor attocell network. The indoor attocell networks rely on the integrated Power Line Communication (PLC) and Visible Light Communication (VLC) system, as illustrated in Fig. 1.2. The basic idea of this integrated system was proposed in [13]. Explicitly, the power lines are connected to either a wired or wireless backhaul network, forwarding data signals to VLC. On the other hand, owing to its energy efficiency, longevity as well as reliability, Light Emitting Diode (LED) is expected to become the dominant light source of the near future, which is used for data transmission in our PLC/VLC setup. Hence, the LED lamps are used for both illumination and wireless signal transmissions. This integrated technology has several advantages. Firstly, it is a cost-efficient technology, since it relies on the existing electrical supply networks and illumination infrastructure. Secondly, the huge unlicensed bandwidth of visible light can be exploited by the integrated PLC/VLC system without inflicting interference upon the existing RF communications. Finally, since the partitioning walls are impervious to visible light, a unity spatial reuse factor can be attained by VLCs operating in different areas. Next, let us briefly describe the integrated PLC/ VLC system.

As shown in Fig. 1.2, the electric signals, which propagate over the power lines, are converted to optical signals by the LED lamp. Then, the emitted visible light, which conveys the information to the end users, is detected by the optical receiver, as shown in Fig. 1.2. In this way, the integrated PLC/VLC system is capable of providing downlink services for customers. Explicitly, two types of communications channels, namely PLC channels and VLC channels, are involved in the integrated PLC/VLC systems. In particular, these physical links are united by the LED associated with the electrical-to-optical conversion. Therefore, it is essential to accurately characterise both the LEDs and the associated pair of communication channels, in order to design an efficient PLC/VLC system, as well as to predict the systems' attainable performance both in fixed and mobile scenarios. The static scenario includes underground platforms, offices, shopping malls, residential properties, etc. By contrast, the mobile scenario includes cars, ships, trains, planes and so forth. Different scenarios have their individual VLC and PLC characteristics. We will focus our attention on the static scenario in this treatise. Before providing more details, let us first present a brief history of both VLC and PLC.

1.2.1 A Brief History of Visible Light Communications and Power Line Communications

The history of VLC dates back to the 1880s, when Alexander Graham Bell invented a device known as the photophone, which was capable of transmitting speech modulated onto sunlight. However, Bell's initial design failed to protect data transmission from atmospheric interference, which prohibited the wide-spread employment of his great invention [14]. Given the rapid development of radio and optical fiber communications, limited attention was paid to VLCs. It was not until the 2000s, when optical wireless was re-discovered as a potential candidate for local area networks. In their seminal paper, Kahn and Barry presented an excellent demonstration of optical wireless communications [15], where LEDs and laser diodes were suggested as the potential optical transmitter for wireless optical communications. As a benefit of the rapid development of LED technology, LEDs are set to replace the conventional incandescent and fluorescent lamps in the near future. Following this trend, in 2003, the Nakagawa Laboratory demonstrated the employment of VLCs using LEDs for transmission [16]. Since then, VLCs have attracted increasing attention worldwide. In 2011, Haas coined the terminology of Light-Fidelity (LiFi) networks in a talk at the TEDGlobal [17], showing the wide range of potential applications of VLC. In the same year, Institute of Electrical and Electronics Engineer (IEEE) published a standard for VLC [18]. In 2016, Qualcomm introduced a technology termed as Lumicast for mobile device positioning in indoor environments [19].

On the other hand, the first patent in the area of PLCs was submitted in 1897 [20]. Since then, devices relying on PLC have been developed for reading meters at remote locations, for remote control of lighting, etc. During World War II, PLC systems were designed for transmitting speech signals, when RF communications was restricted and when most telephone lines were destroyed. Since the 1980s, research interests in PLCs have began to focus on designing high data rate systems in the frequency band between 3 kHz and 500 kHz, which are referred to as the NarrowBand Power Line Communication (NB-PLC) systems. These advances were facilitated by powerful Forward Error Correction (FEC) coding schemes and multicarrier modulation schemes. In 1997, Nortel and Norweb Communications in the U.K. developed a BroadBand Power Line Communication (BB-PLC) system to provide Internet access for customers. However, the development of BB-PLCs was affected by a lot of technical obstacles, which resulted in limited success for BB-PLCs. During the recent decade, a lot of research efforts have been inverted in the implementation of BB-PLCs. Some recent standards and specifications were recommended by the IEEE [21] in 2010, by the International Telecommunication Union (ITU) [22] in 2011, by the HomePlug [23] in 2013, etc.

1.2.2 Problem Statements

Since neither the power line systems nor the lighting systems have been designed for data communications, they constitute a hostile propagation environment and there are still a lot of challenges to be tackled. In particular, the PLC channels and VLC channels have their own technical challenges. Hence, we first decompose the integrated PLC/VLC system into a stand-alone PLC system and a VLC system, and then consider them in isolation, as illustrated in Fig. 1.2. The detailed discussions of the problems will be postponed to Chapter 2, Chapter 3 and Chapter 4, but below we introduce the basic problems of interest.

Generally, in comparison to VLC channels, PLC channels constitute a hostile propagation environment [24] characterised by their propagation path-loss, multipath propagation, as well as impulsive noise. According to its relationship with respect to the mains cycle, impulsive noise can be classified into three types, namely periodic mains-synchronous impulsive noise, periodic impulsive noise that is asynchronous with the mains, as well as asynchronous impulsive noise [25]. Typically, the asynchronous impulsive noise, which is mainly caused by the connection and disconnection of electrical devices, is the major impairment of BB-PLC due to its high power and unpredictable nature. The detailed characterisation of PLC channels will be given in Chapter 2.

We will consider a low-cost, low-complexity non-coherent scheme known as intensity modulation and direct detection (IM/DD) in VLC for modulating the intensity of LEDs. In IM/DD VLC systems, only real-valued and positive signals can be used for modulating the intensity of optical sources, where the intensity envelope is detected by the optical receiver [15]. As verified by experimentations in [26–28], the data rate of VLC can be significantly improved by employing Optical Orthogonal Frequency-Division Multiplexing (O-OFDM) signalling, in comparison to the single carrier modulation schemes, such as On-Off Key (OOK). However, challenges occur when Orthogonal Frequency-Division Multiplexing (OFDM) signalling is employed for high-rate transmissions in IM/DD VLC. Firstly, the classic OFDM signals in the Time-Domain (TD) are complex-valued, due to the inverse Fourier transform. Hence, complex-to-real conversion is required in order to meet the requirements of IM/DD VLC. The corresponding drawback is the reduction of bandwidth efficiency, which constitutes the first VLC problem to be addressed in this report. The second VLC problem to be tackled in this report arises from the limited dynamic range of LEDs. For example, a LED, which radiates optical power from the p-n junction [29], has a limited linear operational range, where the output optical signals increase linearly with the input driving current. As a result, the response becomes nonlinear, when the driving current is either lower than a threshold or higher than a threshold. Hence, the nonlinearity of the LED usually leads to the loss of orthogonality for O-OFDM signals, generating Inter-Carrier Interference (ICI). As a result, the corresponding system's performance may be severely degraded. We refer to [1] for details of other related challenges.

1.2.3 Discussions of the Problems Investigated

> “ *Research motivated by issues of performance versus complexity will always be in fashion, and measures of “complexity” are sure to be redefined by future generations of technology.*”
>
> by D. J. Costello and G. D. Forney in [4]

Following Shannon's celebrated coding theorem, digital communications have been widely studied in terms of error performance, bandwidth efficiency (or Spectral Efficiency (SE)) and power efficiency (or Energy Efficiency (EE)). As a result, these studies have provided an insightful guidance to the advanced design of coding and signal processing techniques, which led to the sweeping success of wireless RF communications in practical applications [1, 5]. Generally, the above-mentioned issues can be tackled with the aid of advanced coding and signal processing, such as those illustrated in Fig. 1.1. However, the techniques designed for wireless RF communications cannot be directly employed to PLC or to VLC, as it will be shown in the following chapters. Typically, high performance is achieved at the cost of high signal processing complexity. As pointed out by Costello and Forney [4], " *Research motivated by issues of performance versus complexity will always be in fashion, and measures of "complexity" are sure to be redefined by future generations of technology.*" Therefore, in this treatise, we focus our attention on tackling the above-mentioned problems with an emphasis on the trade-off between the systems' performance and complexity. Specifically, the popular technique of Compressed Sensing (CS) is applied as the central tool to solve our problems. Next, let us now embark on a rudimentary overview of CS.

1.3 Overview of Compressed Sensing

> *Entia non sunt multiplicanda praeter necessitatem.*
> *(More things should not be used than are necessary.)*
> by William of Ockham (1285-1347)

1.3.1 Background on Compressed Sensing

Let us consider the issues of parameter estimation in linear regression, which constitute a classic topics in the field of statistics and signal processing. For more details about linear regression, we refer to [30]. The task is to estimate the parameters of a linear mapping so that the functional dependence between its inputs and outputs can be accurately described. To elaborate further, let us denote the ith training data as $(y_i, \boldsymbol{a}_i)$, where $\boldsymbol{a}_i \in \mathbb{R}^N$ is the input vector drawn from an N-dimensional vector space containing elements from the filed of real numbers, while $y_i \in \mathbb{R}$ represents the corresponding output also from the field of real numbers. Given m training data samples of $\boldsymbol{y} = [y_0, \ldots, y_{m-1}]^T \in \mathbb{R}^m$ and $\boldsymbol{A} = [\boldsymbol{a}_0, \ldots, \boldsymbol{a}_{m-1}]^T \in \mathbb{R}^{m\times N}$, the model given by $\boldsymbol{y} = \boldsymbol{A}\boldsymbol{x} + \boldsymbol{n}$ indicates that the response is a linear function of the inputs, where each element in the noise vector $\boldsymbol{n} \in \mathbb{R}^m$ is Independent and Identically Distributed (i.i.d.) and is assumed to be real-valued white Gaussian noise obeying $\mathcal{N}(0, \sigma_{\mathrm{n}}^2)$. Here, we assume that the noise variance σ_{n}^2 is known. In this case, the corresponding linear model can be represented by the conditional probability $p(\boldsymbol{y}|\boldsymbol{A}, \boldsymbol{x}) = \mathcal{N}(\boldsymbol{A}\boldsymbol{x}, \sigma_{\mathrm{n}}^2 \boldsymbol{I}_m)$, where $\boldsymbol{I}_m$ represents the $(m \times m)$-element identity matrix. Thus, the goal is to estimate the unknown parameters in $\boldsymbol{x} \in \mathbb{R}^N$ for the above model. The simplest method of addressing the above issue is the well-known Ordinary Least Square (OLS) estimator [30], which is identical to the popular Maximum-Likelihood (ML) estimator in our scenario. For example, when $\boldsymbol{A}$ is of full rank and $m \geq N$, the OLS estimator effectively finds the particular solution that minimises the sum of squared errors, hence yielding the estimates expressed as $\boldsymbol{x}^{\mathrm{OLS}} = (\boldsymbol{A}^T \boldsymbol{A})^{-1} \boldsymbol{A}^T \boldsymbol{y}$. Finding the OLS estimate imposes a low complexity and it is also known as the Best Linear Unbiased Estimator (BLUE) [30]. However, when the problem is ill-posed or the model suffers from overfitting, the OLS estimator may perform poorly. For example, in the scenario of prediction, applying OLS estimation to the current input, which is slightly different from the previous input, may result in an output exhibiting a much larger prediction error than expected. A commonly used technique of ameliorating this problem is regularisation [31], which modifies the cost function by adding a penalised term. A celebrated example is ℓ_2 regularisation, which is also known as ridge regression or Tikhonov regularisation [32]. In ℓ_2 regularisation, a weighted ℓ_2-norm of the unknown vector $\boldsymbol{x}$ is added to the cost function, which is referred to as penalisation. In this case, the solution that minimises the regularised cost function can be formulated as $\boldsymbol{x}^{\ell_2} = (\boldsymbol{A}^T \boldsymbol{A} + \gamma^{-1} \boldsymbol{I}_N)^{-1} \boldsymbol{A}^T \boldsymbol{y}$ with a tuning parameter γ^{-1} introduced for controlling the amount of regularisation. Hence, the ℓ_2 regularisation deals with the above-mentioned problem by introducing bias into the estimator, yielding an improved estimation performance. Typically, both the OLS and the ℓ_2 regularisation have the striking capability of analytically solving estimation problems. This is because their cost functions are in the form of the ℓ_2-norm, which is strictly convex and can hence be solved analytically.

1.3.2 The Manifestation of Sparsity

However, as argued by Tibshirani in [33], ℓ_2 regularisation does not result in an easily interpretable model. To pose the problem, we assume that the unknown parameters in $\boldsymbol{x}$ are correlated and they are only characterised by k features, where k is smaller than the total number of the unknown parameters, i.e. we have $k < N$. In other words, there are k relevant variables and $(N - k)$ redundant variables associated with the N-dimensional unknown vector $\boldsymbol{x}$. When the k relevant variables are given, it is certainly preferred to characterise the corresponding model with the aid of this more compact representation, rather than by all the N parameters in $\boldsymbol{x}$. In this case, ℓ_2 regularisation certainly does not improve the interpretability of the model. In fact, this phenomenon is observed in the spirit of *Occam's razor*, as highlighted at the beginning of this section. This issue can also be encountered in telecommunications, when channel estimation is performed. For example, let us consider the scenario of OFDM systems communicating over a multipath channel characterised by k non-zero valued variables in the TD. The task is to estimate the channel with the aid of the Frequency-Domain (FD) received symbols in order to improve the decoding performance. In this case, for different OFDM systems employing different IFFT/FFT sizes, the corresponding Frequency-Domain CHannel Transfer Factors (FDCHTFs) are different. By contrast, the TD channel coefficients remain the same, which are hence less redundant in terms of characterising the model. Thus, it is convenient to estimate the TD channel coefficients, rather than by the FDCHTFs. This trend becomes more evident, as the FFT size becomes large. A widely used method of addressing the above issues is ℓ_1 regularisation, where the cost function is modified by adding a weighted ℓ_1-norm based penalisation term to the cost function. Based on the specific constraints, ℓ_1 regularisation can be formulated into the Least Absolute Shrinkage and Selection Operator (LASSO) [33] and the Basis Pursuit De-Noising (BPDN) [34]. As shown in [33], upon taking into account the ℓ_1-norm based weighting in the penalised term, the LASSO is capable of performing both adaptive relevance selection and regularisation. Therefore, it is capable of attaining both a good estimation performance, as well as making the model more interpretable. Let us now temporarily turn our attention to the selection of the relevant variables, which is known as the variable selection.

Variable selection (or feature selection) is a widely used technique both in statistics and in machine learning [35]. In variable selection, it is a natural option to set the redundant variables to zero. Let us assume that in the above-mentioned linear model of $\boldsymbol{y} = \boldsymbol{A}\boldsymbol{x} + \boldsymbol{n}$, the N-dimensional parameter vector $\boldsymbol{x}$ contains k variables that accurately represent the model. For the sake of augmented interpretability, it is preferable to perform the estimation by an N-dimensional target vector containing $(N-k)$ zero-valued elements, rather than to estimate all the N variables in $\boldsymbol{x}$. Hence, the corresponding cost function can be modified by a weighted ℓ_p-norm of the target vector $\boldsymbol{x}$, where p is restricted to $0 \leq p \leq 1$. This can be interpreted by invoking the unit ball of the ℓ_p-norm, as investigated in [36] and demonstrated in [33]. Typically, the scaled unit ball of the ℓ_p-norm of $\boldsymbol{x}$ associated with $0 \leq p \leq 1$ usually intersects with the Least Square (LS) loss function of $\|\boldsymbol{y} - \boldsymbol{A}\boldsymbol{x}\|_2^2$ on the coordinate axes, which is certainly not the general case for the scaled unit ball of the ℓ_p-norm associated with $p > 1$, as exemplified in Fig. 1.3. This implies that the specific solution which minimises the ℓ_p-penalised cost function in conjunction with $0 \leq p \leq 1$ contains zero-valued elements, which meets our previous assumption. We refer to Chapter 23 of [37] for further insights concerning the ℓ_p-norm. At this stage, we conclude our discussions concerning the variable selection phase and return to the ℓ_1 regularisation. A more in-depth discussion on the variable selection phase can be found in [38].

Above we have shown that the variable selection phase can be accomplished by adding the weighted ℓ_p-norm for $0 \leq p \leq 1$. However, the ℓ_p-norm associated with $0 \leq p < 1$ is not convex, hence its employment as an optimisation cost function is not conclusive. Typically, a strictly convex function is preferred since it facilitates the derivation of a closed-form solution, as in the above-mentioned OLS and ℓ_2 regularisation. Hence, when both the variable selection phase and high-precision estimation are required, the ℓ_1 regularisation appears to be the best choice. Since the ℓ_1-norm is weakly convex (convex, but not strictly convex), linear programming can be applied to solve the corresponding optimisation problem, see Chapter 10 and Chapter 11 of [39] for details. Therefore, as the terminology suggests, the LASSO first selects the 'non-redundant' subset of variables (forces the 'redundant' variables to zero), and then shrinks their weighting coefficients by invoking a penalisation technique. However, the LASSO has to avoid excessively shrinking the non-redundant variables as well as to arrive at efficient variable selection. In a little more detail, the LASSO often reduces the absolute-value of the weight to avoid shrinking the relevant variables too much. In this way, the estimation results may contain irrelevant variables (or redundancies), which should have been forced to zero. We refer readers to [40, 41] and references therein for deeper insights. The related decision conflict becomes more severe, as the dimensional size of the irrelevant variables becomes much lower than that of the overall dimension of the problem.

Typically, the above-mentioned scenario, where the number of relevant variables within a vector $\boldsymbol{x}$ is much smaller than the total number of elements in $\boldsymbol{x}$, is referred to as a sparse model. In general, diverse signals, which are involved in areas such as biometric, oceanography, astronomy, communications, to name but a few, are found to either be sparse or have sparse representations. The phenomenon of sparsity enjoys the advantage of cost efficiency owing to its reduced complexity, storage and so forth. Furthermore, researchers have gradually realised that sparsity is capable of improving the interpretability of a fitted model. Intuitively, ℓ_0 regularisation, which employs the pseudo-ℓ_0-norm (for the sake of simplicity, the 'pseudo-ℓ_0-norm' is referred to as the 'ℓ_0-norm' in the sequel), rather than the ℓ_1-norm, as the penalisation term of the regularised cost function, can be applied to tackle the above-mentioned problem, since in this way, the selection of relevant variables can be more explicitly dealt with. However, as mentioned before, the ℓ_0-norm is not convex, resulting in the cost function of ℓ_0 regularisation is also not convex. Hence, the solution of the corresponding minimisation problem may not be unique. In this case, guaranteeing a specific worst-case estimation performance is impossible, even when exhaustive search is performed.

1.3.3 The Development of Overcomplete Dictionaries

The sought-after breakthrough came with the development of overcomplete dictionaries in the field of harmonic analysis [34, 42]. For the sake of concreteness, the noiseless scenario of the former linear model of $\boldsymbol{y} = \boldsymbol{A}\boldsymbol{x}$ is invoked, where $\boldsymbol{A} \in \mathbb{R}^{m \times N}$ represents an overcomplete dictionary associated with $m < N$. The task is to decompose a signal denoted by $\boldsymbol{y}$ with the aid of the overcomplete dictionary $\boldsymbol{A}$ into a sparse vector $\boldsymbol{x}$, where the nonzero elements in $\boldsymbol{x}$ are the coefficients that capture the useful characteristics of the signal. Hence the objective is to find a highly sparse decomposition method for the signal. Note that the dictionary can be either fixed or drawn from a vector space. The latter scenario is usually referred to as dictionary learning. An initial contribution was provided in [42], where a greedy search assisted algorithm, namely the Matching Pursuit (MP), was proposed to find the solution by iteratively generating a locally optimised solution. However, since no specific constraint is imposed on the grade of sparsity, the MP may fail to generate sufficiently sparse results in general. To facilitate a sufficiently sparse decomposition, the authors of [34] proposed a decomposition method termed as the Basis Pursuit (BP), which finds coefficients that minimise the ℓ_1-norm in the context of the above linear model. Note that in a noisy scenario, the BPDN, which was also proposed in [34], is equivalent to ℓ_1 regularisation. Based on the above discussions, we can now readily understand why BP is capable of generating sparse results. However, both the BP and the LASSO share the same inherent problems in terms of finding the optimal sparse solutions in a rigorous manner. After an in-depth analysis of both MP and BP, researchers finally focused their attention on connecting the sparsity based regularisation techniques with the research of dictionaries.

The crucial issue to be addressed is the uniqueness of sparse solutions. In [43], the authors demonstrated that when a signal $\boldsymbol{y}$ is decomposed with the aid of a dictionary, which has the specific form of $\boldsymbol{A} = [\boldsymbol{A}_1, \boldsymbol{A}_2] \in \mathbb{R}^{m \times 2m}$, where $\boldsymbol{A}_1$ and $\boldsymbol{A}_2$ are two $(m \times m)$-element orthonormal bases, into a vector $\boldsymbol{x}$ satisfying $\|\boldsymbol{x}\|_0 < (1 + \mu_{\boldsymbol{A}}^{-1})/$

2, the resultant sparse representation $\boldsymbol{x}$ is the unique solution of not only BP but also of the ℓ_0-minimiser subject to $\boldsymbol{y} = \boldsymbol{Ax}$. Here, the so-called mutual coherence $\mu_{\boldsymbol{A}}$ is defined as the largest absolute correlation coefficient between any two columns of the dictionary $\boldsymbol{A}$. The above-mentioned bound of $\|\boldsymbol{x}\|_0$ was further tightened to $\|\boldsymbol{x}\|_0 < 1/\mu_{\boldsymbol{A}}$ by the authors of [44] for the ℓ_0-norm minimisation under the same assumptions. Later in [45], a more generalised result was presented for arbitrary dictionaries, showing that the condition of $\|\boldsymbol{x}\|_0 < (1 + \mu_{\boldsymbol{A}}^{-1})/2$ is a necessary one for uniqueness. The same result was then extended to a realistic noisy scenario in [46]. So far, the focus has been on restricting the sparsity level of $\boldsymbol{x}$, i.e. $\|\boldsymbol{x}\|_0$. It may also be shown that the above condition can be alternatively described as follows. Assuming that a signal $\boldsymbol{y}$ is decomposed with the aid of a dictionary, while satisfying the mutual coherence of $\mu_{\boldsymbol{A}} < 1/(2k - 1)$, provided that the sparsity level of the resultant $\boldsymbol{x}$ is not higher than k, i.e. we have $\|\boldsymbol{x}\|_0 \leq k$. Then, the resultant sparse solution is unique for both ℓ_1 regularisation and for ℓ_0 regularisation. From this perspective, we can observe that the lower the mutual coherence of $\boldsymbol{A}$, the higher the sparsity level of the representations that can be guaranteed to be unique. For this reason, a dictionary associated with a low mutual coherence is preferred, which hence satisfies the so-called Mutual Incoherence Property (MIP).

In the literature, there is another well-known method of checking the uniqueness of sparse solutions from a mathematical perspective [47–49]. In [47], the above-mentioned sparse representation problem was modelled as the problem of finding sparse solutions for strongly underdetermined systems of linear equations. The authors of [47] demonstrated that the uniqueness of sparse solutions can be satisfied, when the Restricted Isometry Property (RIP) defined as the kth restricted isometry constant δ_k of $\boldsymbol{A}$ is the smallest number, which meets the condition of $(1 - \delta_k)\|\boldsymbol{x}\|_2^2 \leq \|\boldsymbol{Ax}\|_2^2 \leq (1 + \delta_k)\|\boldsymbol{x}\|_2^2$. Another property referred to as the Restricted Orthogonality Property (ROP) [47] is also often used at the same time along with the RIP. To elaborate a little furthers, as defined in [47], a matrix $\boldsymbol{A}$ is said to satisfy the ROP, if the (k_1, k_2)-restricted orthogonality constant θ_{k_1,k_2} is the smallest constant satisfying $|\langle \boldsymbol{Ax}_1, \boldsymbol{Ax}_2 \rangle| \leq \theta_{k_1,k_2}\|\boldsymbol{x}_1\|_2\|\boldsymbol{x}_2\|_2$ for any $\boldsymbol{x}_1 \neq \boldsymbol{x}_2$ with $\|\boldsymbol{x}_1\|_0 \leq k_1$ and $\|\boldsymbol{x}_2\|_0 \leq k_2$. Later, the authors of [48] provided a beautiful interpretation of the RIP from a geometric perspective, making the concept of RIP easier to understand. In [48], the issue of sparse representation is modelled as the problem of finding the stable embedding of data points belonging to a high-dimensional space having N elements (corresponding to $\boldsymbol{x}$) into a lower-dimensional space of m elements (corresponding to $\boldsymbol{y}$). Here, the meaning of the stable embedding is two-fold. Firstly, the embedding has to guarantee that for any $\boldsymbol{x}_1 \neq \boldsymbol{x}_2$, we have $\boldsymbol{Ax}_1 \neq \boldsymbol{Ax}_2$. Secondly, the distance of any $\boldsymbol{x}_1 \neq \boldsymbol{x}_2$ should be ‘nearly’ persevered after mapping it into the lower-dimensional space of m elements. We may view the first case as a noiseless scenario, while the second case as a realistic noisy scenario, both of which describe mathematical uniqueness. Based on the Johnson-Lindenstrauss lemma [50], the RIP was proved and the corresponding geometric interpretations were discussed. The motivated reader is referred to [51] for more comprehensive discussions. So far, we have discussed as to why the RIP can also provide a guarantee for uniqueness. As a further improvement, the authors of [52] established connections between the RIP and the MIP, showing that the conditions of $\delta_k \leq (k-1)\mu_{\boldsymbol{A}}$ and $\theta_{k_1,k_2} \leq \mu_{\boldsymbol{A}}\sqrt{k_1 k_2}$ hold. From this result, we can infer that in contrast to specifying the kth restricted isometry constant δ_k, the RIP can also be satisfied by specifying the upper bound of δ_k, i.e. the mutual coherence $\mu_{\boldsymbol{A}}$. Roughly speaking, a dictionary satisfying the MIP also satisfies the RIP. This result became practically important, since it was formally shown in [53] that computing δ_k is NP hard. For this reason, we focus our attention on the MIP in this treatise, when dealing with the theoretical analysis of the uniqueness of sparse solutions. For more details and improvements concerning the RIP, the interested readers may consult [49] for example.

1.3.4 Compressed Sensing

Finally, these developments have given birth to an emerging field known as Compressed Sensing [54] or Compressive Sampling [55] (CS). In this treatise, we opt for compressed sensing as our terminology, since it first appeared in a technical report of Donoho in 2004. Later in 2006, it was published in [54]. Immediately after the concept was introduced, CS has drawn a vast amount of research attentions [56–69]. The basic concept was studied by several superb review articles, e.g. [56–59]. It has also been applied to numerous research areas. For example, a new CS-based camera architecture was proposed in [60]. The authors of [61] showed that CS can be applied to magnetic resonance imaging in order to reduce the scan time. In [62], CS was utilised for the decentralised compression of networked data. In the area of communications, it has been invoked for solving numerous problems, such as channel estimation [63], narrowband interference mitigation [64], spectrum sensing [65], impulsive noise mitigation [66–68], transmit precoding [69] and so on.

In this treatise, we focus our attention in the context of CS on the issues discussed in Section 1.2.2. Accordingly, let us formally describe the associated terminologies and problems, which will be used in the following chapters of this treatise. Firstly, we consider a linear Gaussian model, whose discrete-time expression is given by

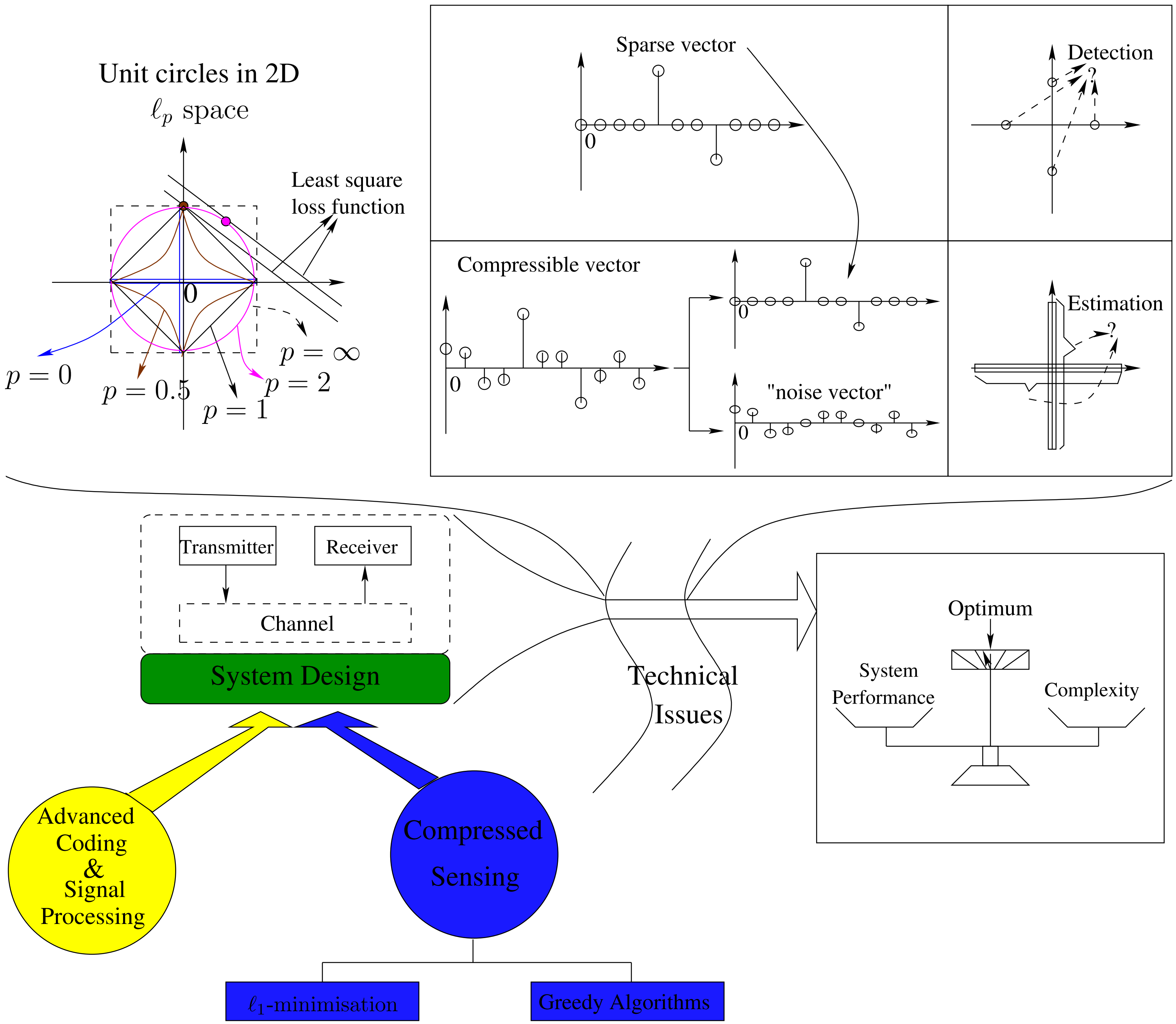

Figure 1.3: The general framework of our CS assisted system design considered in this thesis.

$\boldsymbol{y} = \boldsymbol{A}\boldsymbol{x} + \boldsymbol{n}$, where each noise sample in $\boldsymbol{n} \in \mathbb{C}^m$ is assumed to be i.i.d., which obeys the complex Gaussian distribution [70] with a mean of zero and a variance of σ_{n}^2, i.e., we have $\boldsymbol{n} \sim \mathcal{CN}(\boldsymbol{0}, \sigma_{\mathrm{n}}^2 \boldsymbol{I}_m)$. In particular, we limit ourselves to the case that the N-dimensional symbol vector $\boldsymbol{x}$ is modelled as a k-sparse vector, where the number of nonzero elements in $\boldsymbol{x}$ is no more than k, i.e. we have $\|\boldsymbol{x}\|_0 \leq k \ll N$. Here, it should be noted that the symbol vector may be a compressible vector, which may contain N nonzero elements and $(N-k)$ elements having negligible values, as exemplified in Fig. 1.3. In this case, we usually decompose the compressible vector into a sparse vector containing relevant variables, as well as a noise vector containing the negligible variables, as it will be detailed in Chapter 2. A special case is encountered, when the number of nonzero elements in $\boldsymbol{x}$ is equal to k, i.e. we have $\|\boldsymbol{x}\|_0 = k$. In this case, the symbol vector is exactly k-sparse, which is a favourable sparse model having numerous advantages, as it will be shown in Chapter 3. As depict in Fig. 1.3, we are interested in estimating (Chapter 2) or detecting (Chapter 3) the sparse vector $\boldsymbol{x}$ from its lower-dimensional observations in $\boldsymbol{y} \in \mathbb{C}^m$ associated with $m < N$, whilst ensuring that the target performance can be achieved. More explicitly, we are not seeking to achieve the optimal performance, because we would like to strike a compelling tradeoff between the performance attained and the complexity imposed, as seen in Fig. 1.3. Specifically, the measurement matrix $\boldsymbol{A}$ has to be carefully designed to meet the MIP, so that the uniqueness of the resultant sparse solution can be guaranteed. Specifically, we convert the measurement matrix design problem to the practical design problems associated with pilots in Chapter 2 and with a transmit precoding scheme in Chapter 3.

In CS, algorithms related to both ℓ_0 regularisation and ℓ_1 regularisation can be invoked for estimating or detecting the sparse vector at a low complexity cost. Again, our quantities are modelled as sparse vectors and a flexible performance versus complexity tradeoff is sought. Hence, the classic greedy search based algorithms are employed for ℓ_0 regularisation at an appealingly low complexity. Specifically, beneficial algorithmic improvements will be invoked in Chapter 2 and Chapter 3. Numerous greedy algorithms have been proposed in the literature for solving the ℓ_0 regularisation problem. A simple example is constituted by the MP technique of [42], which has been discussed before. As a further improvement, the authors of [71] proposed the so-called Orthogonal Matching Pursuit (OMP) algorithm, which iteratively updates the results by finding the specific column of $\boldsymbol{A}$ having the maximum correlation with the current residual. It is worth mentioning that the OMP algorithm has also been confused in the past with another celebrated algorithm, namely the orthogonal least square algorithm [72]. The corresponding difference was carefully discussed in [73]. In [74], the Compressive Sampling Matching Pursuit (CoSaMP) algorithm was proposed, which was capable of improving the performance of the OMP algorithm. Meanwhile, the authors of [75] proposed the Iterative Hard Thresholding (IHT) algorithm, whose performance was shown to be similar to that of the CoSaMP algorithm. All of these algorithms share the same heuristic strategy of making locally optimal choices at each step. In this way, a solution, which approximates a globally optimal solution can be generated within a reasonable complexity. Note however that the sparsity level k has to be known *a priori* by the above-mentioned algorithms. Hence, they falter, when the sparsity level is unknown, as it will be shown in Chapter 2. Generally, a stopping criterion, which is based on the statistical characterisation of the noise vector $\boldsymbol{n}$, is used for terminating the algorithm. Explicitly, bounded sets of the noise vector $\boldsymbol{n}$ may be considered, such as the ℓ_2-norm bounded set $\mathcal{B} \triangleq \{\boldsymbol{n} : \|\boldsymbol{n}\|_2 \leq \varepsilon\}$ and the ℓ_∞-norm bounded set $\mathcal{B} \triangleq \{\boldsymbol{n} : \|\boldsymbol{A}^H\boldsymbol{n}\|_\infty \leq \varepsilon\}$. For complex-valued Gaussian sets, the authors of [52] demonstrated that the noise vector belongs to the bounded set characterised by a specific threshold ε with a high probability. Thus, if the residual vector may be deemed to belong to the bounded target set at each iteration of the algorithm, we can safely terminate it, because the correct estimates would have been obtained with a high probability. Explicitly, this is an efficient stopping criterion, especially when the Signal-to-background Noise power Ratio (SNR) is high. Numerous theoretical studies have been carried out for finding sufficient conditions for guaranteeing that the results of the above-mentioned algorithms are indeed close to the globally optimal solution, both in the noiseless case [76–80] and in the noisy case [81–83]. Briefly, the condition of $k < (1 + 1/\mu_{\boldsymbol{A}})/2$ was shown to be sufficient for a guaranteed performance of the OMP algorithm in both the noiseless case [76] and in the noisy case [82].

1.4 Novel Contributions and Thesis Outline

1.4.1 New Contributions of the Thesis

The thesis is based on five published papers, whilst another three papers are about to be submitted. Below, let us briefly summarise our new contributions in the thesis, which will be further detailed in Chapter 2-4.

1. In Chapter 2, a CIS-assisted and Interleaved-Double-FFT (IDFFT) aided system is proposed for mitigating both the multipath effects and the impulsive effects in indoor BB-PLCs. Specifically, the detailed conceptual framework of our CIS relying on the IDFFT system is outlined. Moreover, a Two-Dimensional

(2D) interleaver is conceived for supporting the sparse modelling of the objective vectors containing impairments. Finally, we propose a novel joint CIS estimation and symbol detection algorithm, namely the CIS-assisted detector, to further improve the attainable performance of our IDFFT system.

2. In Chapter 3, we model the bit-to-symbol mapping rule as a codebook and present the theoretical analysis of the generalised system. Then, based on our analytical results, we propose a pair of codebooks based on different design criteria. Firstly, we propose a linear Transmit Pre-Coding (TPC) assisted index modulation codebook, namely the Linear Precoding assisted Index Modulation (LPIM) codebook for maximising both the attainable diversity gain and the coding gain. Secondly, we propose a generalised CSIM codebook based on the maximum diversity gain as well as on the maximum achievable rate criteria. Specifically, we present the detailed conceptual framework of our generalised CSIM. Finally, in order to perform symbol detection at a relatively low complexity, we propose a Generalised Iterative Residual Check Detector (GIRCD) for the LPIM scheme and the CSIM scheme.
3. In Chapter 4, our CSIM scheme is applied to O-OFDM systems experiencing nonlinear distortion, in order to improve the overall system performance. Furthermore, a symmetric piecewise Companding Transform (CT) is conceived for the O-OFDM systems considered in order to mitigate the nonlinear distortion imposed on Quadrature Amplitude Modulation (QAM) constellations. In particular, three types of piecewise companding schemes, namely the Constant Probability sub-Distribution Function (CPsDF), the Linear Probability sub-Distribution Function (LPsDF) and the Non-Linear Probability sub-Distribution Function (NLPsDF) based CT are designed for O-OFDM systems.

1.4.2 Outline of the Thesis

Let us now highlight the outline of this thesis, which is illustrated in Fig. 1.4.

- **Chapter 2: Compressed Impairment Sensing Aided Broadband Power Line Communications**

  In Chapter 2, we propose an asynchronous impulsive noise mitigation solution conceived for PLCs based on CS. Section 2.2 describes the system model, where the PLC channel and the noise model are detailed. In Section 2.3, we provide the statistical characterisation of the FD noise samples. Then, the conceptual framework of our proposed Compressed Impairment Sensing (CIS) is described

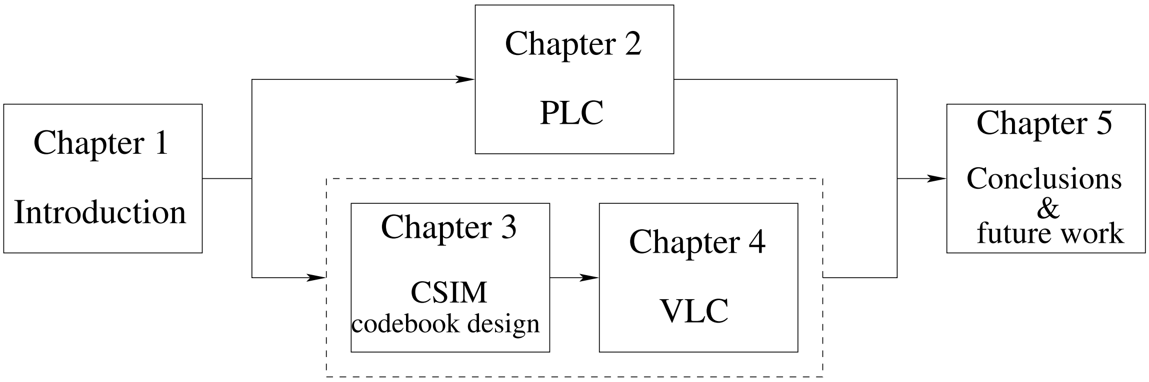

Figure 1.4: Organisation of the thesis.

in Section 2.4. In Section 2.5, the CIS-assisted detector is proposed. Our simulation results are discussed in Section 2.6. Finally, we offer our conclusions of this chapter in Section 2.7.

- **Chapter 3: Compressed Sensing Assisted Index Modulation**
  In Chapter 3, we propose a novel Compressed Sensing assisted Index Modulation (CSIM) scheme. Our system model is described in Section 3.2. In Section 3.3, the system performance and the codebook design criteria are detailed. Then, we propose our LPIM codebook design in Section 3.4. The conceptual framework of our CSIM scheme is detailed in Section 3.5, while in Section 3.6 the generalised iterative residual check detector is proposed. Our simulation results are discussed in Section 3.7. Finally, we conclude this chapter in Section 3.8.

- **Chapter 4: Compressed Sensing Aided Optical OFDM for Visible Light Communications**
  In Chapter 4, our proposed CSIM scheme is applied to VLC for improving the achievable bandwidth efficiency, whilst reducing the LED-induced nonlinear distortions. Explicitly, a companding transform assisted VLC system is proposed for mitigating the nonlinear distortions. In Section 4.2, we describe the system model. The operating principle, design criteria and implementation of the symmetric piecewise CT are detailed in Section 4.3. In Section 4.4, the nonlinear effects are analysed. In Section 4.5, our performance results are studied, followed by our conclusions of this chapter in Section 4.6.

- **Chapter 5: Conclusions and Future Work**
  In Chapter 5, we summarise our conclusions of this thesis and discuss a range of suggestions for future research.

Chapter 2

Compressed Impairment Sensing Aided Broadband Power Line Communications

2.1 Introduction

PLC is expected to play an important role in meeting the dramatic teletraffic increase of telecommunications in the next decade [1]. The main advantage of PLC is its cost-efficiency, which is due to the fact that it relies on the existing grid structure. However, the electrical supply networks have not been designed for data transmissions, hence they constitute a hostile propagation environment [24] and there are still a lot of challenges to be tackled. Specifically, the signals transmitted over power line channels experience both propagation path-loss, as well as multipath propagation and impulsive noise. The path-loss encountered in PLC is the result of the skin effect and dielectric losses [84]. By contrast, the dispersive multipath propagation experienced in PLC is caused by the impedance mismatch between the transmitter and its corresponding receiver [85]. Due to the multipath propagation, a transmitted symbol may be spread over several adjacent symbols at the receiver, hence generating Inter-Symbol Interference (ISI), as detailed in [85]. Measurement results show that the coherence bandwidth of indoor PLC channels is typically 50 kHz to 500 kHz, which is much lower than its total transmission bandwidth. Thus, the PLC channels are usually frequency-selective. Furthermore, the authors of [24] show that the time variation of the PLC channel parameters can be classified into two types, namely into short-term and long-term variations. The long-term variation is usually caused by the switching events experienced in PLC networks, which can be assumed to be time-invariant within a duration of a few seconds. By contrast, the short-term variation is mainly due to the fact that many electrical devices exhibit characteristics that are dependent on the mains frequency [86], which can be assumed to be time-invariant within hundreds of microseconds. Consequently, the latter type of variation is cyclic, and the channel parameters are usually periodical in time. Owing to the above characteristics, the PLC channels are typically slowly time-varying. The statistical characterisations of indoor PLC channels can be found in [87].

On the other hand, in PLC, the noise can usually be classified into two categories: background noise and impulsive noise [25, 88]. The impulsive noise is typically characterised by the duration, inter-arrival time and power of its components [25]. According to its behaviour with respect to the mains cycle, impulsive noise can be classified into three types, namely periodic mains-synchronous impulsive noise, periodic impulsive noise that is asynchronous with the mains, as well as asynchronous impulsive noise [25]. Typically, the asynchronous impulsive noise, which is mainly caused by the connection and disconnection of electrical devices, is the major impairment of BB-PLC due to its high power and unpredictable nature. Therefore, we focus our attention on the mitigation of asynchronous impulsive noise. The measurement results of [25, 88, 89] have shown that the asynchronous impulsive noise bursts experienced in PLC are relatively long in comparison to those in wireless communications. For example, the measurement results of [25] showed that the average duration of the asynchronous impulsive noise bursts in PLC varies between microseconds and milliseconds. By contrast, in wireless communications, the duration of impulsive noise bursts is usually less than 0.1 μs [90]. Naturally, the long impulsive bursts of PLC may inflict bursts of errors. As a result, the system's performance may be severely degraded, especially in high data-rate transmissions relying on short symbol durations.

OFDM, which is the predominant transmission technique of wireless communications at the time writing [91, 92], has also been adopted by the PLC standards, including IEEE P1901 [21], ITU-T G.hn [22] and HomePlug AV2 [23]. A frequency-selective fading channel can be converted into a number of parallel flat-fading subchannels with the aid of the OFDM, thereby, considerably reducing the receiver's complexity as a benefit of using single-tap frequency-domain equalisation [91]. Cyclic Prefix (CP)-based OFDM is employed to avoid the inter-OFDM-symbol interference [91]. Although the conventional OFDM signalling is capable of mitigating the multipath effects of PLC, it experiences a performance loss in the presence of impulsive noise. In more detail, the Discrete Fourier Transform (DFT) spreads the effect of impulsive noise across all the subcarriers. When the duration of an impulsive burst is sig-

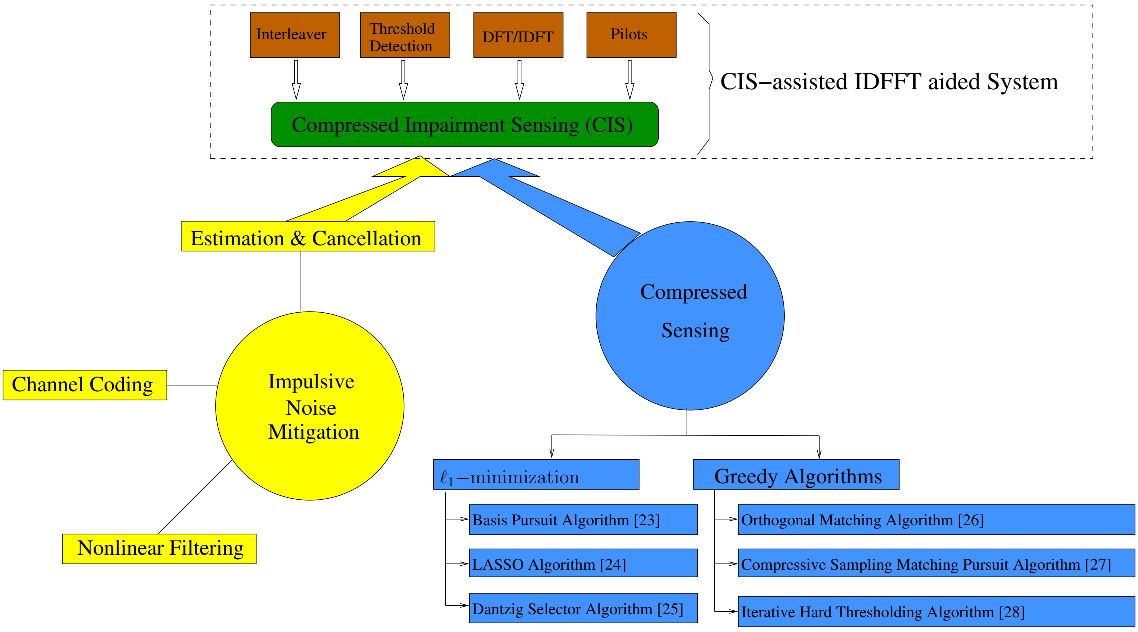

Figure 2.1: Illustration of the relationships between compressed sensing (CS), impulsive noise mitigation as well as compressed impairment sensing (CIS). Explicitly, the aim of CIS is to estimate the impulsive noise based on the principle of CS.

nificantly shorter than the OFDM symbol duration, the associated spreading effect becomes beneficial, since all subcarriers are only marginally contaminated. Unfortunately, as mentioned above, the duration of impulsive noise in PLC may become substantially longer than the OFDM symbol duration, which significantly degrades the system performance, especially, when the power of impulsive noise is high. Therefore, conventional OFDM signalling is incapable of mitigating the impulsive noise in PLC.

As illustrated in the yellow part of Fig. 2.1, several methods have been proposed in the literature in order to mitigate the effect of impulsive noise imposed on OFDM systems communicating over PLC channels, such as nonlinear filtering [93–95], channel coding [96, 97], as well as both parametric and non-parametric estimation techniques [98, 99]. On the other hand, as shown by the blue part of Fig. 2.1, CS, as an emerging theory, has attracted considerable research-attention, as exemplified by the elegant algorithms [33, 34, 41, 74–76] of Fig. 2.1. CS has been proposed to tackle the issues of recovery of vectors in high dimensions from vectors in low dimensions, as detailed in [54]. Recently, CS has been invoked for solving numerous problems in communications systems, such as channel estimation [63], narrowband interference mitigation [64], spectrum sensing [65] and so on. Training-based impulsive noise estimation relying on CS also constitutes an attractive method, since it has several distinct advantages for OFDM systems communicating over PLC channels. Firstly, in practical PLCs, the high-attenuation frequency sub-bands of an OFDM symbol may be disabled for data transmissions [21, 23]. Hence, some of these deactivated tones can be used as training symbols for supporting training-based impulsive noise estimation. Secondly, it is possible to disperse the prolonged impulsive burst affecting numerous TD samples by simply using an interleaver. In this way, the asynchronous impulsive noise can be estimated at a low complexity with the aid of CS. Finally, since the power of asynchronous impulsive noise is usually much higher than that of the background noise in BB-PLC, accurate impulsive noise estimation is attainable by using CS. The idea of applying CS to mitigate the impulse noise in OFDM systems was originally proposed in [66], where the impulse noise estimation was formulated as an ℓ_1-minimisation problem. Later in [67], the mixed ℓ_2/ℓ_1-minimisation has been employed for impulse noise estimation, where the impulsive noise was assumed to appear in form of sparse blocks. It should be noted that in [66] and [67] the duration of impulse noise was assumed to be much lower than that of an OFDM symbol, which is however, not the norm in PLCs. Furthermore, although the ℓ_1-minimisation considered in [66] and the mixed ℓ_2/ℓ_1-minimisation of [67] can be solved within polynomial rather than exponential time, the corresponding computational cost still remains excessive. It is important to emphasise that for both schemes substantial computational resources are required for estimating relatively insignificant impulsive noise, whose instantaneous power is lower than the modulation-dependent detection threshold.

Against the above background, our contributions of this chapter are summarised as follows.

- *We propose a novel CIS-assisted IDFFT system, which is capable of simultaneously mitigating both the multipath effects and the impulsive noise impairments in PLC. It should be noted that similar to Interleaved Frequency Division Multiple Access (IFDMA) [100], the proposed IDFFT system can be viewed as a special case of the DFT-precoded OFDMA with interleaved subcarrier allocation. However, since the IDFFT system is specifically designed for CIS-assisted impulsive noise mitigation, the design objectives of IDFFT and IFDMA are different. The general philosophy of our proposed CIS-assisted IDFFT aided system transpires from Fig. 2.1. In the CIS-assisted IDFFT systems, the transmitter carries out both an FFT and an IFFT operation, which are connected with a 2D interleaver. Correspondingly, the receiver employs a FD equaliser and a CIS-assisted detector. The data symbols in our CIS-assisted IDFFT system are transmitted in the TD, while a FD equaliser is employed in order to achieve the maximum attainable multipath diversity gain [101].*

- *In our CIS, a 2D interleaver is conceived for supporting the sparse modelling of the objective vectors containing impairments. Then, the received pilots are modelled by the mathematical formulation of CS with the aid of our IDFFT system. Next, we show that the measurement matrix design of CS can be equivalent to the pilot design used in our CIS. Moreover, we propose a computationally efficient search algorithm to provide a sub-optimal solution for our pilot design.*
- *As a further improvement, we propose a joint CIS estimation and symbol detection algorithm, namely the CIS-assisted detector, for our IDFFT system. Specifically, our proposed CIS-assisted detector is based on the turbo principle, where our CIS estimator iteratively exchanges ever more reliable information with the symbol detector upon each new iteration. In this way, the impairments associated with high near-instantaneous power, which severely degrade the system performance, can be reliability estimated and eliminated.*
- *Finally, the performance of our CIS-assisted IDFFT aided system is investigated with the aid of simulations. We demonstrate that our CIS-assisted IDFFT aided system outperforms conventional OFDM in realistic PLC environments experiencing both dispersion and asynchronous impulsive noise.*

The rest of the chapter is organised as follows. In Section 2.2, the system model is detailed, where both the PLC channel and noise model are also described. The statistic characterisations of the FD noise samples are detailed in Section 2.3. Then, the conceptual framework of our proposed compressed impairment sensing is described in Section 2.4. In Section 2.5, the CIS-assisted detector is detailed. Our simulation results are studied in Section 2.6. Finally, we offer our conclusions in Section 2.7.

2.2 System Model

2.2.1 Transmitter

The system considered in this chapter is depicted in Fig.2.2. At the transmitter, a sequence of i.i.d. information bits denoted as $\boldsymbol{b}_l$ is mapped onto a stream of M_d Amplitude-Phase Modulated (APM) symbols according to the mapping rule $\mu : \mathbb{B}^{\log_2 Q} \to \mathcal{A}$, where we have $Q = |\mathcal{A}|$. After the symbol mapping, let us denote the lth stream of data symbols as $\boldsymbol{x}_{\mathrm{d},l}^T = [x_{\mathrm{d},l}(0), x_{\mathrm{d},l}(1), \ldots, x_{\mathrm{d},l}(M_\mathrm{d}-1)]$, where we assume that $\mathbb{E}[|x_{\mathrm{d},l}(i)|^2] = 1, \forall x_{\mathrm{d},l}(i) \in \mathcal{A}$. Then, as seen in Fig. 2.2, a total of $(M - M_\mathrm{d})$ zero-valued symbols are inserted into each of the streams of the data symbols, forming an M-length symbol sequence, which are series-to-parallel converted. It should be

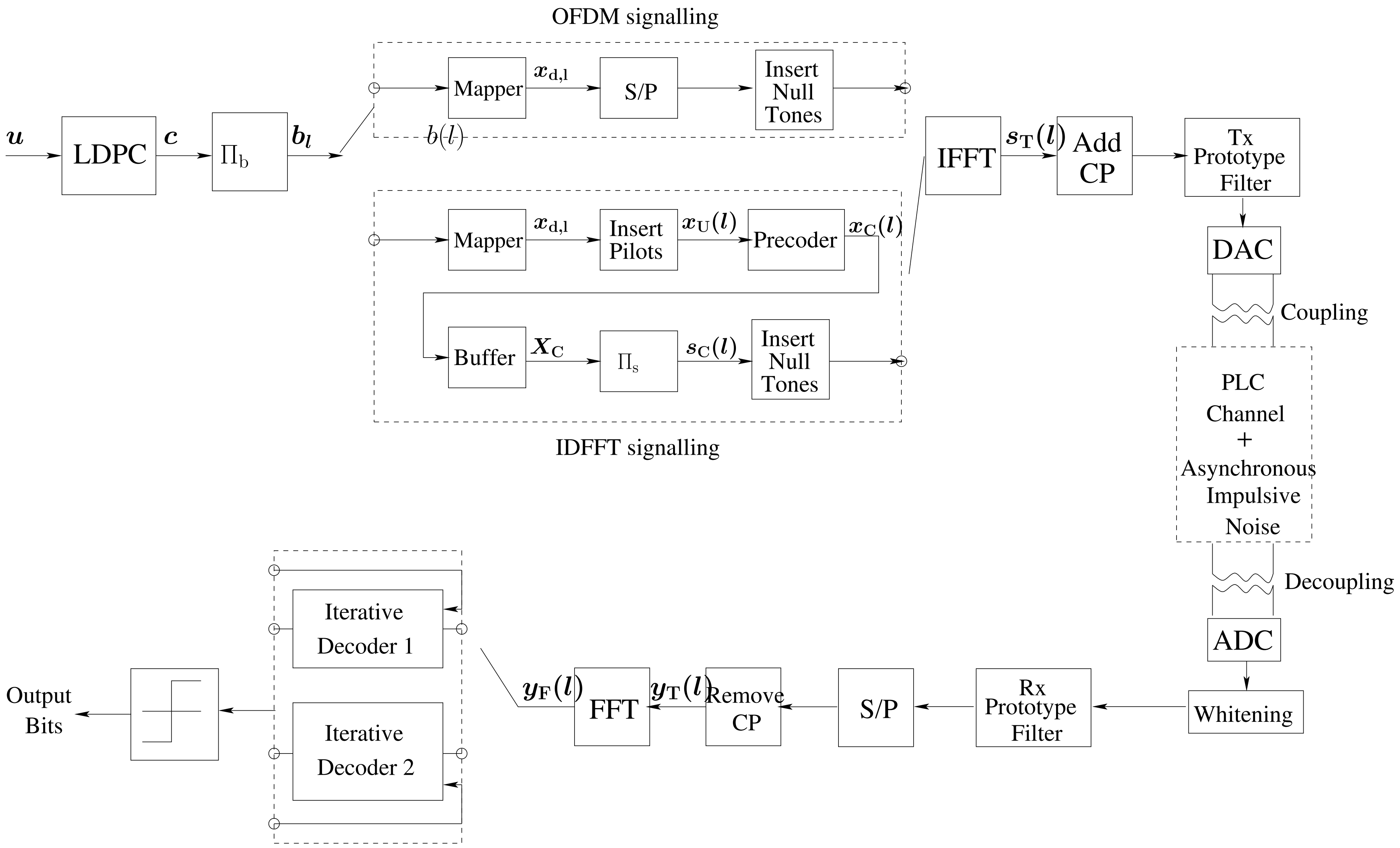

Figure 2.2: Illustration of our system block diagram.

noted that for different systems, the zero-valued symbols inserted play different roles, as detailed next.

Classic OFDM Signalling

In the classic OFDM scheme shown in the upper dashed box of Fig. 2.2, the above-mentioned symbols in $\boldsymbol{x}_{\mathrm{d},l}$ can be viewed as the FD symbols, while, the zero-valued symbols may correspond to the sub-bands that are disabled, due to their high attenuation and/or strong narrowband interference that would otherwise result in unreliable transmission in these sub-bands. Let the positions of the data symbols in the M-sized block form an index set $\mathcal{M}_{\mathrm{d}}$, where we have $|\mathcal{M}_{\mathrm{d}}| = M_{\mathrm{d}}$. Moreover, we assume that the index set $\mathcal{M}_{\mathrm{d}}$ is the same for all the L_M blocks. Hence, we can express the lth block of the FD symbols $\boldsymbol{s}_{\mathrm{F}}(l) = [s_{\mathrm{F}}(0,l), s_{\mathrm{F}}(1,l), \ldots, s_{\mathrm{F}}(M-1,l)]^T$ as

$$\boldsymbol{s}_{\mathrm{F}}(l) = \boldsymbol{\Upsilon}_{\mathcal{M}_{\mathrm{d}}} \boldsymbol{x}_{\mathrm{d},l}, \tag{2.1}$$

where $\boldsymbol{\Upsilon}_{\mathcal{M}_{\mathrm{d}}}$ is a $(M \times M_{\mathrm{d}})$-element mapping matrix derived from $\boldsymbol{I}_M$ based on the index set $\mathcal{M}_{\mathrm{d}}$.

Interleaved-Double-FFT Signalling

In our proposed IDFFT system, the zero-valued symbols can be classified into two types. The first type of the zero-valued symbols, which are inserted before precoding, are used as pilots for impulsive noise estimation. Since the impulsive noise is additive, zero-valued pilots are employed in order to save transmission power. On the other hand, the second type of zero-valued symbols are inserted after precoding into the disabled sub-bands similar to that described in the case operating without precoding. It should be emphasised here that there is no need to increase the bandwidth in comparison to the case operating without precoding. Since a beneficial multipath diversity gain can be obtained by the linear precoding combined with symbol interleaving, some of the disabled frequency sub-bands, namely those experience multipath-induced fading, can be activated for data transmission. Let us assume that m pilots are used before precoding. In this case, we have $N \triangleq M_{\mathrm{d}} + m < M$. Hence, after precoding, a total of $(M - N)$ sub-bands, which suffer both from a high level of attenuation and from narrowband interference, are disabled.

Based on the above-mentioned arrangement, let us describe the transmitted signal as follows. Firstly, let the positions of the data symbols in each N-sized data block form an index set $\mathcal{I}_{\mathrm{d}}$, where we have $|\mathcal{I}_{\mathrm{d}}| = M_{\mathrm{d}}$ and we assume that $\mathcal{I}_{\mathrm{d}}$ is fixed for all data blocks. Correspondingly, the positions of the zero-valued symbols forms a set

$\mathcal{I}_{\mathrm{p}} = \{0, 1, \ldots, N-1\} \backslash \mathcal{I}_{\mathrm{d}}$. Furthermore, the mapping matrices based on the index sets $\mathcal{I}_{\mathrm{d}}$ and $\mathcal{I}_{\mathrm{p}}$ can be formed as $\boldsymbol{\Upsilon}_{\mathcal{I}_{\mathrm{d}}}$ and $\boldsymbol{\Upsilon}_{\mathcal{I}_{\mathrm{p}}}$, respectively. Let us denote the lth data block of symbols as $\boldsymbol{x}_{\mathrm{U}}(l) = [x_{\mathrm{U}}(0,l), x_{\mathrm{U}}(1,l), \ldots, x_{\mathrm{U}}(N-1,l)]^T$. Then, it can be expressed as

$$\boldsymbol{x}_{\mathrm{U}}(l) = \boldsymbol{\Upsilon}_{\mathcal{I}_{\mathrm{d}}} \boldsymbol{x}_{\mathrm{d},l}. \tag{2.2}$$

As shown in the lower dashed box of Fig. 2.2, the lth block of symbols $\boldsymbol{x}_{\mathrm{U}}(l)$ is precoded by an $(N \times N)$-element matrix. In particular, the DFT matrix $\boldsymbol{\mathcal{F}}_N$ is applied as the precoding matrix. Although there exists other types of precoding schemes that are capable of offering a better performance (as it will be shown in Chapter 3), the DFT scheme is used here, since it can be implemented by the FFT algorithm at a low complexity. This practical concern becomes more evident, when N is a large value, which is typically the case in broadband PLCs. Hence, the precoded symbols denoted as $\boldsymbol{x}_{\mathrm{C}}(l) = [x_{\mathrm{C}}(0,l), x_{\mathrm{C}}(1,l), \ldots, x_{\mathrm{C}}(N-1,l)]^T$ can be expressed as

$$\boldsymbol{x}_{\mathrm{C}}(l) = \boldsymbol{\mathcal{F}}_N \boldsymbol{x}_{\mathrm{U}}(l), \tag{2.3}$$

where we have $\mathbb{E}[\|\boldsymbol{x}_{\mathrm{C}}(l)\|_2^2] = M_{\mathrm{d}}/N$, $\forall l$. As shown in the lower dashed box of Fig. 2.2, the L_M blocks of precoded symbols denoted as $\boldsymbol{X}_{\mathrm{C}} = [\boldsymbol{x}_{\mathrm{C}}(0), \ldots, \boldsymbol{x}_{\mathrm{C}}(L_M - 1)] \in \mathbb{C}^{N \times L_M}$ are fed into a 2D interleaver Π_{s} with a length of $L_{\Pi_{\mathrm{s}}} = NL_M$, yielding a new $(N \times L_M)$-element data matrix denoted as $\boldsymbol{S}_{\mathrm{C}} = [\boldsymbol{s}_{\mathrm{C}}(0), \boldsymbol{s}_{\mathrm{C}}(1), \ldots, \boldsymbol{s}_{\mathrm{C}}(L_M - 1)]$, where $\boldsymbol{s}_{\mathrm{C}}(l) = [s_{\mathrm{C}}(0,l), s_{\mathrm{C}}(1,l), \ldots, s_{\mathrm{C}}(N-1,l)]^T$ denotes the lth block of interleaved symbols. Next, the symbols in $\boldsymbol{s}_{\mathrm{C}}(l)$ are allocated to the FD subcarriers $\boldsymbol{s}_{\mathrm{F}}(l) = [s_{\mathrm{F}}(0,l), s_{\mathrm{F}}(1,l), \ldots, s_{\mathrm{F}}(M-1,l)]^T$ according to the index set $\mathcal{M}_{\mathrm{s}}$, which can be expressed as

$$\boldsymbol{s}_{\mathrm{F}}(l) = \boldsymbol{\Upsilon}_{\mathcal{M}_{\mathrm{s}}} \boldsymbol{s}_{\mathrm{C}}(l), \tag{2.4}$$

where $\boldsymbol{\Upsilon}_{\mathcal{M}_{\mathrm{s}}}$ is the mapping matrix based on the index set $\mathcal{M}_{\mathrm{s}}$.

It can be readily inferred from the above discussion that in contrast to the classic OFDM, our proposed IDFFT imposes an additional complexity and signal processing delay, owing to the FFT and to the 2D interleaving. However, in practice, these shortcomings can be alleviated by invoking parallel hardware devices (at the cost of increasing the hardware cost).

For both the schemes, as shown in Fig. 2.2, the lth block of the FD symbols is entered into an M-point IFFT, yielding the TD symbols $\boldsymbol{s}_{\mathrm{T}}(l) = [s_{\mathrm{T}}(0,l), s_{\mathrm{T}}(1,l), \ldots, s_{\mathrm{T}}(M-1,l)]^T$ expressed as

$$\boldsymbol{s}_{\mathrm{T}}(l) = \boldsymbol{\mathcal{F}}_M^H \boldsymbol{s}_{\mathrm{F}}(l). \tag{2.5}$$

Furthermore, in order to avoid ISI, a CP of length $L_{\rm cp}$ is inserted before each block of the TD symbols, resulting in

$$\boldsymbol{s}_{\rm cp}(l) = \boldsymbol{\Upsilon}_{\rm CP}\boldsymbol{s}_{\rm T}(l), \tag{2.6}$$

where $\boldsymbol{\Upsilon}_{\rm CP} = [\boldsymbol{\Upsilon}_{\rm cp}, \boldsymbol{I}_M]^T$ and $\boldsymbol{\Upsilon}_{\rm cp}$ is a mapping matrix formed by the last $L_{\rm cp}$ columns of an identity matrix $\boldsymbol{I}_M$. As shown in Fig. 2.2, following the parallel-to-serial conversion, prototype filtering is applied to the symbols, yielding the lth stream of the transmitted signal $s_l(t)$ expressed as

$$s_l(t) = \sum_i s_{\rm cp}(i,l) g_{\rm Tx}(t - i\Delta t), \tag{2.7}$$

where $g_{\rm Tx}(t)$ is the impulse response of the prototype filter at the transmitter and Δt denotes the duration of successive samples. We assume that the prototype filter $g_{\rm Tx}(t)$ is specifically designed in order to meet the spectral constraints restricted by the ElectroMagnetic Compatibility (EMC) regulations. Finally, with the aid of coupling, the resulted signals are transmitted through the PLC channels imposing asynchronous impulsive noise.

2.2.2 Characterisation of the PLC Channel

Let us assume that the indoor PLC system is operated in the frequency range of ($f_{\rm min}$,$f_{\rm max}$). Hence, the CP-OFDM block duration is given by $T_{\rm Tx} = (1 + L_{\rm cp}/M)T_{\rm s}$, where $T_{\rm s} = 1/f_{\rm B} = M\Delta t$ denotes the OFDM block duration and $f_{\rm B} = (f_{\rm max} - f_{\rm min})$ is the bandwidth. In indoor PLCs, due to the frequent connection and disconnection of various types of loads, as well as the presence of cable branches, an indoor PLC channel exhibits a time-variant frequency-selective Channel Transfer Function (CTF). Let $H(f,t)$ denote the CTF between a given transmitter and its corresponding receive port over a power line at time t and frequency f. As shown in [24, 86], the time variation of PLC channels can be classified into two types, which are the short-term variation and the long-term variation. In this chapter, our focus is on the short-term variation of the PLC channels, which is dependent on the mains frequency and it is usually about hundreds of microseconds. Let us denote the corresponding channel coherence time as $T_{\rm coh}$. Then, we can assume that the PLC channels are time-invariant during $L_{\rm H}$ blocks of transmitted symbols, i.e., we have $L_{\rm H}T_{\rm Tx} < T_{\rm coh}$. Thus, the CTF of a time-invariant transmission period for a given frequency range can be expressed as

$$H(t,f) \triangleq h\,(f) = \sum_{i=0}^{N_{\rm h}-1} h_{{\rm R},i} e^{-\alpha(f) v_{\rm p} \tau_i} e^{-j2\pi f \tau_i}, \tag{2.8}$$

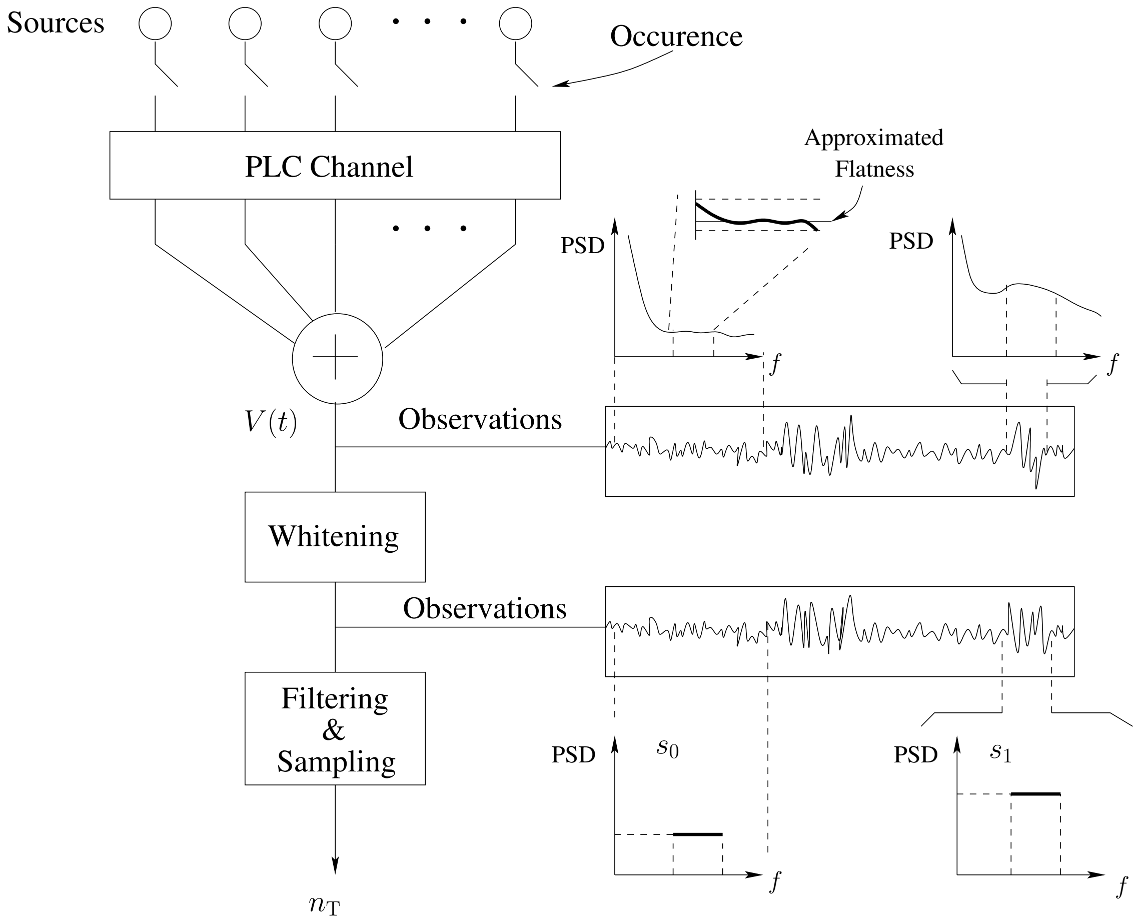

Figure 2.3: Illustration of power line noise.

where N_h denotes the number of non-negligible paths and v_p is the phase velocity. In (2.8), $|h_{\mathrm{R},i}| < 1$ is the reflection factor, which is determined both by the number of discontinuities included in the ith path, as well as by the reflection coefficient and the transmission coefficient of the ith path [102]. Moreover, the frequency-dependent attenuation factor denoted as $\alpha(f)$ is related to both the dielectric losses and the Ohmic losses [84], and finally, τ_i is the delay of the ith reflected path. Correspondingly, the Channel Impulse Response (CIR) can be formulated as $h(t) = \mathcal{F}^{-1}\{h(f)\}$, where $\mathcal{F}^{-1}\{x\}$ denotes the inverse Fourier transform of x.

2.2.3 Noise Modelling

We assume that the PLC channels encounter both background noise and asynchronous impulsive noise. Whilst the background noise is present continuously, the asynchronous impulsive noise is sporadic. Naturally, two states are involved in characterising the noise observations. The first state is denoted as s_0, representing the sole presence of the background noise. By contrast, the second state s_1 represents the presence of both the background noise and the asynchronous impulsive noise.

Classification of Time Intervals

Due to the bursty behaviour, asynchronous impulsive noise is usually observed within a time duration. Explicitly, the duration of an impulsive noise burst corresponds to the state s_1. While, the time interval between two adjacent asynchronous impulsive noise bursts is related to the state s_0.

Noise Whitening

Let us first consider the background noise. The measurement results of [89] have shown that the background noise is colored within the whole frequency band of PLC. Specifically, in the frequency range of NB-PLC, the background noise is strongly colored, while, the Power Spectral Density (PSD) of background noise is relatively flat in the frequency range of BB-PLC [89]. Hence, we assume that in the considered frequency range of $(f_{\min}, f_{\max})$, the background noise has a constant PSD denoted as Φ_{s_0}, meaning that the background noise is white.

In order to gain further insights into the characteristics of asynchronous impulsive noise, the process of generating asynchronous impulsive noise in a power-line network is illustrated in Fig. 2.3. In practice, various appliances and devices, which are represented by the noise sources in Fig. 2.3, may be connected or disconnected from the power line network, generating impulse. Then, the impulses propagating over power line channels are superimposed at the receiver. Since each power line can be viewed as a filter, the impulse received at time t, which is denoted as $V(t)$ can be characterised by its autocorrelation function $\phi_{vv}(\tau)$ expressed as

$$\phi_{vv}(\tau) = \int_{-\infty}^{+\infty} \Phi_{vv}(f) e^{j2\pi f\tau} \mathrm{d}f, \tag{2.9}$$

where $\Phi_{vv}(f)$ denotes the corresponding PSD. Hence, one possible approach of modelling the asynchronous impulsive noise is based on applying an autoregressive process having a matching PSD, as suggested in [25]. However, the corresponding complexity may be deemed excessive. Furthermore, although it is a favourable model for fitting a given measurement results, it may be not a feasible model for system design and analysis. An interesting observation we found is that the above-mentioned noise modelling problem can be significantly simplified by applying a de-correlation process without affecting its impact on the desired data symbols or on the BER, as evident in [103]. Thus, we assume that an adaptive whitening filter [103] is employed so that the PSD of the asynchronous impulsive noise after filtering becomes constant. Finally, since the noise formed by addition of two white noise sources is still white, we denote the PSD of the noise after whitening as Φ_{s_1}, which is also constant. Note furthermore that the whitening processing also has the advantage of simplifying the procedure of noise variance estimation, which is required for detection, as it will be shown in Section. 2.3.

Noise Generation and Statistical Characterisation

Based on the above-mentioned assumptions, the Hidden Semi-Markov Model (HSMM) is applied to generate baseband equivalent noise observations, which are used in the following analysis. Firstly, let us assume that the initial state of the noise process is chosen from $\mathcal{S} = \{s_0, s_1\}$ with equal probability of 0.5. Then, according to the characteristics of the noise process, as shown in Fig. 2.3, the states s_0 and s_1 occur alternatively. Since the noise has been de-correlated by the above-mentioned adaptive whitening filter, the self-transition probabilities of these two states are equal to 0, i.e. we have $P_{00} = P_{11} = 0$, where P_{ij} denotes the transition probability from state s_i to state s_j. Correspondingly, we have the state transition probabilities of $P_{01} = P_{10} = 1$. Next, for the qth generated state $S_q \in \mathcal{S}$, a sequence of noise observations with a sampling duration of Δt is generated as follows. Let D_{S_q} denote the corresponding state-duration obeying a given conditional Probability Mass Function (PMF) defined as

$$\begin{aligned} P_D(d|S_q) &\triangleq \Pr(D = d|S_q = s_i \in \mathcal{S}) \\ &= \frac{1}{\Omega_i} \exp\left(-\frac{d}{\Omega_i}\right), \quad i = 0, 1, \end{aligned} \tag{2.10}$$

where Ω_0 and Ω_1 are the average inter-bursts arrival time and the average duration of asynchronous impulsive bursts, respectively. Specifically, we define the ratio between the average duration time and the average inter-burst arrival time as $\Lambda_\mathrm{T} = \Omega_1/\Omega_0$. Then, as a rule of thumb, we assume that the noise samples in a given state-duration obey the complex-valued Gaussian distribution with a mean of zero. Finally, the noise observations denoted as $\boldsymbol{n}_{D_q} = [n_{S_q}(1), n_{S_q}(2), \ldots, n_{S_q}(D_q)]$ are generated according to a conditional Probability Density Function (PDF) of

$$\begin{aligned} p_n(x|S_q) &\triangleq \Pr(n = x|S_q = s_i \in \mathcal{S}) \\ &= \frac{1}{\pi\sigma_{s_i}^2} \exp\left\{-\frac{|x|^2}{\sigma_{s_i}^2}\right\}, \quad i = 0, 1, \end{aligned} \tag{2.11}$$

where $\sigma_{s_0}^2$ and $\sigma_{s_1}^2$ can be obtained according to Φ_{s_0} and Φ_{s_1}, respectively. Furthermore, we define the power ratio as $\Lambda_\mathrm{P} = \sigma_{s_1}^2/\sigma_{s_0}^2$.

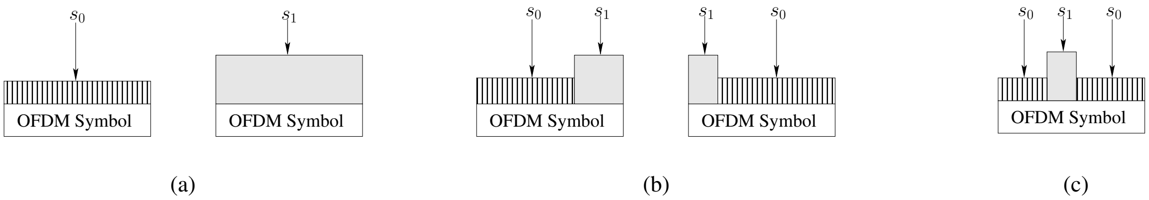

Figure 2.4: Stylized illustration of noise types in the time-domain.

2.2.4 Received FD Symbols

At the receiver, we assume that perfect time synchronisation is achieved. Moreover, the length of the CP is assumed to be higher than the PLC channel's maximum delay spread. Hence, after decoupling, the lth stream of received signal can be formulated as

$$y_l(t) = \int_{\tau} h(\tau) s_l(t-\tau) \mathrm{d}\tau + n_l(t), \tag{2.12}$$

where $h(t)$ denotes the CIR, while $n_l(t)$ contains the background noise and possible asynchronous impulsive noise, as described in Section 2.2.2. Then, the received signal $y_l(t)$ is entered into the prototype filters and sampled at an interval of Δt, the corresponding discrete-time baseband equivalent observations can be expressed as

$$\boldsymbol{y}_{\mathrm{T}}(l) = \boldsymbol{H}_{\mathrm{cir}} \boldsymbol{s}_{\mathrm{T}}(l) + \boldsymbol{n}_{\mathrm{T}}(l), \tag{2.13}$$

where $\boldsymbol{H}_{\mathrm{cir}} \in \mathbb{C}^{M\times M}$ is a circulant matrix, which can be diagonalized by the M-point DFT matrix, i.e., we have $\boldsymbol{H}_{\mathrm{cir}} = \boldsymbol{\mathcal{F}}_M^H \boldsymbol{H} \boldsymbol{\mathcal{F}}_M$. Here, the diagonal matrix $\boldsymbol{H}$ can be expressed as $\boldsymbol{H} = \sqrt{M}\mathrm{diag}\{\boldsymbol{\mathcal{F}}_M \boldsymbol{\Upsilon}_{\mathrm{h}} \boldsymbol{h}_{\mathrm{T}}\}$, where $\boldsymbol{h}_{\mathrm{T}} = [h_{\mathrm{T}}(0), h_{\mathrm{T}}(1), \ldots, h_{\mathrm{T}}(L_{\mathrm{h}}-1)]^T$ represents the chip-sampled baseband equivalent CIR after filtering, while $\boldsymbol{\Upsilon}_{\mathrm{h}}$ is a $(M \times L_{\mathrm{h}})$-element mapping matrix formed by the first L_{h} columns of an identity matrix $\boldsymbol{I}_M$. The statistical modelling of noise samples in $\boldsymbol{n}_{\mathrm{T}}(l)$ is described in Section 2.2.3.

As seen in Fig. 2.2, upon carrying out the FFT of $\boldsymbol{y}_{\mathrm{T}}(l)$, we obtain

$$\begin{aligned}\boldsymbol{y}_{\mathrm{F}}(l) =& \boldsymbol{\mathcal{F}}_M \boldsymbol{y}_{\mathrm{T}}(l)\\ =& \boldsymbol{\mathcal{F}}_M \boldsymbol{\mathcal{F}}_M^H \boldsymbol{H} \boldsymbol{\mathcal{F}}_M \boldsymbol{s}_{\mathrm{T}}(l) + \boldsymbol{\mathcal{F}}_M \boldsymbol{n}_{\mathrm{T}}(l)\\ =& \boldsymbol{H} \boldsymbol{s}_{\mathrm{F}}(l) + \boldsymbol{n}_{\mathrm{F}}(l),\end{aligned} \tag{2.14}$$

where $\boldsymbol{n}_{\mathrm{F}}(l) = \boldsymbol{\mathcal{F}}_M \boldsymbol{n}_{\mathrm{T}}(l)$ denotes the FD noise, as detailed in the next section.

2.3 Statistics of Frequency-Domain Noise Samples

Based on Section 2.2.3, let a noise sequence of $\boldsymbol{n}_T = \{\boldsymbol{n}_{D_1}, \boldsymbol{n}_{D_2}, \ldots, \boldsymbol{n}_{D_T}\}$ be generated according to a state sequence of $\boldsymbol{S} = \{S_1, S_2, \ldots, S_T\}$, where $S_q \in \{s_0, s_1\}$ and D_q is the state duration of S_q, for $q = 1, \ldots T$. For the sake of the demonstration, an infinite implementation is assumed, i.e. we have $T \to \infty$. Let T_i denote the total number of state observations that are from s_i for $i = 0, 1$. Then, we have the approximation of $T_0/T_1 \approx 1$ for $T \to \infty$. When the lth block of OFDM symbols expressed in (2.13) is corrupted by $\boldsymbol{n}_{\mathrm{T}}(l) \in \boldsymbol{n}_T$, three different types can be classified in the TD. The first type shown in Fig. 2.4(a) is when noise samples are all from the same state, either s_0 or s_1. In the second type, the noise samples are from a pair of different states, namely from $\{S_q = s_0, S_{q+1} = s_1\}$ or $\{S_q = s_1, S_{q+1} = s_0\}$, as seen in Fig. 2.4(b). Finally, for the third type, the noise samples are from more than two successive states of $\{S_q, S_{q+1}, \ldots, S_{q+i}\}$, where $i \geq 2$, as exemplified in Fig. 2.4(c). However, in practice, the average inter-arrival time of impulsive bursts is usually much higher than the OFDM symbol duration, i.e. we have $\Omega_0 \Delta t \gg T_s$. Hence, for the third type we may only consider the case of $i = 2$, i.e. the scenario of having three successive states of $\{S_q = s_0, S_{q+1} = s_1, S_{q+2} = s_0\}$.

As inferred from the above observations, we can readily show that the FD noise sample in $\boldsymbol{n}_{\mathrm{F}}(l)$, as defined in (2.14), has the PDF of $\mathcal{CN}(0, \sigma^2_{\mathrm{n},l})$, where the noise variance $\sigma^2_{\mathrm{n},l}$ can be expressed as

$$\sigma^2_{\mathrm{n},l} = \left[1 + \frac{\kappa_l}{M}(\Lambda_{\mathrm{Po}} - 1)\right] \sigma^2_{s_0}, \tag{2.15}$$

where $\kappa_l \in \{0, 1, \ldots, M\}$ denotes the number of TD noise samples in $\boldsymbol{n}_{\mathrm{T}}(l)$ from the state s_1. Clearly, when the OFDM block is impaired by the first type of noise, we have $\kappa_l = 0$ for s_0 and $\kappa_l = M$ for s_1, as shown in Fig. 2.4(a).

We observe from the above analysis that when the power of asynchronous impulsive noise is high, the system's performance may be severely degraded. Moreover, since the occurrence of asynchronous impulsive noise is sporadic, it is challenging for the receiver to obtain information about its occurrence and duration. The grave impact of asynchronous impulsive noise suggests that efficient techniques have to be designed for mitigating its effects, as discussed in the next section.

2.4 Conceptual Framework of Compressed Impairment Sensing

In this section, the detailed conceptual framework of our CIS is described. We first consider the design criteria of our 2D interleaving scheme for the sake of increasing the grade of sparsity. Then, the CIS is formulated and the impairment vector is specified. Next, we show how the compression stability issue of CS is converted into the pilot design issue of our CIS. Finally, we point out some practical recovery problems of CIS.

Firstly, let the symbols in the activated and disabled sub-bands be extracted with the aid of substituting (2.4) into (2.14) as

$$\begin{aligned}\boldsymbol{y}_{\mathrm{C}} =&\boldsymbol{\Upsilon}_{\mathcal{M}_{\mathrm{s}}}^{T}\boldsymbol{y}_{\mathrm{F}}\\ =&\boldsymbol{\Upsilon}_{\mathcal{M}_{\mathrm{s}}}^{T}\boldsymbol{H}\boldsymbol{\Upsilon}_{\mathcal{M}_{\mathrm{s}}}\boldsymbol{s}_{\mathrm{C}}+\boldsymbol{\Upsilon}_{\mathcal{M}_{\mathrm{s}}}^{T}\boldsymbol{n}_{\mathrm{F}}\\ =&\boldsymbol{H}_{\mathrm{s}}\boldsymbol{s}_{\mathrm{C}}+\boldsymbol{n}_{\mathrm{s}}\end{aligned} \tag{2.16}$$

and

$$\begin{aligned}\boldsymbol{y}_{\mathrm{P}} =&\boldsymbol{\Upsilon}_{\mathcal{M}_{\mathrm{p}}}^{T}\boldsymbol{y}_{\mathrm{F}}\\ =&\underbrace{\boldsymbol{\Upsilon}_{\mathcal{M}_{\mathrm{p}}}^{T}\boldsymbol{H}\boldsymbol{\Upsilon}_{\mathcal{M}_{\mathrm{s}}}}_{=\boldsymbol{0}}\boldsymbol{s}_{\mathrm{C}}+\boldsymbol{\Upsilon}_{\mathcal{M}_{\mathrm{p}}}^{T}\boldsymbol{n}_{\mathrm{F}}\\ =&\boldsymbol{n}_{\mathrm{p}},\end{aligned} \tag{2.17}$$

respectively. Then, the symbols in $\boldsymbol{y}_{\mathrm{C}}$ are fed into a single-tap FD equaliser, yielding

$$\begin{aligned}\widetilde{\boldsymbol{y}}_{\mathrm{C}} =&\boldsymbol{W}\boldsymbol{y}_{\mathrm{C}}\\ =&\boldsymbol{W}\boldsymbol{H}_{\mathrm{s}}\boldsymbol{s}_{\mathrm{C}}+\boldsymbol{W}\boldsymbol{n}_{\mathrm{s}}\\ =&\boldsymbol{s}_{\mathrm{C}}+\widetilde{\boldsymbol{n}}_{\mathrm{s}},\end{aligned} \tag{2.18}$$

where $\boldsymbol{W}=[\boldsymbol{H}_{\mathrm{s}}^{H}\boldsymbol{H}_{\mathrm{s}}]^{-1}\boldsymbol{H}_{\mathrm{s}}^{H}$ and $\boldsymbol{n}_{\mathrm{C}}=\boldsymbol{W}\boldsymbol{n}_{\mathrm{s}}$ contains the filtered noise. Next, after 2D de-interleaving, we have

$$\begin{aligned}\boldsymbol{r}_{\mathrm{C}} =&\boldsymbol{x}_{\mathrm{C}}+\boldsymbol{n}_{\mathrm{C}}\\ =&\boldsymbol{\mathcal{F}}_{N}\boldsymbol{x}_{\mathrm{U}}+\boldsymbol{n}_{\mathrm{C}}\\ =&\boldsymbol{\mathcal{F}}_{N}\boldsymbol{\Upsilon}_{\mathcal{I}_{\mathrm{d}}}\boldsymbol{x}_{\mathrm{d}}+\boldsymbol{n}_{\mathrm{C}},\end{aligned} \tag{2.19}$$

where $\boldsymbol{n}_{\mathrm{C}}$ denotes the de-interleaved version of $\widetilde{\boldsymbol{n}}_{\mathrm{s}}$.

2.4.1 Design Criteria of the 2D Interleaver for Sparsity

As shown in Section 2.3, when there is asynchronous impulsive noise, multiple successive symbols may be corrupted, whose effect can be alleviated by interleaving.

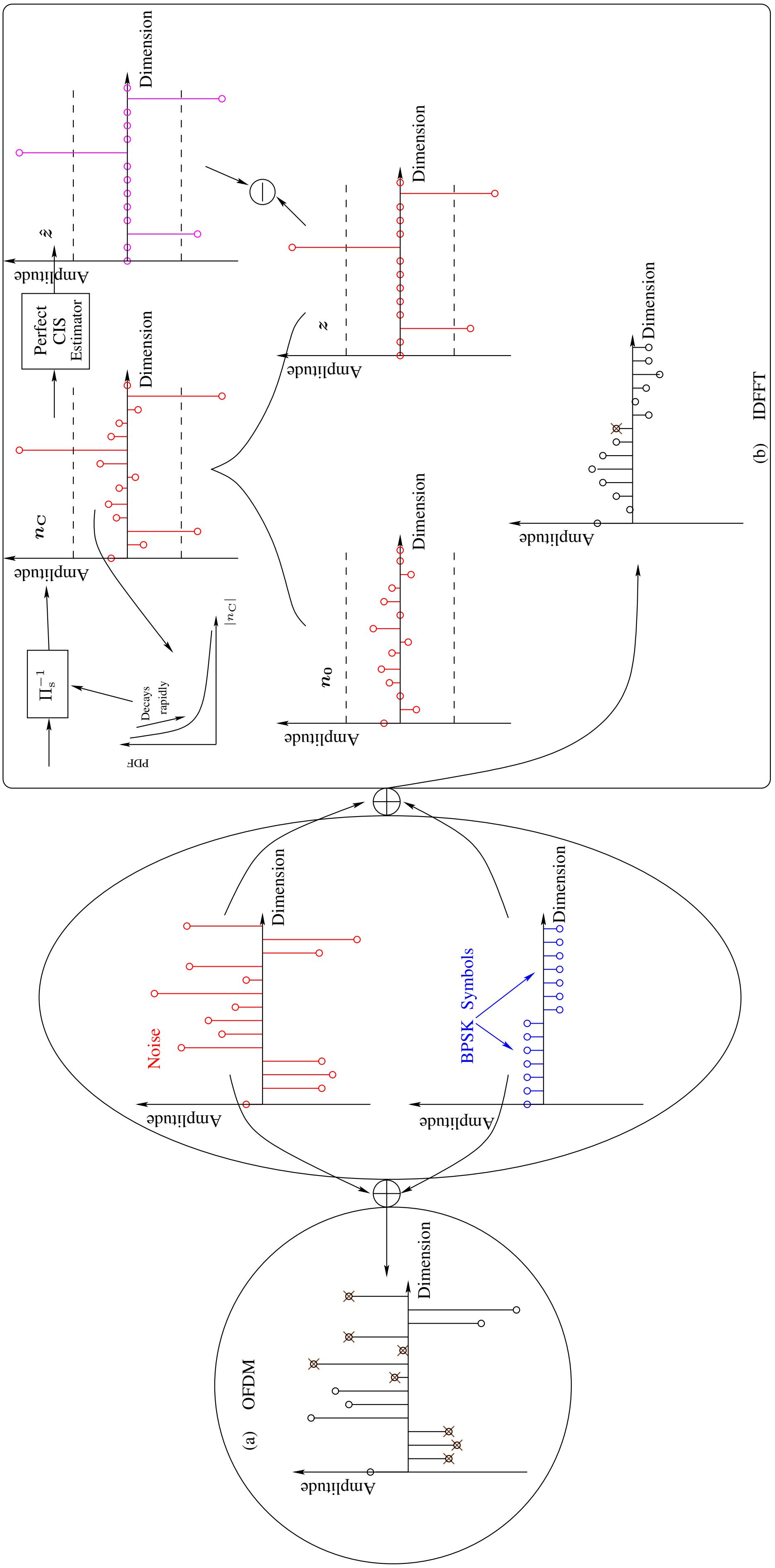

Figure 2.5: Illustration of the framework of our compressed impairment sensing.

Below, the design criteria of the 2D interleaver are detailed.

The *first design criterion* of the 2D interleaver Π_{s} is that the noise vector $\boldsymbol{n}_{\mathrm{C}}$ after de-interleaving has to be compressible. To elaborate further, let us define the best k-term approximation of $\boldsymbol{n}_{\mathrm{C}}$ as

$$\boldsymbol{z} \triangleq \{z(i) = \mathbb{I}[i \in \mathcal{T}]n_{\mathrm{C}}(i), i = 0, 1, \ldots, N-1\}, \tag{2.20}$$

where the indicator function is given by

$$\mathbb{I}[\mathrm{e}] = \begin{cases} 1 & \text{if e is true} \\ 0 & \text{if e is false .} \end{cases} \tag{2.21}$$

Here, indices in the index set $\mathcal{T}$ correspond to the noise samples whose magnitudes are larger than a pre-defined threshold. Moreover, we have $|\mathcal{T}| \leq k$. Then, according to [49], the vector $\boldsymbol{n}_{\mathrm{C}}$ is compressible if the ℓ_p-error defined as $\epsilon_k(\boldsymbol{n}_{\mathrm{C}})_p \triangleq \|\boldsymbol{n}_{\mathrm{C}} - \boldsymbol{z}\|_p$ of its best k-term approximation decays rapidly with k, as illustrated in Fig. 2.5.

Secondly, it is also desirable to evenly spread the effect of an asynchronous impulsive burst to as many blocks as possible, which constitutes our *second design criterion.* In this way, the grade of sparsity k can be minimised. In order to quantify this criterion, we assume that a 2D interleaver having a spreading factor of L_{SF} is designed. Then, the upper bound of k can be derived as

$$k < \left\lceil \frac{L_{\Pi_{\mathrm{s}}}}{L_{\mathrm{SF}}L_M} \right\rceil = \left\lceil \frac{N}{L_{\mathrm{SF}}} \right\rceil, \tag{2.22}$$

where we can readily show that the larger L_{SF}, the lower the sparsity level $k \ll N$ becomes.

Finally, 2D interleaving may result in a reduction of the multipath diversity gain that can be achieved by using precoding. For example, let us consider the extreme case that the data symbols transmitted by the same subchannel are permuted into the same block. In this case, no multipath diversity gain can be obtained from using precoding. Thus, *our third design criterion* is that the subchannel orders of all blocks have to remain unchanged after 2D interleaving.

Based on the above analysis, a 2D interleaver is designed, whose operations are illustrated in Fig 2.6. Explicitly, during the transmission of L_M blocks of symbols denoted as $\boldsymbol{X}_{\mathrm{C}}$, the blocks' order is first interleaved by the S-random interleaver having a minimum distance[1] of $S = \sqrt{a_{\Pi_{\mathrm{s}}} L_M}$ [104–106], where $a_{\Pi_{\mathrm{s}}} > 0$ is a constant. Note that, the S-random interleaver is employed in the first step as a benefit of its

---

[1] As defined in [104], the S-random interleaver is a pseudo-random interleaver with the restriction that any two indices within a distance of S cannot be permuted to indices within a distance of S, where S is known as the minimum distance of the S-random interleaver.

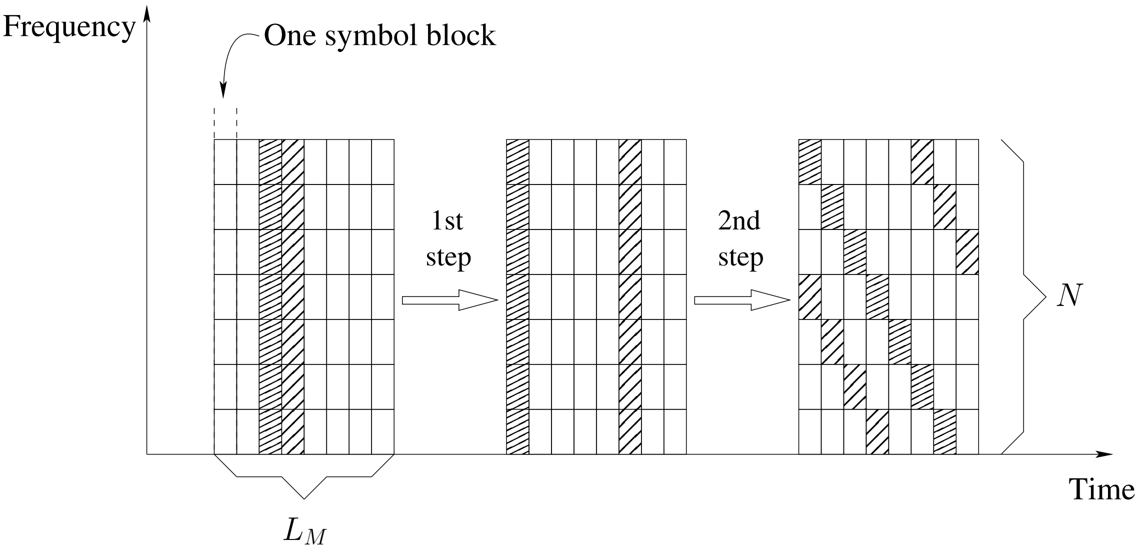

Figure 2.6: Illustration of interleaving process of the 2D Interleaver Π_{s}.

resilience against bursty impulsive noise [107]. Then, as shown in Fig. 2.6, for the ith row of $\boldsymbol{X}_{\mathrm{C}}$, the element in the lth column is circularly shifted to the $l^{\Pi_{\mathrm{s}}}$th column, where we have $l^{\Pi_{\mathrm{s}}} = [(l+i) \mod L_M]$. In this way, even if all the N FD samples of a block experience impulsive noise, after the de-interleaving stage of Fig. 2.6, they will become distributed across L_M different blocks, each of which contains no more than $\lceil N/L_M \rceil$ impulsive noise samples from the impaired original block. Additionally, the interleaving scheme guarantees that the data symbols conveyed by the same subchannel of different blocks will not be permuted to the same block.

In order to facilitate the following descriptions and discussions, we assume that the parameters of our 2D interleaver Π_{s} are carefully chosen to meet all the above-mentioned criteria.

2.4.2 Formulation of Compressed Impairment Sensing

Firstly, the noise vector $\boldsymbol{n}_{\mathrm{C}}$ can be expressed with the aid of its best k-term approximation $\boldsymbol{z}$ defined in (2.20) as

$$\boldsymbol{n}_{\mathrm{C}} = \boldsymbol{n}_0 + \boldsymbol{z}, \tag{2.23}$$

where we have $n_0(i) = \mathbb{I}[i \notin \mathcal{T}]n_{\mathrm{C}}(i)$ for $i = 0, \ldots, N-1$. It should be emphasised here that in comparison to the compressible vector $\boldsymbol{n}_{\mathrm{C}}$, we are more interested in the vector $\boldsymbol{z}$, since it contains noise samples having a high near-instantaneous power that may severely degrade the system's performance, as illustrated in Fig. 2.5. In other words, we are not interested in estimating the insignificant noise contributions that are unlikely to lead to data detection errors. Thus, we can define the vector $\boldsymbol{z}$

associated with a sparsity level of $\|\boldsymbol{z}\|_0 = k$ as the significant impairment vector to be estimated. In this case, the received pilot symbols can be formulated as

$$\begin{aligned}\boldsymbol{r}_{\mathrm{p}} =&\boldsymbol{\Upsilon}_{\mathcal{I}_{\mathrm{p}}}^{T}\boldsymbol{\mathcal{F}}_{N}^{H}\boldsymbol{r}_{\mathrm{C}}\\ =&\underbrace{\boldsymbol{\Upsilon}_{\mathcal{I}_{\mathrm{p}}}^{T}\boldsymbol{\mathcal{F}}_{N}^{H}\boldsymbol{\mathcal{F}}_{N}\boldsymbol{\Upsilon}_{\mathcal{I}_{\mathrm{d}}}}_{=\mathbf{0}}\boldsymbol{x}_{\mathrm{d}}^{T}+\boldsymbol{\Upsilon}_{\mathcal{I}_{\mathrm{p}}}^{T}\boldsymbol{\mathcal{F}}_{N}^{H}(\boldsymbol{n}_0+\boldsymbol{z})\\ =&\boldsymbol{\Upsilon}_{\mathcal{I}_{\mathrm{p}}}^{T}\boldsymbol{\mathcal{F}}_{N}^{H}\boldsymbol{z}+\boldsymbol{\Upsilon}_{\mathcal{I}_{\mathrm{p}}}^{T}\boldsymbol{\Phi}^{H}\boldsymbol{n}_0\\ =&\boldsymbol{A}\boldsymbol{z}+\boldsymbol{n}_{\mathrm{p}},\end{aligned} \tag{2.24}$$

where $\boldsymbol{n}_{\mathrm{p}} = \boldsymbol{\Upsilon}_{\mathcal{I}_{\mathrm{p}}}^{T}\boldsymbol{\mathcal{F}}_{N}^{H}\boldsymbol{n}_0$ contains the samples to be treated as noise by our estimator. Specifically, let $\mathcal{B}$ be a bounded set associated with the noise vector $\boldsymbol{n}_{\mathrm{p}}$. Note that, the noise samples in $\boldsymbol{n}_{\mathrm{p}}$ are not necessary to be Gaussian in our CIS. In (2.24), we define a measurement matrix $\boldsymbol{A} = \boldsymbol{\Upsilon}_{\mathcal{I}_{\mathrm{p}}}^{T}\boldsymbol{\mathcal{F}}_{N}^{H} \in \mathbb{C}^{m\times N}$ for $\boldsymbol{z}$, which is detailed next.

2.4.3 Pilot Design for Compressed Impairment Sensing

In CS, the measurement matrix $\boldsymbol{A}$ is designed for supporting stable information-preserving compression, so that a guaranteed recovery performance can be achieved. According to [43, 47], the measurement matrix $\boldsymbol{A}$ should be designed for satisfying the MIP[2] or the RIP[3]. However, since computing the restricted isometry constant of the RIP has been shown to be NP-hard [53], the MIP is used in this chapter. According to [43], the mutual coherence of $\boldsymbol{A}$ should satisfy $\mu_{\boldsymbol{A}} < 1/(2k-1)$, which is the sufficient condition of guaranteeing that there exists at most one k-sparse vector $\boldsymbol{z}$ such that $\boldsymbol{A}\boldsymbol{z} = \boldsymbol{r}$. Thus, in order to provide a guaranteed estimation performance, the positions of pilots should be chosen so that the measurement matrix $\boldsymbol{A} \in \mathbb{C}^{m\times N}$ satisfies

$$\sqrt{\frac{N-m}{m(N-1)}} \leq \mu_{\boldsymbol{A}} < \frac{1}{2k-1}, \tag{2.25}$$

where the lower bound at the left hand side is the well-known Welch bound [108]. Furthermore, as a striking feature of our system design shown in Section 2.2.1, the values of N and m can be flexibly chosen for adjusting to the positions of pilots, so that the measurement matrix $\boldsymbol{A}$ can be formed to be a Maximum-Welch-Bound-Equality (MWBE) codebook, which is also known as an Equiangular Tight Frame (ETF) [109]. In this case, we have $\mu_{\boldsymbol{A}} = \sqrt{(N-m)/[m(N-1)]}$.

As defined in (2.24), the measurement matrix $\boldsymbol{A}$, which is composed of a row-selection matrix $\boldsymbol{\Upsilon}_{\mathcal{I}_{\mathrm{P}}}^{T}$ and the DFT matrix $\boldsymbol{\mathcal{F}}_{N}^{H}$, is a partial Fourier matrix with the

---

[2] The MIP is defined as the mutual coherence of a matrix is very small [43].

[3] As defined in [47], the RIP is defined as the kth restricted isometry constant δ_k of matrix $\boldsymbol{A}$ is the smallest number such that $(1-\delta_k)\|\boldsymbol{z}\|_2^2 \leq \|\boldsymbol{A}\boldsymbol{z}\|_2^2 \leq (1+\delta_k)\|\boldsymbol{z}\|_2^2$ is satisfied for any k-sparse vectors $\boldsymbol{z}$.

mutual coherence expressed as [108]

$$\begin{aligned}\mu_{\boldsymbol{A}} &= \max_{0\le l_1<l_2\le N-1} \frac{\left|(\boldsymbol{a}(l_1))^H\boldsymbol{a}(l_2)\right|}{\|\boldsymbol{a}(l_1)\|_2\|\boldsymbol{a}(l_2)\|_2} \\ &= \max_{0\le l_1<l_2\le N-1} \frac{1}{m}\left|\sum_{i=0}^{m-1}\exp\left\{j\frac{2\pi\mathcal{I}_{\mathrm{p}}(i)}{N}(l_1-l_2)\right\}\right| \\ &= \max_{1\le l\le N-1}\frac{1}{m}\left|\sum_{i=0}^{m-1}\exp\left\{j\frac{2\pi l}{N}\mathcal{I}_{\mathrm{p}}(i)\right\}\right|, \end{aligned} \tag{2.26}$$

where $\boldsymbol{a}(x)$ denotes the xth column of $\boldsymbol{A}$, while $l = (l_1 - l_2) \bmod N$. As shown in (2.26), the mutual coherence of matrix $\boldsymbol{A}$ depends on the corresponding index set $\mathcal{I}_{\mathrm{p}}$, giving the specific positions of the pilots. Let us define a binary sequence $\boldsymbol{c}_{\mathrm{p}} = [c_{\mathrm{p}}(0), c_{\mathrm{p}}(1), \ldots, c_{\mathrm{p}}(N-1)]^T$, where $c_{\mathrm{p}}(i) = 0$, $\forall i \notin \mathcal{I}_{\mathrm{p}}$, while $c_{\mathrm{p}}(\mathcal{I}_{\mathrm{p}}(i)) = 1$ for $i = 0, 1, \ldots, m-1$. Then, (2.26) can be equivalently expressed as

$$\mu_{\boldsymbol{A}} = \max_{1\le l\le N-1}\frac{1}{m}\left|\sum_{i=0}^{N-1}c_{\mathrm{p}}(i)\exp\left\{j\frac{2\pi il}{N}\right\}\right|. \tag{2.27}$$

Then, in order to achieve the minimum mutual coherence, or in other words to obtain the MWBE codebook for the partial Fourier matrix, the pilots' position indices $\mathcal{I}_{\mathrm{p}}$ or binary sequence $\boldsymbol{c}_{\mathrm{p}}$ can be designed by solving the following problem

$$\begin{aligned}\boldsymbol{c}_{\mathrm{p}}^{(opt)} =& \arg\min_{\boldsymbol{c}_{\mathrm{p}}}\left\{\max_{1\le l\le N-1}\frac{1}{m}\left|\sum_{i=0}^{N-1}c_{\mathrm{p}}(i)\exp\left\{j\frac{2\pi il}{N}\right\}\right|\right\} \\ =& \sqrt{\frac{N-m}{m(N-1)}}. \end{aligned} \tag{2.28}$$

In practice, the Inverse Discrete Fourier Transform (IDFT) matrix $\boldsymbol{\mathcal{F}}_N^H$ is usually selected to satisfy $N = 2^{\alpha}$, in order to achieve high estimation-speed, low-power consumption, as well as low round-off error. When this type of IDFT matrix is considered, there is a paucity of information concerning the MWBE codebook. Furthermore, there are no known analytical approaches for the construction of the MWBE codebook in the case of $N = 2^{\alpha}$. Consequently, the near-optimal codebooks have been proposed in the literature [110–113], aiming at finding the near-optimal binary sequences $\hat{\boldsymbol{c}}_{\mathrm{p}}$ by solving the optimisation problem of

$$\hat{\boldsymbol{c}}_{\mathrm{p}} = \arg\min_{\boldsymbol{c}_{\mathrm{p}}}\left\{\max_{1\le l\le N-1}\frac{1}{m}\left|\sum_{i=0}^{N-1}c_{\mathrm{p}}(i)\exp\left\{j\frac{2\pi il}{N}\right\}\right|\right\}. \tag{2.29}$$

Specifically, in [110], the authors have shown that, when $\boldsymbol{c}_{\mathrm{p}}$ is a binary Golay sequence, it is possible to construct a codebook, whose mutual coherence is approximately $\sqrt{2}$ times higher than the Welch bound, provided that N is sufficiently high. However, this approach is not flexible, since the value of m is fixed. Another concern is that for the design of pilot symbols, the value of m suitable for binary Golay sequences is excessive for practical application. Therefore, often numerical search methods have been applied [111–113]. Specifically, the brute-force search [111], the modified Lloyd search algorithm [112], and a search method based on smooth sequential optimisation relying on the Grassmannian manifold [113] have been considered. However, these search algorithms typically exhibit a high computational complexity. Based on the above observation, in this section, we propose a low-complexity search algorithm for the design of the measurement matrix $\boldsymbol{A}$, which determines the positions of the pilots.

Algorithm 1 Find the Optimal Solution of (2.30)

```
Require: $N$, $m$, $\boldsymbol{\mathcal{F}}_{N-1}^H$
Initialization: Set $\mathcal{I}_N = [0, 1, \ldots, N-1]$, $\hat{\mu} = 1$, the number of candidates to $L_c$, and $\hat{\boldsymbol{c}}_\mathrm{p} = \emptyset$;
for $t = 1$ to $T$ do
    Set $\boldsymbol{C}_\mathrm{p} = \mathbf{0}_{N \times L_c}$;
    for $l = 1$ to $L_c$ do
        Randomly permute $\mathcal{I}_N$; then, collect the first $m$ elements into $\mathcal{I}_\mathrm{p}(l)$;
        The elements in the $l$th column of $\boldsymbol{C}_\mathrm{p}$ are updated by
            $C_\mathrm{p}(i, l_c) = \begin{cases} 1, & \text{if } i \in \mathcal{I}_\mathrm{p}(l_c) \\ 0, & \text{otherwise} \end{cases};$
    end for
    Calculate $\breve{\boldsymbol{C}}_\mathrm{p} = \frac{1}{m}\boldsymbol{\mathcal{F}}_{N-1}^H \boldsymbol{C}_\mathrm{p}$;
    Find the index $\hat{l}_c$ by solving                                    ▷ (2.29)←(2.30)
        $\hat{l}_c = \underset{l_c = 1, 2, \ldots, L_c}{\arg\min} \left\{ \max_{0 \le i \le N-2} \left| \breve{C}_\mathrm{p}(i, l_c) \right| \right\};$
    Obtain $\breve{\mu}(\hat{l}_c) = \max_{0 \le i \le N-2} \left| \breve{C}_\mathrm{p}(i, \hat{l}_c) \right|$;      ▷ (2.30)
    if $\breve{\mu}(\hat{l}_c) < \hat{\mu}$ then
        $\hat{\mu} = \breve{\mu}(\hat{l}_c)$;
        $\hat{\boldsymbol{c}}_\mathrm{p} = \boldsymbol{C}_\mathrm{p}(\hat{l}_c)$;
    end if
end for
return $\hat{\mu}$ and $\hat{\boldsymbol{c}}_\mathrm{p}$.
```

Firstly, let us define $\breve{\boldsymbol{c}}_\mathrm{p} = \boldsymbol{\mathcal{F}}_{N-1}^H \boldsymbol{c}_\mathrm{p}$, where $\boldsymbol{\mathcal{F}}_{N-1}^H$ is obtained by eliminating the zeroth row of $\boldsymbol{\mathcal{F}}_N^H$. Hence, in comparison to the summation given in (2.29), a more friendly expression in matrix form is obtained. In this way, (2.29) can be rewritten as

$$\hat{\boldsymbol{c}}_{\mathrm{p}}^{'} = \arg\min_{\breve{\boldsymbol{c}}_{\mathrm{p}}} \left\{ \max_{0 \le l' \le N-2} \frac{|\breve{c}_{\mathrm{p}}(l')|}{m} \right\}, \tag{2.30}$$

where $\breve{c}_{\mathrm{p}}(l')$ is the l'th element of $\breve{\boldsymbol{c}}_{\mathrm{p}}$. Our search procedure is formulated in Algorithm 1.

To elaborate further on the above algorithm, the mutual coherence is calculated from (2.30), where only the single variable l' is required. Therefore, the complexity of calculating the mutual coherence is on the order of $\mathcal{O}(N)$. For a large N, the complexity of our algorithm is significantly lower than that of the conventional approaches [111, 112]. Moreover, as shown in line 8 of Algorithm 1, by taking advantage of the Fourier transform, the L_c number of candidates can be calculated simultaneously, instead of being calculated successively. Therefore, our algorithm constitutes an efficient search technique.

2.4.4 Recovery Problems of Compressed Impairment Sensing

According to the above-mentioned analysis, given the observation equation in the form of (2.24), the spare vector $\boldsymbol{z}$ can be recovered by solving the classic ℓ_0-minimisation problem described in [46, 82] as

$$\boldsymbol{z}^{\ell_0} = \arg\min_{\boldsymbol{v} \in \mathbb{C}^{N\times 1}} \|\boldsymbol{v}\|_0, \quad \text{s.t.} \quad \boldsymbol{r}_{\mathrm{p}} - \boldsymbol{A}\boldsymbol{v} \in \mathcal{B}, \tag{2.31}$$

where $\boldsymbol{v}$ is an N-length testing vector chosen from the complex vector space $\mathbb{C}^{N\times 1}$. However, the ℓ_0-minimisation problem of (2.31) has been shown to be NP-hard [114]. For this reason, typically the ℓ_1-minimisation based solutions are employed in CS, since they are tractable to solve. Moreover, under the conditions shown in [54], the ℓ_0-minimisation problem of (2.31) is equivalent to solving the ℓ_1-minimisation problem of

$$\boldsymbol{z}^{\ell_1} = \arg\min_{\boldsymbol{v} \in \mathbb{C}^{N\times 1}} \|\boldsymbol{v}\|_1, \quad \text{s.t.} \quad \boldsymbol{r}_{\mathrm{p}} - \boldsymbol{A}\boldsymbol{v} \in \mathcal{B}. \tag{2.32}$$

Note that the ℓ_1-minimisation problem is a well-known convex optimisation problem, which can be solved in polynomial time, for example, by the interior point method [39]. However, for our scenario, the corresponding computational cost is still excessive. In this case, the lower-complexity family of greedy algorithms [74, 76] is preferred.

However, when the existed greedy algorithms are applied, the sparsity level k is usually required to be known as *a priori* information, which is clearly undesirable for our scenario. Since asynchronous impulsive noise is sporadic, the value of k may vary from block-to-block. Explicitly, when $k = 0$, no effort is required to estimate

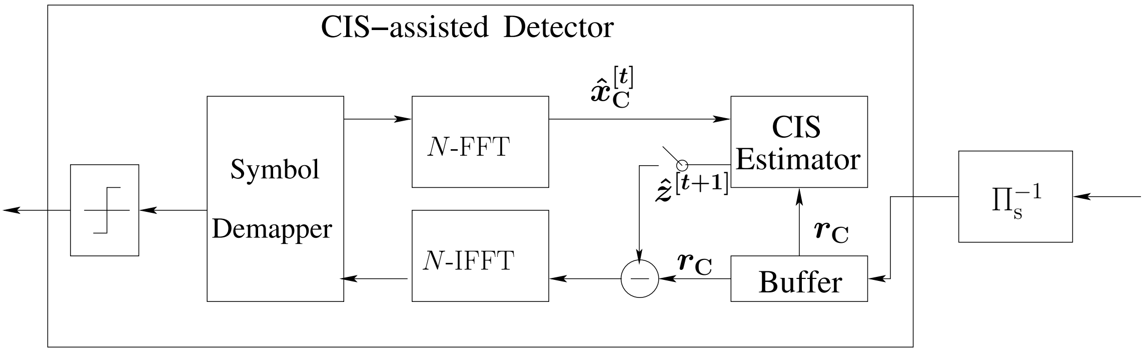

Figure 2.7: Illustration of our proposed joint CIS-assisted estimation and symbol detection scheme.

the impairment vector $\boldsymbol{z}$. By contrast, when $k \neq 0$, an estimation of $\boldsymbol{z}$ shall be operated based on our CIS. To address the above-mentioned issues, we propose a joint impairment estimation and symbol detection scheme, namely the CIS-assisted detector, as detailed in the next section.

2.5 Compressed Impairment Sensing Assisted Detector

As seen in Fig. 2.7, our proposed CIS-assisted detector is constituted by three blocks, which are the impairment estimation based on CIS, the impairment cancellation as well as the symbol detection. The basic idea of our CIS-assisted detector is based on the turbo principle, where the CIS-assisted estimator iteratively exchanges information with the symbol detector. In this way, the impairments associated with high near-instantaneous power, which degrade the system's performance severely, can be reliably estimated and eliminated. We commence by describing our CIS-assisted estimator, as detailed below.

2.5.1 Impairment Estimation Based on Compressed Sensing

During the first operation of our detector, impairment estimation is carried out, which is invoked for solving the recovery problems of the CIS discussed in Section 2.4.4. Based on the basic principle of the greedy algorithms of [42, 71, 72, 74, 75], we propose a low-complexity algorithm to deal with the impairment estimation problem of (2.24), where during each iteration, the columns of the measurement matrix $\boldsymbol{A}$ corresponding to the non-zero locations of the impairment vector $\boldsymbol{z}$ are first estimated (which is referred to as the support estimation in the sequel). Then, a sparse vector is obtained by finding the projections of the measurements $\boldsymbol{r}_{\mathrm{p}}$ onto these columns as an estimate of the current iteration.

Firstly, let us consider the support estimation of the CIS formulation given in (2.24). A commonly used method in CS for the support estimation at the $(t+1)$th iteration is to find the columns of $\boldsymbol{A}$ that have the strongest correlation of the residual vector of $(\boldsymbol{r}_{\mathrm{p}} - \boldsymbol{A}\hat{\boldsymbol{z}}^{[t]})$, where $\hat{\boldsymbol{z}}^{[t]}$ denotes the estimate extracted from the tth iteration. However, when the current block is not impaired by any high instantaneous power, i.e. when we have $\boldsymbol{z} = \boldsymbol{0}$ in conjunction with $k = 0$, the above-mentioned support estimation is not required, similarly to the impairment estimation problem discussed in Section 2.4.4. In order to tackle this problem, we propose a support estimation approach, which is capable of making a decision for activating impairment estimation, as well as of implementing the support estimation. In more detail, during the $(t+1)$th iteration, the previous detected symbols are fed into the CIS estimator, as seen in Fig. 2.7. Let us denote each block of detected data symbols at the tth iteration as $\hat{\boldsymbol{x}}_{\mathrm{d}}^{[t]}$, which is precoded by $\boldsymbol{\mathcal{F}}_N$, yielding $\hat{\boldsymbol{x}}_{\mathrm{C}}^{[t]} = \boldsymbol{\mathcal{F}}_N \boldsymbol{\Upsilon}_{\mathcal{I}_{\mathrm{d}}} \hat{\boldsymbol{x}}_{\mathrm{d}}^{[t]} \in \mathbb{C}^N$. Specifically, we let $\hat{\boldsymbol{x}}_{\mathrm{C}}^{[0]} = \boldsymbol{0}$ at the initial step. Then, as shown in Fig. 2.7, the symbols in $\hat{\boldsymbol{x}}_{\mathrm{C}}^{[t]}$ are fed into the CIS estimator as the *a priori* information. Hence, the support estimate at the $(t+1)$th iteration can be obtained as

$$\hat{\mathcal{T}}^{[t+1]} \triangleq \left\{ i : \left| r_{\mathrm{C}}(i) - \hat{x}_{\mathrm{C}}^{[t]}(i) \right|^2 > \varepsilon_{\mathrm{TH}}^{[t]} \text{ for } i = 0, \ldots, N-1 \right\}, \tag{2.33}$$

where $\varepsilon_{\mathrm{TH}}^{[t]}$ is a pre-defined threshold at the tth iteration.

As inferred from (2.19) and (2.23), the reliability of the decoder is increased during each iteration, hence the support estimation performance can be improved, since the estimated support $\hat{\mathcal{T}}^{[t+1]}$ becomes more and more close to $\mathcal{T}$ defined in (2.20). Meanwhile, it can be readily shown that when $\left|\hat{\mathcal{T}}^{[t+1]}\right| = 0$, CIS is not required at this iteration. By contrast, when we have $\left|\hat{\mathcal{T}}^{[t+1]}\right| \neq 0$, CIS is activated for estimating the respective sparse parameter vector. In this case, based on the estimated support $\hat{\mathcal{T}}^{[t+1]}$, the locally optimal solution can be obtained by solving

$$\boldsymbol{\Upsilon}_{\hat{\mathcal{T}}^{[t+1]}}^{T} \hat{\boldsymbol{z}}^{[t+1]} = \underset{\boldsymbol{v} \in \mathbb{C}^{k \times 1}}{\arg\min} \left\| \boldsymbol{r}_{\mathrm{p}} - \boldsymbol{A} \boldsymbol{\Upsilon}_{\hat{\mathcal{T}}^{[t+1]}} \boldsymbol{v} \right\|_2^2 . \tag{2.34}$$

The optimisation problem of (2.34) can be solved by the well-known OLS approach, yielding

$$\hat{\boldsymbol{z}}^{[t+1]} = \boldsymbol{\Upsilon}_{\hat{\mathcal{T}}^{[t+1]}} \left(\boldsymbol{\Upsilon}_{\hat{\mathcal{T}}^{[t+1]}}^{T} \boldsymbol{A}^H \boldsymbol{r}_{\mathrm{p}} \right). \tag{2.35}$$

2.5.2 Impairment Cancellation and Symbol Detection

As seen in Fig. 2.7, during the $(t+1)$th iteration, with the aid of the estimate $\hat{\boldsymbol{z}}^{[t+1]}$ given in (2.35), the impairment cancellation is carried out. Then, the soft decision variables for each block of received data symbols can be obtained as

$$\begin{aligned}\hat{\boldsymbol{r}}_{\mathrm{d}}^{[t+1]} &= \boldsymbol{\Upsilon}_{\mathcal{I}_{\mathrm{d}}}^{T}\boldsymbol{\mathcal{F}}_{N}^{H}\left(\boldsymbol{r}_{\mathrm{C}}-\hat{\boldsymbol{z}}^{[t+1]}\right)\\ &= \boldsymbol{\Upsilon}_{\mathcal{I}_{\mathrm{d}}}^{T}\boldsymbol{\mathcal{F}}_{N}^{H}\boldsymbol{\mathcal{F}}_{N}\boldsymbol{\Upsilon}_{\mathcal{I}_{\mathrm{d}}}\boldsymbol{x}_{\mathrm{d}}+\boldsymbol{\Upsilon}_{\mathcal{I}_{\mathrm{d}}}^{T}\boldsymbol{\mathcal{F}}_{N}^{H}\left(\boldsymbol{n}_{\mathrm{C}}-\hat{\boldsymbol{z}}^{[t+1]}\right)\\ &= \boldsymbol{x}_{\mathrm{d}}+\hat{\boldsymbol{n}}_{\mathrm{d}}^{[t+1]},\end{aligned} \tag{2.36}$$

where, for simplicity, we define $\hat{\boldsymbol{n}}_{\mathrm{d}}^{[t+1]} = \boldsymbol{\Upsilon}_{\mathcal{I}_{\mathrm{d}}}^{T}\boldsymbol{\mathcal{F}}_{N}^{H}\left(\boldsymbol{n}_{\mathrm{C}}-\hat{\boldsymbol{z}}^{[t+1]}\right)$. Note that when N is sufficient large, the vector $\hat{\boldsymbol{n}}_{\mathrm{d}}^{[t+1]}$ can be approximated as a Gaussian vector. Since candidates in $\mathcal{A}$ have been assumed to be equiprobable, the ith detected symbol at the $(t+1)$th iterations can be obtain by invoking the ML principle as

$$\hat{x}_{\mathrm{d}}^{[t]}(i) = \arg\min_{\forall a_q\in\mathcal{A}} \left\|\hat{r}_{\mathrm{d}}^{[t+1]}(i)-a_q\right\|^2, \tag{2.37}$$

which is used for the next iteration step.

Based on the above analysis, our proposed joint CIS estimation and symbol detection algorithm is summarised in Algorithm 2. Note that after a certain number of iterations, the algorithm is terminated, since the impairment cancellation has achieved its target performance. It can be readily shown that the specific choice of the threshold $\varepsilon_{\mathrm{TH}}^{[t]}$ defined in (2.33) plays an important role in determining the performance of our CIS-assisted detector, since it determines the accuracy of the CIS estimator. Explicitly, when the threshold at a certain iteration is inappropriately chosen, it may lead to an incorrect estimation, which usually yields a degraded detection performance. As a result, the overall performance may be severely degraded. However, it is hard to derive an analytical expression for the optimal threshold $\varepsilon_{\mathrm{TH}}^{[t]}$. Thus, in this chapter, simulations are relied upon for finding the optimal value of the threshold $\varepsilon_{\mathrm{TH}}^{[t]}$, as it will be shown in Section 2.6.

2.5.3 Complexity Analysis

In the classic OFDM system, the complexity of the ML detection of M_{d} data symbols is on the order of $\mathcal{O}(M_{\mathrm{d}})$. By contrast, the complexity of our proposed CIS-assisted detector is composed of three parts, which are the CIS, the symbol detector, as well as the IFFT/FFT. Here, we should emphasise that the computational cost related to the mapping matrices, e.g. $\boldsymbol{\Upsilon}_{\mathcal{I}_{\mathrm{d}}}$ and $\boldsymbol{\Upsilon}_{\mathcal{I}_{\mathrm{p}}}$ can be neglected, since in practice they only represent row or column selection operations. Bearing this in mind, let us detail the complexity of each component below.

Firstly, the complexity of our CIS is due to the support estimation of (2.33) and the impairment estimation of (2.35). Explicitly, at each iteration, we can readily

Algorithm 2 CIS-Assisted Symbol Detector

```
Require: $\boldsymbol{A} = \boldsymbol{\Upsilon}_{\mathcal{I}_{\mathrm{p}}}^{T} \boldsymbol{\mathcal{F}}_{N}^{H}$, $\boldsymbol{r}_{\mathrm{C}}$, $\mathcal{I}_{\mathrm{d}}$, $\varepsilon_{\mathrm{TH}}^{[t]}$;
Initialisation: Set the symbol vector $\hat{\boldsymbol{x}}_{\mathrm{C}}^{[0]} = \mathbf{0}$,
for $t = 1 \to t_{\mathrm{stop}}$ do
    CIS :
    Obtain the received pilot symbol as                                   ▷ (2.24);
        $\boldsymbol{r}_{\mathrm{p}} = \boldsymbol{A} \boldsymbol{r}_{\mathrm{C}},$
    Obtain the support estimate $\hat{\mathcal{T}}^{[t+1]}$               ▷ (2.33);
        $\hat{\mathcal{T}}^{[t+1]} \triangleq \left\{ i : \left| r_{\mathrm{C}}(i) - \hat{x}_{\mathrm{C}}^{[t]}(i) \right|^{2} > \varepsilon_{\mathrm{TH}}^{[t]} \text{ for } i = 0, \ldots, N-1 \right\},$
    if $\left| \hat{\mathcal{T}}^{[t+1]} \right| = 0$ then
        exit
    else
        Obtain the estimate $\hat{\boldsymbol{z}}^{[t+1]}$                ▷ (2.34)←(2.35);
            $\hat{\boldsymbol{z}}^{[t+1]} = \boldsymbol{\Upsilon}_{\hat{\mathcal{T}}^{[t+1]}} \left( \boldsymbol{\Upsilon}_{\hat{\mathcal{T}}^{[t+1]}}^{T} \boldsymbol{A}^{H} \boldsymbol{r}_{\mathrm{p}} \right).$
    end if
    Symbol Detection
    Calculate the soft decision variables for the current block of received data symbols as   ▷ (2.36);
        $\hat{\boldsymbol{r}}_{\mathrm{d}}^{[t+1]} = \boldsymbol{\Upsilon}_{\mathcal{I}_{\mathrm{d}}}^{T} \boldsymbol{\mathcal{F}}_{N}^{H} \left( \boldsymbol{r}_{\mathrm{C}} - \hat{\boldsymbol{z}}^{[t+1]} \right)$
    for $i = 0 \to M_{\mathrm{d}} - 1$ do
        Obtain the detection result $\hat{x}_{\mathrm{d}}(m, l)$ as       ▷ (2.37);
            $\hat{x}_{\mathrm{d}}^{[t]}(i) = \underset{\forall a_q \in \mathcal{A}}{\arg\min} \left\| \hat{r}_{\mathrm{d}}^{[t+1]}(i) - a_q \right\|^{2},$
    end for
    if $t = t_{\mathrm{stop}}$ then
        exit
    else
        Calculate the feedback as;
            $\hat{\boldsymbol{x}}_{\mathrm{C}}^{[t]} = \boldsymbol{\mathcal{F}}_{N} \boldsymbol{\Upsilon}_{\mathcal{I}_{\mathrm{d}}} \hat{\boldsymbol{x}}_{\mathrm{d}}^{[t]},$
    end if
end for
return $\hat{\boldsymbol{x}}_{\mathrm{d}}$.
```

show that the computational complexity of (2.33) is on the order of $\mathcal{O}(N)$. Then, assuming that the CIS aided impairment estimation is activated at the tth iteration, the computational complexity of (2.35) is on the order of $\mathcal{O}\left(k_S^{[t]} m^2\right)$, where $k_S^{[t]}$ characterises the total number of estimated impairments at the tth iteration. Since the values of $k_S^{[t]}$ and m are significantly lower than N, the overall complexity of our CIS is on order of $\mathcal{O}(t_{\text{stop}} N)$ for t_{stop} iterations.

Secondly, since symbol-by-symbol detection is invoked by Algorithm 2, the complexity of the detection process for m data symbols is on the order of $\mathcal{O}(mQ)$. Thus, the overall computational cost of the symbol detector is on order of $\mathcal{O}(t_{\text{stop}} mQ)$ for t_{stop} iterations.

Finally, as seen in Fig. 2.7, the N-point IFFT is used for generating the received data symbols. Hence, we can readily show that the complexity of the N-point IFFT is on order of $\mathcal{O}(N \log_2 N)$. Furthermore, when the feedback process is activated (i.e. when we set $t_{\text{stop}} > 1$ for Algorithm 2), the complexity of the N-point IFFT (for feedforward process) and the N-point FFT (for the feedback process) is given by $\mathcal{O}(2N \log_2 N)$ for each iteration step. Assuming that Algorithm 2 terminates at the t_{stop}th iteration, the complexity associated with the IFFT/FFT can be shown to be on the order of $\mathcal{O}(N \log_2 N) + \mathcal{O}(2(t_{\text{stop}} - 1) N \log_2 N)$.

Based on the above analysis, we can now readily see that the overall complexity of our CIS-assisted detector is on the order of

$$\mathcal{O}\left[N \log_2 N\right] + \mathcal{O}\left[2(t_{\text{stop}} - 1) N \log_2 N\right] = \mathcal{O}\left[(2t_{\text{stop}} - 1) N \log_2 N\right] \tag{2.38}$$

for a predefined t_{stop}. Generally, the detection performance becomes saturated after a few iterations ($t_{\text{stop}} = 2$ is sufficient, as it will be shown in Section 2.6). Thus, the complexity of our CIS-assisted detector may be deemed acceptable in comparison to the performance gain attained, as it will be studied with the aid of simulation results in the next section.

2.6 Simulation Results

In this section, simulation results are provided for characterising the achievable performance of our proposed system. Firstly, let us consider the system setup and the parameters used in our simulations, which are summarised in Table 2.1.

Table 2.1: Parameters for All Simulations

Channel	$\lvert h_{\mathrm{F}}(a)\rvert \sim$Log-$\mathcal{N}(\Omega_H(a), \sigma_H^2(a))$ $\Omega_H(a) = 0.537a^{-0.496} + 0.001512$ [87] $\sigma_H(a) = 0.445a^{-0.256} - 0.025574$ [87] Phase$(h_{\mathrm{F}}(a)) \sim$ Unif$(-\pi, \pi)$
Noise	$\Omega_0 = 15.2$ ms, $\Lambda_{\mathrm{T}} = -30$ dB $\Lambda_{\mathrm{P}} = 50$ dB
System	$M = 256$, $L_{\mathrm{cp}} = 60$, $\Delta t = 31.25$ ns $L_{\Pi_{\mathrm{s}}} = L_M N$, $a_{\Pi_{\mathrm{s}}} = 0.5$, $L_{\mathrm{SF}} = \sqrt{a_{\Pi_{\mathrm{s}}} L_M} + 1$

2.6.1 System Setup and Parameters

In our simulations, we assume an OFDM system employing $M = 256$ subcarriers and operated in the 1.813-17.813 MHz frequency range. The subcarrier spacing is 62.5 kHz. We consider the scenario of the power grid in Europe, where the mains frequency is 50 Hz. Based on the measurement results of [86], the PLC channel is assumed to be time-invariant within a duration of about 600 μs. In this case, we assume that a total of $L_H = 50$ blocks of OFDM symbols are transmitted during each time-invariant channel segment. For each time-invariant duration, the FDCHTF is generated based on Section 2.2.2 and the corresponding parameters are given in Table 2.1. The average attenuation of the PLC channel is assumed to be constant. In our IDFFT aided system, the CP length is chosen to be $L_{\mathrm{cp}} = 60$. For the background and asynchronous impulsive noise, the noise model described in Section 2.2.3 is considered in conjunction with the parameters listed in Table 2.1. In particular, the PSD level of the background noise is chosen to be -110 dBm/kHz. Furthermore, as shown by measurement results of [25], the power ratio between the asynchronous impulsive noise and the background noise is typically $\Lambda_{\mathrm{P}} = 50$ dB. For reasons of statistical relevance, all simulation results are obtained from the average of the results obtained in a duration of 10 seconds. Throughout this section, the SNR per bit denoted as γ_0 is the ratio between the transmitted power per bit and the power of background noise.

2.6.2 Performance Results

In Fig. 2.8, the BER performance of the proposed IDFFT aided system and of the conventional OFDM system is compared, when communicating over indoor PLC

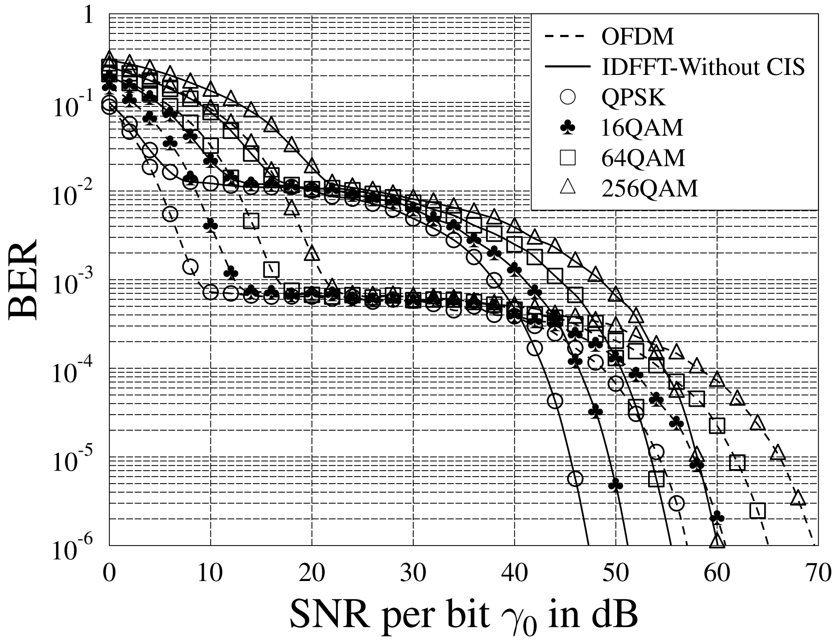

Figure 2.8: Performance comparison between the IDFFT aided PLC system without CIS and the conventional OFDM system, when communicating over the dispersive PLC channel contaminated by both background noise and asynchronous impulsive noise. The parameters are $L_{\Pi_\mathrm{s}} = 50 \times 256$, $\Lambda_\mathrm{T} = -30$ dB, $\Lambda_\mathrm{P} = 50$ dB. All other system parameters are summarised in Table 2.1.

channels contaminated by both the background noise and the impulsive noise. In this figure, four signal constellations are considered, which are Quadrature Phase-Shift Keying (QPSK), 16QAM, 64QAM and 256QAM. The parameters used for characterising the impulsive noise are chosen to be $\Lambda_\mathrm{T} = -30$ dB and $\Lambda_\mathrm{P} = 50$ dB. The IDFFT aided system employs the 2D interleaver size of $L_{\Pi_\mathrm{s}} = L_M \times N$, where we have $L_M = 50$ and $N = M = 256$, i.e., all subcarriers are used for data transmission. Furthermore, in Fig. 2.8, the CIS-assisted impairment estimation is not employed and hence no pilots are used. From the results of Fig. 2.8, we observe that the IDFFT aided system outperforms the conventional OFDM system in the relatively high SNR range, which becomes more pronounced, as γ_0 increases. This observation can be explained as follows. In the IDFFT aided system, there are two types of spreading, namely the FD spreading by the IFFT and the 2D spreading by the interleaver Π_s, as seen in Fig. 2.2. Because of these two spreading schemes, every data symbol is conveyed by all the L_M blocks of transmitted signals, as shown in (2.3). By contrast, every data symbol is only conveyed by a single block of signals in the conventional OFDM system, since its transmitter can only generate the FD spreading effect by the IFFT operation. In principle, the detection performance is mainly affected by the FDCHTF and the impulsive noise, when the SNR is high. In this case, in the IDFFT aided system, the effect of both the FDCHTF and of the impulsive noise is distributed (or averaged) over all the L_M blocks of signals, hence resulting in a steep decay of the average BER curve, as the SNR increases. By contrast, in conventional OFDM systems, the above-mentioned effect is only distributed over a single block of signals, which has a substantial impact on the average error probability. From another angle, we can say that the IDFFT aided system achieves a higher multipath-induced diversity gain than the conventional OFDM system. However, we should note that in the low SNR range, the BER performance is dominated by the background noise. The IFFT-induced spreading effect may introduce more errors for the IDFFT aided system, since in this case, more blocks are impaired by impulsive noise. Consequently, in the low SNR range, the conventional OFDM system achieves a better BER performance than the IDFFT aided system.

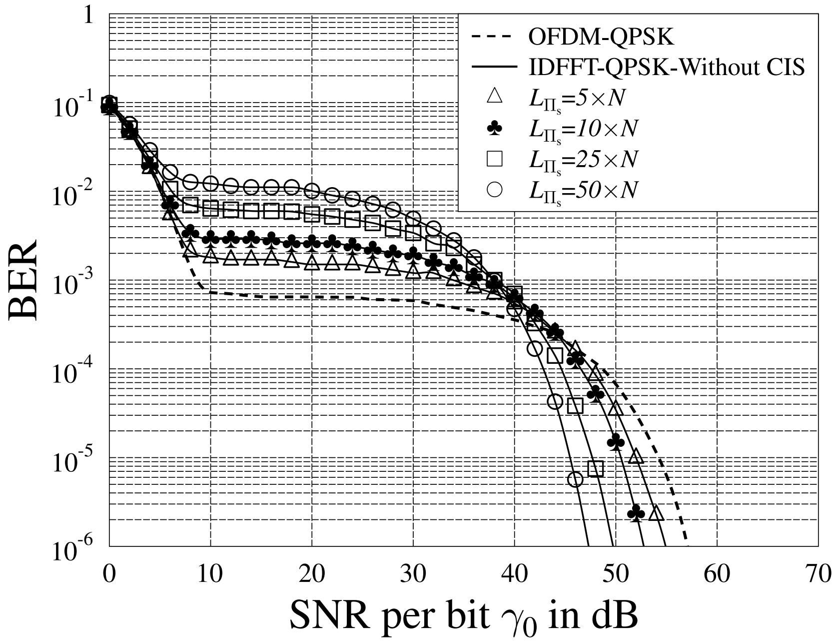

Figure 2.9: BER performance of the IDFFT PLC system using QPSK and different interleaver sizes L_{Π_s}, when communicating over the PLC channel experiencing both asynchronous impulsive noise and background noise. The parameter is given by $N = M = 256$. All other system parameters are summarised in Table 2.1.

Fig. 2.9 shows the effect of the interleaver's size on the BER performance of our IDFFT aided system using QPSK modulation, when communicating over the indoor PLC channels experiencing both background noise and asynchronous impulsive noise. In this figure, the size of the 2D interleaver Π_s of Fig. 2.6 is chosen to be $L_{\Pi_s} = L_M N$, where $L_M = 5$, 10, 25 or 50. Moreover, all subcarriers are activated for data transmission, i.e. we have $N = M = 256$. Again, in this figure, no CIS-assisted impairment estimation is considered. Fig. 2.9 shows that in the high-SNR region, increasing the size of the interleaver is capable of improving the attainable BER performance. However, in the low-to-medium SNR region, the BER performance degrades, as the interleaver size increases. This observation can be explained with the aid of (2.22). By substituting the spreading factor L_{SF} shown in Table 2.1 into (2.22), it can be readily shown that the higher the value of L_M, the high the dispersion capability of the 2D interleaver Π_{s} becomes. Hence, when the SNR is high enough, the spreading effect of the 2D interleaver Π_{s} becomes beneficial, since all subcarriers are only marginally contaminated. By contrast, when the SNR is lower than a certain value, such as $\gamma_0 = 40$ dB in Fig. 2.9, the 2D spreading effect of Π_{s} degrades the attainable BER performance, since after de-interleaving, more errors are introduced into those specific blocks that were originally not impaired by impulsive noise. It should be noted that when choosing the size of the interleaver Π_{s}, a tradeoff has to be struck between the performance gain attained and the time delay imposed.

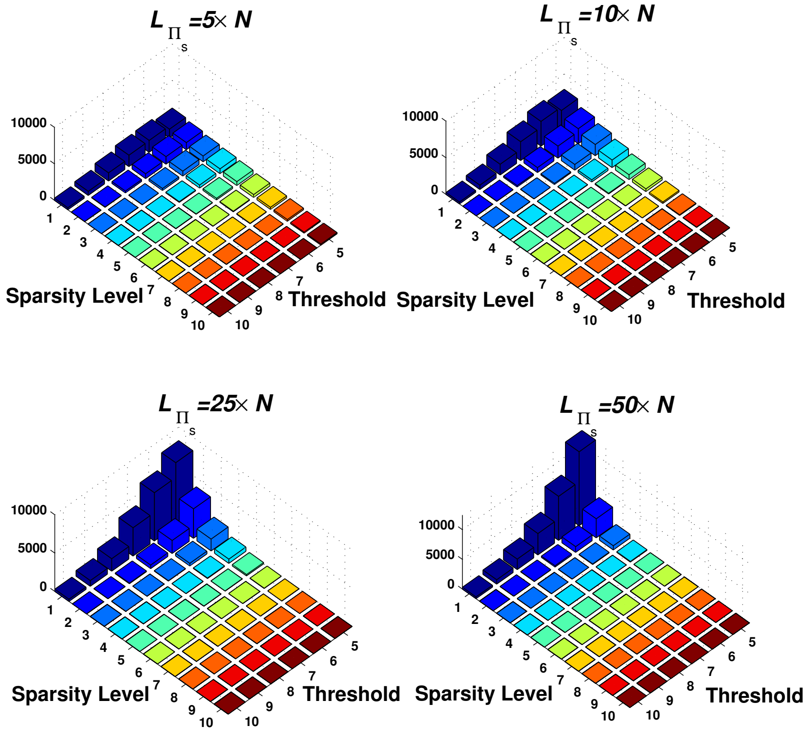

Figure 2.10: Sparsity level k associated with the impairment vector $\boldsymbol{z}$ versus the threshold $\varepsilon_{\mathrm{TH}}^{[1]}$ at the first iteration step, for the IDFFT aided system using QPSK modulation communicating over dispersive PLC channels contaminated by both asynchronous impulsive noise and background noise. The parameter is given by $N = M = 256$. The SNR per bit is $\gamma_0 = 35$ dB. All other system parameters are summarised in Table 2.1.

In Fig. 2.10, we investigate the effects of sparsity level k associated with the impairment vector $\boldsymbol{z}$ defined in (2.20) by varying both the threshold $\varepsilon_{\mathrm{TH}}^{[1]}$ and the interleaver size $L_{\Pi_{\mathrm{s}}}$. In this figure, the IDFFT system operates at the SNR per bit value of $\gamma_0 = 35$ dB without employing CIS-assisted impairment estimation. As depicted in Fig. 2.10, when the interleaver size $L_{\Pi_{\mathrm{s}}}$ increases from $L_M = 5M$ to $L_M = 50M$, the sparsity level distribution of the impairment vector $\boldsymbol{z}$ becomes more "peaky" around the low values of k and $\varepsilon_{\mathrm{TH}}^{[1]}$. Furthermore, when the interleaver size $L_{\Pi_{\mathrm{s}}}$ is fixed, the higher the threshold $\varepsilon_{\mathrm{TH}}^{[1]}$, the more sparse the impairment vector $\boldsymbol{z}$ becomes. These observations confirm our analysis in Section 2.4.1, namely that the sparsity condition of (2.22) can be satisfied with the aid of the 2D interleaver Π_{s}. Therefore, it is indeed possible to estimate the impairment vector $\boldsymbol{z}$ by exploiting the principle of CS.

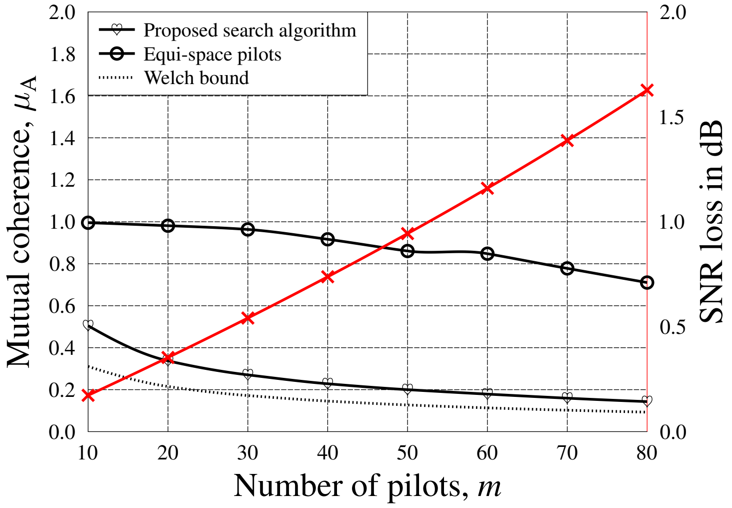

Figure 2.11: Mutual coherence μ and SNR loss versus the number of pilots m, when our proposed search algorithm is applied for constructing the measurement matrix $\boldsymbol{A}$ of size $m \times N$, where we have $N = M = 256$. All other system parameters are summarised in Table 2.1.

In Fig. 2.11 and Fig. 2.12, we investigate the BER performance of the CIS-assisted IDFFT aided system using QPSK upon varying the number of pilots, when communicating over the dispersive PLC channels contaminated by both impulsive noise and background noise. In this figure, the interleaver size is chosen to be $L_{\Pi_{\mathrm{s}}} = 50 \times N$, where we have $N = M = 256$ and $M_{\mathrm{d}} = N - m$. Specifically, the CIS-assisted detector is performed within a single iteration step, i.e. we have $t_{\mathrm{stop}} = 1$. Firstly, as seen in Fig. 2.11, in comparison to the equi-spaced pilots, which is usually used in the conventional pilot-assisted estimation scheme, Algorithm 1 provides a significantly reduced mutual coherence of the measurement matrix $\boldsymbol{A}$. Hence, as stated in Sec-

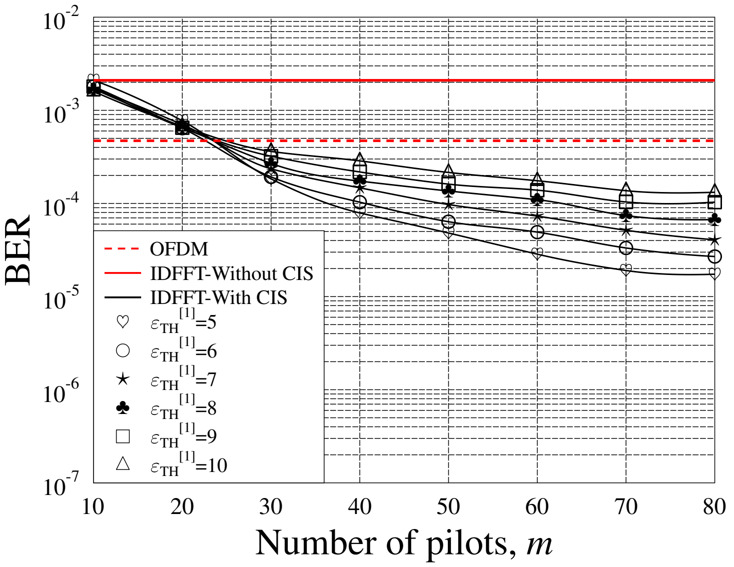

Figure 2.12: BER versus the number of pilots m, when the CIS-assisted IDFFT aided system using QPSK modulation for communicating over dispersive PLC channels contaminated by both asynchronous impulsive noise and background noise. The parameters are $L_{\Pi_s} = 50 \times N$, $N = M = 256$ and $\gamma_0 = 35$ dB. The CIS-assisted detector is performed within a single iteration step, i.e. we have $t_{\text{stop}} = 1$. All other system parameters are summarised in Table 2.1.

tion 2.4.3, when an estimation problem is solved with the aid of CS, the performance achieved by our proposed design of the pilot positions should be better than that achieved by the equi-spaced scheme. Secondly, Fig. 2.11 shows that upon increasing the number of pilots, a measurement matrix $\boldsymbol{A}$ having a lower mutual coherence can be obtained, which implies that a better overall performance can be attained. This inference can be verified by the simulation results shown in Fig. 2.12. As observed in Fig. 2.12, when the number of pilots increases, the BER performance of the CIS-assisted IDFFT system improves. Thirdly, the performance improvements achieved by our proposed CIS-assisted detector are achieved at the cost of an SNR loss imposed by using a higher proportion of pilots, as seen in Fig. 2.11. This tradeoff is confirmed by the simulation results of Fig. 2.12. As seen in Fig. 2.12, when the number of pilots increases, the attainable performance gain becomes more marginal. This implies that for a high proportion of pilots, the performance gain achieved by the CIS-assisted detection becomes saturated. Thus, as inferred from Fig. 2.11 and Fig. 2.12, there is an optimal value for m, which allows our proposed CIS-assisted detection algorithm to attain its best performance. Fourthly, as observed from Fig. 2.12, for a given number of pilots, the achievable performance gain is reduced, as the threshold $\varepsilon_{\text{TH}}^{[1]}$ is increased. This observation can be explained with the aid of Fig. 2.10. When the threshold $\varepsilon_{\mathrm{TH}}^{[1]}$ is increased, the number of impairment events detected by the threshold-based estimator of (2.33) is reduced. Hence, the attainable performance gain becomes limited. Finally, we can infer from both Fig. 2.8 and Fig. 2.12 that the BER performance can be significantly improved by our CIS-assisted IDFFT aided system in comparison to the conventional OFDM system.

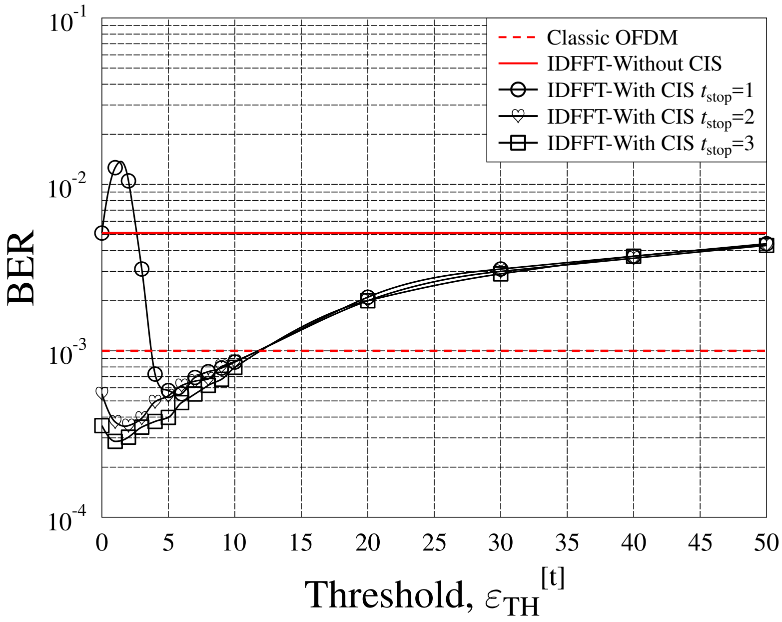

Figure 2.13: BER performance versus the threshold of our CIS-assisted detector with t_{stop} iterations, for the IDFFT system using QPSK communicating over the dispersive PLC channels contaminated by both impulsive noise and background noise. The parameters associated with the IDFFT system are given by $M_{\mathrm{d}} = 214$, $m = 20$ and $N = M_{\mathrm{d}} + m = 234$. All other system parameters are summarised in Table 2.1.

In Fig. 2.13-2.15, we investigate the BER performance of our IDFFT system employs a CIS-assisted detector in conjunction with various thresholds, when communicating over the dispersive PLC channels contaminated by both impulsive noise and background noise. In these figures, the IDFFT system transmits $M_{\mathrm{d}} = 214$ symbols in each block of data. Moreover, the CIS-assisted detector associated with $t_{\mathrm{stop}} = 1, 2$ or 3, which is given in Algorithm 2, is employed for the IDFFT systems. In Fig. 2.13, the number of pilots is set to $m = 20$, giving a total of $(M - M_{\mathrm{d}} - m) = 22$ FD subcarriers that are disabled for data transmission either due to high-attenuation or owing to strong narrowband interference, or both. By contrast, in Fig. 2.14, we consider a more aggressive situation, when the number of pilots is set to $m = 40$, giving a total of $(M - M_{\mathrm{d}} - m) = 2$ FD subcarriers that are disabled for data transmission due to high-attenuation and/or strong narrowband interference. In these figures, the

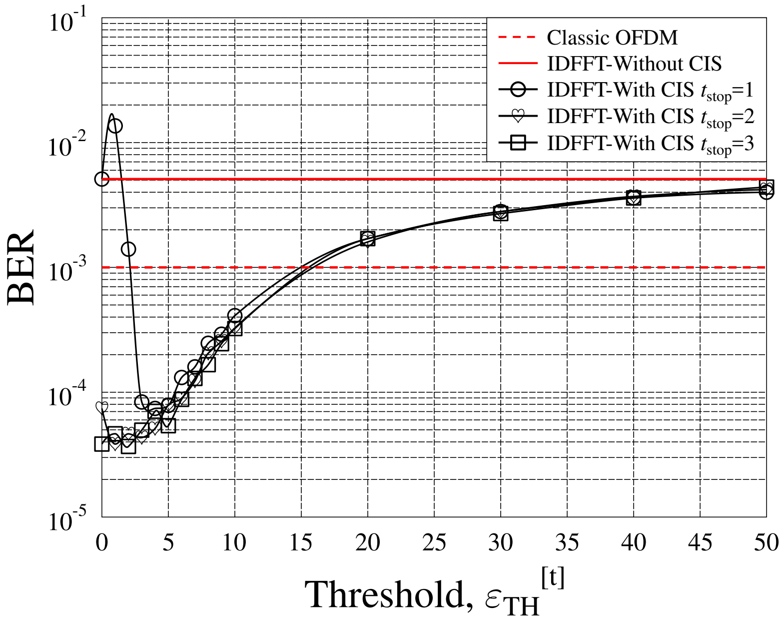

Figure 2.14: BER performance versus the threshold of our CIS-assisted detector with t_{stop} iterations, for the IDFFT system using QPSK communicating over the dispersive PLC channels contaminated by both impulsive noise and background noise. The parameters associated with the IDFFT system are given by $M_{\text{d}} = 214$, $m = 40$ and $N = M_{\text{d}} + m = 254$. All other system parameters are summarised in Table 2.1.

interleaver size is chosen to be $L_{\Pi_{\text{s}}} = 50 \times N$, where we have $N = (M_{\text{d}} + m) < M$. Based on the results of Fig. 2.13-2.15, we infer the following observations.

Firstly, we can observe from Fig. 2.13 and Fig. 2.14 that at each iteration step of our CIS-assisted detector, there exists an optimal threshold. Furthermore, the BER performance can be significant improved, when the optimal threshold is used by our CIS-assisted detector. By contrast, when the threshold is not carefully chosen, the BER performance may become severely degraded, as seen in Fig. 2.13 and Fig. 2.14. In particular, we observe from Fig. 2.13 and Fig. 2.14 that before the threshold increases to the optimal point, the BER performance of our CIS-assisted detector associated with a single iteration first degrades and then improves. This is because at the first iteration, some symbols having a high peak may be mis-treated as impairments, especially when the threshold is low; hence yielding a certain amount of information loss after the CIS estimation and the cancellation process. In this case, the corresponding BER performance is degraded. Thus, it is important for our CIS-assisted detector to use the optimal threshold, so that the best BER performance can be achieved. Secondly, as shown in Fig. 2.13 and Fig. 2.14, as the number of iterations increases, the improvement of the BER performance at the optimal point

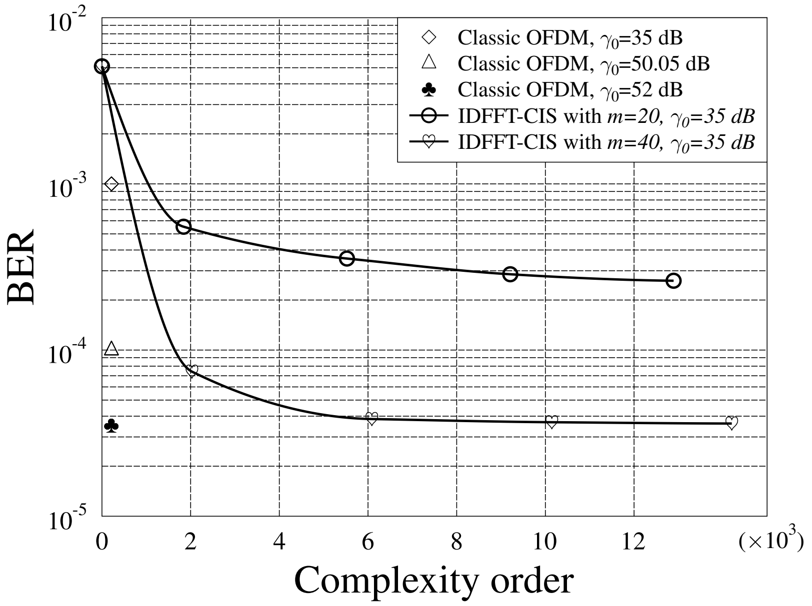

Figure 2.15: BER performance versus the complexity order of our CIS-assisted detector for the IDFFT system using QPSK communicating over the dispersive PLC channels contaminated by both impulsive noise and background noise. The parameters associated with the IDFFT system are given by $M_{\text{d}} = 214$, $m = 40$ and $N = M_{\text{d}} + m = 254$. All other system parameters are summarised in Table 2.1.

becomes limited. Furthermore, it can be shown that two iterations are sufficient for our CIS-assisted detector to attain a good BER performance. On the other hand, as shown in Fig. 2.15, the improvement of the BER performance of our CIS-assisted detector, which is achieved upon increasing the number of iterations, becomes less and less attractive in the light of its complexity. Therefore, in order to strike a trade-off between the performance gain attained and the complexity imposed, one or two iterations may be deemed appropriate for our CIS-assisted detector. Thirdly, observe from Fig. 2.13-2.14 that as the number of pilots increases, the BER performance is improved. Finally, as observed from Fig. 2.15, in comparison to the classic OFDM system, our proposed CIS-assisted IDFFT system is capable of providing a better BER performance, albeit at a higher computational cost.

2.7 Conclusions

In this chapter, CIS-assisted IDFFT aided systems have been proposed for broadband indoor PLCs, in order to mitigate the deleterious effects of the multipath fading and the asynchronous impulsive noise. In this section, we summarise the basic design guidelines of our CIS-assisted IDFFT aided system.

- The 2D interleaver of the proposed CIS-assisted IDFFT aided system has to be carefully designed in order to efficiently randomise the impulsive noise bursts at the cost of the lowest possible time delay.
- The design of pilot symbols also commands special attention in order to facilitate the accurate estimation and efficient mitigation of asynchronous impulsive noise, because both the specific position and the number of pilots critically affects the CS-based estimation performance. Hence, the proposed search algorithm is recommended for designing the positions of the pilots in an offline manner. The number of pilots has to be optimised for striking a flexible trade-off between the performance gain attained and the effective transmission rate reduction imposed by the pilot-overhead.
- Finally, based on the 2D interleaver and pilot design, the proposed CIS-assisted symbol detector is advocated, which has been shown to be capable of significantly improving the attainable system performance in comparison to the conventional OFDM system. Upon following these design guidelines, the computational complexity of the proposed CIS-assisted symbol detector remains low. The extra complexity is mainly contributed by the additional FFT and IFFT operations.

Chapter 3

Compressed Sensing Assisted Index Modulation

3.1 Introduction

Recently, a paradigm shift took place from the development of spectrally efficient communication techniques to the conception of both spectral- and energy-efficient communication techniques, as detailed in [115–120]. Indeed, as pointed out in [115], striking a compelling compromise between the SE (or the bandwidth efficiency) and EE (or the power efficiency) is essential for the design state-of-the-art networks. Hence, various joint SE and EE solutions have been proposed for the different protocol layers [118, 120]. Specifically, in the physical layer, more and more attention is paid to the SE and EE of communications systems, including both the digital signal processing and the analog front-end.

As the predominant transmission technique of broadband communications, at the time writing [91, 92], OFDM is mainly characterised by its high degree of flexibility and high spectral efficiency [5]. Generally, a frequency-selective fading channel can be converted into a number of parallel flat-fading subchannels with the aid of OFDM, thereby, considerably reducing the receiver's complexity as a benefit of using single-tap FD equalisation. Moreover, CP-based OFDM can be employed for avoiding inter-OFDM-symbol interference. Recently, OFDM has been combined with index modulation (OFDM-IM) [121–123]. In [121, 122], the Subcarrier Index Modulation (SIM) concept has been proposed based on a principle reminiscent of the implicit information conveyed by the activated antenna index in Spatial Modulation (SM) based Multiple-Input-Multiple-Output (MIMO) systems [116, 124–126]. Then, a generalised IM scheme has been proposed and analysed in [123]. The historical timeline

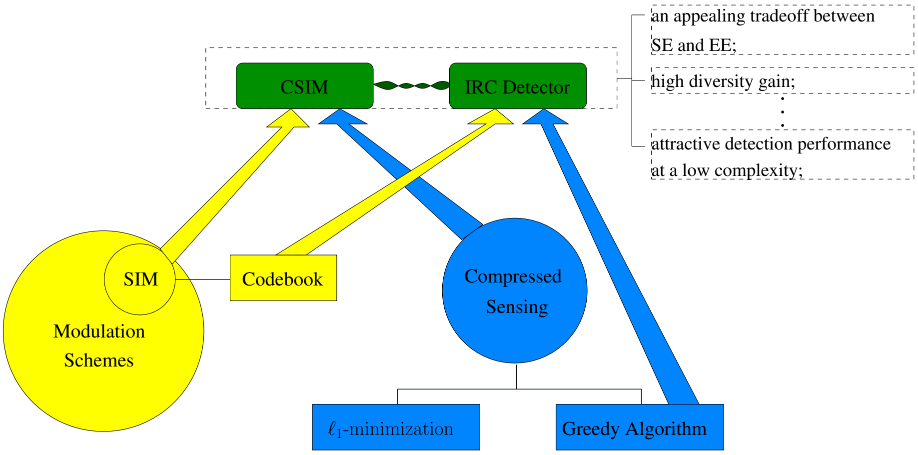

Figure 3.1: Illustration of the relationships between compressed sensing (CS), subcarrier index modulation (SIM), CS-assisted index modulation (CSIM) as well as our iterative residual check (IRC) detector.

of the SIM can be found in [127]. While, further details and a comprehensive overview of SIM is given in [128, 129].

The most appealing aspect of SIM is its flexibility in terms of striking a tradeoff between the SE and EE, as analyzed in [130, 131]. Hence, SIM has the potential of representing a win-win alternative in scenarios, such as Device-to-Device (D2D) communications, in-vechicle communications [132], sensor networks, etc. However, since it is an emerging technique, there are also some open issues. Apart from the above-mentioned SE and EE aspects of SIM, we will also consider the complexity issues and associated BER performance, which will also be addressed in this chapter. The complexity of SIM has to be separately considered at the transmitter and receiver side. In [133], a generalised look-up table has been proposed in order to improve the SE of SIM. However, in light of the limited SE improvement, the implementation complexity imposed may be deemed excessive. At the receiver side, since the information is conveyed in both the APM symbols and the SIM symbols, it is quite a challenge to design a detection scheme, which provides a good detection performance at a low complexity. In [123], the Joint Maximum-Likelihood (JML) detector has been conceived. As a further development, based on the fact that the FD symbols are either zero valued or non-zero valued, the authors of [123] have proposed a Log-Likelihood Ratio (LLR) based detector, which has been shown to have the same detection performance as the JML detector, but at a lower complexity cost. Later, the JML and the LLR detectors have been modified in [134]. On the other hand, as demonstrated in [123, 127], the BER performance of the OFDM-SIM system is better than that of the OFDM-QAM system, for a SE lower than 2 bits/s/Hz. In [135], a block interleaver has been employed to improve the BER performance of the SIM scheme. Later in [134], the Coordinate Interleaved Orthogonal Design (CIOD) of [136] has been employed in OFDM-SIM systems for improving the attainable transmitter diversity gain. However, the attainable multipath diversity gain has not been fully exploited by these schemes and no generalised analytical results are available for the achievable diversity order of the OFDM-SIM system. In order to gain insights into the concept of diversity, let us review some existed work as follows.

Generally, the potentially most powerful contributor to reliable communications for transmission over mutipath propagation channels is diversity, including modulation diversity, temporal diversity, frequency diversity and space diversity, as detailed in [137, 138]. During the last two decades, considerable research attention has been paid to the context of diversity, especially to MIMO scenarios, to name but a few [5, 124, 137, 139–142]. In this chapter, we limit ourselves to diversity techniques conceived for OFDM systems. We shall emphasise that both MIMO and OFDM signalling schemes share the same mathematical fundamentals in the context of diversity invoked for combating channel fading. Hence, the diversity schemes designed for OFDM signalling may also be applied to MIMO signalling. The early contribution in [138] has demonstrated that the BER performance of fading channels approaches that of the Gaussian channels, when the diversity order tends to infinity. On the other hand, it is widely exploited [143] that a high bandwidth efficiency can be achieved by signal constellations having lattice structure, such as the classic QAM scheme. Indeed, lattices from algebraic number fields serve as the theoretical foundations for the design of full-diversity codes. Accordingly, various constellation-rotation based modulation diversity approaches have been proposed, such as those given in [138, 139, 144, 145]. Specifically, the authors of [144] proposed a Linear Constellation Precoded OFDM (LCP-OFDM) system for maximising both the achievable diversity gain as well as the coding gain. However, the above-mentioned sophisticated approaches rely on the high-complexity ML detection of full diversity codes at the receiver side. Later in [101], Liu demonstrated that a beneficial multipath diversity gain can be attained by Single-Carrier Frequency-Division Multiple Access (SC-FDMA), when a FD equaliser is employed between a IFFT/FFT pair, (as seen in Fig. 2.2 of our design of the IDFFT system in Chapter 2). In [144], an optimal symbol interleaver was designed, which relies on FD subcarrier grouping, as a means of further increasing the coding gain of a precoded OFDM system. Later, the subcarrier grouping based symbol interleaving has been extensively investigated in [141, 146]. In particular, the authors of [141] demonstrated that in comparison to random permutation, about 1-3 dB performance gan can be achieved by the optimal design of the subcarrier grouping based symbol interleaver. For further details, we refer to [146, 147]. As a further advance in the field, Xia *et al* proposed cyclotomic lattices for modelling the full diversity codes in [140], yielding a generalised optimal design for the existing classic modulation constellations, such as QAM and Phase-Shift Keying (PSK). However, to the best of author's knowledge, this design philosophy has not been applied to the SIM scheme, which has been recently recognised as a beneficial modulation scheme [69].

On the other hand, CS, as an emerging theory, has attracted considerable research-attention. Initially, CS has been proposed for recovering vectors in high dimensions from vectors in low dimensions, as detailed in [54]. Then, it has been invoked for solving numerous problems in communications systems, such as channel estimation [63], narrowband interference mitigation [64], spectrum sensing [65], impulsive noise mitigation [68] and so on. In [69], we proposed a CS-assisted IM scheme for OFDM. The basic idea transpires from Fig. 3.1. Specifically, when an OFDM-SIM system is designed for the aforementioned EE communications scenarios, the number of activated subcarriers should be small. By taking advantage of this condition, each group of subcarriers can be potentially represented by a sparse vector. Hence, according to CS, it is also possible to detect (or recover) the corresponding sparse vector with the aid of algorithms such as the family of ℓ_1-minimisation algorithms [33, 34, 41] and greedy algorithms [42, 71, 72, 74, 75]. However, our scheme proposed in [69] has some limitations, since our full diversity design of CSIM relies on having an even number of activated subcarriers for the realisation of coordinate interleaving. Hence, the CSIM scheme of [69] may not be able to achieve the maximum attainable diversity gain, when the number of activated subcarriers is an odd value. Furthermore, although a generalised analysis of the attainable diversity gain was provided in [69], the corresponding coding gain was not quantified for practical scenarios.

To address the aforementioned issues, the new contributions of this chapter are summarised as follows.

- *A generalised system model is constructed, following by a unified system performance analysis. Specifically, without loss of generality, the bit-to-symbol mapping rule is modelled by a codebook specifically designed for the OFDM system. Furthermore, an in-depth analysis of the diversity gain, of the coding gain and of the achievable rate is provided as the design criteria for the optimal codebook.*
- *We propose a linear TPC assisted index modulation codebook, namely LPIM codebook for short, based on maximising the diversity gain and the coding gain as our design criteria. Specifically, we first model the IM symbols as lattice points from the ring of Gaussian integers. Then, based on algebraic number*

theory, an optimal linear TPC matrix is introduced for the IM scheme. As a further improvement, a symbol interleaver is conceived for improving the coding gain of our LPIM assisted OFDM (LPIM-OFDM) system. We provide both analytical and simulation results for characterising the overall performance of the LPIM-OFDM system. It is demonstrated that the proposed LPIM-OFDM system is capable of achieving the maximum attainable diversity gain as well as coding gain, hence yielding a significant BER performance improvement.

- *In order to further explore the promising potential of the IM scheme, we propose a generalised CSIM codebook, which is based on the philosophy of our CSIM scheme detailed in [69]. As shown in [69], the basic idea of our CSIM is that the conventional IM is implemented in a high-dimensional virtual digital-domain and then the high-dimensional IM symbols are compressed into the low-dimensional subcarriers of the FD with the aid of CS. Again, the design of our generalised CSIM codebook is based on the maximum diversity gain and maximum achievable rate criteria. As a further improvement, we propose a novel design method, which is based on the theoretical analysis of our LPIM codebook design, for the precoding matrix in our generalised CSIM scheme. We demonstrated that with the aid of the proposed design method, our generalised CSIM scheme becomes capable of achieving the maximum diversity gain, as well as providing a performance guarantee for symbol detection. Our simulation results show that an attractive tradeoff between the SE and the EE can be struck by the generalised CSIM assisted OFDM (CSIM-OFDM) system. Moreover, the proposed system is shown to be capable of attaining a high achievable rate at a low complexity cost.*
- *For the sake of performance comparison, we first invoke the ML detection for both the LPIM scheme and the CSIM scheme. Since the complexity of the ML detector may be deemed excessive in practice, we propose a low-complexity detector, namely the GIRCD, for our systems. The proposed GIRCD is an improved version of the Iterative Residual Check Detector (IRCD) proposed in [69]. Similar to our IRCD, the proposed GIRCD philosophy is based on the greedy algorithms of [42, 71, 72, 74, 75], which update their estimates one step at a time by making locally optimal choices at each step. In particular, the estimation of the indices of nonzero elements in an IM symbol vector is based on a reliability estimation process, which further develops the idea given in [148]. We demonstrate that an attractive detection performance can be attained by the GIRCD using as few as one or two iterations, yielding a low complexity.*

The rest of the chapter is organised as follows. In Section 3.2, our system model is

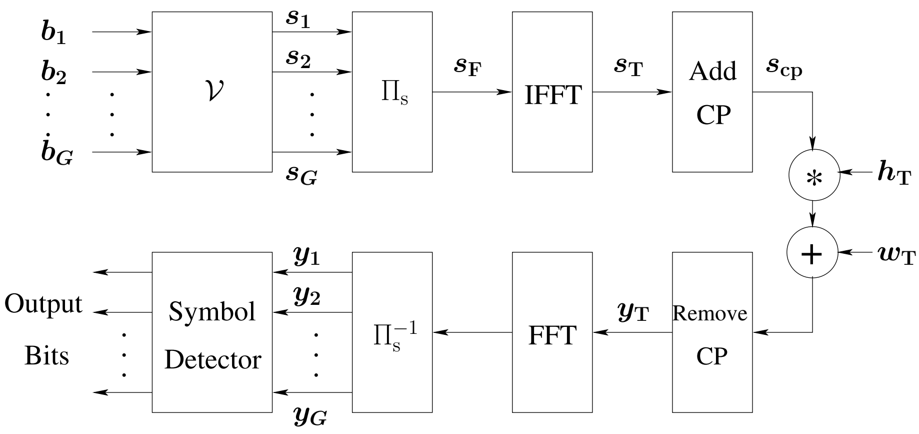

Figure 3.2: Illustration of the OFDM system employing a codebook $\mathcal{V}$ and an interleaver $\Pi_{\rm s}$.

described. Then, the system performance analysis and codebook design criteria are detailed in Section 3.3. In Section 3.4, we propose our LPIM codebook design. The conceptual framework of our CSIM scheme is detailed in Section 3.5. In Section 3.6, the generalised iterative residual check detector is proposed. Our simulation results are discussed in Section 3.7. Finally, we offer our conclusions in Section 3.8.

3.2 System Model

3.2.1 Description of Transmitter

We assume a multicarrier system employing M subcarriers. The M subcarriers are divided into G groups, each of which contains $m = M/G$ subcarriers. As seen in Fig. 3.2, the information bits in $\boldsymbol{b} \in \mathbb{B}^{LG}$ are first split into G groups denoted as $\boldsymbol{b} = [\boldsymbol{b}_1, \ldots, \boldsymbol{b}_G]$, where we have $\boldsymbol{b}_g \in \mathbb{B}^L$ for $g = 1, \ldots, G$. Then, during the transmission of the gth group, the bits in $\boldsymbol{b}_g$ are mapped into the gth group of symbols denoted as $\boldsymbol{s}_g$ according to a specifically designed codebook of

$$\mathcal{V} \triangleq \left\{\boldsymbol{v}_1, \ldots, \boldsymbol{v}_{2^L} : \boldsymbol{v}_i \in \mathbb{C}^m, i = 1, \ldots, 2^L\right\}, \tag{3.1}$$

which will be detailed in Section 3.4 and Section 3.5. In particular, we assume that $\mathbb{E}[\|\boldsymbol{s}_g\|_2^2] = k \leq m, \forall g$. Next, all the G groups of symbols are fed into an interleaver $\Pi_{\rm s}$ shown in Fig. 3.2, yielding the FD symbols expressed as $\boldsymbol{s}_{\rm F} = [s_{\rm F}(0), s_{\rm F}(1), \ldots, s_{\rm F}(M-1)]^T$. The design and discussions of the interleaver $\Pi_{\rm s}$ will be given in Section 3.4.3. For the sake of demonstration, let $\boldsymbol{\Upsilon}_{\Pi_g}$ represent the $(M \times m)$-element mapping matrix based on $\Pi_{\rm s}$ for the gth group. Furthermore, we can show that $\boldsymbol{\Upsilon}_{\Pi_g}^T \boldsymbol{\Upsilon}_{\Pi_g} = \boldsymbol{I}_m$ and $\boldsymbol{\Upsilon}_{\Pi_g}^T \boldsymbol{\Upsilon}_{\Pi_{g'}} = \boldsymbol{0}$ for $g' \neq g$, which can be used for characterising the de-interleaving process, as it will be used in Section 3.2.2. Hence, the FD symbols can be expressed as

$$\boldsymbol{s}_{\mathrm{F}}=\sum_{g=1}^{G}\boldsymbol{\Upsilon}_{\Pi_g}\boldsymbol{s}_g, \tag{3.2}$$

which are input to the M-point IFFT, yielding the TD symbols $\boldsymbol{s}_{\mathrm{T}}=\boldsymbol{\mathcal{F}}_M^H\boldsymbol{s}_{\mathrm{F}}$, as seen in Fig. 3.2. Finally, after adding a CP of length L_{cp}, the transmitted baseband symbols can be expressed as $\boldsymbol{s}_{\mathrm{cp}}=\boldsymbol{\Upsilon}_{\mathrm{CP}}^T\boldsymbol{s}_{\mathrm{T}}$, where $\boldsymbol{\Upsilon}_{\mathrm{CP}}=[\boldsymbol{\Upsilon}_{\mathrm{cp}},\boldsymbol{I}_M]$ and $\boldsymbol{\Upsilon}_{\mathrm{cp}}$ is a $(M\times L_{\mathrm{cp}})$-element mapping matrix obtained from the last L_{cp} columns of an identity matrix $\boldsymbol{I}_M$.

3.2.2 Received Signals

We assume an L_{h}-tap frequency-selective Rayleigh fading channel, which has a CIR of $\boldsymbol{h}_{\mathrm{T}}=[h_{\mathrm{T}}(0),h_{\mathrm{T}}(1),\ldots,h_{\mathrm{T}}(L_{\mathrm{h}}-1)]^T$, where each element in $\boldsymbol{h}_{\mathrm{T}}$ is assumed to be an i.i.d. random variable that obeys $\mathcal{CN}(0,1/L_{\mathrm{h}})$. Furthermore, we assume that $L_{\mathrm{cp}}\geq L_{\mathrm{h}}$ and that perfect synchronisation is achieved at the receiver. Meanwhile, the bandwidth of each subchannel is assumed to be much lower than the channel's coherence bandwidth. Then, as shown in Fig. 3.2, after removing the CP, the received baseband equivalent observations $\boldsymbol{y}_{\mathrm{T}}=[y_{\mathrm{T}}(0),y_{\mathrm{T}}(1),\ldots,y_{\mathrm{T}}(M-1)]^T$ can be formulated as

$$\boldsymbol{y}_{\mathrm{T}}=\boldsymbol{H}_{\mathrm{cir}}\boldsymbol{s}_{\mathrm{T}}+\boldsymbol{n}_{\mathrm{T}}, \tag{3.3}$$

where $\boldsymbol{H}_{\mathrm{cir}}$ is an $(M\times M)$-element circulant matrix, which can be diagonalised by the DFT operations, giving $\boldsymbol{H}_{\mathrm{cir}}=\boldsymbol{\mathcal{F}}_M^H\boldsymbol{H}\boldsymbol{\mathcal{F}}_M$, where $\boldsymbol{H}=\mathrm{diag}\{\sqrt{M}\boldsymbol{\mathcal{F}}_M\boldsymbol{\Upsilon}_{\mathrm{h}}\boldsymbol{h}_{\mathrm{T}}\}$ with $\boldsymbol{\Upsilon}_{\mathrm{h}}$ being a $(M\times L_{\mathrm{h}})$-element mapping matrix formed by the first L_{h} columns of an identity matrix $\boldsymbol{I}_M$. In (3.3), $\boldsymbol{n}_{\mathrm{T}}$ is the complex Additive White Gaussian Noise (AWGN) with a mean of zero and a variance of $N_0\boldsymbol{I}_M$. As shown in Fig. 3.2, after the FFT operation and de-interleaving, the gth group of received FD symbols can be expressed as

$$\begin{aligned}
\boldsymbol{y}_g=&\boldsymbol{\Upsilon}_{\Pi_g}^T\left(\boldsymbol{\mathcal{F}}_M\boldsymbol{y}_{\mathrm{T}}\right)\\
=&\boldsymbol{\Upsilon}_{\Pi_g}^T\left(\boldsymbol{H}\boldsymbol{s}_{\mathrm{F}}+\boldsymbol{\mathcal{F}}_M\boldsymbol{n}_{\mathrm{T}}\right)\\
=&\boldsymbol{\Upsilon}_{\Pi_g}^T\boldsymbol{H}\sum_{g=1}^{G}\boldsymbol{\Upsilon}_{\Pi_g}\boldsymbol{s}_g+\boldsymbol{\Upsilon}_{\Pi_g}^T\left(\boldsymbol{\mathcal{F}}_M\boldsymbol{n}_{\mathrm{T}}\right) && \text{(3.4a)}\\
=&\boldsymbol{\Upsilon}_{\Pi_g}^T\boldsymbol{H}\boldsymbol{\Upsilon}_{\Pi_g}\boldsymbol{s}_g+\bar{\boldsymbol{n}}_g && \text{(3.4b)}\\
=&\bar{\boldsymbol{H}}_g\boldsymbol{s}_g+\bar{\boldsymbol{n}}_g, && \text{(3.4c)}
\end{aligned}$$

where by definition $\bar{\boldsymbol{n}}_g=\boldsymbol{\Upsilon}_{\Pi_g}^T\left(\boldsymbol{\mathcal{F}}_M\boldsymbol{n}_{\mathrm{T}}\right)$ contains the gth group of de-interleaved FD noise samples. Note that, since $\boldsymbol{H}$ is a diagonal matrix, we can readily show that

$\boldsymbol{\Upsilon}_{\Pi_g}^T \boldsymbol{H} \boldsymbol{\Upsilon}_{\Pi_{g'}} = \mathbf{0}$ for $g \neq g'$, which is applied in (3.4a) to obtain (3.4b). In (3.4c), the diagonal matrix $\bar{\boldsymbol{H}}_g$ can be explicitly expressed as

$$\begin{aligned}
\bar{\boldsymbol{H}}_g =& \boldsymbol{\Upsilon}_{\Pi_g}^T \boldsymbol{H} \boldsymbol{\Upsilon}_{\Pi_g} \\
=& \boldsymbol{\Upsilon}_{\Pi_g}^T \mathrm{diag}\left\{\sqrt{M} \boldsymbol{\mathcal{F}}_M \boldsymbol{\Upsilon}_{\mathrm{h}} \boldsymbol{h}_{\mathrm{T}}\right\} \boldsymbol{\Upsilon}_{\Pi_g} \\
=& \mathrm{diag}\left\{\sqrt{M} \boldsymbol{\Upsilon}_{\Pi_g}^T \boldsymbol{\mathcal{F}}_M \boldsymbol{\Upsilon}_{\mathrm{h}} \boldsymbol{h}_{\mathrm{T}}\right\} \\
=& \mathrm{diag}\left\{\boldsymbol{F}_{\mathrm{h},\Pi_g} \boldsymbol{h}_{\mathrm{T}}\right\} = \mathrm{diag}\{\bar{h}_g(0), \ldots, \bar{h}_g(m-1)\},
\end{aligned} \tag{3.5}$$

where by definition $\boldsymbol{F}_{\mathrm{h},\Pi_g} = \sqrt{M} \boldsymbol{\Upsilon}_{\Pi_g}^T \boldsymbol{\mathcal{F}}_M \boldsymbol{\Upsilon}_{\mathrm{h}} \in \mathbb{C}^{m \times L_{\mathrm{h}}}$. It can be shown that $\bar{h}_g(i) \sim \mathcal{CN}(0,1)$ and $\bar{n}_g(i) \sim \mathcal{CN}(0, N_0)$, $\forall g, i$. Hence, the average SNR per symbol is given by

$$\gamma_s \triangleq \frac{\mathbb{E}[\|\boldsymbol{s}_g\|_2^2]}{\mathbb{E}[\|\bar{\boldsymbol{n}}_g\|_2^2]} = \frac{k}{m N_0}. \tag{3.6}$$

Moreover, we can observe from (3.4c) that $\boldsymbol{y}_g$ has the complex Gaussian distribution with the conditioned PDF of

$$p\left(\boldsymbol{y}_g | \boldsymbol{s}_g\right) = \frac{1}{(\pi N_0)^m} \exp\left\{-\frac{\|\boldsymbol{y}_g - \bar{\boldsymbol{H}}_g \boldsymbol{s}_g\|_2^2}{N_0}\right\}. \tag{3.7}$$

3.3 System Performance Analysis and Codebook Design Criteria

In this section, we analyse the system performance and discuss the design criteria of the codebook $\mathcal{V}$. We commence by describing the ML detection, which is the detection scheme used throughout this section for the sake of performance evaluation. Then, the SE and EE of the system are derived. Next, the analytical results of the diversity and coding gain are detailed. Finally, we discuss the design criteria of the codebook $\mathcal{V}$.

3.3.1 Maximum Likelihood Detection

Typically, the optimum symbol detector for our system shown in Section 3.2 invokes the Maximum *A Posterior* (MAP) principle by solving the optimisation problem of

$$\boldsymbol{s}_g^{\mathrm{MAP}} = \arg \max_{\boldsymbol{v}_i \in \mathcal{V}} \left\{p\left(\boldsymbol{v}_i | \boldsymbol{y}_g\right)\right\}, \tag{3.8}$$

where $p\left(\boldsymbol{v}_i | \boldsymbol{y}_g\right)$ is the *a posteriori* probability of $\boldsymbol{v}_i$ given the receiver's output of $\boldsymbol{y}_g$. Let us assume that the candidates in $\mathcal{V}$ are equiprobable and independent. Then, the MAP detector of (3.8) becomes the ML detector, which can be described with the aid of (3.7) as

$$\boldsymbol{s}_g^{\mathrm{ML}} = \arg\min_{\boldsymbol{v}_i \in \mathcal{V}} \left\{ \left\| \boldsymbol{y}_g - \bar{\boldsymbol{H}}_g \boldsymbol{v}_i \right\|_2^2 \right\}. \tag{3.9}$$

In the following analysis, we assume that the ML detection is performed with perfect Channel State Information at the Receiver side (CSIR).

3.3.2 Spectral Efficiency and Energy Efficiency

Let us assume that the uncoded system is operated within a frequency band of f_{B} Hertz. The total power consumed by transmitting the data at a reliable information rate of $\mathcal{R}_{\mathrm{r}}$ in bit-per-second within a symbol duration of T_{s} is denoted as P_{T} Watts. We consider the specific case when the total power consumed is equal to the total power of the transmitted signal, i.e. we have $P_{\mathrm{T}} = P_{\mathrm{Tx}}$. Then, the SE of $\eta_{\mathrm{SE}} = \mathcal{R}_{\mathrm{r}}/f_{\mathrm{B}}$ can be measured in bit-per-second-per-Hertz. Since each group is independent, the SE of the system shown in Section 3.2 can be expressed in terms of the channel SNR as [149]

$$\begin{aligned} f_{\mathrm{SE}}(\gamma_s) =& \frac{\mathcal{R}_{\mathrm{r}}}{f_{\mathrm{B}}} \\ =& \frac{\sum_{g=1}^{G} I(\boldsymbol{s}_g; \boldsymbol{y}_g)}{T_s f_{\mathrm{B}}} = \frac{\sum_{g=1}^{G} I(\boldsymbol{s}_g; \boldsymbol{y}_g)}{M}, \end{aligned} \tag{3.10}$$

where $I(\boldsymbol{s}_g; \boldsymbol{y}_g)$ denotes the mutual information [150] of the transmission of the gth group. Here, the rate reduction caused by the CP is ignored. Then, based on the results derived in Appendix A, we have

$$\begin{aligned} f_{\mathrm{SE}}(\gamma_s) =& \frac{1}{M} \sum_{g=1}^{G} \left\{ \mathbb{E}_{\bar{\boldsymbol{H}}_g, \bar{\boldsymbol{n}}_g} [-\log_2 \epsilon(\bar{\boldsymbol{n}}_g, \bar{\boldsymbol{H}}_g, \gamma_s)] - m \log_2 \left(\frac{\pi e k}{m \gamma_s} \right) \right\} \\ =& \frac{G}{M} \left\{ \mathbb{E}_{\bar{\boldsymbol{H}}_g, \bar{\boldsymbol{n}}_g} [-\log_2 \epsilon(\bar{\boldsymbol{n}}_g, \bar{\boldsymbol{H}}_g, \gamma_s)] - m \log_2 \left(\frac{\pi e k}{m \gamma_s} \right) \right\} \\ =& \frac{1}{m} \mathbb{E}_{\bar{\boldsymbol{H}}_g, \bar{\boldsymbol{n}}_g} [-\log_2 \epsilon(\bar{\boldsymbol{n}}_g, \bar{\boldsymbol{H}}_g, \gamma_s)] - \log_2 \left(\frac{\pi e k}{m \gamma_s} \right), \end{aligned} \tag{3.11}$$

where $\epsilon(\bar{\boldsymbol{n}}_g, \bar{\boldsymbol{H}}_g, \gamma_s)$ is the *implementation function*, as defined in (A.7). It should be noted that it is hard to further simplify (3.11) to obtain a closed-form expression. Nevertheless, according to (A.7), the first term of (3.11) can be evaluated by Monte Carlo simulations, while the second term of (3.11) is constant for given parameters. Therefore, the SE of (3.11) can be obtained accordingly, as it will be shown in Section 3.7. Furthermore, we can readily show with the aid of (A.10) that the rate achieved by the codebook $\mathcal{V}$ is given by

$$\begin{aligned} R_{\max,\mathcal{V}} &\triangleq \lim_{\gamma_s \to \infty} f_{\mathrm{SE}}(\gamma_s) \\ &= \lim_{\gamma_s \to \infty} \sum_{g=1}^{G} \frac{I(\boldsymbol{s}_g; \boldsymbol{y}_g)}{M} \\ &= \frac{L}{m} \quad \text{in bits/s/Hz}, \end{aligned} \tag{3.12}$$

where $R_{\max,\mathcal{V}}$ is practically attainable, when the average SNR per symbol γ_s is sufficiently high.

On the other hand, the EE can be defined in terms of the unit of Joule-per-bit per noise level [149], or bit-per-Joule [117, 151], or bit-per-Joule per noise level [115]. In this chapter, only the signal's transmission power is considered, hence the EE definition of [115] is adopted. In this case, given the SE value of $f_{\mathrm{SE}}(\gamma_s) = \eta_{\mathrm{SE}}$, the corresponding EE can be expressed as [115]

$$\begin{aligned} \eta_{\mathrm{EE}} &= \frac{\eta_{\mathrm{SE}}}{P_{\mathrm{T}}/N_0} = \frac{\eta_{\mathrm{SE}}}{P_{\mathrm{Tx}}/N_0} \\ &= \frac{\eta_{\mathrm{SE}}}{\gamma_s} = \frac{\eta_{\mathrm{SE}}}{f_{\mathrm{SE}}^{-1}(\eta_{\mathrm{SE}})}, \end{aligned} \tag{3.13}$$

where the last equality is arrived at by expressing γ_s as an inverse function of the SE η_{SE}, which gives the SNR per symbol required for achieving the SE of η_{SE}. Again, since it is an open challenge to derive a closed-form expression for the EE shown in (3.13), the tradeoff between the SE and EE of our proposed system is studied by Monte Carlo simulations, as it will be shown in Section 3.7.

Furthermore, let us define the received SNR per bit (or SNR per reliable bit) as $\gamma_b^{\mathrm{Rx}} \triangleq E_b^{\mathrm{Rx}}/N_0$, where $E_b^{\mathrm{Rx}} = P_{\mathrm{Tx}}/\eta_{\mathrm{SE}}$ is the received energy per bit in Joule-per-bit. Hence, we can explicitly show that γ_b^{Rx} can be formulated in terms of the EE defined in (3.13) as

$$\begin{aligned} \gamma_b^{\mathrm{Rx}} = \frac{\gamma_s}{\eta_{\mathrm{SE}}} &= \frac{f_{\mathrm{SE}}^{-1}(\eta_{\mathrm{SE}})}{\eta_{\mathrm{SE}}} \\ &= \frac{1}{\eta_{\mathrm{EE}}}, \end{aligned} \tag{3.14}$$

which can be used for quantifying the minimum received signal energy per information bit required for reliable communication, as it will be studied by simulation results shown in Section 3.7.

3.3.3 Diversity and Coding Gains

Let us first define the pairwise error event as $\{\boldsymbol{s}_g^{\mathrm{c}} \to \boldsymbol{s}_g^{\mathrm{e}}\}$, where $\boldsymbol{s}_g^{\mathrm{c}} = \boldsymbol{v}_i$ is the transmitted symbol vector, while $\boldsymbol{s}_g^{\mathrm{e}} = \boldsymbol{v}_j$ denotes the corresponding incorrect detection results of the ML detection shown in (3.9), i.e. we have $\boldsymbol{v}_i \neq \boldsymbol{v}_j$ for $\boldsymbol{v}_i, \boldsymbol{v}_j \in \mathcal{V}$. Then, similar to [142], the conditional Pairwise Error Probability (PEP) can be expressed as

$$\begin{aligned} P\left(\boldsymbol{s}_g^{\mathrm{c}} \rightarrow \boldsymbol{s}_g^{\mathrm{e}} | \bar{\boldsymbol{H}}_g\right) =& Q\left(\sqrt{\frac{m\gamma_s \left\|\bar{\boldsymbol{H}}_g\left(\boldsymbol{s}_g^{\mathrm{c}} - \boldsymbol{s}_g^{\mathrm{e}}\right)\right\|^2}{2k}}\right) \\ =& \frac{1}{\pi}\int_0^{\frac{\pi}{2}} \exp\left(-\frac{m\gamma_s d^2\left(\boldsymbol{z}_g^{\mathrm{c}}, \boldsymbol{z}_g^{\mathrm{e}}\right)}{4k\sin^2\theta}\right) \mathrm{d}\theta, \end{aligned} \tag{3.15}$$

where $d^2\left(\boldsymbol{z}_g^{\mathrm{c}}, \boldsymbol{z}_g^{\mathrm{e}}\right) = \left\|\boldsymbol{z}_g^{\mathrm{c}} - \boldsymbol{z}_g^{\mathrm{e}}\right\|^2$ denotes the squared Euclidean distance between $\boldsymbol{z}_g^{\mathrm{c}} = \bar{\boldsymbol{H}}_g \boldsymbol{s}_g^{\mathrm{c}}$ and $\boldsymbol{z}_g^{\mathrm{e}} = \bar{\boldsymbol{H}}_g \boldsymbol{s}_g^{\mathrm{e}}$. With the aid of (3.5), we have

$$\begin{aligned} d^2\left(\boldsymbol{z}_g^{\mathrm{c}}, \boldsymbol{z}_g^{\mathrm{e}}\right) &= \left\|\bar{\boldsymbol{H}}_g\left(\boldsymbol{s}_g^{\mathrm{c}} - \boldsymbol{s}_g^{\mathrm{e}}\right)\right\|^2 \\ &= \left\|\mathrm{diag}\{\boldsymbol{F}_{\mathrm{h},\Pi_g}\boldsymbol{h}_{\mathrm{T}}\}\left(\boldsymbol{v}_i - \boldsymbol{v}_j\right)\right\|^2 \\ &= \left\|\mathrm{diag}\{\boldsymbol{F}_{\mathrm{h},\Pi_g}\boldsymbol{h}_{\mathrm{T}}\}\boldsymbol{e}\right\|^2 \\ &= \left\|\boldsymbol{E}\boldsymbol{F}_{\mathrm{h},\Pi_g}\boldsymbol{h}_{\mathrm{T}}\right\|^2 \\ &= \boldsymbol{h}_{\mathrm{T}}^H \boldsymbol{D}_g \boldsymbol{h}_{\mathrm{T}}, \end{aligned} \tag{3.16}$$

where we have $\boldsymbol{E} = \mathrm{diag}\{\boldsymbol{e}\} \in \mathbb{C}^{m\times m}$ with $\boldsymbol{e} \in \mathcal{E}$ defined in (A.5) and $\boldsymbol{D}_g = \boldsymbol{F}_{\mathrm{h},\Pi_g}^H \boldsymbol{E}^H \boldsymbol{E} \boldsymbol{F}_{\mathrm{h},\Pi_g} \in \mathbb{C}^{L_{\mathrm{h}}\times L_{\mathrm{h}}}$. Furthermore, let the nonzero eigenvalues of $\boldsymbol{D}_g$ be denoted as λ_i for $i = 1, \ldots, V_{\mathrm{D}}$, where

$$\begin{aligned} V_{\mathrm{D}} =& \mathrm{rank}\left(\boldsymbol{D}_g\right) = \mathrm{rank}(\boldsymbol{F}_{\mathrm{h},\Pi_g}^H \boldsymbol{E}^H \boldsymbol{E} \boldsymbol{F}_{\mathrm{h},\Pi_g}) \\ =& \min\left\{\mathrm{rank}\left(\boldsymbol{E}\right), \mathrm{rank}\left(\boldsymbol{F}_{\mathrm{h},\Pi_g}\right)\right\}. \end{aligned} \tag{3.17}$$

We can readily show that we have $\mathrm{rank}(\boldsymbol{E}) = \|\boldsymbol{e}\|_0 \leq m$ and $\mathrm{rank}(\boldsymbol{F}_{\mathrm{h},\Pi_g}) = \min\{m, L_{\mathrm{h}}\}$, which gives

$$V_{\mathrm{D}} = \min_{\forall \boldsymbol{e}\in\mathcal{E}}\{\|\boldsymbol{e}\|_0, L_{\mathrm{h}}\}. \tag{3.18}$$

Since $\boldsymbol{h}_{\mathrm{T}}$ is assumed to be an i.i.d. Gaussian distributed vector, after integrating the conditional PEP of (3.15) with respect to the distribution of the squared Euclidean distance of $d^2\left(\boldsymbol{z}_g^{\mathrm{c}}, \boldsymbol{z}_g^{\mathrm{e}}\right)$ by following the approach shown in [92], the average PEP can be expressed as

$$P\left(\boldsymbol{s}_g^{\mathrm{c}} \rightarrow \boldsymbol{s}_g^{\mathrm{e}}\right) = \frac{1}{\pi}\int_0^{\frac{\pi}{2}} \prod_{i=1}^{V_{\mathrm{D}}} \left(1 + \frac{\lambda_i m\gamma_s}{4k\sin^2\theta}\right)^{-1} \mathrm{d}\theta. \tag{3.19}$$

Furthermore, for sufficiently high SNRs, (3.19) is upper bounded by [137, 144]

$$P\left(\boldsymbol{s}_g^{\mathrm{c}} \rightarrow \boldsymbol{s}_g^{\mathrm{e}}\right) \leq \left(V_{\mathrm{C}}\frac{m\gamma_s}{4k}\right)^{-V_{\mathrm{D}}}, \tag{3.20}$$

where V_{D} gives the diversity order of the ML detection, while

$$V_{\mathrm{C}} = \min_{\forall \Pi_{\mathrm{s}}, \boldsymbol{e} \in \mathcal{E}} \left(\prod_{i=1}^{V_{\mathrm{D}}} \lambda_i \right)^{1/V_{\mathrm{D}}} \tag{3.21}$$

is the coding gain of the transmission scheme. We can see from (3.20) that the diversity order V_{D} determines how rapidly the average PEP decreases with the increase of the SNR, while the coding gain V_{C} determines the SNR-shift of this PEP curve relative to a benchmark error rate curve of $(\gamma_s/4)^{-V_{\mathrm{D}}}$. Typically, it is desirable to design such a codebook $\mathcal{V}$ that the maximum diversity order can be achieved in order to combat multipath induced fading. When the maximum diversity order is achieved, the coding gain is expected to be maximised for further improving the system performance.

3.3.4 Design Criteria of Codebook $\mathcal{V}$

Based on the above analysis, let us now discuss the design criteria invoked for the codebook $\mathcal{V}$. Specifically, three aspects are considered, which are described as follows.

Diversity Gain Criterion

Firstly, it can be readily inferred from (3.18) that the design of $\mathcal{V}$ with the goal of achieving the maximum diversity gain is equivalent to solving the optimisation problem of

$$\begin{aligned} \mathcal{V}^{\mathrm{C1}} =& \arg \max_{\mathcal{V}} V_{\mathrm{D}} \\ =& \arg \max_{\mathcal{V}} \left\{ \min_{\forall \boldsymbol{e} \in \mathcal{E}} \{ \|\boldsymbol{e}\|_0, L_{\mathrm{h}} \} \right\} \end{aligned} \tag{3.22}$$

for $\|\boldsymbol{e}\|_0 \leq m$. Clearly, the solution of (3.22) is dependent on the minimum number of non-zero elements of the m-dimensional error vector $\boldsymbol{e} \in \mathcal{E}$, as discussed below.

The first case is when the number of channel taps L_{h} is fixed and known to the transmitter. In this case, the codebook $\mathcal{V}$ can be designed so that the condition of $m \geq \min_{\boldsymbol{e} \in \mathcal{E}} \|\boldsymbol{e}\|_0 \geq L_{\mathrm{h}}$ is satisfied, yielding the so-called maximum multipath diversity gain of L_{h}. Specifically, in slow fading scenarios, typically the maximum multipath diversity criterion is employed, since the transmitter is capable of acquiring *a priori* information about the CIR and hence L_{h}. However, when the CIR changes rapidly over time, the transmitter becomes unable to collect reliable information concerning L_{h}. In this case, the following design criterion may be preferred.

The second scenario is that the codebook $\mathcal{V}$ is designed so that only the equality of $\min\limits_{\boldsymbol{e}\in\mathcal{E}} \|\boldsymbol{e}\|_0 = m$ is met. It should be noted that since $\|\boldsymbol{e}\|_0 \leq m$, this design criterion is equivalent to that of $\|\boldsymbol{e}\|_0 = m$ for any $\boldsymbol{e} \in \mathcal{E}$. Clearly, the ideal case is when the maximum multipath diversity gain is attained, i.e. we have $\|\boldsymbol{e}\|_0 = m = L_{\mathrm{h}}$, $\forall \boldsymbol{e} \in \mathcal{E}$, since in this case a beneficial tradeoff between the computational complexity and the performance gain can be struck. However, when the number of channel taps L_{h} is unknown, the dimension m has to be sufficiently high in order to obtain as high a diversity gain as possible. The corresponding drawback is the resultant high complexity.

Coding Gain Criterion

Specifically, for the optimal codebook $\mathcal{V}^{\mathrm{C1}}$ of (3.22) associated with a maximum diversity order of $V_{\mathrm{D,max}}$, the $(L_{\mathrm{h}} \times L_{\mathrm{h}})$-element matrix $\boldsymbol{D}_g$ defined in (3.16) becomes of full rank. In this case, the product of the nonzero eigenvalues of $\boldsymbol{D}_g$ becomes equal to its determinant denoted as $\det(\boldsymbol{D}_g)$. Moreover, since the interleaver Π_{s} and the codebook $\mathcal{V}^{\mathrm{C1}}$ are independent, we can formulate the corresponding coding gain based on (3.21) as

$$\begin{aligned} V_{\mathrm{C}}^{\mathrm{C1}} =& \min_{\forall \boldsymbol{e}\in\mathcal{E}} \left[\det(\boldsymbol{D}_g)\right]^{\frac{1}{V_{\mathrm{D,max}}}} \\ =& \min_{\forall \boldsymbol{e}\in\mathcal{E}} \left[\det(\boldsymbol{F}_{\mathrm{h},\Pi_g}^H \boldsymbol{E}^H \boldsymbol{E} \boldsymbol{F}_{\mathrm{h},\Pi_g})\right]^{\frac{1}{V_{\mathrm{D,max}}}} \\ =& \min_{\forall g} \left[\det(\boldsymbol{F}_{\mathrm{h},\Pi_g}^H \boldsymbol{F}_{\mathrm{h},\Pi_g})\right]^{\frac{1}{V_{\mathrm{D,max}}}} \min_{\forall \boldsymbol{e}\in\mathcal{E}} \left[\det(\boldsymbol{E}^H \boldsymbol{E})\right]^{\frac{1}{V_{\mathrm{D,max}}}} \\ =& (\delta_{\Pi}^{\mathrm{C1}} \delta_{\mathcal{E}}^{\mathrm{C1}})^{\frac{1}{V_{\mathrm{D,max}}}}, \end{aligned} \tag{3.23}$$

where by definition, we have

$$\delta_{\Pi}^{\mathrm{C1}} \triangleq \min_{\forall g} \det(\boldsymbol{F}_{\mathrm{h},\Pi_g}^H \boldsymbol{F}_{\mathrm{h},\Pi_g}) \tag{3.24}$$

and

$$\delta_{\mathcal{E}}^{\mathrm{C1}} \triangleq \min_{\forall \boldsymbol{e}\in\mathcal{E}} \det(\boldsymbol{E}^H \boldsymbol{E}). \tag{3.25}$$

Specifically, for the codebook $\mathcal{V}^{\mathrm{C1}}$, the matrix $\boldsymbol{E} = \mathrm{diag}(\boldsymbol{e}) \in \mathbb{C}^{m\times m}$ defined in (3.16) is a full-rank diagonal matrix. In this case, we can rewrite (3.25) as

$$\begin{aligned} \delta_{\mathcal{E}}^{\mathrm{C1}} \triangleq& \min_{\forall \boldsymbol{e}\in\mathcal{E}} \det(\boldsymbol{E}^H \boldsymbol{E}) \\ =& \min_{\forall \boldsymbol{e}\in\mathcal{E}} \prod_{i=1}^{m} |e(i)|^2, \end{aligned} \tag{3.26}$$

which is known as the squared Minimum Product Distance (MPD). Then, it can be readily inferred from (3.23) that maximising the coding gain is equivalent to solving the joint optimisation problems of

$$\begin{aligned}\left\{\Pi_{\mathrm{s}}^{\mathrm{opt}}, \mathcal{V}^{\mathrm{C2}}\right\} =& \arg\max_{\Pi_{\mathrm{s}},\mathcal{V}^{\mathrm{C1}}} V_{\mathrm{C}}^{\mathrm{C1}} \\ =& \left\{\arg\max_{\Pi_{\mathrm{s}}} \delta_{\Pi}^{\mathrm{C1}}, \arg\max_{\mathcal{V}^{\mathrm{C1}}} \delta_{\mathcal{E}}^{\mathrm{C1}}\right\},\end{aligned} \tag{3.27}$$

yielding our design criterion for the interleaver Π_{s} and for the codebook $\mathcal{V}$, which can be formulated as

$$\Pi_{\mathrm{s}}^{\mathrm{opt}} = \arg\max_{\Pi_{\mathrm{s}}} \delta_{\Pi}^{\mathrm{C1}} \tag{3.28}$$

and

$$\mathcal{V}^{\mathrm{C2}} = \arg\max_{\mathcal{V}^{\mathrm{C1}}} \delta_{\mathcal{E}}^{\mathrm{C1}}, \tag{3.29}$$

respectively.

Achievable Rate Criterion

When the optimality of the codebook $\mathcal{V}^{\mathrm{C2}}$ of (3.29) is achieved, we are also interested in simultaneously maximising the achievable rate of $\mathcal{V}^{\mathrm{C2}}$. In this case, the design criterion can be readily formulated with the aid of (3.12) as

$$\begin{aligned}\mathcal{V}^{\mathrm{C3}} =& \arg\max_{\mathcal{V}^{\mathrm{C2}}} R_{\max,\mathcal{V}} \\ =& \arg\max_{\mathcal{V}^{\mathrm{C2}}} \frac{L}{m} \\ =& \arg\max_{\mathcal{V}^{\mathrm{C2}}} L\end{aligned} \tag{3.30}$$

for a fixed value of m. Here, we can observe from (3.12) and (3.20) that both the achievable rate and the attainable diversity gain are valid for the high-SNR region. On one hand, the diversity gain shown in (3.20), as a means of combating fading characterises the speed that the error probability decays at, as the SNR increases. On the other hand, the achievable rate given in (3.12) indicates the upper bound of the number of bits that can be reliably transmitted given a specific codebook. In our cases, the tradeoff between the achievable rate and the diversity gain can be used as a performance metric for comparing different codebook designs, as it will be investigated in Section 3.7.

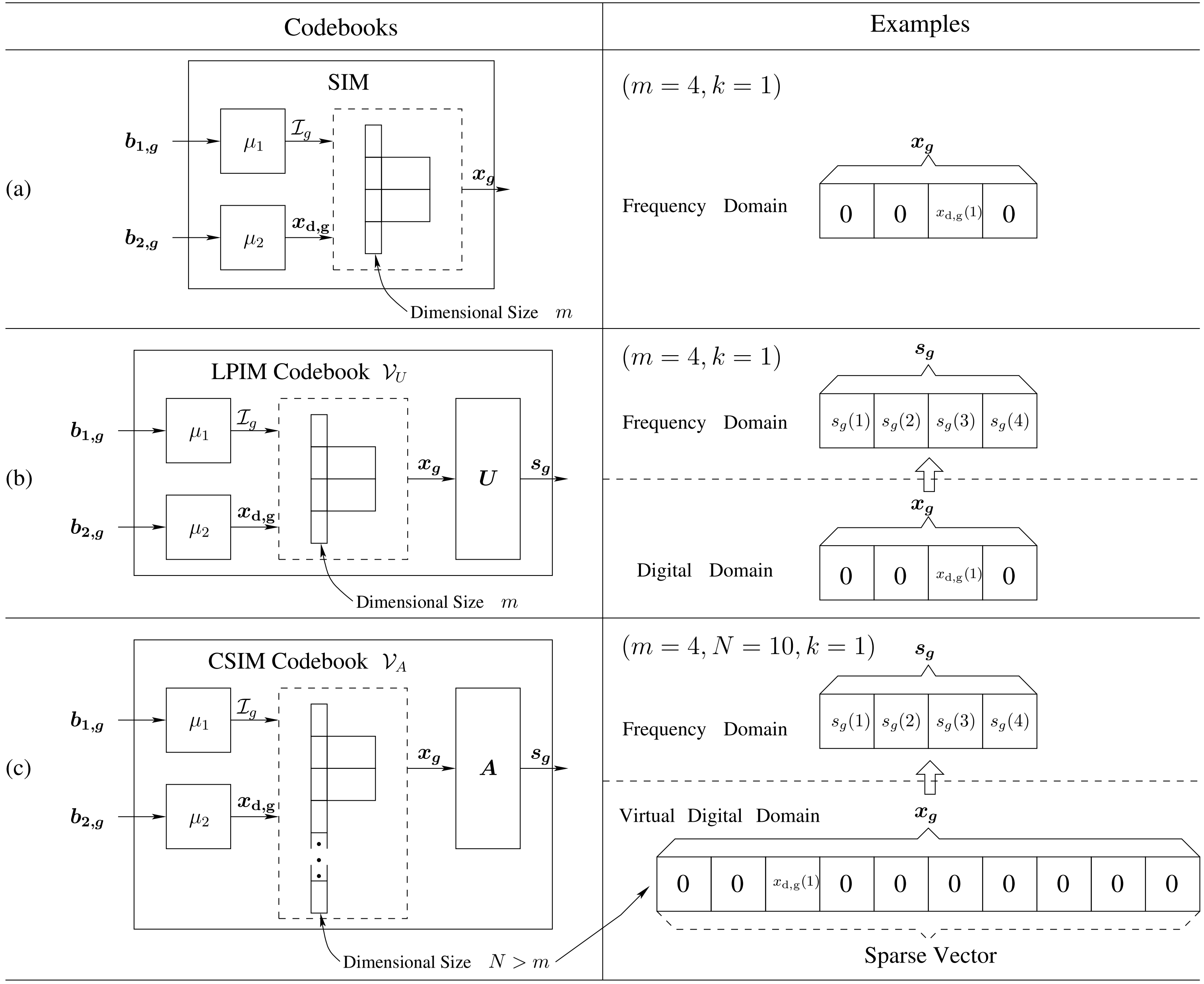

Figure 3.3: Illustration of the SIM codebook, the LPIM codebook $\mathcal{V}_{\boldsymbol{U}}$ and the CSIM codebook $\mathcal{V}_{\boldsymbol{A}}$, where μ_1 and μ_2 denote the index symbol mapper and the APM symbol mapper, respectively.

3.4 Linear Transmit Precoding Assisted Index Modulation Codebook Design

In this section, a LPIM codebook is proposed. Specifically, our LPIM codebook is designed based on the maximum diversity and coding gain criteria discussed in Section 3.3.4. We commence by describing the conventional SIM scheme. Then, our proposed LPIM codebook is detailed. Finally, as a further improvement, the optimal design of the subcarrier interleaver Π_s is shown.

3.4.1 Review of Subcarrier Index Modulation

As shown in Fig. 3.3(a), the conventional SIM scheme of [123] comprises an index mapper μ_1 and an APM mapper μ_2. Specifically, the bits in $\boldsymbol{b}_g$, as defined in Section 3.2.1, are partitioned into two sub-sequences denoted as $\boldsymbol{b}_{1,g} \in \mathbb{B}^{L_1}$ and $\boldsymbol{b}_{2,g} \in \mathbb{B}^{L_2}$, where we have $L = L_1 + L_2$. The bits in $\boldsymbol{b}_{1,g}$ are mapped into an index symbol $\mathcal{I}_g$ according to $\mu_1 : \mathbb{B}^{L_1} \rightarrow \mathcal{Z}$, where $\mathcal{Z} = \{\mathcal{Z}_1, \ldots \mathcal{Z}_C\}$ contains $C = 2^{L_1}$ index subsets, each of which is formed with the aid of k indices chosen from m available indices. Thereby, we have $L_1 = \log_2 C = \lfloor \log_2 \binom{m}{k} \rfloor$. Let the cth index subset of $\mathcal{Z}$ be denoted as $\mathcal{Z}_c = \{\mathcal{Z}_c(0), \ldots, \mathcal{Z}_c(k-1)\} \subset \mathcal{Z}$, where $\mathcal{Z}_c(i) \in \mathbb{Z}_+^N$ for $i = 0, \ldots, k-1$. Let us assume that the gth group of data bits is mapped into the cth candidate in $\mathcal{Z}$, i.e. we have $\mathcal{I}_g = \mathcal{Z}_c \subset \mathcal{Z}$. On the other hand, the bits in $\boldsymbol{b}_{2,g}$ are mapped onto k APM symbols based on $\mu_2 : \mathbb{B}^{\log_2 Q} \rightarrow \mathcal{A}$, where $\mathcal{A} \triangleq \{a_1, \ldots, a_Q\}$ is the constellation alphabet of a Q-ary QAM/PSK scheme. Hence, we have $L_2 = k \log_2 Q$. Let us denote the gth group of APM symbols as $\boldsymbol{x}_{\text{d},g} = [x_{\text{d},g}(0), \ldots, x_{\text{d},g}(k-1)]^T$, where we assume that $\mathbb{E}[|x_{\text{d},g}(i)|^2] = 1, \forall x_{\text{d},g}(i) \in \mathcal{A}$. Then, the symbols in $\boldsymbol{x}_{\text{d},g}$ are respectively assigned to the k active subcarrier indices in $\mathcal{I}_g$, yielding the gth group of symbols $\boldsymbol{x}_g = [x_g(0), \ldots, x_g(m-1)]^T$, which can be expressed as

$$\boldsymbol{x}_g = \boldsymbol{\Upsilon}_{\mathcal{I}_g} \boldsymbol{x}_{\text{d},g}, \tag{3.31}$$

where $\boldsymbol{\Upsilon}_{\mathcal{I}_g}$ is a $(m \times k)$-element mapping matrix based on $\mathcal{I}_g$.

3.4.2 Codebook Design

The proposed LPIM scheme is illustrated in Fig. 3.3(b). Firstly, based on (3.31), a specifically designed TPC matrix $\boldsymbol{U} \in \mathbb{C}^{m \times m}$ is applied to $\boldsymbol{x}_g$, yielding

$$\boldsymbol{s}_g = \boldsymbol{U} \boldsymbol{x}_g, \tag{3.32}$$

where the TPC matrix $\boldsymbol{U}$ is assumed to be normalised so that we have $\mathbb{E}[\|\boldsymbol{s}_g\|_2^2] = \mathbb{E}[\|\boldsymbol{x}_g\|_2^2] = k, \forall g$. In this case, the LPIM codebook denoted as $\mathcal{V}_{\boldsymbol{U}}$ is composed by all the legitimate versions of $\boldsymbol{s}_g$. Additionally, we can show that since LP is achieved without reducing the transmission rate, the attainable rate of $\mathcal{V}_{\boldsymbol{U}}$ can be expressed as

$$\begin{aligned} R_{\mathcal{V}_{\boldsymbol{U}}} =& \frac{L}{m} = \frac{L_1 + L_2}{m} \\ =& \frac{1}{m}\left(\left\lfloor \log_2 \binom{m}{k} \right\rfloor + k \log_2 Q\right) \quad \text{in bits/s/Hz}, \end{aligned} \tag{3.33}$$

which is fixed for the given values of m, k and Q. Furthermore, it can be readily shown that the LPIM codebook design is equivalent to the design of the LP matrix $\boldsymbol{U}$ based on a given IM scheme. Hence, by following the design criteria detailed in Section 3.3.4, our LPIM codebook design is detailed below.

Firstly, let us consider the diversity gain criterion, as discussed in Section 3.3.4. Based on the pairwise error event $\{\boldsymbol{s}_g^{\mathrm{c}} \rightarrow \boldsymbol{s}_g^{\mathrm{e}}\}$ defined in Section 3.3.3, let us express the error vector associated with (3.32) as

$$\begin{aligned} \boldsymbol{e} =& \boldsymbol{s}_g^{\mathrm{c}} - \boldsymbol{s}_g^{\mathrm{e}} \\ =& \boldsymbol{U}\left(\boldsymbol{x}_g^{\mathrm{c}} - \boldsymbol{x}_g^{\mathrm{e}}\right), \end{aligned} \tag{3.34}$$

where $\boldsymbol{x}_g^{\mathrm{c}}$ and $\boldsymbol{x}_g^{\mathrm{e}}$ denote the transmitted and the incorrect detection results of a symbol vector $\boldsymbol{x}_g$, respectively. As analysed in (3.22), the diversity gain achieved by a codebook, e.g., say $\mathcal{V}_{\boldsymbol{U}}$, is dependent on the minimum number of non-zero elements in all the possible error vectors that can be obtained from the codebook $\mathcal{V}_{\boldsymbol{U}}$. Furthermore, we can infer from (3.34) that the number of non-zero elements in $\boldsymbol{e}$ is dependent on the uniqueness of the linear combination results of the activated symbols in $\boldsymbol{x}_g$. For example, let us assume that all elements in the symbol vector $\boldsymbol{s}_g$ of (3.32), which are obtained from the linear combinations of the activated symbols in $\boldsymbol{x}_g$, are unique. Then, we can readily show that the number of non-zero elements in all the possible error vectors related to $\boldsymbol{s}_g$ becomes identical to its dimension, i.e. we have $\|\boldsymbol{e}\|_0 = m, \forall \boldsymbol{s}_g^{\mathrm{e}} \in \mathcal{V}_{\boldsymbol{U}}$. By contrast, if there exists a symbol vector $\boldsymbol{x}_g^{\mathrm{e}} \neq \boldsymbol{x}_g^{\mathrm{c}}$ so that after the LP of (3.32), we have $\boldsymbol{s}_g^{\mathrm{e}} = \boldsymbol{s}_g^{\mathrm{c}}$ due to the unfavourable design of the LP matrix $\boldsymbol{U}$. In this case, we have $\|\boldsymbol{e}\|_0 = 0$ for $\boldsymbol{s}_g^{\mathrm{c}}$, since the same results are obtained by the linear combinations of the activated symbols in $\boldsymbol{x}_g^{\mathrm{e}}$ and $\boldsymbol{x}_g^{\mathrm{c}}$. Here, we are interested in the former case, which leads to a codebook resulting in the maximum diversity gain. Similar design issues have been investigated in [138–141, 143, 144, 152]. Specifically, we adopt the cyclotomic lattice design scheme studied in [139, 140, 143], where the precoding matrix $\boldsymbol{U}$ is treated as the generator matrix of an m-dimensional complex lattice constructed from the cyclotomic field $\mathbb{Q}(\alpha_P)$, with $\alpha_P = \exp(j2\pi/P)$ being a primitive Pth root of unity in the complex field $\mathbb{C}$. In more detail, the

$(m \times m)$-element generator matrix $\boldsymbol{U}$ is defined as

$$\boldsymbol{U} = \frac{1}{\sqrt{m}} \mathrm{diag}\left\{\alpha_P^{p_1}, \alpha_P^{p_2}, \ldots, \alpha_P^{p_m}\right\} \begin{bmatrix} 1 & \alpha_P^{p_1} & \alpha_P^{2p_1} & \ldots & \alpha_P^{(m-1)p_1} \\ 1 & \alpha_P^{p_2} & \alpha_P^{2p_2} & \ldots & \alpha_P^{(m-1)p_2} \\ \vdots & \vdots & \vdots & \ddots & \vdots \\ 1 & \alpha_P^{p_m} & \alpha_P^{2p_m} & \ldots & \alpha_P^{(m-1)p_m} \end{bmatrix}, \tag{3.35}$$

which is the product of a diagonal matrix multiplied by a Vandermonde matrix having a normalisation factor of $1/\sqrt{m}$. In (3.35), the diagonal elements $\{\alpha_P^{p_1}, \alpha_P^{p_2}, \ldots, \alpha_P^{p_m}\}$ are the roots of the minimal polynomial of α_P, where we have $p_1 = 1$ for $\alpha_P = \alpha_P^{p_1}$ and $\gcd(p_i, P) = 1$ for $i = 1, \ldots, m$. Furthermore, we will also show that the first row of the Vandermonde matrix of (3.35), which becomes $\left[1, \alpha_P, \alpha_P^2, \ldots, \alpha_P^{m-1}\right]$ for $p_1 = 1$, is a basis of the cyclotomic field $\mathbb{Q}(\alpha_P)$. Hence, based on Theorem 2 of [140], we have the following results

Proposition 1. *The codebook $\mathcal{V}_{\boldsymbol{U}}$ associated with the TPC matrix of* (3.35) *achieves the maximum diversity order of* (3.23)*.*

Remark 1. *Here, it is convenient to rewrite the IM symbol vector $\boldsymbol{x}_g$ given in* (3.31) *as $\boldsymbol{x}_g = \sqrt{E_s}\check{\boldsymbol{x}}_g$, where $\sqrt{E_s}$ is the constellation normalisation factor. Then, we can model each symbol in $\check{\boldsymbol{x}}_g$ as a point from the ring of Gaussian integers, which is defined as $\mathbb{Z}[j] = \{a + jb : a, b \in \mathbb{Z}\}$. Explicitly, it can be readily shown that the activated symbols in $\check{\boldsymbol{x}}_g$ belong to $\mathbb{Z}[j]$, since they are drawn from the square QAM constellation. Moreover, we can also show that the zero-valued symbols in $\check{\boldsymbol{x}}_g$ correspond to the origin of $\mathbb{Z}[j]$. Similarly, we can point out that when the activated symbols in $\check{\boldsymbol{x}}_g$ are drawn from the triangular QAM/PSK constellation, each symbol in the IM symbol vector $\check{\boldsymbol{x}}_g$ given in* (3.31) *can be modelled as a point from the ring of Eisenstein integers, which is defined as $\mathbb{Z}[\omega] = \{a + \omega b : a, b \in \mathbb{Z}\}$ with $\omega \triangleq \exp(j2\pi/3)$.*

Next, let us consider the coding gain design criterion of the codebook $\mathcal{V}_{\boldsymbol{U}}$. More particularly, we assume that the maximum diversity gain is achieved by employing the TPC matrix of (3.35) in the following analysis. Firstly, based on (3.34), the squared MPD of (3.26) can be rewritten as

$$\begin{aligned} \delta_{\mathcal{E}}^{\mathrm{C1}} &= \min_{\forall \boldsymbol{e} \in \mathcal{E}} \prod_{i=1}^{m} |e(i)|^2 \\ &= \min_{\forall \boldsymbol{x}_g} \prod_{i=1}^{m} \left| \sum_{t=1}^{m} u_{i,t} \left[x_g^{\mathrm{c}}(t) - x_g^{\mathrm{e}}(t)\right] \right|^2, \end{aligned} \tag{3.36}$$

where $u_{i,t}$ denotes the entry in the ith row and tth column of $\boldsymbol{U}$. Then, for a given QAM/PSK constellation, the parameters of the TPC matrix given in (3.35) are obtained so that the corresponding coding gain can be maximised. Hence, the optimal TPC matrix can be finally obtained by solving the optimisation problem of

$$\begin{aligned}\mathcal{V}_{\boldsymbol{U}}^{\text{C2}} =&\arg\max_{\boldsymbol{U}} \delta_{\mathcal{E}}^{\text{C1}} \\ =& \arg\max_{\{P,p_2,\ldots,p_m\}} \min_{\forall \boldsymbol{x}_g} \prod_{i=1}^{m} \left| \sum_{t=1}^{m} u_{i,t} \left[x_g^{\text{c}}(t) - x_g^{\text{e}}(t) \right] \right|^2 ,\end{aligned} \tag{3.37}$$

where, we have $u_{i,t} = \alpha_P^{tp_i}/\sqrt{m}$. On the other hand, observe in (3.23) that the coding gain of the system is also dependent on the design of the interleaver Π_{s}, which is detailed next.

3.4.3 Optimal Design of the Interleaver Π_{s}

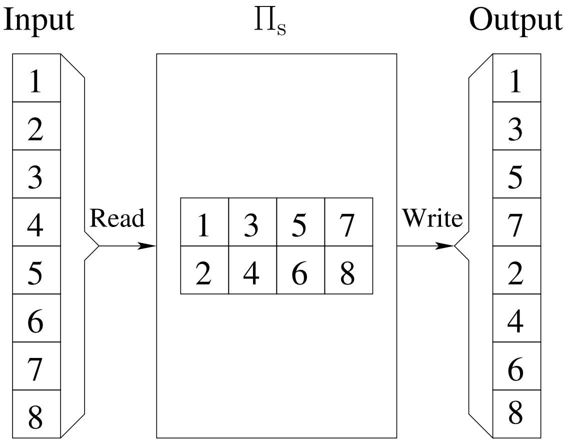

Figure 3.4: Illustration of the interleaver Π_{s} with a depth of $G = 4$.

Again, the interleaver Π_{s} governs the OFDM subcarriers grouping, which is usually characterised by δ_{Π}^{C1} defined in (3.24). Furthermore, the optimal design of the interleaver Π_{s} can be obtained by solving the optimisation problem of (3.28). As shown in [141, 144], the depth-G interleaver of Fig. 3.4 permutes the $(m \times G)$-element input symbols by entering them on a column-by-column basis and outputting them on a row-by-row basis. Thus, the $(M \times m)$-element matrix $\boldsymbol{\Upsilon}_{\Pi_g}$ shown in (3.2) for the gth group of symbols is characterised by $s_g(i) = s_{\text{F}}(g - 1 + iG)$ for $g = 1, \ldots, G$ and $i = 0, 1, \ldots, m - 1$. In this case, we have

$$\begin{aligned}\delta_{\Pi}^{\text{C1}} =& \min_{\forall g} \det \left(\boldsymbol{F}_{\text{h},\Pi_g}^H \boldsymbol{F}_{\text{h},\Pi_g} \right) \\ =& \min_{\forall g} \det \left(\boldsymbol{\Upsilon}_{\text{h}} \boldsymbol{\mathcal{F}}_M^H \boldsymbol{\Upsilon}_{\Pi_g} \boldsymbol{\Upsilon}_{\Pi_g}^T \boldsymbol{\mathcal{F}}_M \boldsymbol{\Upsilon}_{\text{h}}^T \right) \\ =& \det \left(\boldsymbol{\Upsilon}_{\text{h}} \boldsymbol{\mathcal{F}}_M^H \boldsymbol{\Upsilon}_{\Pi_1} \boldsymbol{\Upsilon}_{\Pi_1}^T \boldsymbol{\mathcal{F}}_M \boldsymbol{\Upsilon}_{\text{h}}^T \right) = \ldots, = \det \left(\boldsymbol{\Upsilon}_{\text{h}} \boldsymbol{\mathcal{F}}_M^H \boldsymbol{\Upsilon}_{\Pi_G} \boldsymbol{\Upsilon}_{\Pi_G}^T \boldsymbol{\mathcal{F}}_M \boldsymbol{\Upsilon}_{\text{h}}^T \right) ,\end{aligned} \tag{3.38}$$

which is a constant value for all groups due to the constant depth G of the interleaver Π_{s}.

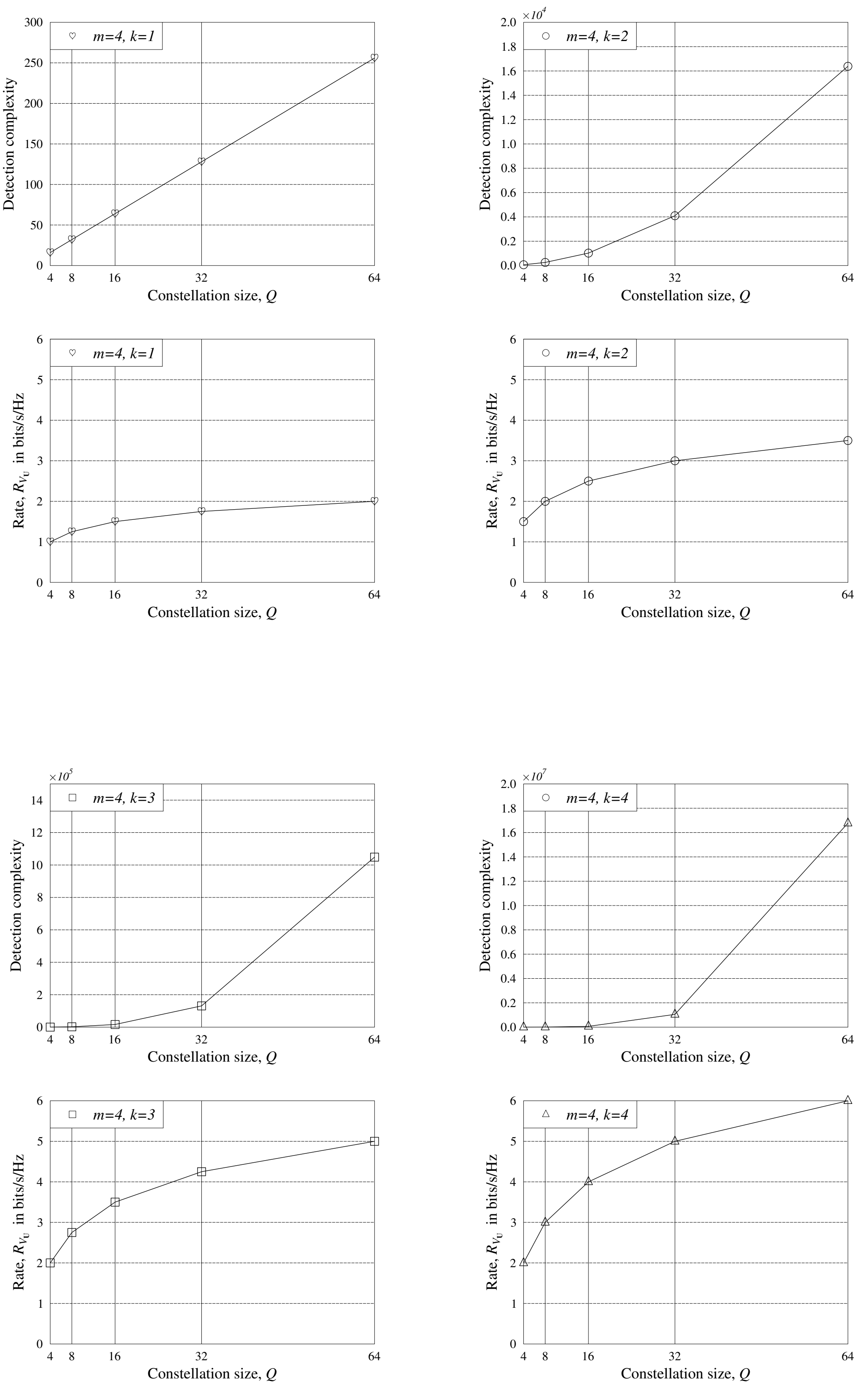

Figure 3.5: The detection complexity and the achievable rate $R_{\mathcal{V}_U}$ versus the constellation size Q for our LPIM codebook $\mathcal{V}_U$ associated with $m = 4$. The detection complexity and the achievable rate are obtained according to (3.39) and (3.33), respectively.

3.4.4 Complexity Analysis

In comparison to the conventional SIM scheme of [123], an additional complexity is imposed on both the transmitter and the receiver by our LPIM scheme. We point out here that the complexity of multiplications by zero-valued deactivated symbols can be neglected, since these operations can be avoided in practice. Bearing this in mind, let us detail the complexity associated with our LPIM codebook as follows.

Firstly, at the transmitter side, upon substituting (3.31) into (3.32), we can infer that the complexity order of precoding each group of IM symbols is given by $\mathcal{O}(k)$, i.e. by the computational cost of multiplying k activated symbols with the corresponding entries in the TPC matrix $\boldsymbol{U}$. Let us assume for a moment that the ML detection of (3.9) is employed at the receiver side. Hence, the corresponding complexity of detecting each group of LPIM symbols is dominated by searching through the space of all possible candidates in our LPIM codebook $\mathcal{V}_{\boldsymbol{U}}$, which is on order of $\mathcal{O}(2^L)$. Since we have $k \leq m < 2^L$, the overall complexity related to our LPIM codebook can be expressed with the aid of (3.33) as

$$\mathcal{O}(2^L) = \mathcal{O}\left(2^{\lfloor \log_2 \binom{m}{k} \rfloor} Q^k\right). \tag{3.39}$$

Based on (3.39), we can show that for the case of $2 \leq k \leq m$, the overall complexity may become excessive even for a moderate constellation size of Q. Furthermore, it can be shown with the aid of (3.33) that there is a tradeoff between the achievable rate and the complexity of our LPIM scheme. Moreover, in order to achieve a high rate, the corresponding detection complexity may become excessive. We note that a special case is when $k = 1$, yielding a complexity order of $\mathcal{O}(2^{\lfloor \log_2 m \rfloor} Q)$. In this case, the overall complexity is linearly increased with the constellation size Q, which is a desirable feature for practical implementations. However, the corresponding achievable rate is limited, as seen in Fig. 3.5. Thus, it is challenge to design a codebook that is capable of attaining a high rate at a relatively low complexity, as detailed in the next section.

3.5 The Conceptual Framework of Compressed Sensing Assisted Index Modulation

In this section, the detailed conceptual framework of our CSIM codebook is described. We commence by showing the basic idea of our CSIM. Then, our CSIM scheme is described. Next, we propose our design of CSIM codebook. Finally, the recovery problem is discussed.

3.5.1 The Concept of the Compressed Sensing Assisted Index Modulation

As discussed in Section 3.4, the LPIM codebook $\mathcal{V}_{\boldsymbol{U}}$ is designed based on maximising both the diversity gain and the coding gain. As argued in Section 3.4.4, it is desirable to design a codebook based on the maximum diversity gain criterion, as well as to improve the achievable rate at a relatively low complexity. We emphasise here that our attention is focused on designing such a codebook without increasing the total number of subcarriers for a given bandwidth, as well as without increasing the constellation size for the activated symbols. Bearing these constraints in mind, our observations of the conventional SIM scheme shown in Section 3.4.1 are discussed as follows.

Firstly, as observed from Fig. 3.5, the complexity can be reduced by choosing a small value of k. The drawback is that the achievable rate is also reduced. In detail, since the number of information bits conveyed by the index symbols (i.e., L_1) is a nonlinear function of k, the value of L_1 may remain unchanged, when the value of k is reduced. For example, for a fixed value of $m = 4$, we have $L_1 = 2$ for $k = 3$, while when the value of k is reduced to 2, we also have $L_1 = 2$. Hence, the reduction of the rate is mainly caused by the reduction in the number of information bits conveyed by the activated QAM/PSK symbols. For a given constellation size, this reduction becomes inevitable. In this scenario, a feasible way of addressing the above-mentioned issue is to increase the total number of available indices, so that as many as possible of the L_1 bits can be mapped to non-zero symbol indices in each group. As a result, the corresponding transmission rate may even be increased. However, as previously stated, the bandwidth is fixed to a specific value. Thus, this idea cannot be directly applied to the indices of the FD subcarriers. Intuitively, a remedy of this issue is to compress the high-dimensional IM symbol vector into a low-dimensional FD subcarrier vector, as shown in [69]. We may also note that the above-mentioned IM symbol vector can be modelled as a sparse vector with a sparsity level of k. Then, CS can be invoked to solve this problem, as detailed next.

3.5.2 Formulation of Compressed Sensing Assisted Index Modulation

As shown in Fig. 3.3(c), our proposed CSIM scheme is consisted of two steps, which are the bit mapping step and the symbol compression step. In the bit mapping step, the IM is implemented in a high-dimensional virtual digital domain. In detail, we first define an N-dimensional virtual digital domain seen in Fig. 3.3(c), where we have $N > m$ and $N \gg k$. Then, each group of IM symbols is obtained by activating

k indices from N virtual indices in the virtual digital domain. Correspondingly, the mapping rule can be defined as $\mu_1 : \mathbb{B}^{L_1} \rightarrow \mathcal{Z}$, where $\mathcal{Z} = \{\mathcal{Z}_1, \ldots \mathcal{Z}_C\}$ contains $C = 2^{L_1}$ index subsets, resulting in $L_1 = \log_2 C = \lfloor \log_2 \binom{N}{k} \rfloor$. Next, the activated indices are allocated by APM symbols from the constellation alphabet of a Q-ary QAM/PSK scheme, which is omitted here since it has been described in Section 3.4.1. Let us denote the gth group of APM symbols as $\boldsymbol{x}_{\mathrm{d},g} = [x_{\mathrm{d},g}(0), \ldots, x_{\mathrm{d},g}(k-1)]^T$, where we assume that $\mathbb{E}[|x_{\mathrm{d},g}(i)|^2] = 1, \forall x_{\mathrm{d},g}(i) \in \mathcal{A}$. Hence, the gth group of symbols denoted as $\boldsymbol{x}_g = [x_g(0), \ldots, x_g(N-1)]^T$ can be formulated as

$$\boldsymbol{x}_g = \boldsymbol{\Upsilon}_{\mathcal{I}_g} \boldsymbol{x}_{\mathrm{d},g}, \tag{3.40}$$

where $\boldsymbol{\Upsilon}_{\mathcal{I}_g}$ is a $(N \times k)$-element mapping matrix based on $\mathcal{I}_g$.

In the symbol compression step seen in Fig. 3.3(c), a measurement matrix $\boldsymbol{A} \in \mathbb{C}^{m \times N}$ is employed for compressing the N-dimensional symbol vector $\boldsymbol{x}_g$ from the virtual digital domain to an m-dimensional vector $\boldsymbol{s}_g$ in the FD, which can be formulated as

$$\boldsymbol{s}_g = \boldsymbol{A}\boldsymbol{x}_g, \tag{3.41}$$

where each column of $\boldsymbol{A}$ is assumed to be of unity length to yield the power constraint of $\mathbb{E}[\|\boldsymbol{x}_g\|_2^2] = \mathbb{E}[\|\boldsymbol{s}_g\|_2^2] = k$. Hence, our proposed CSIM codebook denoted as $\mathcal{V}_{\boldsymbol{A}}$ is composed by all the legitimate versions of $\boldsymbol{s}_g$. Furthermore, we can readily show that the achievable rate of $\mathcal{V}_{\boldsymbol{A}}$ is given by

$$\begin{aligned} R_{\mathcal{V}_{\boldsymbol{A}}} =& \frac{L}{m} = \frac{L_1 + L_2}{m} \\ =& \frac{1}{m}\left(\left\lfloor \log_2 \binom{N}{k} \right\rfloor + k \log_2 Q \right) \quad \text{in bits/s/Hz.} \end{aligned} \tag{3.42}$$

We can now show that for the given values of m, k and Q, the CSIM codebook $\mathcal{V}_{\boldsymbol{A}}$ is capable of attaining a higher achievable rate in comparison to the LPIM codebook $\mathcal{V}_{\boldsymbol{U}}$ given in (3.33). This can be simply achieved by increasing the dimension size N of the virtual digital domain of our CSIM scheme.

We can observe from the above description that due to the constraint of $N \gg k$, the N-dimensional symbol vector $\boldsymbol{x}_g$ given in (3.40) is a sparse vector associated with a sparsity level of k. Furthermore, since the dimensional size of the compressed symbol vector $\boldsymbol{s}_g$ is less than that of the sparse symbol vector $\boldsymbol{x}_g$, Eq. (3.41) represents a classical mathematic modelling of CS [54], whose recovery performance (or detection performance in our scenario) is determined by the specific characteristics of the measurement matrix $\boldsymbol{A}$. Meanwhile, from the codebook design point of view, the measurement matrix $\boldsymbol{A}$ should be carefully designed to meet the diversity gain and coding gain criteria discussed in Section 3.3.4. In order to address these issues, we propose the CSIM codebook design, as detailed below.

3.5.3 Compressed Sensing Assisted Index Modulation Codebook Design

Based on the above discussions, we are aware that the achievable rate of our CSIM scheme can be readily improved by increasing the dimensionality of the virtual digital domain. Hence, we can focus our attention on designing a CSIM codebook for a given dimension N, where two salient aspects have to be considered. Firstly, the design of the codebook $\mathcal{V}_{\boldsymbol{A}}$ has to meet both the diversity gain and coding gain criteria of (3.22) and (3.29), respectively. Secondly, the codebook $\mathcal{V}_{\boldsymbol{A}}$ should be designed for supporting stable information-preserving compression, so that a guaranteed recovery performance can be achieved. Generally speaking, it is hard to obtain a deterministic solution for the above-mentioned codebook design. Below, we propose a plausible technique of designing the CSIM codebook to meet our considerations.

Firstly, let us define a dictionary matrix $\boldsymbol{\mathcal{U}} \in \mathbb{C}^{N\times N}$. Moreover, let us assume that the measurement matrix $\boldsymbol{A} \in \mathbb{C}^{m\times N}$ is formed by selecting m rows from $\boldsymbol{\mathcal{U}}$. Specifically, let the indices of the selected rows of $\boldsymbol{\mathcal{U}}$ be collected into an index set $\mathcal{P}$, where we have $m = |\mathcal{P}|$. Then, the measurement matrix $\boldsymbol{A}$ can be expressed as

$$\boldsymbol{A} = \boldsymbol{\Upsilon}_{\mathcal{P}}^T \boldsymbol{\mathcal{U}}. \tag{3.43}$$

Then, based on (3.43) and on our discussions in Section 3.4.2, we have the following proposition.

Proposition 2. *If the dictionary matrix* $\boldsymbol{\mathcal{U}} \in \mathbb{C}^{N\times N}$ *is designed to achieve full diversity for a given IM scheme, the precoding matrix of* (3.43) *also achieves full diversity for any row selection set* $\mathcal{P}$*.*

Proof. Firstly, let us express the error vector associated with (3.41) as

$$\begin{aligned}\boldsymbol{e} =&\boldsymbol{s}_g^{\mathrm{c}} - \boldsymbol{s}_g^{\mathrm{e}}\\ =&\boldsymbol{A}(\boldsymbol{x}_g^{\mathrm{c}} - \boldsymbol{x}_g^{\mathrm{e}})\\ =&\boldsymbol{\Upsilon}_{\mathcal{P}}^T\boldsymbol{\mathcal{U}}(\boldsymbol{x}_g^{\mathrm{c}} - \boldsymbol{x}_g^{\mathrm{e}})\\ =&\boldsymbol{\Upsilon}_{\mathcal{P}}^T\boldsymbol{e}_{\mathcal{V}_{\boldsymbol{\mathcal{U}}}},\end{aligned} \tag{3.44}$$

where, by definition, $\boldsymbol{e}_{\mathcal{V}_{\boldsymbol{\mathcal{U}}}} \in \mathbb{C}^N$ represents the error vector associated with $\boldsymbol{\mathcal{U}}\boldsymbol{x}_g \in \mathbb{C}^N$. Let us also suppose that the dictionary matrix $\boldsymbol{\mathcal{U}}$ is designed to achieve the full diversity criterion of

$$\boldsymbol{\mathcal{U}} \quad \text{s.t.} \quad \|\boldsymbol{e}_{\mathcal{V}_{\boldsymbol{\mathcal{U}}}}\|_0 = N, \quad \forall\{\boldsymbol{x}_g^{\mathrm{c}}, \boldsymbol{x}_g^{\mathrm{e}}\}, \tag{3.45}$$

as it has been detailed in Section 3.4.2. We can observe from (3.44) that our target error vector $\boldsymbol{e} \in \mathbb{C}^m$ is formed from $\boldsymbol{e}_{\mathcal{V}_{\boldsymbol{\mathcal{U}}}}$ by selecting the specific elements whose indices are in the index set $\mathcal{P}$. Thus, it can be readily shown that

$$\|\boldsymbol{e}\|_0 = \|\boldsymbol{\Upsilon}_{\mathcal{P}}^T \boldsymbol{e}_{\mathcal{V}_{\mathcal{U}}}\|_0 = m, \quad \forall\{\boldsymbol{x}_g^{\mathrm{c}}, \boldsymbol{x}_g^{\mathrm{e}}, \mathcal{P}\} \tag{3.46}$$

for a given measurement matrix $\boldsymbol{A} = \boldsymbol{\Upsilon}_{\mathcal{P}}^T \boldsymbol{\mathcal{U}}$, where $\boldsymbol{\mathcal{U}}$ satisfies (3.45). □

In the following analysis, we assume that the maximum diversity gain criterion of (3.22) is satisfied by specifying the dictionary matrix $\boldsymbol{\mathcal{U}}$ according to our Proposition 2. More specifically, the dictionary matrix $\boldsymbol{\mathcal{U}}$ is assumed to be designed based on our scheme given in (3.35). Hence, we can now consider the design of the row-selecting matrix $\boldsymbol{\Upsilon}_{\mathcal{P}}^T$, which is dependent on the index set $\mathcal{P}$. According to [43, 47], the measurement matrix $\boldsymbol{A}$ should be designed for satisfying the MIP or the RIP. However, since computation of the restricted isometry constant of the RIP has been shown to be NP-hard [53], the MIP is used in this chapter. The mutual coherence of the above-mentioned measurement matrix $\boldsymbol{A}$ can be formulated as

$$\begin{aligned}\mu_{\boldsymbol{A}} &= \max_{0 \le l_1 < l_2 \le N-1} \frac{\left|\sum_{i=1}^{m} \alpha_P^{-\mathcal{P}_i p_{l_1}} \alpha_P^{l_2 p_{\mathcal{P}_i}}\right|}{N} \\ &= \max_{0 \le l_1 < l_2 \le N-1} \frac{1}{N} \left|\sum_{i=1}^{m} \exp\left\{j\frac{2\pi}{P}\left(-\mathcal{P}_i p_{l_1} + l_2 p_{\mathcal{P}_i}\right)\right\}\right|,\end{aligned} \tag{3.47}$$

where $\mathcal{P}_i$ denotes the ith element in $\mathcal{P}$. According to [43], the mutual coherence of $\boldsymbol{A}$ should satisfy $\mu_{\boldsymbol{A}} < 1/(2k-1)$, which is the sufficient condition of guaranteeing that there exists at most one k-sparse vector $\boldsymbol{x}_g$ satisfying $\boldsymbol{A}\boldsymbol{x}_g = \boldsymbol{s}_g$. Thus, in order to achieve a guaranteed detection performance, the measurement matrix $\boldsymbol{A} \in \mathbb{C}^{m \times N}$ is designed for satisfying

$$\sqrt{\frac{N-m}{m(N-1)}} \le \mu_{\boldsymbol{A}} < \frac{1}{2k-1}, \tag{3.48}$$

where the lower bound at the left hand side is the well-known Welch bound [108]. If the mutual coherence $\mu_{\boldsymbol{A}}$ succeeds in matching the Welch bound, we say that matrix $\boldsymbol{A}$ is a MWBE codebook [153], which is also known as an ETF [109]. However, the MWBE codebook design of $\boldsymbol{A}$ may not exist for some cases. In cases such as these, the index set $\mathcal{P}$ can be chosen by solving the following problem

$$\mathcal{P} = \arg\min_{\mathcal{P}'} \left\{ \max_{0 \le l_1 < l_2 \le N-1} \frac{1}{N} \left|\sum_{i=1}^{m} \exp\left\{j\frac{2\pi}{P}\left(-\mathcal{P}_i' p_{l_1} + l_2 p_{\mathcal{P}_i'}\right)\right\}\right| \right\}. \tag{3.49}$$

Note that for a relatively low-dimensional size N, the solution of (3.49) can be simply obtained by brute-force search. However, the corresponding computational cost may be excessive even for a moderate dimension of N, as it will be discussed in Section 3.6.3.

Finally, we can conclude that for a given IM scheme, our CSIM codebook design is equivalent to solving the joint optimisation problem of

$$\{\mathcal{P},\boldsymbol{\mathcal{U}}\} \quad \text{s.t.} \quad (3.44)\ \&\ (3.49). \tag{3.50}$$

In the sequel, we assume that the precoding matrix $\boldsymbol{A}$ is obtained by solving (3.50).

3.5.4 Complexity Analysis

In comparison to the conventional IM scheme, an additional complexity is imposed both on the transmitter and on the receiver by our CSIM codebook. Firstly, the complexity associated with our CSIM codebook is the same as that of the LPIM codebook, which is the computational complexity of multiplying k activated symbols with the corresponding entries in the precoding matrix $\boldsymbol{A}$, which is on the order of $\mathcal{O}(k)$. We shall point out here that in comparison to the LPIM codebook, a larger buffer is required to store the entries of our CSIM codebook.

At the receiver side, we also assume that the ML detection of (3.9) is employed for symbol detection. Hence, the corresponding complexity imposed by detecting each group of LPIM symbols is mainly due to searching through the space of all possible candidates in our CSIM codebook $\mathcal{V}_{\boldsymbol{A}}$, which is on the order of $\mathcal{O}(2^L)$. Since we have $k \leq m < 2^L$, the overall complexity related to our CSIM codebook can be expressed with the aid of (3.42) as

$$\mathcal{O}(2^L) = \mathcal{O}\left(2^{\lfloor \log_2 \binom{N}{k} \rfloor} Q^k\right). \tag{3.51}$$

Below, let us discuss some of the information recovery problems of our CSIM scheme.

3.5.5 Recovery Problem Discussions

Firstly, upon substituting (3.41) into (3.4c), we arrive at

$$\begin{aligned} \boldsymbol{y}_g =& \bar{\boldsymbol{H}}_g \boldsymbol{A} \boldsymbol{x}_g + \bar{\boldsymbol{n}}_g \\ =& \boldsymbol{\Phi}_g \boldsymbol{x}_g + \bar{\boldsymbol{n}}_g, \end{aligned} \tag{3.52}$$

where by definition we have $\boldsymbol{\Phi}_g = \bar{\boldsymbol{H}}_g \boldsymbol{A}$ and $\boldsymbol{\Phi}_{g,\mathcal{I}_g} = \boldsymbol{\Phi}_g \boldsymbol{\Upsilon}_{\mathcal{I}_g}$. In (3.52), the N-dimensional symbol vector $\boldsymbol{x}_g$ shown in Section 3.5.2 is exactly k-sparse, which is observed in the spaces of m dimensions. Hence, according to the CS principles, it can be recovered by solving the classic ℓ_0-minimisation problem described in [46, 82] as

$$\boldsymbol{x}_g^{\ell_0} = \arg \min_{\boldsymbol{v} \in \mathbb{C}^{N \times 1}} \|\boldsymbol{v}\|_0, \quad \text{s.t.} \quad \boldsymbol{y}_g - \boldsymbol{\Phi}_g \boldsymbol{v} \in \mathcal{B}, \tag{3.53}$$

where $\mathcal{B}$ is a bounded set associated with the noise vector $\bar{\boldsymbol{n}}_g$, while $\boldsymbol{v}$ is an N-length testing vector chosen from the complex vector space $\mathbb{C}^{N\times 1}$.

However, the ℓ_0-minimisation problem of (3.53) has been shown to be NP-hard [114]. For this reason, typically the ℓ_1-minimisation based solutions are employed in CS, since they are tractable to solve. Moreover, under the conditions shown in [54], the ℓ_0-minimisation problem of (3.53) is equivalent to solving the ℓ_1-minimisation problem of

$$\boldsymbol{x}_g^{\ell_1} = \arg\min_{\boldsymbol{v}\in\mathbb{C}^{N\times 1}} \|\boldsymbol{v}\|_1, \quad \text{s.t.} \quad \boldsymbol{y}_g - \boldsymbol{\Phi}_g \boldsymbol{v} \in \mathcal{B}. \tag{3.54}$$

Note that the ℓ_1-minimisation problem is a well-known convex optimisation problem, which can be solved in polynomial time, for example, by the interior point method [39]. However, for our detection problem, the computational cost of solving the ℓ_1-minimisation problem may still be excessive. Moreover, in our CSIM scheme, the sparsity level k of the symbol vector $\boldsymbol{x}_g$ is determined by the number of activate indices, which is a fixed and known value. In this case, the lower-complexity family of greedy pursuit algorithms [74, 76] is preferred. However, the existing greedy algorithms can only provide relatively good detection performance, when the SNR is relatively high. Another concern is that for the existing greedy algorithms, the sparse estimation is operated without any restrictions on the signal space. Thus, the existing greedy algorithms cannot be directly invoked for detection in our scenario. In order to address the above-mentioned issues, we propose the a low-complexity detector, as detailed in the next section.

3.6 Generalised Iterative Residual Check Detector

In general, the optimum symbol detection scheme is based on the ML principle, as discussed in Section 3.3.1. However, the corresponding complexity cost may be prohibitively excessive, even for a moderate-sized codebook $\mathcal{V}$. In order to alleviate this problem, we propose a low-complexity detection scheme, namely the GIRCD, in this section. Specifically, the proposed GIRCD is a generalised detection scheme, which can be used by both the LPIM and CSIM schemes. We first discuss the generalised detection problems for both the schemes, and then, detail the proposed GIRCD. Throughout this section, the group index g is neglected for notional brevity, since each group of received symbols is decoded in a similar way.

3.6.1 Generalised Detection Problems

Based on Section 3.4 and Section 3.5, we can readily show that each group of received symbols can be formulated in a general way as

$$\boldsymbol{y} = \boldsymbol{\Phi}\boldsymbol{x} + \bar{\boldsymbol{n}} \tag{3.55a}$$

$$= \boldsymbol{\Phi}\boldsymbol{\Upsilon}_{\mathcal{I}}\boldsymbol{x}_{\mathrm{d}} + \bar{\boldsymbol{n}} \tag{3.55b}$$

$$= \boldsymbol{\Phi}_{\mathcal{I}}\boldsymbol{x}_{\mathrm{d}} + \bar{\boldsymbol{n}}, \tag{3.55c}$$

where by definition, we have $\boldsymbol{\Phi}_{\mathcal{I}} = \boldsymbol{\Phi}\boldsymbol{\Upsilon}_{\mathcal{I}} \in \mathbb{C}^{m\times k}$ with $\boldsymbol{\Phi} \in \mathbb{C}^{m\times\mathfrak{D}(\boldsymbol{x})}$ defined as

$$\begin{cases} \boldsymbol{\Phi} = \bar{\boldsymbol{H}}\boldsymbol{U} \ \& \ \mathfrak{D}(\boldsymbol{x}) = m, & \text{for the LPIM codebook } \mathcal{V}_{\boldsymbol{U}}, \\ \boldsymbol{\Phi} = \bar{\boldsymbol{H}}\boldsymbol{A} \ \& \ \mathfrak{D}(\boldsymbol{x}) = N, & \text{for the CSIM codebook } \mathcal{V}_{\boldsymbol{A}}, \end{cases} \tag{3.56}$$

where $\mathfrak{D}(\boldsymbol{x})$ represents the dimension of the symbol vector $\boldsymbol{x}$. Let us assume that both the IM symbols in $\mathcal{Z}$ and the classic APM symbols in $\mathcal{A}$ are equiprobable and independent. Then, the conditional PDF of $\boldsymbol{y}$ can be formulated based on (3.7) and (3.55) as

$$\begin{aligned} p(\boldsymbol{y}|\boldsymbol{x}) &= p(\boldsymbol{y}|\boldsymbol{\Upsilon}_{\mathcal{I}}\boldsymbol{x}_{\mathrm{d}}) \\ &= p(\boldsymbol{y}|\mathcal{I}, \boldsymbol{x}_{\mathrm{d}}) \\ &= \frac{1}{(\pi N_0)^{\mathfrak{D}(\boldsymbol{x})}} \exp\left\{-\frac{\|\boldsymbol{y} - \boldsymbol{\Phi}\boldsymbol{\Upsilon}_{\mathcal{I}}\boldsymbol{x}_{\mathrm{d}}\|_2^2}{N_0}\right\}, \end{aligned} \tag{3.57}$$

which yields the JML detection of

$$\left(\mathcal{I}^{\mathrm{ML}}, \boldsymbol{x}_{\mathrm{d}}^{\mathrm{ML}}\right) = \underset{\mathcal{Z}_c\subset\mathcal{Z}, \boldsymbol{a}\in\mathcal{A}^k}{\arg\min} \left\{\|\boldsymbol{y} - \boldsymbol{\Phi}\boldsymbol{\Upsilon}_{\mathcal{Z}_c}\boldsymbol{a}\|_2^2\right\}, \tag{3.58}$$

where $\boldsymbol{\Upsilon}_{\mathcal{Z}_c}$ is a mapping matrix based on $\mathcal{Z}_c$. In order to detect the IM symbols and APM symbols at low computational cost, below we propose the GIRCD.

3.6.2 Generalised Iterative Residual Check Detector

The basic idea of the GIRCD is inspired by the principle of greedy algorithms [42, 71, 72, 74, 75], which provides an approximated estimate by making locally optimal choices at each step. Furthermore, similar to the approach presented in [148], the support estimation of our GIRCD is based on a reliability estimation scheme. Specifically, our GIRCD is divided into two stages, an initialisation stage and an iterative detection stage, as detailed below.

Firstly, at the initialisation stage, the GIRCD invokes the Minimum Mean Square Error (MMSE) processing to obtain a $\mathfrak{D}(\boldsymbol{x})$-dimensional soft estimate $\hat{\boldsymbol{x}}$ for $\boldsymbol{x}$ from the m-dimensional observations $\boldsymbol{y}$ seen in (3.55a), yielding

$$\hat{\boldsymbol{x}} = \left(\boldsymbol{\Phi}^H\boldsymbol{\Phi} + \frac{1}{\gamma_s}\boldsymbol{I}_{\mathfrak{D}(\boldsymbol{x})}\right)^{-1}\boldsymbol{\Phi}^H\boldsymbol{y}. \tag{3.59}$$

In principle, the active elements in $\boldsymbol{x}$ should generate relatively high magnitudes in $\hat{\boldsymbol{x}}$ with high probability. Therefore, similar to [148], we order the elements in $\hat{\boldsymbol{x}}$ in descending order according to their magnitudes as

$$|\hat{x}(i_1)|^2 \geq |\hat{x}(i_2)|^2 \geq \ldots \geq |\hat{x}(i_{\mathfrak{D}(\boldsymbol{x})})|^2, \tag{3.60}$$

which more or less reflects the reliabilities of the IM detection. Since the set $\{i_1, i_2, \ldots, i_{\mathfrak{D}(\boldsymbol{x})}\}$ contains k active indices and $(\mathfrak{D}(\boldsymbol{x})-k)$ inactive indices, the leftmost $\hat{x}_g(i_1)$ has the highest probability to be one of the active indices, while the rightmost $\hat{x}_g(i_{\mathfrak{D}(\boldsymbol{x})})$ has the highest probability to be one of the inactive indices. With the aid of this information, the IRCD then proceeds to the second stage, where both the IM and the classic APM symbols can be detected using the principle of greedy pursuits, as detailed next.

During the second stage, the GIRCD carries out iterative detection of both the IM symbols in $\mathcal{I}$ and the classic APM symbols in $\boldsymbol{x}_\text{d}$ by first identifying a candidate set, and then testing the candidates based on the likelihood principle of (3.57). In detail, during the first iteration, the GIRCD first derives a candidate set from the index i_1 of $\hat{x}_g(i_1)$, since it has the highest probability to be an active index. Let this candidate set be expressed as

$$\mathcal{Z}^1 = \{\mathcal{Z}_1^1, \mathcal{Z}_2^1, \ldots, \mathcal{Z}_{C_1}^1\} \subset \mathcal{Z} \tag{3.61}$$

where i_1 is a member of each of the candidates, i.e., we have $\bigcap_{c_1=1}^{C_1} \mathcal{Z}_{c_1}^1 = i_1$. Here, we can readily show that the number of candidates in $\mathcal{Z}^1$ of (3.61) obeys $C_1 \leq \binom{\mathfrak{D}(\boldsymbol{x})-1}{k-1} < C$, where $C = 2^{L_1}$ denotes the total number of subsets of $\mathcal{Z}$, as shown in Section 3.2.1. Then, based on the candidate $\mathcal{Z}_{c_1}^1$, which is treated as the *a priori* information for the following activated symbol detection, the corresponding local optimal results can be obtained with the aid of (3.55c) by solving the optimisation problem of

$$\breve{\boldsymbol{x}}_\text{d}(c_1) = \arg \min_{\boldsymbol{v} \in \mathbb{C}^{k\times 1}} \left\| \boldsymbol{y} - \boldsymbol{\Phi}_{\mathcal{Z}_{c_1}^1} \boldsymbol{v} \right\|_2^2. \tag{3.62}$$

Meanwhile, for notational brevity, we define the Moore-Penrose pseudoinverse matrix of

$$\boldsymbol{\Phi}_{\mathcal{Z}_{c_1}^1}^{\dagger} = \left(\boldsymbol{\Phi}_{\mathcal{Z}_{c_1}^1}^H \boldsymbol{\Phi}_{\mathcal{Z}_{c_1}^1}\right)^{-1} \boldsymbol{\Phi}_{\mathcal{Z}_{c_1}^1}^H, \quad \mathcal{Z}_{c_1}^1 \subset \mathcal{Z}^1 \subset \mathcal{Z}, \tag{3.63}$$

where $\boldsymbol{\Phi}_{\mathcal{Z}_{c_1}^1} = \boldsymbol{\Phi} \boldsymbol{\Upsilon}_{\mathcal{Z}_{c_1}}^1 \in \mathbb{C}^{m\times k}$ is of full column-rank when $k < m$, while $\boldsymbol{\Upsilon}_{\mathcal{Z}_{c_1}}^1$ is a $(\mathfrak{D}(\boldsymbol{x}) \times k)$-element mapping matrix formed based on $\mathcal{Z}_{c_1}^1$. By invoking the well-known OLS approach, the solution for the optimisation problem of (3.62) is given by

$$\begin{aligned}\breve{\boldsymbol{x}}_{\rm d}(c_1) =&\boldsymbol{\Phi}^{\dagger}_{\mathcal{Z}^1_{c_1}}\boldsymbol{y}\\ =&\boldsymbol{\Phi}^{\dagger}_{\mathcal{Z}^1_{c_1}}\boldsymbol{\Phi}_{\mathcal{I}}\boldsymbol{x}_{\rm d}+\boldsymbol{\Phi}^{\dagger}_{\mathcal{Z}^1_{c_1}}\bar{\boldsymbol{n}}\\ =&\boldsymbol{x}_{\rm d}+\boldsymbol{r}_{\mathcal{I},\mathcal{Z}^1_{c_1}}+\breve{\boldsymbol{n}}, \end{aligned}\tag{3.64}$$

where $\boldsymbol{r}_{\mathcal{I},\mathcal{Z}^1_{c_1}}$ is the potential residual interference caused by the indices in $\mathcal{I}$, but not included in $\mathcal{Z}^1_{c_1}$, i.e., $\mathcal{Z}^1_{c_1}\neq\mathcal{I}$. Otherwise, if $\mathcal{Z}^1_{c_1}=\mathcal{I}$, i.e., both $\mathcal{I}$ and $\mathcal{Z}^1_{c_1}$ contain the same set of indices representing a correct detection of the index symbols, then we have $\boldsymbol{r}_{\mathcal{I},\mathcal{Z}^1_{c_1}}=\boldsymbol{0}$. In (3.64), the noise vector $\breve{\boldsymbol{n}}=\boldsymbol{\Phi}^{\dagger}_{\mathcal{Z}^1_{c_1}}\bar{\boldsymbol{n}}\in\mathbb{C}^{k\times 1}$ is the linear combination of Gaussian noise samples, which is also a Gaussian noise vector. Based on (3.64), a simple symbol-by-symbol ML detection can be carried out, yielding

$$a^1(i,c_1)=\mathop{\arg\min}_{a_q\in\mathcal{A}_\phi}\left|\breve{x}_{\rm d}(i,c_1)-a_q\right|^2,\ i=0,\ldots,k-1.\tag{3.65}$$

So far, we have obtained the estimations of the classic APM symbols $\boldsymbol{a}^1(c_1)=[\boldsymbol{a}^1(0,c_1),\ldots,\boldsymbol{a}^1(k-1,c_1)]^T$ from the candidate set $\mathcal{Z}^1_{c_1}\in\mathcal{Z}^1$. Similarly, we can obtain the estimates of the classic APM symbols from the other candidates in $\mathcal{Z}^1$ of (3.61). Based on the estimates, let us define a set $\mathcal{A}^1=\{\boldsymbol{a}^1(1),\ldots,\boldsymbol{a}^1(C_1)\}\subset\mathcal{A}^k$ for all the possible APM symbols detected using the indices in $\mathcal{Z}^1$. Then, the best one among them after the first iteration can be found by solving the optimisation of

$$\left(\mathcal{I}^{[1]},\boldsymbol{x}_{\rm d}^{[1]}\right)=\mathop{\arg\min}_{\mathcal{Z}^1_{c_1}\in\mathcal{Z}^1,\boldsymbol{a}^1(c_1)\in\mathcal{A}^1}\left\|\boldsymbol{y}-\boldsymbol{\Phi}_{\mathcal{Z}^1_{c_1}}\boldsymbol{a}^1(c_1)\right\|^2.\tag{3.66}$$

Correspondingly, the residual error $\varepsilon^{[1]}$ is given by

$$\varepsilon^{[1]}=\left\|\boldsymbol{y}-\boldsymbol{\Phi}_{\mathcal{I}^{[1]}}\boldsymbol{x}_{\rm d}^{[1]}\right\|^2.\tag{3.67}$$

Let $\varepsilon_{\rm TS}$ be a threshold, which is used for terminating the search process, when the detection is believed to have achieved the required reliability. Then, if $\varepsilon_g^{[1]}\leq\varepsilon_{\rm TS}$, the search process is completed, and the results given in (3.66) are taken as the final estimates of the received IM and the classic APM symbols. Otherwise, the search process forwards to the next iteration.

Similarly to the first iteration, during the second iteration, the GIRCD first identifies a candidate set based on the index i_2 of the second largest in magnitude of the variables given in (3.60). It can be shown that the number of new candidates containing i_2 as a member satisfies $C_2\leq\binom{\mathfrak{D}(\boldsymbol{x})-1}{k-1}-\binom{\mathfrak{D}(\boldsymbol{x})-2}{k-2}=\binom{\mathfrak{D}(\boldsymbol{x})-2}{k-1}<C$, after excluding those having been considered in association with the candidates derived from index i_1. Having obtained the candidate set for the second iteration, the other processes are repeated in the same way as in the first iteration. In general, when

the GIRCD enters into the tth iteration, the number of new candidates including i_t as a member satisfies $C_t \leq \binom{\mathfrak{D}(\boldsymbol{x})-t}{k-1} < C$. Based on the above-mentioned method, when all the N indices are checked, we can readily show that $\sum_{t=1}^{\mathfrak{D}(\boldsymbol{x})} C_t = C = 2^{L_1}$. This implies that all the candidates in $\mathcal{Z} = \{\mathcal{Z}_1, \ldots \mathcal{Z}_C\}$ have been checked by the GIRCD.

Finally, if the condition of $\varepsilon^{[t]} \leq \varepsilon_{\mathrm{TS}}$ cannot be fulfilled after the maximum affordable number of iterations, the detection result giving the minimum number of residual errors is output. In summary, our proposed GIRCD can be stated as in Algorithm 3.

3.6.3 Complexity Analysis of GIRCD

Firstly, based on our analysis detailed in Section 3.4.4 and Section 3.5.4, we know that since the size of the search space is exponential in the blocklength of each code in $\mathcal{V}$, the complexity of the ML detection of each block either of the LPIM symbols or of the CSIM symbols is given by $\mathcal{O}(2^L)$, as shown either in (3.39) for the LPIM scheme or in (3.51) for the CSIM scheme. Secondly, for the proposed GIRCD shown in Algorithm 3, the complexity cost is determined by the number of iterations as well as the number of candidates in each iteration. Explicitly, the best case is that the detection is completed within a single iteration by testing only one candidate. In this case, we can readily show that the complexity is on the order of $\mathcal{O}_{\mathrm{GIRCD}}^{\mathrm{best}}(Qk)$. On the other hand, the worst case is that all the candidates in $\mathcal{Z}$ are checked. In this case, the corresponding complexity is given by $\mathcal{O}_{\mathrm{GIRCD}}^{\mathrm{worst}}(2^{L_1}Qk)$. Note that for $k > 1$ active indices, the probability that i_1 seen in (3.60) is not an active index is usually very small. Therefore, in most cases, our GIRCD requires a single iteration for testing the $C_1 \leq \binom{\mathfrak{D}(\boldsymbol{x})-1}{k-1} < C$ candidates, where $\mathfrak{D}(\boldsymbol{x})$ is a generalised notation defined in (3.56) either for the LPIM scheme or for the CSIM scheme. In this case, the detection complexity is given by $\mathcal{O}_{\mathrm{GIRCD}}^{\mathrm{usually}}(C_1Qk)$. In fact, our GIRCD can be constrained to simply carry out one or two iterations, as it will be shown in Section 3.7.

Specifically, for the CSIM scheme shown in Section 3.5, we shall point out here that there exists a tradeoff between the complexity cost and the maximum achievable rate. In detail, the maximum achievable rate of our CSIM codebook $\mathcal{V}_{\boldsymbol{A}}$ can be improved by increasing the virtual dimensional size N, as discussed in Section 3.5.2. However, the corresponding complexity cost for both the IM and APM symbols may be excessive, even for our GIRCD. We shall also note that the complexity of designing the precoding matrix $\boldsymbol{A}$ shown in Section 3.5.3 may too high for a large size of N. Thus, the virtual dimensional size N of our CSIM scheme should be carefully chosen

Algorithm 3 Generalised Iterative Residual Check Detector

```
Require: $\boldsymbol{y}$, $\boldsymbol{\Phi}$, $\gamma_s$, $\mathcal{Z}$, $\varepsilon_{\text{TS}}$
Initialization: Set the maximum number of iterations to $t_{\text{stop}}$, a check space of $\mathcal{Z}_{\text{check}} = \mathcal{Z}$, $\varepsilon_0 = \infty$, $\mathcal{I}^{\text{GIRCD}} = \emptyset$ and $\boldsymbol{x}_{\text{d}}^{\text{GIRCD}} = \emptyset$.
MMSE detection based on (3.59), expressed as
    $$\hat{\boldsymbol{x}} = \left(\boldsymbol{\Phi}^H\boldsymbol{\Phi} + \frac{1}{\gamma_s}\boldsymbol{I}_{\mathfrak{D}(\boldsymbol{x})}\right)^{-1}\boldsymbol{\Phi}^H\boldsymbol{y};$$
Order the elements in $\hat{\boldsymbol{x}}$ in descending order according to their magnitudes as
    $$|\hat{x}(i_1)|^2 \geq |\hat{x}(i_2)|^2 \geq \ldots \geq |\hat{x}(i_{\mathfrak{D}(\boldsymbol{x})})|^2.$$
for $t = 1$ to $t_{\text{stop}}$ do
    Obtain $\mathcal{Z}^t = \{\mathcal{Z}_1^t, \mathcal{Z}_2^t, \ldots, \mathcal{Z}_{C_t}^t\}$ from $\mathcal{Z}_{\text{check}}$, where $\bigcap_{c_t=1}^{C_t} \mathcal{Z}_{c_t}^t = i_t$;
    if $\mathcal{Z}^t = \emptyset$ then
    else
        For $c_t = 1, \ldots, C_t$, calculate
            $$\breve{\boldsymbol{x}}_{\text{d}}(c_t) = \boldsymbol{\Phi}_{\mathcal{Z}_{c_t}^t}^{\dagger}\boldsymbol{y};$$
        Generate the estimates for the APM symbols associated with the candidates of $c_t = 1, \ldots, C_t$ according to (3.65) as
            $$a^t(i, c_t) = \arg\min_{a_q \in \mathcal{A}} |\breve{x}_{\text{d},g}(i, c_t) - a_q|^2, \quad i = 0, 1, \ldots, k-1$$
        Find the best estimates according to (3.66) as
            $$\left(\mathcal{I}^{[t]}, \boldsymbol{x}_{\text{d}}^{[t]}\right) = \arg\min_{\mathcal{Z}_{c_t}^t \in \mathcal{Z}^t, \boldsymbol{a}^t(c_t) \in \mathcal{A}^t} \left\|\boldsymbol{y} - \boldsymbol{\Phi}_{\mathcal{Z}_{c_t}^t}\boldsymbol{a}^t(c_t)\right\|^2.$$
        Calculate the residual error according to (3.67) as
            $$\varepsilon^{[t]} = \left\|\boldsymbol{y} - \boldsymbol{\Phi}_{\mathcal{I}^{[t]}}\boldsymbol{x}_{\text{d}}^{[t]}\right\|^2;$$
        if $\varepsilon_g^{[t]} < \varepsilon_{\text{TS}}$ then
            Update $\mathcal{I}^{\text{GIRCD}} = \mathcal{I}^{[t]}$ and $\boldsymbol{x}_{\text{d}}^{\text{GIRCD}} = \boldsymbol{x}_{\text{d}}^{[t]}$.
            exit
        else if $\varepsilon_g^{[t]} < \varepsilon_0$ then
            Update $\mathcal{Z}_{\text{check}} = \mathcal{Z}_{\text{check}} \backslash \mathcal{Z}^t$, $\varepsilon_0 = \varepsilon^{[t]}$, $\mathcal{I}^{\text{GIRCD}} = \mathcal{I}^{[t]}$ and $\boldsymbol{x}_{\text{d}}^{\text{GIRCD}} = \boldsymbol{x}_{\text{d}}^{[t]}$.
        else
        end if
    end if
end for
return $\mathcal{I}^{\text{GIRCD}}$ and $\boldsymbol{x}_{\text{d}}^{\text{GIRCD}}$.
```

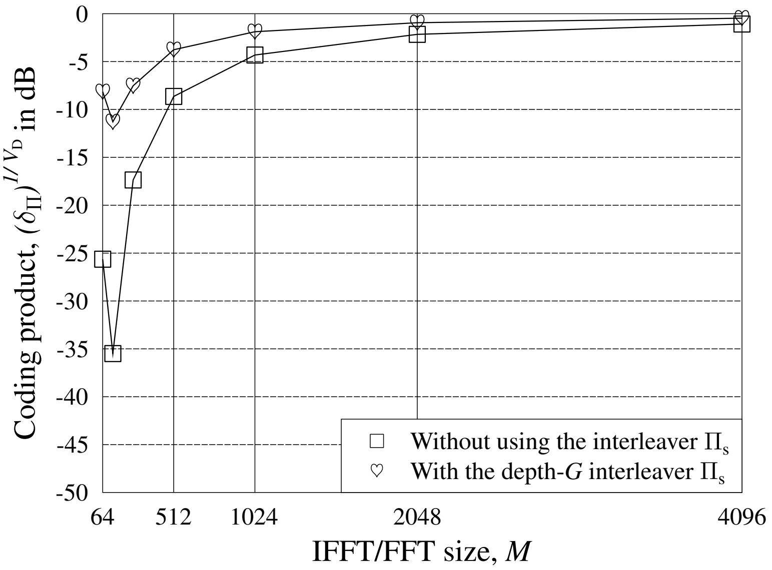

Figure 3.6: Coding product $(\delta_{\Pi}^{\rm C1})^{1/V_{\rm D}}$ versus the IFFT/FFT size M for the OFDM-LPIM system communicating over an $L_{\rm h} = 10$-path Rayleigh fading channel. The depth-G interleaver $\Pi_{\rm s}$ is configured to use $G = 16$. The coding product $(\delta_{\Pi}^{\rm C1})^{1/V_{\rm D}}$ is obtained according to (3.38).

from the feasibility point of view.

3.7 Performance Results

In this section, simulation results are provided for characterising the achievable performance of the proposed LPIM, CSIM, as well as GIRCD. For all simulations, a ten-path (i.e. $L_{\rm h} = 10$) slow-varying Rayleigh fading channel is considered, which is based on Section 3.2.2. We assume an OFDM system employing $M = 256$ subcarriers and a CP of length of $L_{\rm cp} = 16$. The measurement matrix $\boldsymbol{A}$ is designed based on (3.50) for our CSIM scheme. Furthermore, the depth-G interleaver given in Section 3.4.3 is employed. The analytical results of the diversity gain and the coding gain of both the LPIM codebook and the CSIM codebook are summarised in Table 3.1 and Table 3.2, respectively.

3.7.1 Performance Results of the LPIM Scheme

In Fig. 3.6-3.8, the performance of the OFDM-LPIM system employing the depth-G interleaver is investigated, when communicating over multipath Rayleigh fading channels. In these figures, the depth-G interleaver $\Pi_{\rm s}$ is designed based on the

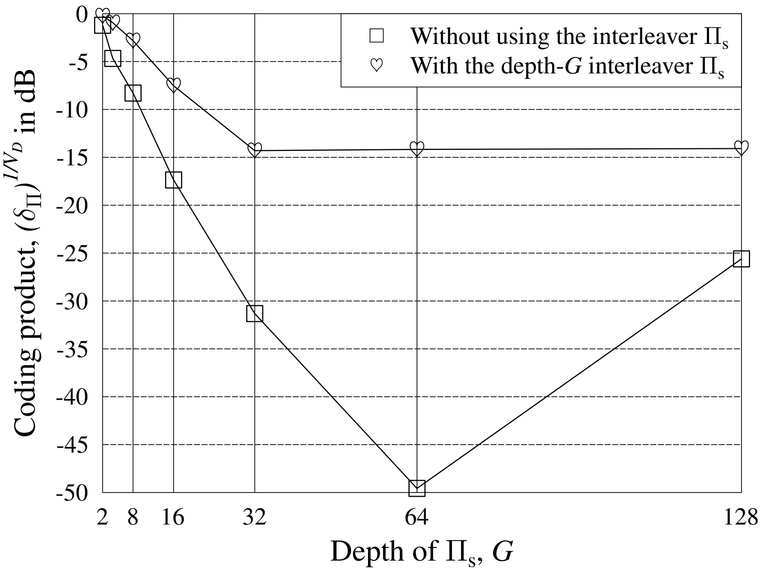

Figure 3.7: Coding product $(\delta_{\Pi}^{\mathrm{C1}})^{1/V_{\mathrm{D}}}$ versus the depth G of the interleaver Π_{s} for the OFDM-LPIM system employing $M = 256$ subcarriers, when communicating over an $L_{\mathrm{h}} = 10$-path Rayleigh fading channel. The coding product $(\delta_{\Pi}^{\mathrm{C1}})^{1/V_{\mathrm{D}}}$ is obtained according to (3.38).

scheme shown in Section 3.4.3. Moreover, the corresponding coding product denoted as $(\delta_{\Pi}^{\mathrm{C1}})^{1/V_{\mathrm{D}}}$ is calculated according to (3.38), which is shown to be dependent on the parameters of M, G and L_{h}. Specifically, the full diversity code is assumed in Fig. 3.6-3.8, where we have $V_{\mathrm{D}} = m = M/G$. Hence, in each figure, the effect of each parameter on the coding product of (3.38) is evaluated by keeping all other parameters fixed. Based on the performance results shown in Fig. 3.6-3.8, we have the following observations.

Firstly, we can observe from Fig. 3.6-3.8 that the OFDM-LPIM system employing the depth-G interleaver Π_{s} always achieves a higher coding gain than the system without using the interleaver Π_{s}. Secondly, as shown in Fig. 3.6, for the parameters G, L_{h} and $M > 64$, the higher the IFFT/FFT size, the larger the coding gain of the OFDM-LPIM system becomes. However, it should be noted that the increased coding gain is achieved at the cost of an increased complexity. Thirdly, observe from Fig. 3.7 that when the parameters M and L_{h} are fixed, increasing the depth of the interleaver Π_{s} leads to a reduction of the coding gain that can be achieved by the OFDM-LPIM system. As indicated in Fig. 3.4, we can show that when the depth G of the interleaver Π_{s} is low, the minimum distance of any two symbols after interleaving is large, yielding a high coding gain. For example, the minimum distance of any two symbols after interleaving is 2 for the case of $G = 4$ given in Fig. 3.4.

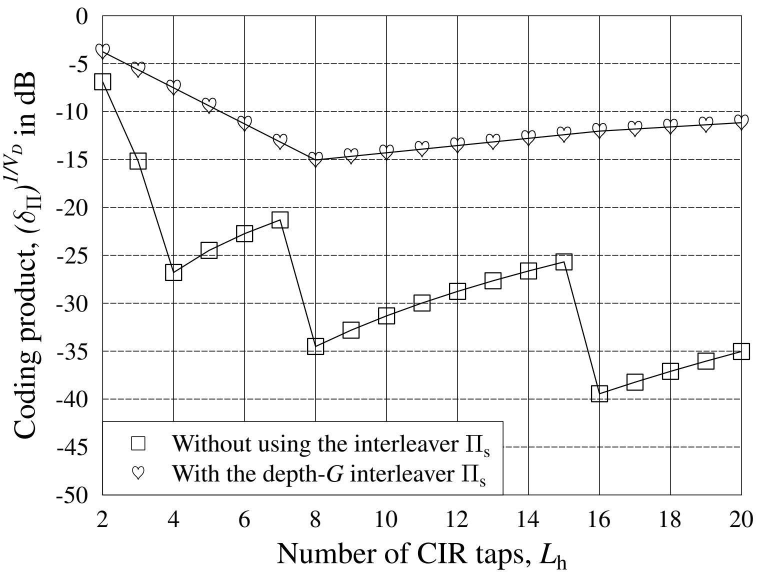

Figure 3.8: Coding product $(\delta_{\Pi}^{C1})^{1/V_D}$ versus the number of CIR taps L_h of the Rayleigh fading channel for the OFDM-LPIM system employing $M = 256$ subcarriers. The depth-G interleaver Π_s is configured to use $G = 16$. The coding product $(\delta_{\Pi}^{C1})^{1/V_D}$ is obtained according to (3.38).

When the depth G of Fig. 3.4 is reduced to 2, the corresponding output is given by $\{1, 5, 2, 6, 3, 7, 4, 8\}$, yielding a minimum distance of 3. The corresponding drawback is the resultant high complexity of both the precoding and detection processes, since the corresponding number of subcarriers of each group is large. Finally, as seen in Fig. 3.8, in comparison to the OFDM-LPIM system operating without an interleaver Π_s, the coding gain of the system employing the depth-G interleaver Π_s is relative stable. Based on the above observations, we may conclude that in order to strike a tradeoff between the coding gain and the complexity, moderate values of M and G are preferred.

The BER performance of the classic OFDM, of the conventional OFDM-SIM and of our OFDM-LPIM system is compared in Fig. 3.9-3.11. In these figures, all systems employ $M = 256$ subcarriers, which are detected by the ML detector of Section 3.3.1. Specifically, only the OFDM-LPIM system employs the depth-G interleaver Π_s. The related parameters and the analytical results of both the OFDM-SIM and the OFDM-LPIM systems are summarised in Table 3.1. Note that the corresponding analytical results are obtained based upon substituting the results of (3.36) and (3.38) into (3.23). The LPIM codebook is designed based on Section 3.4.2. Based on the simulation results of Fig. 3.9-3.11, we can infer the following observations. Firstly, for a given maximum achievable rate, our proposed LPIM scheme significantly outperforms

Table 3.1: The Analytical Results of the LPIM Codebooks

Rate $R_{\mathcal{V}_U}$ in bits/s/Hz	Codebook Parameters (m, k, Q)	Diversity Gain	Coding Gain in dB
0.625	$(8, 1, 4)$	8	-23.3255
	$(16, 2, 4)$	16	-19.5664
1.0	$(4, 1, 4)$	4	-20.1916
	$(8, 2, 4)$	8	-23.3298
1.5	$(4, 1, 16)$	4	-27.1813
	$(4, 2, 4)$	4	-20.1916
	$(8, 2, 16)$	8	-30.3195

both the classic OFDM and the conventional SIM scheme, when communicating over multipath fading channels. This observation can be explained with the aid of our analysis discussed in Section 3.3.3. We can readily show that the diversity order of both the classic OFDM and the conventional OFDM-SIM systems is 1, while our OFDM-LPIM system achieves the maximum attainable diversity order due to Proposition 1 of Section 3.4.2. Moreover, the coding gain achieved by our OFDM-LPIM system employing the depth-G interleaver is also much higher than that attained by both the classic OFDM and the conventional OFDM-SIM systems. Thus, a much higher performance gain can be attained by our OFDM-LPIM system. Secondly, we can observe from Fig. 3.9-3.11 that for a given maximum achievable rate, the higher the diversity order of the LPIM codebook, the better the BER performance of the system. For example, as shown in Fig. 3.6, the diversity order of the LPIM scheme associated with $m = 16$ is given by $V_{\mathrm{D}} = \min\{m, L_{\mathrm{h}}\} = L_{\mathrm{h}} = 10$, while the diversity order of the LPIM scheme using $m = 8$ is $V_{\mathrm{D}} = \min\{m, L_{\mathrm{h}}\} = m = 8$. Furthermore, recalling the results of Fig. 3.7, we can see that the coding gain achieved by the interleaver Π_{s} associated with $G = M/m = 256/16 = 16$ is higher than that achieved with $G = M/m = 256/8 = 32$. Thus, the LPIM having a higher diversity order achieves a better BER performance. Finally, as shown in Fig. 3.11, when the achievable rate and the diversity order are fixed, the lower the constellation size of the activated symbols, the better the BER performance becomes. This is because a low constellation size exhibits a high minimum distance for the codebook. In this case, the corresponding squared MPD $\delta_{\mathcal{E}}^{\mathrm{C1}}$ shown in (3.36) is high. This can be readily verified by our analytical results of the coding gain shown in Table 3.1, where

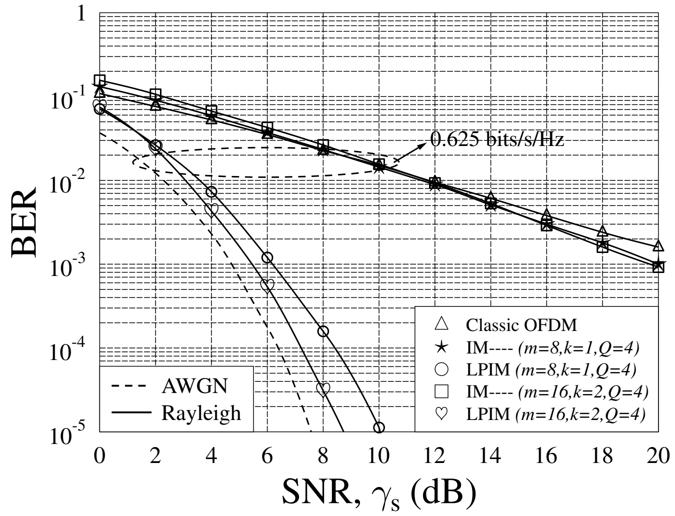

Figure 3.9: BER performance of the classic OFDM, of the conventional OFDM-IM and of our OFDM-LPIM systems employing $M = 256$ subcarriers and ML detection, when communicating over an $L_{\mathrm{h}} = 10$-path Rayleigh fading channel. The OFDM-LPIM system uses the depth-G interleaver, while the OFDM-IM system does not employ the interleaver Π_{s}. The maximum achievable rate is constraint to be 0.625 bits/s/Hz for all systems.

for a given maximum achievable rate of 1.5 bits/s/Hz, the coding gain of the LPIM associated with $(m = 4, k = 2, Q = 4)$ is about 6.5 dB higher than that of the LPIM using $(m = 4, k = 1, Q = 16)$. As a result, the coding gain of the codebook obtained from (3.23) is high, hence yielding a good BER performance.

Fig. 3.12 plots the maximum achievable rate $R_{\mathcal{V}_U}$ versus the diversity order V_{D} of the proposed codebook $\mathcal{V}_U$. In this figure, the IM schemes associated with $m = V_{\mathrm{D}}$, $k = 1, 2$ and $Q = 4, 16, 64$ are employed. Observe from Fig. 3.12 that as expected, when the diversity order achieved by our proposed LPIM codebook increases, the maximum achievable rate is reduced. This observation follows the well-known diversity-multiplexing tradeoff of conventional MIMO systems. Next, as seen in Fig. 3.12, for codebooks associated with the same value of k, the larger the constellation size Q, the better the tradeoff between the diversity order and the maximum achievable rate becomes. Moreover, when the constellation size Q is fixed, increasing the number of activated indices in each group (i.e., increasing the value of k) yields an improved tradeoff between the diversity order and the maximum achievable rate.

Finally, in Fig. 3.13 and Fig. 3.14, we investigate the performance of the proposed OFDM-LPIM system employing the depth-G interleaver Π_{s}. The related parameters

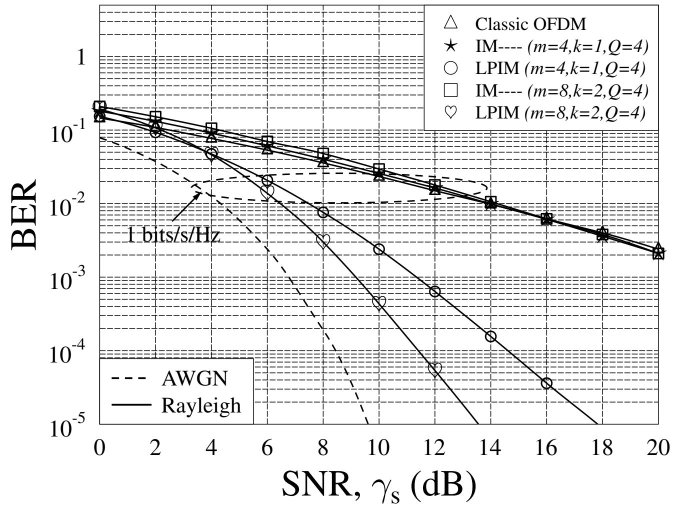

Figure 3.10: BER performance of the classic OFDM, of the conventional OFDM-IM and of our OFDM-LPIM system employing $M = 256$ subcarriers and ML detection, when communicating over an $L_{\mathrm{h}} = 10$-path Rayleigh fading channel. The OFDM-LPIM system uses the depth-G interleaver, while the OFDM-IM system does not employ the interleaver Π_{s}. The maximum achievable rate is constraint to be 1 bits/s/Hz for all systems.

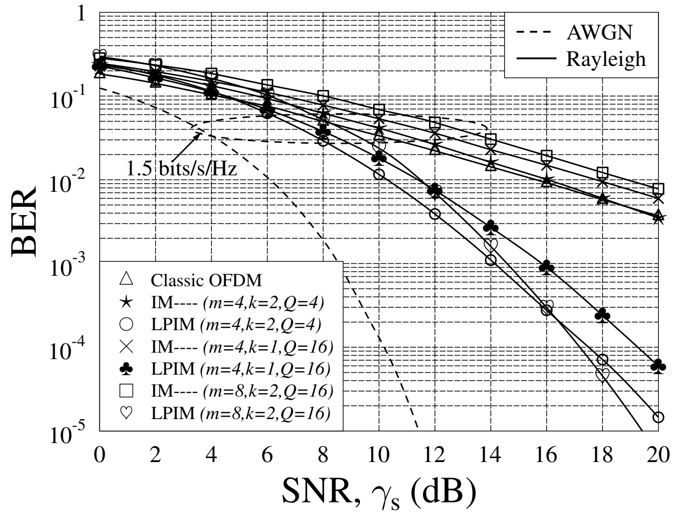

Figure 3.11: BER performance of the classic OFDM, of the conventional OFDM-IM and of our OFDM-LPIM systems employing $M = 256$ subcarrier and ML detection, when communicating over an $L_{\mathrm{h}} = 10$-path Rayleigh fading channel. The OFDM-LPIM system uses the depth-G interleaver, while the OFDM-IM system does not employ the interleaver Π_{s}. The maximum achievable rate is constraint to be 1.5 bits/s/Hz for all systems.

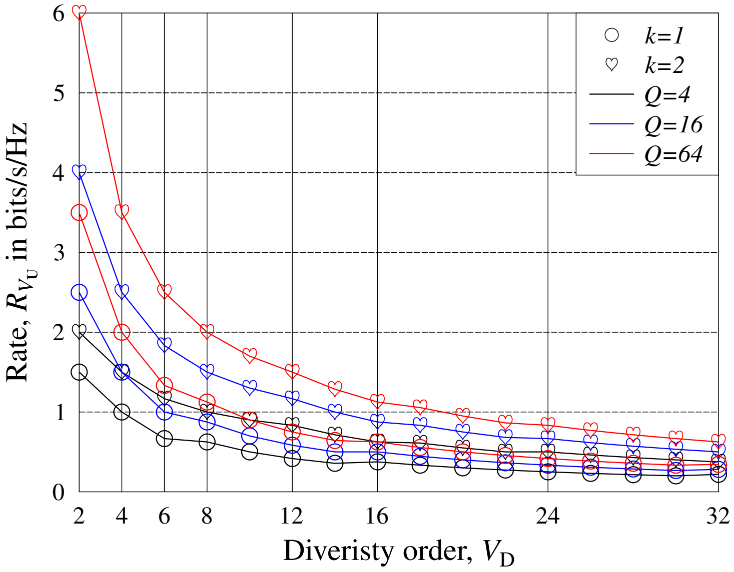

Figure 3.12: The rate $R_{\mathcal{V}_{\boldsymbol{U}}}$ versus diversity order V_D of the proposed codebook $\mathcal{V}_{\boldsymbol{U}}$. The IM schemes associated with $m = V_\mathrm{D}$, $k = 1, 2$ and $Q = 4, 16, 64$ are employed. The maximum achievable rate $R_{\mathcal{V}_{\boldsymbol{U}}}$ is obtained according to (3.33).

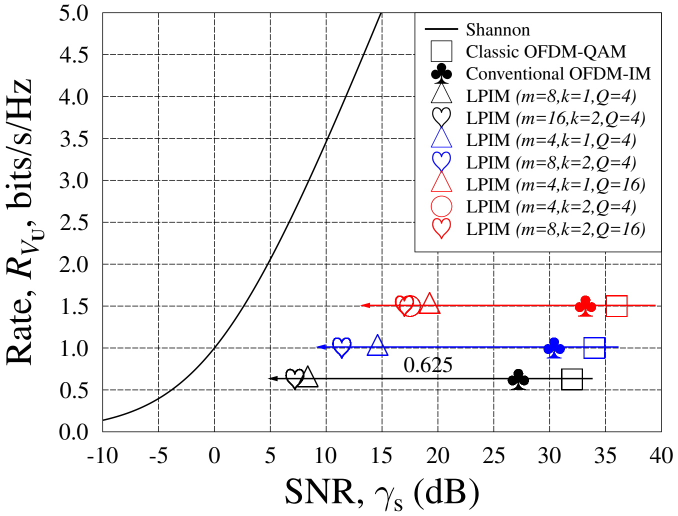

Figure 3.13: The rate $R_{\mathcal{V}_{\boldsymbol{U}}}$ versus SNR per symbol γ_s at the BER of 10^{-4} for the OFDM-LPIM systems employing the depth-G interleaver Π_s, when communicating over an $L_\mathrm{h} = 10$-path Rayleigh fading channel. The system parameters are given in Table 3.1, where the maximum achievable rate $R_{\mathcal{V}_{\boldsymbol{U}}}$ is obtained according to (3.33).

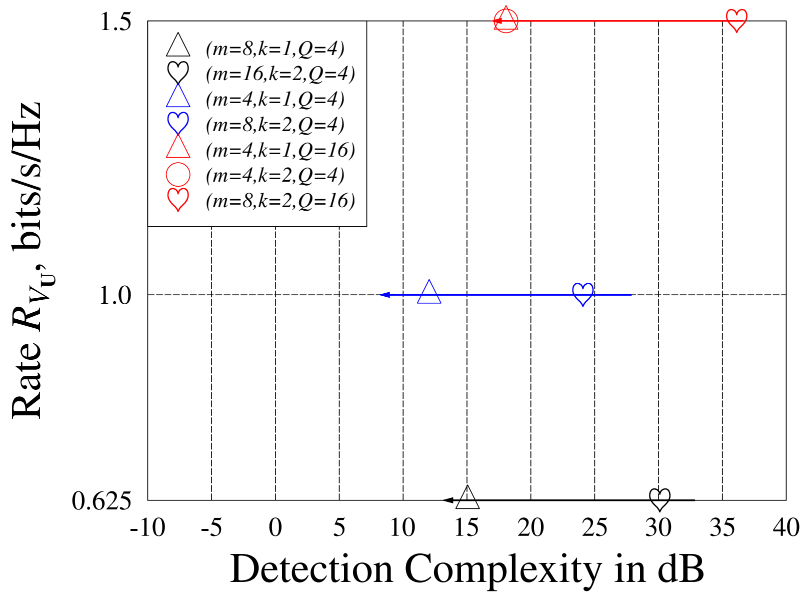

Figure 3.14: Detection Complexity versus rate $R_{\mathcal{V}_U}$ for the OFDM-LPIM systems employing the depth-G interleaver Π_s, when communicating over an $L_h = 10$-path Rayleigh fading channel. The system parameters are given in Table 3.1, where the maximum achievable rate $R_{\mathcal{V}_U}$ is obtained according to (3.33).

are given in Table 3.1. In Fig. 3.13, the SNR per symbol γ_s at the BER of 10^{-4} required for the OFDM-LPIM system communicating over an $L_h = 10$-path Rayleigh fading channel is plotted. Based on our previous study, we can now show that in order to attain a performance that is closer to Shannon capacity, the parameters of our proposed LPIM scheme should be chosen based on Fig. 3.9-3.11. However, as shown in Fig. 3.14, the corresponding price to pay is the associated complexity cost. In particular, we are interested in observing from Fig. 3.13 that our LPIM codebook associated with $(m = 4, k = 2, Q = 4)$ performs closer to the Shannon capacity than the one using $(m = 4, k = 1, Q = 16)$, when the same maximum achievable rate $R_{\mathcal{V}_U} = 1.5$ bits/s/Hz and the same complexity cost shown in Fig. 3.14. Thus, we may conclude that the optimal parameters of our proposed LPIM codebook should be chosen to strike a tradeoff between the distance from the Shannon capacity and the complexity cost.

3.7.2 Performance Results of the CSIM Scheme

In Fig. 3.15, both the SE and EE are investigated as a function of the SNR in dB for both the OFDM-SIM and the OFDM-CSIM systems, when communicating over Rayleigh fading channels. In this figure, the depth-G interleaver are not employed.

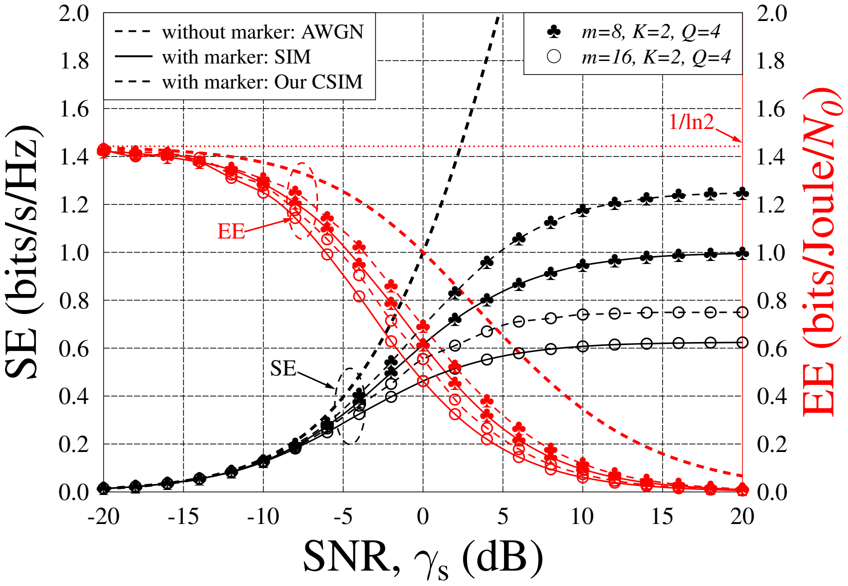

Figure 3.15: SE and EE as a function of the SNR in dB for both the OFDM-SIM and the OFDM-CSIM systems communicating over an $L_\mathrm{h} = 10$-path Rayleigh fading channel. The system parameters are given in Table 3.2

Furthermore, both the OFDM-SIM and the OFDM-CSIM systems employ the ML detector of Section 3.3.1 for the sake of comparison. Firstly, we observe from Fig. 3.15 that the achievable SE of the proposed CSIM scheme is higher than that of the conventional SIM scheme. This observation can be explained with the aid of the analytical results of (3.33) and (3.42). Explicitly, when the value of m is fixed, the achievable SE of both the SIM and the CSIM schemes depend on the number of data bits L transmitted by each group. Furthermore, when the values of k and Q are fixed, more data bits can be transmitted by the CSIM associated with $N > m$ than by the SIM using $N = m$, as exemplified in Section 3.5.2. Thus, the attainable SE of the CSIM is higher than that of the conventional SIM. Moreover, we can also show that the corresponding SE is reduced both for the CSIM and for the SIM, as the

Table 3.2: The Analytical Results of the CSIM Codebooks

Rate $R_{\mathcal{V}_A}$ in bits/s/Hz	Codebook Parameters (m, N, k, Q)	Diversity Gain	Coding Gain in dB
1.5	$(4, 16, 1, 4)$	4	-26.8739
2.0	$(4, 16, 1, 16)$	4	-33.8636
2.5	$(4, 16, 1, 64)$	4	-47.5681

value of m is increased. Secondly, as seen in Fig. 3.15, for a given SNR, our proposed CSIM scheme is capable of achieving a higher EE than the conventional SIM scheme. Meanwhile, the SE of our CSIM scheme is also higher than that of the conventional SIM scheme. In other words, our proposed CSIM scheme is capable of striking a more appealing tradeoff between the SE and EE than the conventional SIM scheme. This observation can be explained with the aid of the analytical results of (3.13) and the numerical SE results shown in this figure. As observed in Fig. 3.15, for a given SE, the SNR required by our CSIM scheme is lower than that of the SIM scheme. Since the EE defined by (3.13) is inversely proportional to the SNR for a given SE, the EE of our CSIM is in turn higher than that of the conventional SIM. Thirdly, as shown in Fig. 3.15, the maximum EE that can be attained by both schemes is about $1/\ln 2 \approx 1.4427$. This result inferred from (3.14) represents the minimum energy per bit required for reliable communication, which is given by $\gamma_{b,\min}^{\mathrm{Rx}} = \ln 2$. This confirms the analytical result given in [149]. As demonstrated in [149], when the SNR is low, the minimum energy per bit required for reliable communication is $\ln 2$, which is independent of the fading. Hence, for OFDM systems having a fixed transmission power, bandwidth and IFFT/FFT size, our proposed CSIM scheme is capable of striking a more appealing tradeoff between the SE and EE than the conventional SIM scheme.

The BER performance of the classic OFDM, OFDM-SIM and OFDM-CSIM systems is compared in Fig. 3.16-3.18. In these figures, the OFDM-CSIM systems employ the depth-G interleaver as well as ML detectors. Explicitly, both the parameters and analytical results of the OFDM-CSIM systems are summarised in Table 3.2. Note that the corresponding analytical results are obtained upon substituting the related results into (3.23). For the sake of comparison, some of the FD subcarriers are disabled for data transmission in both the classic OFDM and the conventional OFDM-SIM systems, so that the same transmission rate can be met. Here, we should point out that reducing the number of active subcarriers results in a certain power gain reduction, rather than in a BER curve slope-change. We can observe from these figures that the OFDM-CSIM significantly outperforms both the classic OFDM and the OFDM-SIM. Furthermore, in the high-SNR region, the gradient of the BER curves of the OFDM-CSIM systems are almost the same. This observation confirms our analytical results concerning the diversity gain shown in Table 3.2, where the same diversity gain is achieved by our CSIM schemes in Fig. 3.16-3.18.

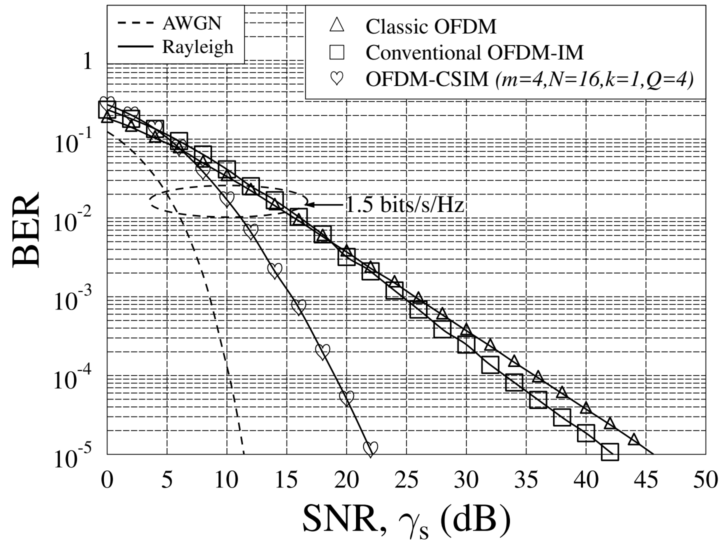

Figure 3.16: BER performance of the classic OFDM, OFDM-SIM, OFDM-LPIM and OFDM-CSIM systems communicating over an $L_{\mathrm{h}} = 10$-path Rayleigh fading channel. Both the OFDM-LPIM and the OFDM-CSIM systems employ a depth-G interleaver as well as ML detectors. The maximum achievable rate is constraint to be 1.5 bits/s/Hz for all systems.

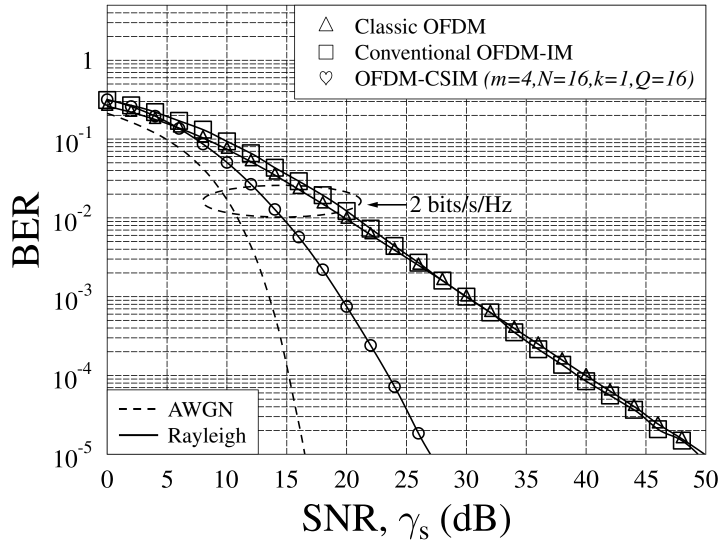

Figure 3.17: BER performance of the classic OFDM, OFDM-SIM and OFDM-CSIM systems communicating over an $L_{\mathrm{h}} = 10$-path Rayleigh fading channel. The OFDM-CSIM systems employ a depth-G interleaver as well as ML detectors. The maximum achievable rate is constraint to be 2 bits/s/Hz for all systems.

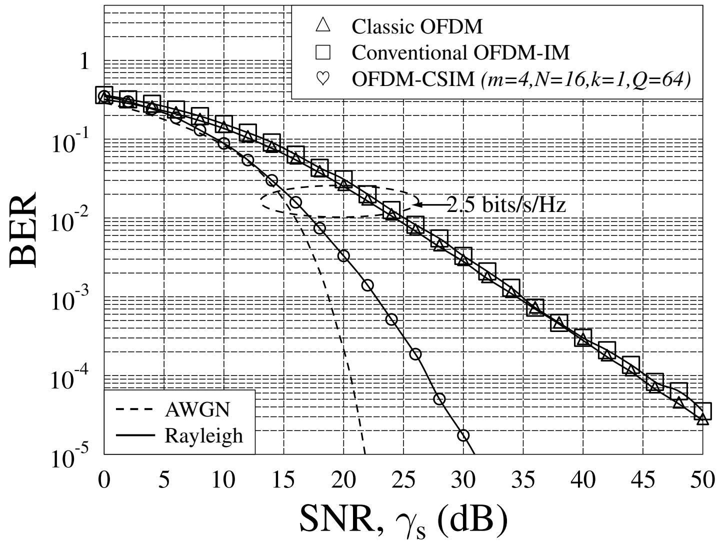

Figure 3.18: BER performance of the classic OFDM, OFDM-SIM and OFDM-CSIM systems communicating over an $L_{\rm h} = 10$-path Rayleigh fading channel. The OFDM-CSIM systems employ a depth-G interleaver as well as ML detectors. The maximum achievable rate is constraint to be 2.5 bits/s/Hz for all systems.

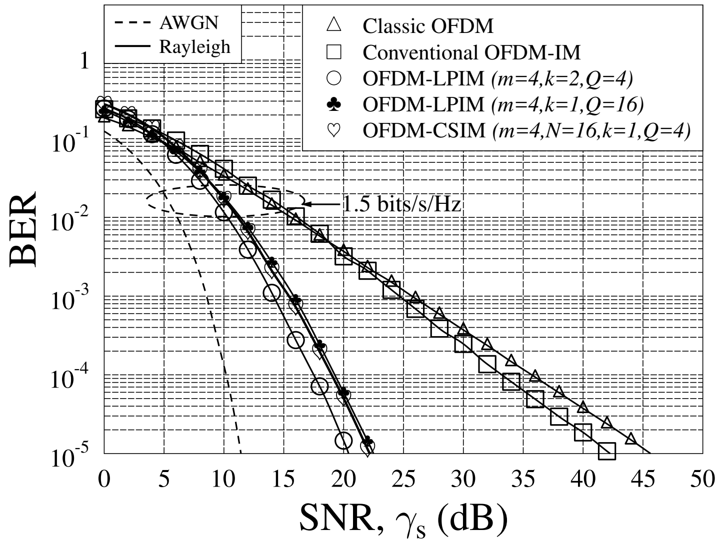

Figure 3.19: BER performance of OFDM-LPIM and OFDM-CSIM systems communicating over an $L_{\rm h} = 10$-path Rayleigh fading channel. Both the OFDM-LPIM and the OFDM-CSIM systems employ a depth-G interleaver as well as ML detectors. The maximum achievable rate is constraint to be 1.5 bits/s/Hz for all systems.

The BER performance of the OFDM-LPIM and OFDM-CSIM systems is compared in Fig. 3.19. In this figure, both the OFDM-LPIM and the OFDM-CSIM systems employ the depth-G interleaver as well as ML detectors. Explicitly, the parameters of the OFDM-LPIM system and of the OFDM-CSIM system are summarised inTable 3.1 and Table 3.2, respectively. For the sake of comparison, the codebook rate is set to 1.5 bits/s/Hz for both schemes. We can observe from Fig. 3.19 that when the same diversity gain is achieved by both the LPIM and the CSIM schemes, the BER performance of the CSIM scheme becomes slightly better than that of the LPIM scheme. Furthermore, we can also infer from (3.39) and (3.51) that the complexity of these two schemes is the same. Although Fig. 3.19 shows that the LPIM scheme associated with $(m = 4, k = 2, Q = 4)$ outperforms the CSIM scheme at the same maximum achievable rate, the corresponding complexity is high, as shown in Fig. 3.14. Therefore, the CSIM scheme is capable of striking a tradeoff between the complexity and the BER performance, when the ML detector is employed for a high-rate scenario.

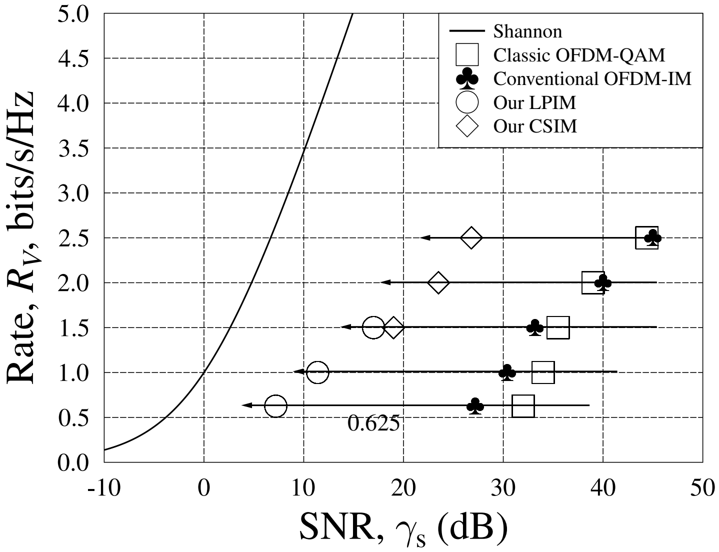

Figure 3.20: Maximum achievable rate $R_{\mathcal{V}}$ versus SNR per symbol γ_s at the BER of 10^{-4} for both the OFDM-LPIM and OFDM-CSIM systems employing the depth-G interleaver Π_s, when communicating over an $L_h = 10$-path Rayleigh fading channel. The system parameters are given in Table 3.2 and Table 3.1. The maximum achievable rate of both the systems are obtained based on (3.33) and (3.42).

Finally, in Fig. 3.20 and Fig. 3.21, the performance of the OFDM-CSIM system employing the depth-G interleaver Π_s is investigated. In these figures, the related parameters and analytical results are given in Table 3.2. Fig. 3.20 plots the SNR per symbol γ_s at the BER of 10^{-4} for both the OFDM-LPIM and the OFDM-CSIM systems communicating over an $L_h = 10$-path Rayleigh fading channel. As shown in

Fig. 3.20, both the LPIM and CSIM schemes are capable of attaining a performance that is closer to the Shannon capacity in comparison to both the classic OFDM and the conventional OFDM-SIM. Moreover, we can observe from Fig. 3.21 that our CSIM scheme is capable of achieving a high maximum rate at a relatively low complexity, even for a high constellation size and for ML detection. Therefore, we can now show that when a low maximum rate is required, such as $R_{\mathcal{V}} \leq 1$, the OFDM-LPIM system using the ML detector can be employed to attain a good BER performance. By contrast, for a high maximum rate, the OFDM-CSIM system using ML detection can be employed to strike a tradeoff between the BER performance attained and the complexity imposed.

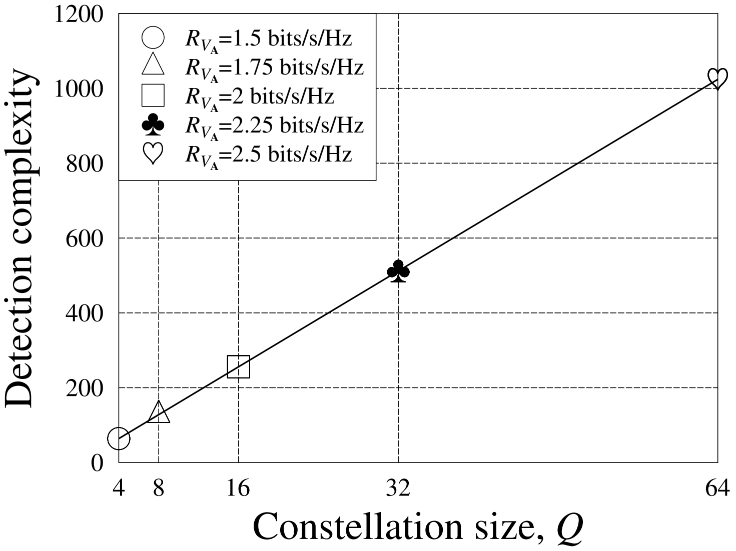

Figure 3.21: Detection complexity versus constellation size Q for the OFDM-CSIM systems employing the depth-G interleaver Π_{s}, when communicating over an $L_{\text{h}} =$ 10-path Rayleigh fading channel. The system parameters are given in Table 3.2. The complexity of the ML detector is calculated according to (3.51)

3.7.3 Performance Results of the GIRCD

Table 3.3: Simulation Results of System Complexity at 1.5 bits/s/Hz

Codebook $\mathcal{V}$	Parameters (m, N, k, Q)	Complexity order of JMLD in dB	Complexity order of GIRCD in dB
LPIM $\mathcal{V}_{\boldsymbol{U}}$	$(4, 4, 2, 4)$	18.0618	12.1761
CSIM $\mathcal{V}_{\boldsymbol{A}}$	$(4, 16, 1, 4)$	18.0618	7.5257

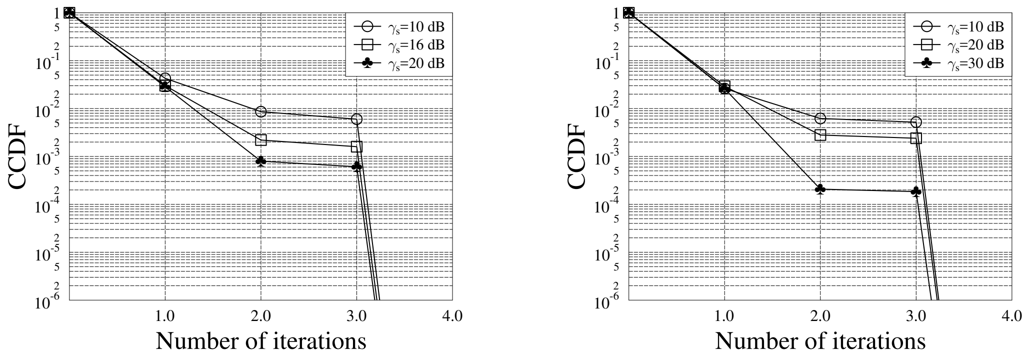

(a) (b)

Figure 3.22: CCDF of the number of iterations of the GIRCD for the LPIM employing the depth-G interleaver and operating at (a) $R_{\mathcal{V}_{\boldsymbol{U}}} = 1.5$ bits/s/Hz and $\gamma_s = 10$ dB, 16 dB or 20 dB; (b) $R_{\mathcal{V}_{\boldsymbol{U}}} = 2.5$ bits/s/Hz and $\gamma_s = 10$ dB, 20 dB or 30 dB, when communicating over an $L_{\mathrm{h}} = 10$-path Rayleigh fading channel. The rate $R_{\mathcal{V}_{\boldsymbol{U}}}$ is obtained based on (3.33).

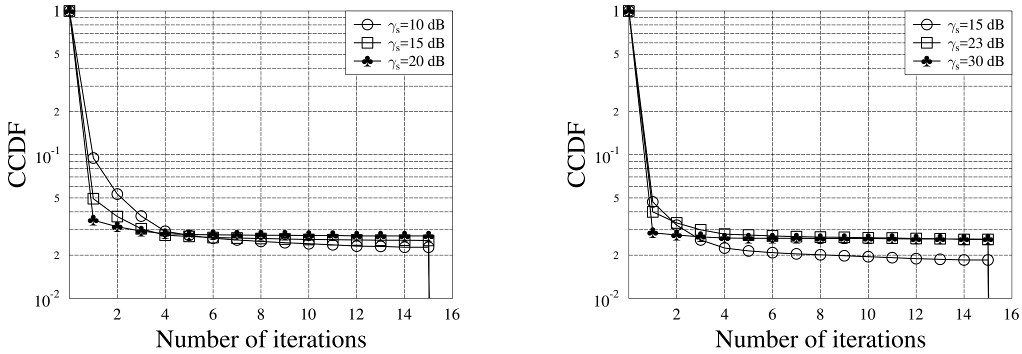

(a) (b)

Figure 3.23: CCDF of the number of iterations of the GIRCD for the CSIM employing the depth-G interleaver and operating at (a) $R_{\mathcal{V}_{\boldsymbol{A}}} = 1.5$ bits/s/Hz and $\gamma_s = 10$ dB, 15 dB or 20 dB; (b) $R_{\mathcal{V}_{\boldsymbol{A}}} = 2.5$ bits/s/Hz and $\gamma_s = 15$ dB, 23 dB or 30 dB, when communicating over an $L_{\mathrm{h}} = 10$-path Rayleigh fading channel. The rate $R_{\mathcal{V}_{\boldsymbol{A}}}$ is calculated according to (3.42).

Fig. 3.22 and Fig. 3.23 respectively plot the Complementary Cumulative Distribution Function (CCDF) of the number of iterations in the proposed GIRCD for both the OFDM-LPIM and OFDM-CSIM systems employing the depth-G interleaver, when communicating over an $L_{\mathrm{h}} = 10$-path Rayleigh fading channel. Generally, the CCDF represents the probability that a random variable X will take a value higher than x, i.e. we have $\mathrm{CCDF}_X(x) \triangleq P(X > x)$. As shown in Fig. 3.22 and Fig. 3.23, the CCDF curves first exhibit a sharp decay and then become flat as the number of iterations increases. This observation implies that with a near-unity probability, the GIRCD completes the detection in just a single iteration. Furthermore, when just a single iteration is considered, the difference of the probabilities for a given LPIM or CSIM operating at different SNR per bit values is unnoticeable. Thus, it can be inferred that the performance of the GIRCD using a single iteration is stable at all SNR per bit values. Finally, we can also see that as the EE of the CSIM system increases, the probability of completing the detection process is increased only by one or two iterations. It should be noted that the complexity of our GIRCD is dependent on the number of iterations actually invoked, rather than on the maximum number of iterations t_{stop}, as analysed in Section 3.6.3. Thus, our GIRCD can be deemed to be an efficient detector, since it usually terminates after a single or two iterations.

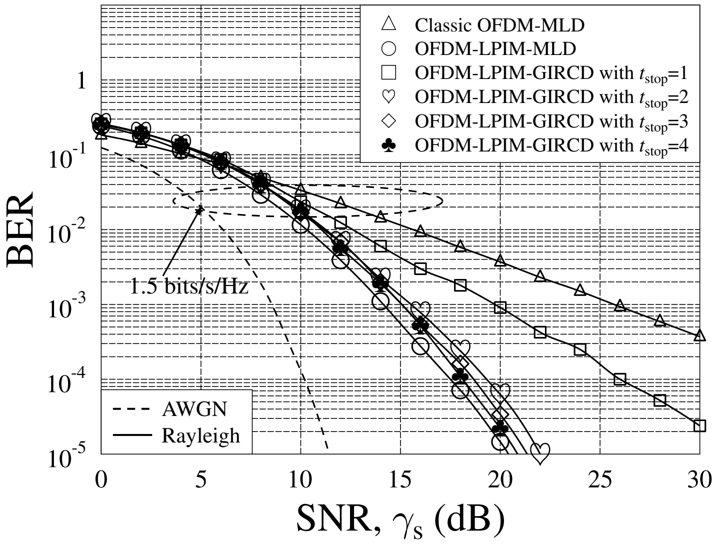

Figure 3.24: BER versus SNR for the OFDM-LPIM using the JMLD and the GIRCD. The OFDM-LPIM system employs the depth-G interleaver and operates at 1.5 bits/s/Hz. For the GIRCD shown in Algorithm 3, the maximum number of iterations is chosen to be $t_{\text{stop}} = 1$, 2, 3 or 4. The maximum achievable rate is constraint to be 1.5 bits/s/Hz for all systems.

In Fig. 3.24-3.27, we investigate the BER performance of both the Joint Maximum-Likelihood Detector (JMLD) and the GIRCD designed for the OFDM-LPIM and OFDM-CSIM systems employing the depth-G interleaver, when communicating over an $L_{\text{h}} = 10$-path Rayleigh fading channel. Specifically, the OFDM-LPIM systems are characterised by $(m = 4, k = 2, Q = 4)$ for $R_{\mathcal{V}_U} = 1.5$ bits/s/Hz and by $(m = 4, k = 2, Q = 16)$ for $R_{\mathcal{V}_U} = 2.5$ bits/s/Hz in Fig. 3.24 and Fig. 3.25, respec-

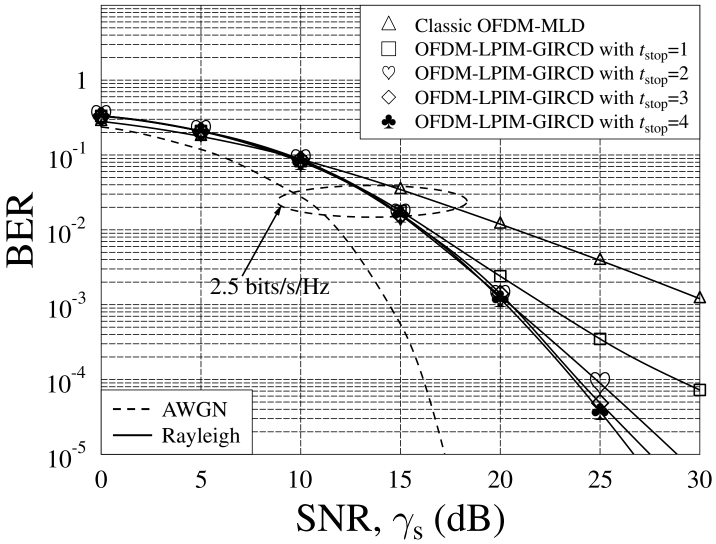

Figure 3.25: BER versus SNR for the OFDM-LPIM using the JMLD and the GIRCD. The OFDM-LPIM system employs the depth-G interleaver and operates at 2.5 bits/s/Hz. For the GIRCD shown in Algorithm 3, the maximum number of iterations is chosen to be $t_{\text{stop}} = 1$, 2, 3 or 4. The maximum achievable rate is constraint to be 2.5 bits/s/Hz for all systems.

tively. Furthermore, the parameters of the OFDM-CSIM systems used in Fig. 3.24 and Fig. 3.25 are respectively characterised by $(m = 4, N = 16, k = 1, Q = 4)$ for $R_{\mathcal{V}_U} = 1.5$ bits/s/Hz and by $(m = 4, N = 16, k = 1, Q = 64)$ for $R_{\mathcal{V}_U} = 2.5$ bits/s/Hz. We observe from the results of Fig. 3.24 and Fig. 3.25 that the BER performance of the OFDM-LPIM system using our GIRCD invoking two iterations is stable for all SNR values. Furthermore, as seen in Fig. 3.24 and Fig. 3.25, a good BER performance is attainable for the GIRCD using as few as two iterations. On the other hand, as observed from Fig. 3.26 and Fig. 3.27, when the maximum number of iterations is set to $t_{\text{stop}} = 10$, a good BER performance can be attained by our OFDM-CSIM systems. Here, it should be emphasised that the notation t_{stop} serves as an upper bound of the number of iterations in our GIRCD of Algorithm 3. In fact, as shown in Fig. 3.22 and Fig. 3.23, our GIRCD usually terminates after just a single or two iterations, imposing a low-complexity. Next, we can observe from Fig. 3.24 and Fig. 3.26 that the OFDM-LPIM system attains a better BER performance than the OFDM-CSIM system, when GIRCD is employed for both systems. However, as shown in Table 3.3, the complexity of our OFDM-CSIM employing GIRCD is much lower than that of the OFDM-LPIM using GIRCD. Moreover, as seen in Table 3.3, our GIRCD is capable of providing a much lower complexity in comparison to the

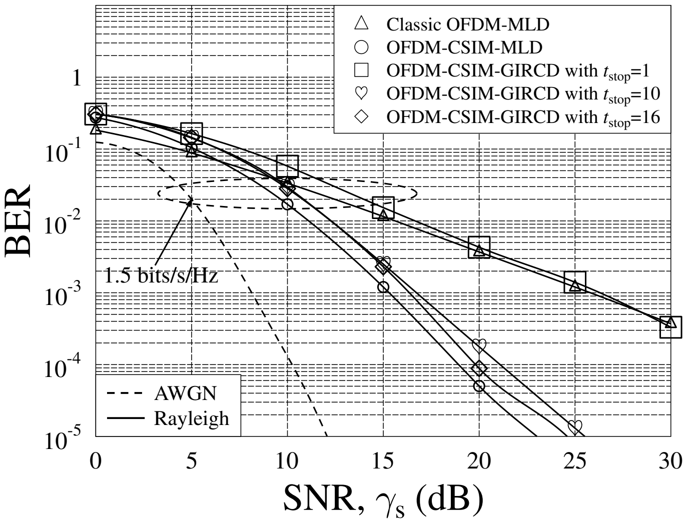

Figure 3.26: BER versus SNR for the OFDM-CSIM using the JMLD and the GIRCD. The OFDM-CSIM system employs the depth-G interleaver and operates at 1.5 bits/s/Hz. For the GIRCD shown in Algorithm 3, the maximum number of iterations is chosen to be $t_{\text{stop}} = 1$, 10 or 16. The maximum achievable rate is constraint to be 1.5 bits/s/Hz for all systems.

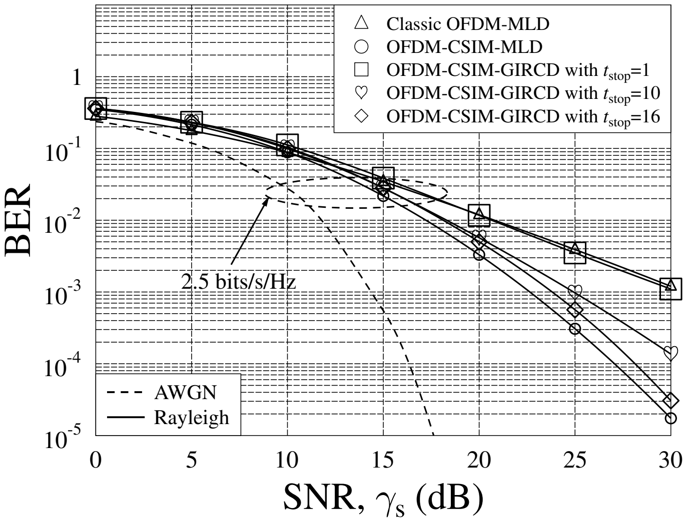

Figure 3.27: BER versus SNR for the OFDM-CSIM using the JMLD and the GIRCD. The OFDM-CSIM system employs the depth-G interleaver and operates at 2.5 bits/s/Hz. For the GIRCD shown in Algorithm 3, the maximum number of iterations is chosen to be $t_{\text{stop}} = 1$, 10 or 16. The maximum achievable rate is constraint to be 2.5 bits/s/Hz for all systems.

JMLD. The reason is two fold. Firstly, each index is uniquely checked, as shown in Algorithm 3. In this way, the repeated reliability computations of the same index are avoided. The other reason can be readily inferred from comparing (3.65) to (3.58), where the APM symbols are detected on a symbol-by-symbol basis by the GIRCD, while the joint group detection is carried out by the JMLD. Finally, based on the above observations, we can show that our proposed OFDM-LPIM system employing GIRCD is capable of attaining a good BER performance associated with a high SE at a low complexity. Furthermore, our OFDM-CSIM system is capable of achieving an even lower complexity, albeit a slight degradation of the BER performance.

3.8 Conclusions

In this chapter, the generalised system model of Section 3.2 and the unified performance analysis of Section 3.3 were provided for OFDM systems, where the bit-to-symbol mapping rule is modelled as a codebook. Based on our theoretical analysis, the relevant codebook design criteria have been provided in terms of the diversity gain, the coding gain, as well as the maximum achievable rate. Then, based on the diversity gain and the coding gain design criteria, a LPIM codebook has been proposed in Section 3.4. Both the analytical and simulation results have shown that the LPIM scheme is capable of attaining a compelling BER performance. Next, in Section 3.5, a generalised CSIM codebook has been proposed based on the maximum diversity gain and the maximum achievable rate design criteria. Moreover, in Section 3.5.3, we also proposed a novel measurement matrix design for our CSIM codebook in order to meet the maximum diversity gain criterion, while also satisfying the MIP. Finally, the GIRCD has been proposed in Section 3.6 for both the LPIM and the CSIM in order to reduce the corresponding detection complexity. In Section 3.7, simulation results have been provided for characterising the overall system performance.

Our investigations demonstrated that our OFDM-LPIM and OFDM-CSIM is capable of achieving a much better BER performance than both the classic OFDM and the conventional OFDM-SIM. Then, in comparison to the conventional SIM and LPIM schemes, the CSIM scheme strikes an appealing tradeoff between the SE and the EE. Furthermore, for a given maximum achievable rate and JMLD, the LPIM scheme is capable of achieving a better BER performance than the CSIM scheme, but a much higher complexity. The GIRCD can be employed for significantly reducing the complexity for both the LPIM and CSIM schemes. At a high rate, the LPIM scheme using GIRCD has been shown to be capable of attaining a good BER performance at a reduced complexity cost. An even lower complexity cost is attained by the CSIM scheme using GIRCD, albeit a slight performance loss. Nonetheless, as it will be shown in the next chapter, the inherent sparsity of our CSIM scheme may be able to provide a good BER performance when the OFDM systems suffer from ICI.

Chapter 4

Compressed Sensing Aided Optical OFDM for Visible Light Communications

4.1 Introduction

VLC has been recognised as a compelling technique of alleviating teletraffic congestion in the near future. The main advantage of VLCs is that a wide unlicensed visible light spectrum can be used for data transmission without inflicting interference upon the existing RF communications [1]. Furthermore, since partitioning is impervious to visible light, a unity spatial reuse factor can be attained by VLCs operating in different rooms. Owing to their energy efficiency, longevity as well as reliability, LEDs are expected to be the dominant light sources, which can also be used for data transmission in VLCs. For this reason, the installation cost of VLCs is rather low, especially when power line communication is used as the backhaul technology for VLCs [13]. There are many applications for VLCs, such as RF/VLC cooperation in the cellular network, device-to-device communications, underwater communications, as well as some others as described in [154, 155].

However, there are still a lot of open challenges concerning the implementation of high-performance VLC systems. Due to its low-cost and simplicity, a noncoherent scheme, which is known as IM/DD, is commonly used in VLCs. In IM/DD VLC systems, only the real and positive signals can be used for modulating the intensity of optical sources, where the intensity envelope is detected by the optical receiver. For high data rate transmission of IM/DD signals over NLOS channels, although the multipath induced fading may be mitigated by exploiting the fact that the dimen-

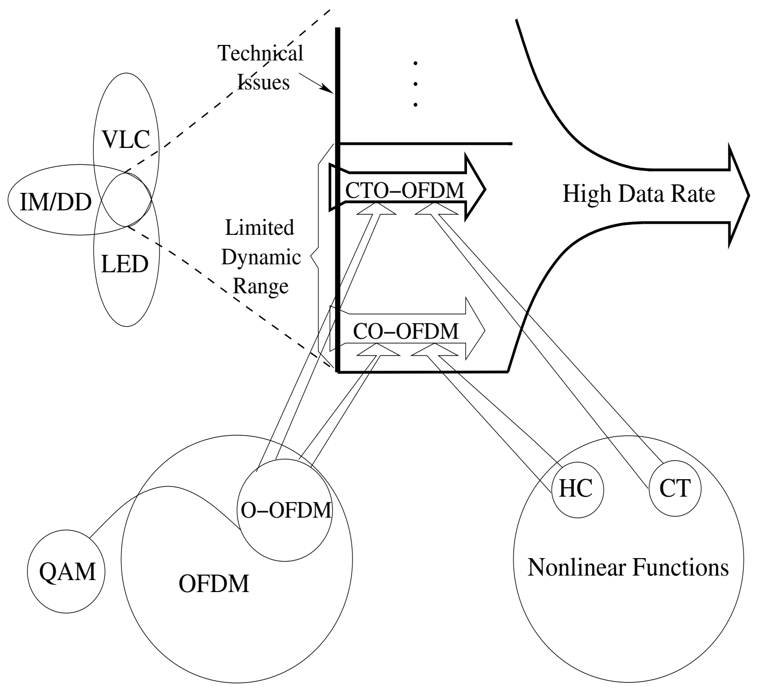

Figure 4.1: Illustration of the relationships between optical OFDM (O-OFDM), clipping-based O-OFDM (CO-OFDM relying on hard clipping (HC)), as well as companding transform (CT) assisted O-OFDM (CTO-OFDM).

sions of optical detectors are usually much larger than the wavelength of visible light, the ISI caused by multipath propagation may still degrade the overall system performance. Thus, OFDM, which is capable of combating the multipath effects in radio communications [91, 92], has also become an attractive candidate for VLCs [156–158].

In the classic OFDM schemes, the IDFT and the DFT are applied for the implementation of the discrete multicarrier modulation and demodulation, respectively. Owing to the employment of the FFT and cyclic prefix, the DFT-based OFDM scheme is capable of mitigating ISI with the aid of a low-complexity implementation [159], when communicating over dispersive frequency-selective fading channels. However, the classic OFDM scheme cannot be directly employed for operation in dispersive IM/DD optical systems, since the TD symbols are complex-valued owing to modulation by FFT-based techniques. By contrast, only unipolar signals can be transmitted in the IM/DD systems [160]. In order to render the classic OFDM scheme suitable for the IM/DD systems, a range of O-OFDM solutions have been proposed [161–163]. In these approaches, the Hermitian symmetry is imposed on the FD subcarriers, in order to obtain real-valued baseband signals. Then, the real-valued baseband signals are converted to unipolar signals, for example, by adding a DC bias [161] (Direct Current biased Optical OFDM (DCO-OFDM)), by asymmetric clipping [162] (Asymmetric Clipping based Optical OFDM (ACO-OFDM)), as well as by joint asymmetric clipping and DC bias [163] (Asymmetric clipping and Direct-current-bias based Optical OFDM (ADO-OFDM)), etc. However, the major drawback of these approaches is their low bandwidth efficiency imposed by the Hermitian symmetry.

Nevertheless, due to the simplicity of implementation, the Clipping-based Optical OFDM (CO-OFDM) solutions, which include the DCO-OFDM and ACO-OFDM systems, have attracted considerable research attention in VLCs. As the investigations in [162–164] show, the ACO-OFDM has a higher optical power efficiency than the DCO-OFDM, when a low or moderate constellation size is used [162]. For a large constellation size, the optical power efficiency of the DCO-OFDM is higher than that of ACO-OFDM [164]. The reason for the above effects is that for a small or moderate-sized constellation, an insufficient DC bias degrades the system performance. By contrast, for a large constellation, the inefficient usage of bandwidth becomes the dominant limitation of the achievable performance [163, 164]. Furthermore, as shown in [165] that for a fixed symbol rate, the computational complexity of DCO-OFDM is lower than that of ACO-OFDM. However, we should emphasise that the above-mentioned observations are obtained based on the assumption that the upper clipping bound is infinite. In practice, however, the illumination level is limited for eye safety [161, 166]. Meanwhile, the electrical power consumption should be controlled by considering the efficiency of both the Digital-to-Analog Conversion (DAC) and the power amplifier [167]. Thus, the dynamic range of O-OFDM systems is limited [168]. Furthermore, due to the anti-symmetric property [162], clipping the negative parts of ACO-OFDM signals does not introduce any loss of information, whilst clipping of the high positive peaks of ACO-OFDM signals results in nonlinear distortion, which degrades the system performance.

Another fundamental issue in OFDM is the high PAPR problem, making OFDM signals sensitive to nonlinear devices. Nonlinear distortion leads to both in-band distortion and out-of-band radiation, both of which degrade the system performance. In the literature, numerous PAPR reduction techniques have been proposed, see [169–171] and the references therein. Among these techniques, a simple yet effective method is the employment of a CT [172–180], which reduces the PAPR by applying a compander (a “compressor” and “expander” pair) to the time-domain signals, before their transmissions. A compander compresses the high signal peaks, while expanding the low-magnitude signals, thereby striking an attractive tradeoff between PAPR reduction and the BER performance achieved. Specifically, in [172], the so-called μ-law compander originally used in speech coding has been introduced for PAPR reduction. Later in [174], the design criteria of the CT has been derived for striking a tradeoff between the PAPR reduction and BER performance attained. Substantial research attention has been dedicated to transforming the amplitude distribution of the original OFDM signals to particular distributions, such as the uniform distribution [175], the trapezoidal distribution [176] and so forth. Note that in these techniques, the average power has not been changed by the CT. Most recently, the design of efficient companders based on piecewise modification of the signal's amplitude distribution has been considered [177–180]. In these so-called piecewise companders, the amplitude distribution of original signals is only partially changed, whilst ensuring that both the PAPR reduction and BER performance can be improved.

Against the above background, the contributions of this chapter are summarised as follows.

- *As a practical implementation, the CSIM scheme proposed in Chapter 3 is applied to O-OFDM systems. For the sake of comparison, the QAM constellation having unity energy is assumed for modulating the activated symbols, so that the minimum distance of the CSIM signalling proposed becomes the same as that of the classic QAM signalling, yielding the same sensitivity to nonlinear effects. We provide analytical results to show that under hard clipping, the SINR attained by the CSIM scheme is higher than that attained by the QAM scheme. Furthermore, both an additional diversity gain and an coding gain can be achieved by our CSIM scheme, albeit at a higher complexity cost, as analysed in Chapter 3. Hence, in comparison to the classic QAM signalling, a much better BER performance can be attained by the CSIM signalling, which is verified by our simulation results. Moreover, we demonstrate that the Maximum Achievable Rate (MAR) of the DCO-OFDM system using a certain QAM scheme can be further increased by employing our CSIM scheme associated with the same QAM constellation for modulating the activated symbols. However, this is achieved at the cost of increasing the complexity of the receiver. Thus, the SE, which is about halved by the Hermitian symmetry transform of O-OFDM signalling, can be enhanced by our CSIM schemes.*
- *As a further improvement, a symmetric piecewise CT is conceived for the O-OFDM systems in order to mitigate the nonlinear effect imposed on high-order QAM schemes. Generally, the high-order QAM schemes are sensitive to nonlinear distortions, hence the system performance may be severely degraded even by moderate nonlinear distortion, even for our CSIM signalling. Hence, an advanced nonlinear distortion mitigation technique is required for supporting high-rate transmissions in O-OFDM systems. The underlying concept is illustrated in Fig. 4.1. The general principles and design criteria of the piecewise CT*

> *schemes are studied in the context of VLC. Accordingly, three types of piecewise companding schemes, namely the CPsDF, the LPsDF and the NLPsDF based CT are designed for O-OFDM systems. In our CT-based optical OFDM (CTO-OFDM) systems, the CT is invoked for mitigating the clipping of high-peak TD signals. Thus, the system's performance can be improved, especially, when high-order QAM is used, which is sensitive to nonlinear distortions. In this paper, we investigate both the hard-clipping and the CT induced nonlinear effects imposed on O-OFDM systems relying on both analytical and on simulation approaches. Our studies show that the both the CTO-OFDM and DCO-OFDM systems are capable of attaining a higher bandwidth efficiency, than the ACO-OFDM system. Moreover, we demonstrate that the CTO-OFDM system outperforms the DCO-OFDM system both in terms of its reliability and flexibility, when supporting high-rate transmission experiencing nonlinear distortions.*

The rest of the chapter is organised as follows. In Section 4.2, we describe the system model. The operating principle, design criteria and implementation of the symmetric piecewise CT are detailed in Section 4.3. In Section 4.4, the nonlinear effects are analysed. In Section 4.5, our performance results are studied. Finally, we offer our conclusions in Section 4.6.

4.2 System Model

4.2.1 Description of the Transmitter

Fig. 4.2 illustrates a generalised O-OFDM scheme invoked in IM/DD optical communication systems, which will be discussed below. Let us assume that an L_{b}-length sequence of i.i.d. bits is transmitted, which is first mapped to N_{d} data symbols, according to a codebook $\mathcal{V}$. Specifically, in this chapter, we consider two types of codebooks, both of which are associated with QAM constellations. Moreover, our attention is focused on investigating the nonlinear effects imposed on O-OFDM systems. Hence, for the sake of comparison, we assume that the constellation energy of the QAM scheme is normalised to be unity, so that the sensitivity of a given QAM scheme to nonlinear distortions remains the same for the different O-OFDM systems considered. Bearing this in mind, the two codebooks are detailed as follows.

QAM scheme When the QAM scheme is considered, a total of $\log_2(Q)$ bits are mapped to a data symbol according to the Q-ary QAM constellation relying on the alphabet $\mathcal{A} = \{a(1), \ldots, a(Q)\}$. Hence, we have the relationship of $L_{\mathrm{b}} = N_{\mathrm{d}} \log_2(Q)$.

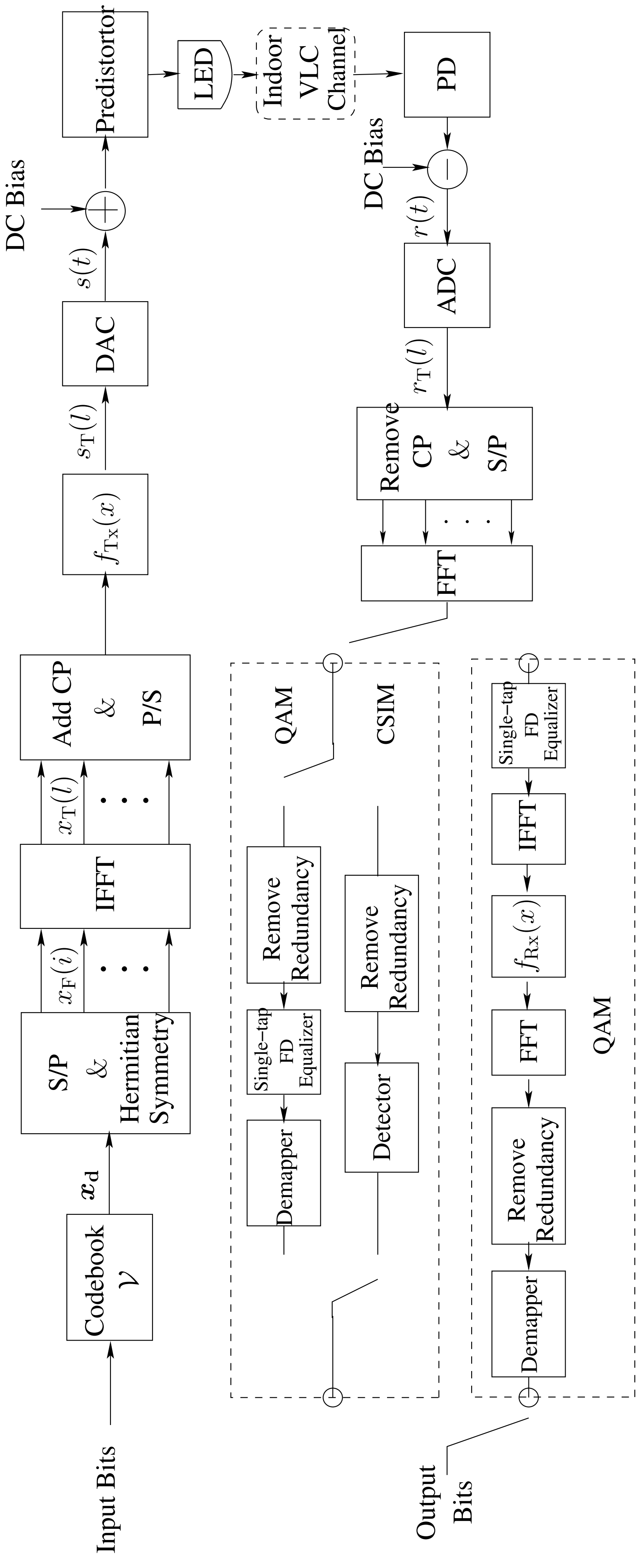

Figure 4.2: Illustration of the O-OFDM systems.

Let us denote the N_d data symbols by $\boldsymbol{x}_\mathrm{d} = [x_\mathrm{d}(0), \ldots, x_\mathrm{d}(N_\mathrm{d}-1)]^T$, where we have $x_\mathrm{d}(i) \in \mathcal{A}$ and $\mathbb{E}[|x_\mathrm{d}(i)|^2] = 1$.

CSIM scheme When the CSIM scheme is considered, as detailed in Section 3.5.2, a total of L bits are first mapped to an N-dimensional IM symbols associated with k activated symbols of the Q-ary QAM constellation and then compressed into the m-dimensional symbols in the FD. Here, we have $L = \left\lfloor \log_2 \binom{N}{k} \right\rfloor + k \log_2 Q$. Upon invoking the depth-G interleaver of Section 3.4.3, the gth group of symbols can be represented as $\boldsymbol{x}_{\mathrm{d},g} = [x_{\mathrm{d},g}(0), \ldots, x_{\mathrm{d},g}(m-1)]^T$, where we have $\mathbb{E}[\|\boldsymbol{x}_{\mathrm{d},g}\|_2^2] = k$ for $g = 1, \ldots, G$. Here, the total number of groups is chosen to be $G = \lfloor N_\mathrm{d}/m \rfloor$. Furthermore, we observe that the case of $mG < N_\mathrm{d}$ may occur for a given CSIM scheme. Hence, without loss of generality, we let the remaining $0 \leq (N_\mathrm{d} - mG) < m$ symbols be modulated by the same Q-ary QAM scheme. Finally, we obtain the N_d data symbols represented as $\boldsymbol{x}_\mathrm{d} = [x_\mathrm{d}(0), \ldots, x_\mathrm{d}(N_\mathrm{d}-1)]^T$.

As shown in Fig. 4.2, the data symbols in $\boldsymbol{x}_\mathrm{d}$ are arranged to form M FD symbols denoted as $\boldsymbol{x}_\mathrm{F} = [x_\mathrm{F}(0), \ldots, x_\mathrm{F}(M-1)]^T$, where the elements satisfy the Hermitian symmetry formulated as $x_\mathrm{F}(0) = x_\mathrm{F}(M/2) = 0$ and $x_\mathrm{F}(M-i) = [x_\mathrm{F}(i)]^*$ for any $i \neq 0$. Furthermore, for both the DCO-OFDM and CTO-OFDM systems, we have the mappings of $x_\mathrm{F}(i) = x_\mathrm{d}(i-1)$ for $i = 1, 2, \ldots, (M-2)/2$, yielding $N_\mathrm{d} = (M-2)/2$. By contrast, for the ACO-OFDM system, the data symbols in $\boldsymbol{x}_\mathrm{d}$ are successively mapped to the odd-indexed subcarriers of the first half of $\boldsymbol{x}_\mathrm{F}$, while all the even indexed subcarriers of $\boldsymbol{x}_\mathrm{F}$ are set to zero, which gives $N_\mathrm{d} = M/4$. From the above description, we infer that the bandwidth efficiency of both the DCO-OFDM and CTO-OFDM systems is higher than that of the ACO-OFDM system.

As shown in Fig. 4.2, the FD symbols are entered into an M-point IFFT, yielding the TD symbols denoted as $\boldsymbol{x}_\mathrm{T} = [x_\mathrm{T}(0), \ldots, x_\mathrm{T}(M-1)]^T \in \mathbb{R}^{M\times 1}$, where the lth TD symbol can be expressed as

$$x_\mathrm{T}(l) = \frac{1}{\sqrt{M}} \sum_{i=0}^{M-1} x_\mathrm{F}(i) \exp\left(j2\pi \frac{i}{M} l\right) \tag{4.1}$$

for $l = 0, 1, \ldots M-1$. It is widely recognized that when M is sufficiently large, the TD symbols in $\boldsymbol{x}_\mathrm{T}$ can be approximated by Gaussian random variables with zero mean and a variance of $\sigma_X^2 = \mathbb{E}[|x_\mathrm{T}(l)|^2]$. As shown in Fig. 4.2, after adding a sufficiently long CP and following parallel-to-serial conversion, the TD symbols in (4.1) are subjected to the specifically designed function $\{f_\mathrm{Tx}(x) : \mathbb{R} \to \mathbb{R}\}$. Explicitly, at the transmitter side, $f_\mathrm{Tx}(x)$ is used for guaranteeing that the information-bearing signals after adding a DC bias become real and positive. Let $s_\mathrm{T}(l) = f_\mathrm{Tx}[x_\mathrm{T}(l)]$ represent the output of the transmitter processor shown in Fig. 4.2, when $x_\mathrm{T}(l)$ expressed in (4.1)

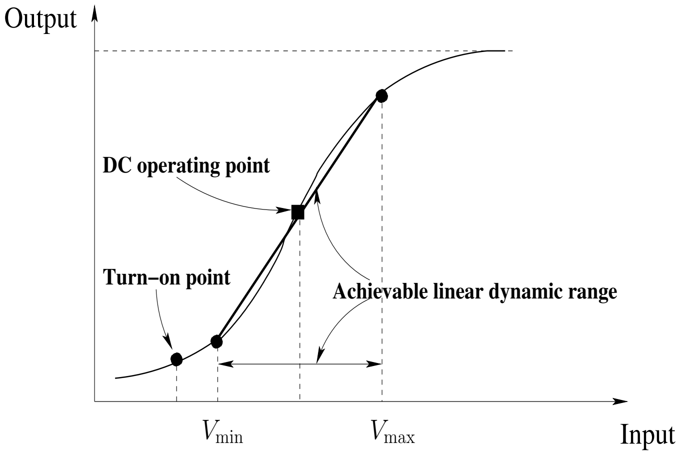

Figure 4.3: Illustration of the linear dynamic range of a LED, which can be achieved by either employing a pre-distortor at the transmitter or using a post-distortor at the receiver.

is the corresponding input. Then, as seen in Fig. 4.2, the outputs of the transmitter processor are fed into a DAC, where a DC bias associated with a level of A_{DC} is added in order to finally output the electric current signal denoted as $(s(t) + A_{\mathrm{DC}}) \in \mathbb{R}_{+}$. It should be noted that the inherent nonlinearity of LEDs often results in nonlinear distortion of the transmitted signals. In order to compensate for the nonlinearity of the LEDs, the electric current signal $s(t)$ can be pre-distorted [181]. An alternative technique of compensating for the nonlinearity is to employ a post-distorter [182] at the receiver. Finally, as seen in Fig. 4.2, the pre-distorted signals are input to the LED to modulate the intensity of the LED's light.

4.2.2 VLC Channels

Let us assume that the LEDs have the optical conversion factor of ρ_{LED} in Watt-per-ampere (W/A) and a PhotoDetector (PD) with the responsivity of ρ_{PD} in ampere-per-Watt (A/W). Without loss of generality, let us assume that $\rho_{\mathrm{PD}}\rho_{\mathrm{LED}} = 1$ in order to simplify our analysis. Moreover, we assume that perfect pre-distortion or post-distortion is implemented at the transmitter or receiver, respectively. Under these assumptions, the IM/DD system can be assumed to be operated in the linear dynamic range, as shown in Fig. 4.3. Typically, in the IM/DD systems, information is conveyed by the optical intensity in response to the input electrical current, while the receiver outputs the electrical current proportional to the received optical intensity. In this paper, we assume that the optical intensity signals propagate over an indoor multipath VLC channel. In general, the variation of indoor VLC channels versus time is very slow. Hence, in our studies, we assume that the indoor VLC channels are time-invariant. Consequently, as seen in Fig. 4.2, after removing the DC bias, the electrical photocurrent signal obtained at the receiver can be expressed as

$$\begin{aligned} r(t) &= \int_{-\infty}^{\infty} \rho_{\mathrm{PD}}\rho_{\mathrm{LED}} h(t) s(t-\tau)\mathrm{d}\tau + n(t) \\ &= \int_{-\infty}^{\infty} h(t) s(t-\tau)\mathrm{d}\tau + n(t), \end{aligned} \tag{4.2}$$

where $h(t)$ denotes the VLC's channel impulse response and $n(t)$ is the noise. In particular, Barry's VLC channel model of [15, 183] is introduced in our study, which is formulated as

$$h(t) = \sum_{i=0}^{\infty} h_{\mathrm{B}}(i)\delta[t - \tau_{\mathrm{B}}(i)], \tag{4.3}$$

where $h_{\mathrm{B}}(i)$ and $\tau_{\mathrm{B}}(i)$ are the gain and delay of the ith bounce, respectively. Note that the gain and delay of the current bounce are dependent on that of the previous bounces. Let the frequency response of the VLC channel be denoted as $h(f)$, which can be obtained by taking the Fourier transform of (4.3). In practice, since the diameter of photodetectors is usually much larger than the wavelength of visible light, multipath propagation in VLCs does not impose fading on the optical signals. However, when signals carrying high-rate information are transmitted over such a channel, the time dispersion usually results in ISI. In (4.2), the noise $n(t)$ contains the effects of ambient light shot noise and thermal noise, which can commonly be modelled as mutually independent white Gaussian noise [15]. Therefore, we have $n(t) \sim \mathcal{N}(0, \sigma_{\mathrm{n}}^2)$.

4.2.3 Electrical Receiver

As seen in Fig. 4.2, the electrical current is low-pass filtered and analog-to-digital converted. Let us assume that perfect synchronisation is achieved at the receiver. Then, the lth received TD sample can be expressed as

$$r_{\mathrm{T}}(l) = \sum_{i=0}^{L_{\mathrm{h}}-1} h_{\mathrm{B}}(i) s_{\mathrm{T}}(l-i) + n_{\mathrm{T}}(l), \tag{4.4}$$

where L_{h} denotes the maximum number of resolvable paths. Generally, a receiver processor is employed as a nonlinear mapping function of the received symbols. However, for the multipath propagation scenario of Section 4.2.2, such a receiver may lead to excessive ICI in the FD, whilst additionally amplifying the noise. As a result, the system performance may in fact become degraded. In order to alleviate the nonlinearity-induced performance degradation, two different schemes are considered in this chapter. To elaborate a little further, observe in Fig. 4.2 that, after removing the CP and carrying out the FFT, the received FD symbol can be formulated as

$$y_{\mathrm{F}}(i) = \frac{1}{\sqrt{M}} \sum_{l=0}^{M-1} r_{\mathrm{T}}(l) \exp\left(-j2\pi \frac{l}{M} i\right) \tag{4.5}$$

for $i = 0, 1, \ldots, M-1$. Then, the received FD symbol of (4.5) is fed into a single-tap FD equaliser, yielding $\widetilde{y}_{\mathrm{F}}(i) = y_{\mathrm{F}}(i)/h_{\mathrm{F}}(i)$, where without loss of generality h_{F} represents the FDCHTF of the ith subchannel, which can be obtained from Section 4.2.2. Here, we stipulate the idealised simplifying assumption that perfect channel estimation is achieved at the receiver. Next, either a low-complexity or a high-complexity receiver scheme is considered.

The low-complexity scheme is shown in the upper dashed box of Fig. 4.2. Explicitly, when the O-OFDM system using QAM is considered, the equalised symbols are symbol-by-symbol de-mapped into the received bits relying on the ML detection principle, resulting in an adequate performance. By contrast, when the O-OFDM system using CSIM is employed, the ML detector of Chapter 3 is used for symbol detection.

However, when the nonlinearity induced performance degradation becomes severe at a high data rate, the higher-complexity scheme shown in the lower dashed box in Fig. 4.2 is selected. For the ease of understanding, let us temporarily employ vectored expressions. Firstly, without any ambiguity, the equalised symbols denoted as $\widetilde{\boldsymbol{y}}_{\mathrm{F}} = [\widetilde{y}_{\mathrm{F}}(0), \widetilde{y}_{\mathrm{F}}(1), \ldots, \widetilde{y}_{\mathrm{F}}(M-1)]^T$ can be expressed as

$$\widetilde{\boldsymbol{y}}_{\mathrm{F}} = \boldsymbol{\mathcal{F}}_M f_{\mathrm{Tx}}(\boldsymbol{x}_{\mathrm{T}}) + \widetilde{\boldsymbol{n}}_{\mathrm{F}}, \tag{4.6}$$

where $\widetilde{\boldsymbol{n}}_{\mathrm{F}}$ represents the filtered noise. Then, as seen in Fig. 4.2, the equalised symbols are entered into an M-point IFFT, yielding

$$\begin{aligned} \widetilde{\boldsymbol{y}}_{\mathrm{T}} &= \boldsymbol{\mathcal{F}}_M^H \widetilde{\boldsymbol{y}}_{\mathrm{F}} \\ &= f_{\mathrm{Tx}}(\boldsymbol{x}_{\mathrm{T}}) + \widetilde{\boldsymbol{n}}_{\mathrm{T}}, \end{aligned} \tag{4.7}$$

where, by definition, we have $\widetilde{\boldsymbol{n}}_{\mathrm{T}} = \boldsymbol{\mathcal{F}}_M^H \widetilde{\boldsymbol{n}}_{\mathrm{F}}$. Without loss of generality, we assume that a perfect expander is employed, i.e. we have $f_{\mathrm{Rx}}(x) = f_{\mathrm{Tx}}^{-1}(x)$. Hence, upon invoking an expansion by $f_{\mathrm{Rx}}(\widetilde{\boldsymbol{y}}_{\mathrm{T}})$, the resultant symbols are subjected to an M-point FFT, yielding

$$\begin{aligned} \boldsymbol{y}_{\mathrm{F}}^{'} &= \boldsymbol{\mathcal{F}}_M f_{\mathrm{Rx}}(\widetilde{\boldsymbol{y}}_{\mathrm{T}}) \\ &= \boldsymbol{\mathcal{F}}_M \boldsymbol{x}_{\mathrm{T}} + \boldsymbol{\mathcal{F}}_M f_{\mathrm{Rx}}(\widetilde{\boldsymbol{n}}_{\mathrm{T}}) \\ &= \boldsymbol{x}_{\mathrm{F}} + \boldsymbol{n}_{\mathrm{F}}^{'}, \end{aligned} \tag{4.8}$$

where, for convenience, we define $\boldsymbol{n}_{\mathrm{F}}^{'} = \boldsymbol{\mathcal{F}}_M f_{\mathrm{Rx}}(\widetilde{\boldsymbol{n}}_{\mathrm{T}})$. Finally, each symbol in $\boldsymbol{y}_{\mathrm{F}}^{'}$ is de-mapped by the conventional QAM demodulator, yielding the received bits. Specifically, when the transmitter processor is a CT function, the system's performance can be substantially improved by designing an effective CT function, which is detailed in the next section.

Complexity Analysis

For the sake of comparison, we consider the complexity of the dashed boxes in Fig. 4.2, involving each OFDM block. Firstly, we can readily show that the complexity of the O-OFDM systems employing QAM is due to both the equalisation and the symbol-by-symbol ML detection, as seen in the upper dashed box of Fig. 4.2. Hence, the corresponding complexity can be readily shown to be on the order of

$$\mathcal{O}(N_{\mathrm{d}} + N_{\mathrm{d}}Q). \tag{4.9}$$

By contrast, for the O-OFDM system using CSIM, the complexity of the ML detection of each group of symbols is given by $\mathcal{O}(2^L)$, as analysed in Chapter 3. Moreover, we note that the complexity of detecting the remaining $(N_{\mathrm{d}} - mG)$ QAM symbols is much lower than the overall complexity of G groups of CSIM symbols. Hence, the corresponding complexity of the dashed box for CSIM is given by $\mathcal{O}(G2^L)$. Specifically, as shown in Chapter 3, an attractive tradeoff can be struck between the BER performance and the complexity by setting $k = 1$ for our CSIM scheme. In this case, we can show that the detection complexity of the O-OFDM system using CSIM is given by

$$\mathcal{O}(G2^L) = \mathcal{O}(GNQ) \approx \mathcal{O}\left(\frac{N}{m} N_{\mathrm{d}} Q\right), \tag{4.10}$$

where the approximation becomes accurate for $N_{\mathrm{d}} \approx mG \gg m$. Hence, we can now show that the detection complexity given in (4.10) for our CSIM signalling scheme is on the same order as that in (4.9) for the classic QAM signalling, since both of them are linearly increased with the constellation size Q. On the other hand, when the scheme in the lower dashed box of Fig. 4.2 is used for mitigating the nonlinear effects, we can readily show that the corresponding complexity is dominated by the IFFT and FFT operations, as well as by the symbol-by-symbol ML detection, giving a total order of

$$\mathcal{O}(2M \log_2(M) + N_{\mathrm{d}}Q), \tag{4.11}$$

which is much higher than those given in (4.9) and (4.10), since we have $M > N_{\mathrm{d}}$. Nonetheless, the high complexity cost shown in (4.11) is imposed, when reliably supporting high-rate transmissions in VLCs, as we will show in Section 4.5.

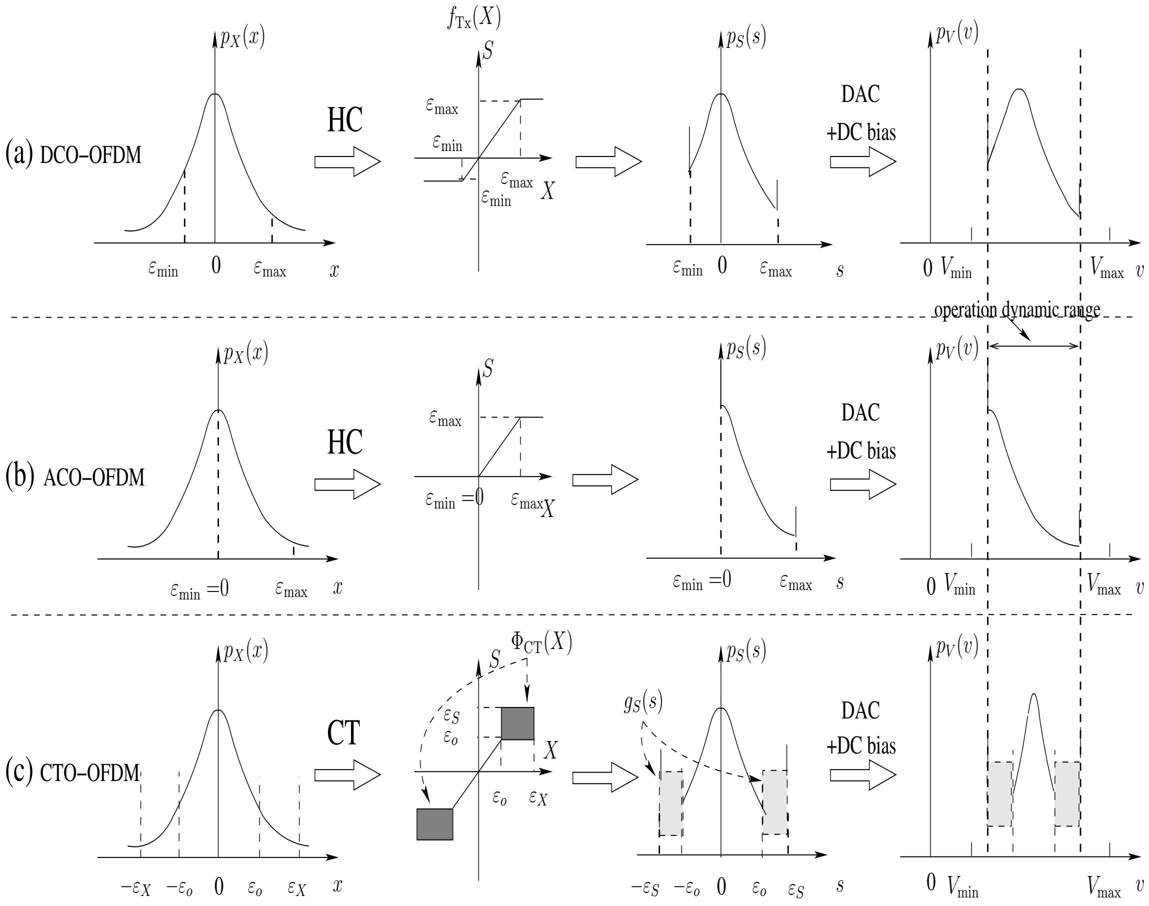

Figure 4.4: Illustration of the nonlinear transformation that may be used by the transmitter processor.

4.3 Companding Transform of DCO-OFDM Signals

In the conventional CO-OFDM systems, the transmitter processor seen in Fig. 4.2 simply applies hard clipping. Explicitly, in DCO-OFDM systems, hard clipping tends to lead to a certain level of information loss, which degrades the attainable system performance. By contrast, in ACO-OFDM systems, due to the anti-symmetry property [162], clipping the negative part does not lead to any loss of information. Nonetheless, as shown in Section 4.2.1, the anti-symmetric property is achieved at the cost of reduced bandwidth efficiency. In order to achieve a higher bandwidth efficiency at a reduced information loss, and furthermore, to guarantee that the DC-biased information-bearing signals are real and positive valued, in this paper, we introduce a particular type of CTs, namely the symmetric piecewise CT, as the transmitter processor. Before providing further details, let us first review the hard clipping operation of conventional CO-OFDM systems.

4.3.1 Statistical of O-OFDM Signals

Firstly, let us model the input and output of the transmitter processor as random processes of

$$\Big\{X : X_l \triangleq x_{\mathrm{T}}(l) \in \mathbb{R}\Big\}; \tag{4.12a}$$

$$\Big\{S : S_l \triangleq s_{\mathrm{T}}(l) \in \mathbb{R}\Big\}, \tag{4.12b}$$

respectively. Moreover, we have $S_l = f_{\mathrm{Tx}}(X_l)$ with respect to $s_{\mathrm{T}}(l) = f_{\mathrm{Tx}}(x_{\mathrm{T}}(l))$. Furthermore, according to Section 4.2.1, the PDF and the Cumulative Distribution Function (CDF) of the amplitudes of TD symbols can be approximated as

$$p_X(x) = \frac{Q_1\left(0, \frac{x}{\sigma_X}\right)}{\sigma_X\sqrt{2\pi}} \tag{4.13}$$

and as

$$P_X(x) = 1 - Q\left(\frac{x}{\sigma_X}\right), \tag{4.14}$$

respectively. In (4.13), we define the notation of $Q_1(0,x) \triangleq \exp(-x^2/2)$, which is actually a special case of the first order Marcum Q-function.

QAM Scheme When the QAM scheme is considered, the variance of the TD symbols $\boldsymbol{x}_{\mathrm{T}}$ given in (4.1) can be expressed as

$$\sigma^2_{X_{1\text{ or }2}} = \frac{2\mathbb{E}[\|\boldsymbol{x}_{\mathrm{d}}\|_2^2]}{M} = \frac{2N_{\mathrm{d}}}{M}, \tag{4.15}$$

where we can show that $\sigma^2_{X_1} \approx 1$ for the DCO-OFDM system using QAM, provided that M is sufficient large, whilst we have $\sigma^2_{X_2} = 1/2$ for the ACO-OFDM system using QAM. Hence, we now know that for a given QAM scheme having a unity normalised constellation energy, the variance of ACO-OFDM signals is about half of DCO-OFDM signals.

CSIM Scheme Let us now consider the CSIM scheme of Section 4.2.1. For the sake of analysis, let us define $N_{\mathrm{d}} = mG + \kappa$, where $\kappa = 0, 1, \ldots, m-1$. In this case, the variance of the TD symbols $\boldsymbol{x}_{\mathrm{T}}$ given in (4.1) can be formulated as

$$\begin{aligned}
\sigma^2_{X_3} =& \frac{2\mathbb{E}[\|\boldsymbol{x}_{\mathrm{d}}\|_2^2]}{M} = \frac{2G\mathbb{E}[\|\boldsymbol{x}_{\mathrm{d},g}\|_2^2] + 2(N_{\mathrm{d}} - mG)}{M} \\
=& \frac{2Gk + 2\kappa}{M} = \left(\frac{2N_{\mathrm{d}}}{M}\right)\frac{k}{m} + \frac{2\kappa}{M}\left(1 - \frac{k}{m}\right) \\
\approx& \left(\frac{2N_{\mathrm{d}}}{M}\right)\frac{k}{m}
\end{aligned} \tag{4.16}$$

for sufficient large M. Since we have $k < m$ for our CSIM scheme, the signal variance given in (4.16) for the CO-OFDM system using CSIM is much lower than that given in (4.15) of CO-OFDM systems using QAM, when the same nonlinear sensitivity is assumed. This may lead to some advantages, as it will be discussed in Section 4.4.2.

4.3.2 Review of Hard Clipping

In the conventional CO-OFDM systems, hard clipping is applied at the transmitter, implying that we have $f_{\mathrm{Tx}}(X) = f_{\mathrm{HC}}(X)$, where the hard clipping function can be expressed as

$$S = f_{\mathrm{HC}}(X) = \begin{cases} \varepsilon_{\min}, & \text{if } X \in \mathcal{X}_1^{\mathrm{HC}} \\ x, & \text{if } X \in \mathcal{X}_2^{\mathrm{HC}} \\ \varepsilon_{\max}, & \text{if } X \in \mathcal{X}_3^{\mathrm{HC}}, \end{cases} \tag{4.17}$$

where $\mathcal{X}_1^{\mathrm{HC}} = (-\infty, \varepsilon_{\min}]$, $\mathcal{X}_2^{\mathrm{HC}} = (\varepsilon_{\min}, \varepsilon_{\max})$ and $\mathcal{X}_3^{\mathrm{HC}} = [\varepsilon_{\max}, +\infty)$ are three disjoint regions of amplitudes satisfying $\bigcup_i \mathcal{X}_i^{\mathrm{HC}} = \mathbb{R}$. The effect of (4.17) is shown in Fig. 4.4(a) and Fig. 4.4(b), where $\varepsilon_{\min} \leq 0$ and $\varepsilon_{\max} \geq 0$ denote the minimum and maximum clipping level, respectively. It should be noted that both the values of $\varepsilon_{\min}$ and $\varepsilon_{\max}$ are dependent on the achievable linear operational region of the LED, as depicted in Fig. 4.3 and Fig. 4.4. As shown in Fig. 4.4(b), the minimum clipping level associated with the ACO-OFDM system is given by $\varepsilon_{\min} = 0$, i.e., all the negative components are clipped. By contrast, for the DCO-OFDM system shown in Fig. 4.4(a), only some of the high-peak negative components are clipped.

Based on (4.14) and (4.17), we can show that the PDF of the clipped symbol can be formulated as

$$p_S(s) = \begin{cases} P_X(\varepsilon_{\min}) = Q\left(-\frac{\varepsilon_{\min}}{\sigma_X}\right), & \text{if } s = \varepsilon_{\min} \\ \frac{Q_1\left(0, \frac{s}{\sigma_X}\right)}{\sigma_X\sqrt{2\pi}}, & \text{if } s \in \mathcal{S}_2^{\mathrm{HC}} \\ 1 - P_X(\varepsilon_{\max}) = Q\left(\frac{\varepsilon_{\max}}{\sigma_X}\right), & \text{if } s = \varepsilon_{\max} \\ 0, & \text{otherwise}, \end{cases} \tag{4.18}$$

where $\mathcal{S}_2^{\mathrm{HC}} = \mathcal{X}_2^{\mathrm{HC}}$ is the region of unchanged amplitudes. Here, the relationship between the PDF of the input amplitude and the PDF of the corresponding output amplitude of HC is shown. Typically, applying hard clipping to the transmitted symbols may result in information loss, which is undesirable.

4.3.3 Principles of Symmetry Piecewise Companding Transform

As shown in Fig. 4.4(c), instead of using hard clipping, a specifically designed compander may be employed so that the biased signals can be operated in the desired region of the transmitter LED. In this case, we can let $f_{\mathrm{Tx}}(x) = f_{\mathrm{CT}}(x)$, where $f_{\mathrm{CT}}(x)$ denotes the CT function used at the transmitter. The basic concept of a symmetric piecewise compander is illustrated in Fig. 4.4(c). Below, we develop the underlying principles in order to gain insights into the design of the symmetric piecewise compander.

Firstly, let us divide the TD amplitudes of O-OFDM symbols into five regions denoted as $\mathcal{X}^{\mathrm{CT}}_{1,-} = (-\infty, -\varepsilon_X]$, $\mathcal{X}^{\mathrm{CT}}_{3,-} = (-\varepsilon_X, -\varepsilon_o]$, $\mathcal{X}^{\mathrm{CT}}_{2} = (-\varepsilon_o, \varepsilon_o)$, $\mathcal{X}^{\mathrm{CT}}_{3,+} = [\varepsilon_o, \varepsilon_X)$, $\mathcal{X}^{\mathrm{CT}}_{1,+} = [\varepsilon_X, +\infty)$, which can be further classified based on their magnitude into three types denoted as $\mathcal{X}^{\mathrm{CT}}_{1} = \mathcal{X}^{\mathrm{CT}}_{1,-} \bigcup \mathcal{X}^{\mathrm{CT}}_{1,+}$, $\mathcal{X}^{\mathrm{CT}}_{2}$ and $\mathcal{X}^{\mathrm{CT}}_{3} = \mathcal{X}^{\mathrm{CT}}_{3,-} \bigcup \mathcal{X}^{\mathrm{CT}}_{3,+}$. The first region $\mathcal{X}^{\mathrm{CT}}_{1}$ contains the high-peak components, which are hard clipped in our design. By contrast, in the second region $\mathcal{X}^{\mathrm{CT}}_{2}$, the corresponding magnitudes are small enough so that they remain unchanged. Finally, the amplitudes within the third region $\mathcal{X}^{\mathrm{CT}}_{3}$, which have moderate absolute values, are companded, as shown in Fig. 4.4(c). To simplify the implementation, we arrange for the CT function be symmetric about the origin. Hence, based on the above considerations, we can express the piecewise CT function as

$$S = f_{\mathrm{CT}}(X) = \begin{cases} \mathrm{sgn}(X)\varepsilon_S, & \text{if } X \in \mathcal{X}^{\mathrm{CT}}_{1} \\ X, & \text{if } X \in \mathcal{X}^{\mathrm{CT}}_{2} \\ \mathrm{sgn}(X)\Phi_{\mathrm{CT}}(|X|), & \text{if } X \in \mathcal{X}^{\mathrm{CT}}_{3}, \end{cases} \tag{4.19}$$

where the signum function is given by

$$\mathrm{sgn}(X) = \begin{cases} -1, & \text{if } X < 0 \\ 0, & \text{if } X = 0 \\ 1, & \text{if } X > 0. \end{cases} \tag{4.20}$$

In (4.19), the sub-function denoted as $\mathrm{sgn}(X)\Phi_{\mathrm{CT}}(|X|)$ is applied for transforming its input amplitude $X \in \mathcal{X}^{\mathrm{CT}}_{3}$ to the output amplitude in S, as shown by the shaded boxes in Fig. 4.4(c). Since there is an infinite variety of implementations for $\Phi_{\mathrm{CT}}(|X|)$, we have to set up some conditions for narrowing the range of choices for the companding functions. At this moment, we should note that in order to strike an attractive tradeoff between the PAPR reduction and the bit error performance, the companded signals should be mapped smoothly to the desirable range of the LEDs. Bearing this in mind, some necessary conditions may be stated as

C.1 $f_{\mathrm{CT}}(x)$ is symmetric across the origin;

C.2 $f_{\mathrm{CT}}(x)$ has to be a bijective function over $X \in \mathcal{X}_2^{\mathrm{CT}} \bigcup \mathcal{X}_3^{\mathrm{CT}}$;

C.3 $\mathrm{sgn}(X)\Phi_{\mathrm{CT}}(|X|)$ has to be a strictly monotonically increasing function over $X \in \mathcal{X}_3^{\mathrm{CT}}$;

C.4 $\Phi_{\mathrm{CT}}(|X|)$ can be expressed in closed-form;

C.5 The PDF of companded signals denoted as $p_S(s)$ has to satisfy the usual probability condition of $\int\limits_{-\infty}^{+\infty} p_S(s)\mathrm{d}s = 1$.

Based on these conditions, we can now continue by showing the relationship between the companding function and the PDF of the corresponding output amplitudes as follows.

Based on **C.1**, it may be readily shown that the PDF of the corresponding output amplitudes is symmetric about the y-axis, as seen in the third sub-figure of Fig. 4.4(c). Hence, the PDF of the companded signals' amplitude in S given in (4.19) can be formulated as

$$p_S(s) = \begin{cases} Q\left(\frac{\varepsilon_X}{\sigma_X}\right), & \text{if } s = \varepsilon_S \text{ or } -\varepsilon_S \\ \frac{Q_1\left(0, \frac{s}{\sigma_X}\right)}{\sigma_X\sqrt{2\pi}}, & \text{if } s \in \mathcal{S}_2^{\mathrm{CT}} \\ g_S(|s|), & \text{if } s \in \mathcal{S}_3^{\mathrm{CT}} \\ 0, & \text{otherwise,} \end{cases} \tag{4.21}$$

where due to **C.2**, two output amplitude regions are given by $\mathcal{S}_2^{\mathrm{CT}} = \mathcal{X}_2^{\mathrm{CT}} = (-\varepsilon_o, \varepsilon_o)$ and $\mathcal{S}_3^{\mathrm{CT}} = \mathcal{S}_{3,-}^{\mathrm{CT}} \bigcup \mathcal{S}_{3,+}^{\mathrm{CT}}$, with $\mathcal{S}_{3,-}^{\mathrm{CT}} = (-\varepsilon_S, -\varepsilon_o]$ and $\mathcal{S}_{3,+}^{\mathrm{CT}} = [\varepsilon_o, \varepsilon_S)$ corresponding to $\mathcal{X}_{3,-}^{\mathrm{CT}}$ and $\mathcal{X}_{3,+}^{\mathrm{CT}}$, respectively. Here, as shown in Fig. 4.4(c), the notation ε_o represents the break-points of the compander, while ε_X and ε_S are the cutoff levels associated with the input X and the output S of the compander, respectively. In (4.21), $g_S(|s|)$, which is symmetric about the y-axis, represents the Probability sub-Distribution Function (PsDF) of the amplitudes within $\mathcal{S}_3^{\mathrm{CT}}$, as represented by the shaded boxes in Fig. 4.4(c).

Bearing the symmetry of $g_S(s)$ in mind, we can simplify our forthcoming discussions by considering the CT of only the positive amplitudes. In this case, we have $S = \mathrm{sgn}(X)\Phi_{\mathrm{CT}}(|X|) = \Phi_{\mathrm{CT}}(X)$ and $g_S(|s|) = g_S(s)$ for the case of $X \in \mathcal{X}_{3,+}^{\mathrm{CT}}$ and $S \in \mathcal{S}_{3,+}^{\mathrm{CT}}$. To meet **C.5**, it is desirable to design a compander so that for each random variable $X_+ \in \mathcal{X}_{3,+}^{\mathrm{CT}}$, we have

$$\int\limits_{\varepsilon_o}^{X_+} p_X(u_x)\mathrm{d}u_x = \int\limits_{\varepsilon_o}^{\Phi_{\mathrm{CT}}(X_+)} g_S(u_s)\mathrm{d}u_s, \tag{4.22}$$

where we have $\Phi_{\mathrm{CT}}(X_+) \geq \varepsilon_o$ for $\Phi_{\mathrm{CT}}(X_+) \in \mathcal{S}_{3,+}^{\mathrm{CT}}$ due to the condition of **C.3**. Firstly, the Left-Hand-Side (LHS) of (4.22) can be calculated with the aid of (4.14)

$$S = f_{\mathrm{CT}}(X) = \begin{cases} \mathrm{sgn}(X)\varepsilon_S, & \text{if } X \in \mathcal{X}_1^{\mathrm{CT}} \\ X, & \text{if } X \in \mathcal{X}_2^{\mathrm{CT}} \\ \mathrm{sgn}(X) G_S^{-1}\left\{Q\left(\frac{\varepsilon_o}{\sigma_X}\right) - Q\left(\frac{|X|}{\sigma_X}\right) + G_S(\varepsilon_o)\right\}, & \text{if } X \in \mathcal{X}_3^{\mathrm{CT}} \end{cases} \tag{4.22}$$

---

as

$$\begin{aligned}\int_{\varepsilon_o}^{X_+} p_X(u_x)\mathrm{d}u_x =& P_X(X_+) - P_X(\varepsilon_o) \\ =& Q\left(\frac{\varepsilon_o}{\sigma_X}\right) - Q\left(\frac{X_+}{\sigma_X}\right). \end{aligned} \tag{4.23}$$

Before proceeding with the Right-Hand-Side (RHS) of (4.22), let us denote $G_S(s) = \int_{-\infty}^{s} g_S(u)\mathrm{d}u$ as the CDF of $g_S(s)$. Moreover, due to **C.4**, we restrict our attention to specific PsDF having closed-form expressions for both $G_S(s)$ and for its inverse function $G_S^{-1}(s)$. Then, the RHS of (4.22) can be formulated as

$$\int_{\varepsilon_o}^{\Phi_{\mathrm{CT}}(X_+)} g_S(u_s)\mathrm{d}u_s = G_S\left[\Phi_{\mathrm{CT}}(X_+)\right] - G_S(\varepsilon_o). \tag{4.24}$$

Upon substituting (4.23) and (4.24) into (4.22), we arrive at

$$Q\left(\frac{\varepsilon_o}{\sigma_X}\right) - Q\left(\frac{X_+}{\sigma_X}\right) = G_S\left[\Phi_{\mathrm{CT}}(X_+)\right] - G_S(\varepsilon_o). \tag{4.25}$$

With the aid of (4.25), the heuristic companding sub-function can now be expressed as

$$\Phi_{\mathrm{CT}}(X_+) = G_S^{-1}\left\{Q\left(\frac{\varepsilon_o}{\sigma_X}\right) - Q\left(\frac{X_+}{\sigma_X}\right) + G_S(\varepsilon_o)\right\} \tag{4.21}$$

for each input random variable of $X_+ \in \mathcal{X}_{3,+}^{\mathrm{CT}}$. Based on the symmetry, the general companding function for the amplitude of the TD symbols can be finally formulated in (4.22), as shown at the top of this page.

So far, we have demonstrated the relationship between the companding function $S = f_{\mathrm{CT}}(X)$ and the PDF $p_S(s)$ of the corresponding output amplitude. In particular, for a given PsDF $g_S(|s|)$, the companding sub-function $\mathrm{sgn}(X)\Phi_{\mathrm{CT}}(|X|)$ can be obtained with the aid of (4.21), which implies that we can design a compander in the probability domain. Below, we explore the characteristics of the PsDF $g_S(|s|)$ with the goal of identifying the conditions that can be used for the design of a compander.

4.3.4 Restrictions on the Design of the PsDF

As shown in (4.19), the companding sub-function $\mathrm{sgn}(X)\Phi_{\mathrm{CT}}(|X|)$ determines the final design of the symmetric piecewise compander. Furthermore, as shown in (4.22), the companding sub-function $\mathrm{sgn}(X)\Phi_{\mathrm{CT}}(|X|)$ can be obtained by specifying the PsDF $g_S(|s|)$ in the probability domain. Below, we detail some further restrictions imposed on the design of the PsDF.

Among the five necessary conditions of **C.1-C.5**, we can readily show that **C.2** and **C.5** can be used for quantifying both the PsDF and the companding sub-function, giving

$$G_S(\varepsilon_S) - G_S(\varepsilon_o) = Q\left(\frac{\varepsilon_o}{\sigma_X}\right) - Q\left(\frac{\varepsilon_X}{\sigma_X}\right). \tag{4.23}$$

We point out furthermore that since $\pm\varepsilon_o$ are unique partitioning points (i.e. we have $f_{\mathrm{CT}}(\pm\varepsilon_o) = \pm\varepsilon_o$), as a result of **C.2** and **C.5**, the PDF $p_S(s)$ should also be continuious at the break points of $\pm\varepsilon_o$, yielding

$$g_S(|\pm\varepsilon_o|) = p_X(\pm\varepsilon_o) = \frac{Q_1\left(0, \frac{\varepsilon_o}{\sigma_X}\right)}{\sigma_X\sqrt{2\pi}}. \tag{4.24}$$

Next, let us consider the moments of S, which are important metrics directly affecting the system's performance. Firstly, due to the symmetry of the PDF $p_S(s)$, it can be readily shown that the first moment or the mean of S is given by

$$\mu_S \triangleq \mathbb{E}[S] = \int_{-\infty}^{+\infty} s p_S(s)\mathrm{d}s = 0. \tag{4.25}$$

Secondly, the second moment of S can be derived as

$$\begin{aligned}
\mathbb{E}[S^2] &= \int_{-\infty}^{+\infty} s^2 p_S(s)\mathrm{d}s \\
&= 2\varepsilon_S^2 Q\left(\frac{\varepsilon_X}{\sigma_X}\right) + \int_{\mathcal{S}_2^{\mathrm{CT}}} s^2 \frac{Q_1\left(0, \frac{s}{\sigma_X}\right)}{\sigma_X\sqrt{2\pi}}\mathrm{d}s + \int_{\mathcal{S}_3^{\mathrm{CT}}} s^2 g_S(|s|)\mathrm{d}s \\
&= 2\varepsilon_S^2 Q\left(\frac{\varepsilon_X}{\sigma_X}\right) + \sigma_X^2 - 2\sigma_X^2 Q\left(\frac{\varepsilon_o}{\sigma_X}\right) - \varepsilon_o\sigma_x\sqrt{\frac{2}{\pi}}Q_1\left(0, \frac{\varepsilon_o}{\sigma_X}\right) \\
&\quad + 2\int_{\mathcal{S}_{3,+}^{\mathrm{CT}}} s^2 g_S(|s|)\mathrm{d}s,
\end{aligned} \tag{4.26}$$

which is actually the average electrical power level of the companded signals. Intuitively, the lower the power-loss of the companded signals, the better the system performance becomes. Hence, let us define an average power-loss function as

$$\begin{aligned}\mathcal{L}_{\mathrm{Po}} \triangleq & \mathbb{E}[X^2] - \mathbb{E}[S^2] \\ = & \sigma_X^2 - 2\varepsilon_S^2 Q\left(\frac{\varepsilon_X}{\sigma_X}\right) - \sigma_X^2 + 2\sigma_X^2 Q\left(\frac{\varepsilon_o}{\sigma_X}\right) \\ & + \varepsilon_o \sigma_x \sqrt{\frac{2}{\pi}} Q_1\left(0, \frac{\varepsilon_o}{\sigma_X}\right) - 2 \int\limits_{\mathcal{S}_{3,+}^{\mathrm{CT}}} s^2 g_S(|s|) \mathrm{d}s \\ = & 2\sigma_X^2 Q\left(\frac{\varepsilon_o}{\sigma_X}\right) - 2\varepsilon_S^2 Q\left(\frac{\varepsilon_X}{\sigma_X}\right) + \varepsilon_o \sigma_x \sqrt{\frac{2}{\pi}} Q_1\left(0, \frac{\varepsilon_o}{\sigma_X}\right) \\ & - 2 \int\limits_{\mathcal{S}_{3,+}^{\mathrm{CT}}} s^2 g_S(|s|) \mathrm{d}s, \end{aligned} \tag{4.27}$$

where $\mathcal{L}_{\mathrm{Po}} < 0$ means that the average power of signals is amplified after the CT, while $\mathcal{L}_{\mathrm{Po}} > 0$ indicates that there is a certain power loss due to the CT. Generally, it is preferred to design a compander, which is capable of minimising the average power-loss after the CT.

In summary, the PsDF $g_S(s)$ has to be designed to meet both (4.23) and (4.24), as well as to minimise the average power loss after the CT. Below, we consider the implementation of the symmetric piecewise compander.

4.3.5 Implementation of the Symmetric Piecewise Compander

Here we consider three types of functions as the implementation options for the PsDF, which we refer to as the CPsDF, the LPsDF as well as the NLPsDF. Again, we only detail the PsDF of positive amplitudes to simplify the presentation. We should note that in the following analysis, the value of ε is fixed since it is restricted by the operation dynamic range of the LED, as shown in Fig. 4.4.

CPsDF In this scheme, the sub-function is chosen as $g_S(s) = \alpha_1$ for $s \in \mathcal{S}_{3,+}^{\mathrm{CT}}$, where α_1 is a constant. Correspondingly, we can readily see that $G_S(s) = \alpha_1 s + \alpha_2$ and $G_S^{-1}(s) = (s - \alpha_2)/\alpha_1$, where α_2 is also a constant. Hence, with the aid of (4.22), $\Phi_{\mathrm{CT}}(|X|)$ for $X \in \mathcal{X}_3^{\mathrm{CT}}$ can be formulated as

$$\Phi_{\mathrm{CT}}(|X|) = \frac{1}{\alpha_1}\left[-Q\left(\frac{|X|}{\sigma_X}\right) + Q\left(\frac{\varepsilon_o}{\sigma_X}\right)\right] + \varepsilon_o, \tag{4.28}$$

where the constant α_1 can be obtained for meeting (4.23) and (4.24) as

$$\alpha_1 = \frac{Q\left(\frac{\varepsilon_o}{\sigma_X}\right) - Q\left(\frac{\varepsilon_X}{\sigma_X}\right)}{\varepsilon_S - \varepsilon_o} = \frac{Q_1\left(0, \frac{\varepsilon_o}{\sigma_X}\right)}{\sigma_X \sqrt{2\pi}}. \tag{4.29}$$

In particular, based on (4.29), ε_X can be expressed in terms of ε_o as

$$\varepsilon_X = \sigma_X Q^{-1}\left\{Q\left(\frac{\varepsilon_o}{\sigma_X}\right) - \frac{\varepsilon_S - \varepsilon_o}{\sigma_X\sqrt{2\pi}} Q_1\left(0, \frac{\varepsilon_o}{\sigma_X}\right)\right\}, \tag{4.30}$$

where the value of ε_o should be chosen to minimise the average power-loss of companded signals, under the constraint of

$$Q\left(\frac{\varepsilon_o}{\sigma_X}\right) - \frac{\varepsilon_S - \varepsilon_o}{\sigma_X\sqrt{2\pi}} Q_1\left(0, \frac{\varepsilon_o}{\sigma_X}\right) \geq 0 \tag{4.31}$$

for a given value of ε_S. As proved in the Appendix B, for a given $0 < \varepsilon_S \leq \sigma_X\sqrt{2/\pi}$, the value of ε_o is bounded by $0 \leq \varepsilon_o \leq \varepsilon_S$, while, for a given $\varepsilon_S > \sigma_X\sqrt{2/\pi}$, the value of ε_o is bounded by $\varepsilon_{o,\min} \leq \varepsilon_o < \varepsilon_S$, where $\varepsilon_{o,\min}$ is the lower bound of ε_o still meeting the condition of (4.31).

Then, upon substituting (4.30) and $g_S(s) = \alpha_1$ into (4.27), the average power-loss function can be obtained as

$$\mathcal{L}_{\text{Po}} = 2(\sigma_X^2 - \varepsilon_S^2) Q\left(\frac{\varepsilon_o}{\sigma_X}\right) + \frac{1}{\sigma_X}\sqrt{\frac{2}{\pi}} Q_1\left(0, \frac{\varepsilon_o}{\sigma_X}\right)\left[\frac{1}{3}\varepsilon_o^3 + \varepsilon_o(\sigma_X^2 - \varepsilon_S^2) + \frac{2}{3}\varepsilon_S^3\right]. \tag{4.32}$$

In order to obtain the optimal value of ε_o for minimising $\mathcal{L}_{\text{Po}}$, let us take the first derivative of $\mathcal{L}_{\text{Po}}$ with respect to ε_o, yielding

$$\frac{\mathrm{d}\mathcal{L}_{\text{Po}}}{\mathrm{d}\varepsilon_o} = -\frac{1}{3\sigma_X^2}\sqrt{\frac{2}{\pi}} Q_1\left(0, \frac{\varepsilon_o}{\sigma_X}\right)\varepsilon_o(\varepsilon_o + 2\varepsilon_S)(\varepsilon_o - \varepsilon_S)^2 \leq 0 \tag{4.33}$$

for any $0 \leq \varepsilon_o < \varepsilon_S$. Eq.(4.33) implies that the average-power loss function $\mathcal{L}_{\text{Po}}$ is a non-increasing function. Hence, the optimal solution for $\min_{\varepsilon_o} |\mathcal{L}_{\text{Po}}|$ is $\varepsilon_o = \varepsilon_S$. In this case, the CT becomes HC, which goes against the goal of applying CT. Let the minimum average power-loss be expressed as

$$\mathcal{L}_{\text{Po,min}} = \sigma_X^2\left[2\left(1 - \frac{\varepsilon_S^2}{\sigma_X^2}\right) Q(\varepsilon_S) + \sqrt{\frac{2}{\pi}}\frac{\varepsilon_S}{\sigma_X} Q_1\left(0, \frac{\varepsilon_S}{\sigma_X}\right)\right]. \tag{4.34}$$

Then, a sub-optimal solution is to find $\varepsilon_o < \varepsilon_S$ so that the difference between the resultant average power-loss and the minimum average power-loss $\mathcal{L}_{\text{Po,min}}$ is within a tolerable margin of $\mathcal{L}_{\text{C}}$, i.e., the value of ε_o is chosen to satisfy

$$\mathcal{L}_{\text{Po}} - \mathcal{L}_{\text{Po,min}} \leq \mathcal{L}_{\text{C}}, \tag{4.35}$$

where based on a certain value of $\mathcal{L}_{\text{C}}$, let us denote the corresponding parameters as $\varepsilon_o^{\mathcal{L}_{\text{C}}}$ and $\varepsilon_X^{\mathcal{L}_{\text{C}}}$. Finally, based on the values of $\varepsilon_o^{\mathcal{L}_{\text{C}}}$, $\varepsilon_X^{\mathcal{L}_{\text{C}}}$ and α_1, the desired CPsDF based compander can be obtained with the aid of substituting (4.28) into (4.22).

LPsDF In the context of this scheme, the PsDF is chosen to be a linear function expressed as $g_S(s) = \alpha_1 s + \alpha_2$ for $s \in \mathcal{S}_{3,+}^{\text{CT}}$, where both α_1 and α_2 are constants.

Correspondingly, we can find that $G_S(s) = \alpha_1[s + (\alpha_2/\alpha_1)]^2/2 + \alpha_3 - \alpha_2^2/(2\alpha_1)$ and $G_S^{-1}(s) = [\sqrt{2\alpha_1 s + \alpha_2^2 - 2\alpha_1\alpha_3} - \alpha_2]/\alpha_1$, where α_3 is a constant. Then, with the aid of (4.22), $\Phi_{\mathrm{CT}}(|X|)$ for $X \in \mathcal{X}_3^{\mathrm{CT}}$ can be formulated as

$$\Phi_{\mathrm{CT}}(|X|) = -\sqrt{\frac{-2Q\left(\frac{|X|}{\sigma_X}\right) + 2Q\left(\frac{\varepsilon_o}{\sigma_X}\right)}{\alpha_1} + \left(\varepsilon_o + \frac{\alpha_2}{\alpha_1}\right)^2} - \frac{\alpha_2}{\alpha_1}, \tag{4.36}$$

where the constants α_1 and α_2 required to satisfy (4.23) and (4.24) can be found to be

$$\alpha_1 = 2\left[\frac{Q\left(\frac{\varepsilon_o}{\sigma_X}\right) - Q\left(\frac{\varepsilon_X}{\sigma_X}\right)}{(\varepsilon_S - \varepsilon_o)^2} - \frac{Q_1\left(0, \frac{\varepsilon_o}{\sigma_X}\right)}{\sigma_X\sqrt{2\pi}(\varepsilon_S - \varepsilon_o)}\right] \tag{4.37}$$

and

$$\alpha_2 = \frac{(\varepsilon_S + \varepsilon_o)Q_1\left(0, \frac{\varepsilon_o}{\sigma_X}\right)}{\sigma_X\sqrt{2\pi}(\varepsilon_S - \varepsilon_o)} - \frac{2\varepsilon_o\left[Q\left(\frac{\varepsilon_o}{\sigma_X}\right) - Q\left(\frac{\varepsilon_X}{\sigma_X}\right)\right]}{(\varepsilon_S - \varepsilon_o)^2}, \tag{4.38}$$

respectively. Note that as a result of (4.22), the LPsDF $g_S(s) = \alpha_1 s + \alpha_2$ is restricted to be a non-increasing function in the region of $\mathcal{S}_{3,+}^{\mathrm{CT}}$. Furthermore, the general condition of $g_S(s) = \alpha_1 s + \alpha_2 \geq 0$ always has to be satisfied. Thus, the values of ε_o and ε_X should be chosen to satisfy

$$\frac{Q_1\left(0, \frac{\varepsilon_o}{\sigma_X}\right)}{2\sigma_X\sqrt{2\pi}}(\varepsilon_S - \varepsilon_o) < Q\left(\frac{\varepsilon_o}{\sigma_X}\right) - Q\left(\frac{\varepsilon_X}{\sigma_X}\right) < \frac{Q_1\left(0, \frac{\varepsilon_o}{\sigma_X}\right)}{\sigma_X\sqrt{2\pi}}(\varepsilon_S - \varepsilon_o). \tag{4.39}$$

Next, based on (4.27), the average power-loss function of the LPsDF-based CT can be expressed as

$$\begin{aligned}\mathcal{L}_{\mathrm{Po}} =& 2\Bigg\{Q\left(\frac{\varepsilon_X}{\sigma_X}\right)[(\varepsilon_o + \varepsilon_S)^2 + \varepsilon_S^2] - Q\left(\frac{\varepsilon_o}{\sigma_X}\right)[(\varepsilon_o + \varepsilon_S)^2 + 2\varepsilon_S^2 - 1] \\ &+ \frac{Q_1\left(0, \frac{\varepsilon_o}{\sigma_X}\right)}{\sigma_X\sqrt{2\pi}}[2\varepsilon_o^3 + \varepsilon_o^2\varepsilon_S + \varepsilon_o\varepsilon_S^2 + \varepsilon_o\sigma_X^2 + 2\varepsilon_S^3]\Bigg\}.\end{aligned} \tag{4.40}$$

Since both the values of ε_o and ε_X are unknown, it is not easy to derive a closed-form expression for the minimum average power-loss in this case. Nevertheless, for the sake of comparison, we can simply let ε_X be equal to the parameter obtained by the CPsDF-based CT, i.e. we have $\varepsilon_X = \varepsilon_X^{\mathcal{L}_{\mathrm{C}}}$. Then, the value of ε_o can be obtained by solving the optimisation problem of

$$\varepsilon_o^{\mathrm{L}} = \min_{\varepsilon_o} \mathcal{L}_{\mathrm{Po}} \quad \text{s.t.} \quad (4.39) \tag{4.41}$$

for given values of ε and $\varepsilon_X = \varepsilon_X^{\mathcal{L}_{\mathrm{C}}}$. Finally, based on the parameters $\varepsilon_o^{\mathrm{L}}$, $\varepsilon_X^{\mathcal{L}_{\mathrm{C}}}$ and ε_S, the desired LPsDF based compander can be obtained with the aid of substituting (4.36) into (4.22).

NLPsDF In this scenario, we consider a specific type of nonlinear functions, which is the square-root based function expressed as $g_S(s) = [\alpha_1(s + \alpha_2)]^{-\frac{1}{2}} + \alpha_3$ for $s \in \mathcal{S}_{3,+}^{\mathrm{CT}}$, where α_1, α_2 and α_3 are constants. Note that, other types of NLPsDF can be similarly analysed. However, we leave other types of NLPsDF for our future research. Similarly, we can find $G_S(s) = 2\sqrt{(s + \alpha_2)/\alpha_1} + \alpha_3 s + \alpha_4$ and $G_S^{-1}(s) = \{\sqrt{[s - \alpha_4 + \alpha_3\alpha_2 + 1/(\alpha_1\alpha_3)]/\alpha_3} - 1/(\alpha_3\sqrt{\alpha_1})\}^2 - \alpha_2$, where α_4 is a constant. Therefore, with the aid of (4.22), $\Phi_{\mathrm{CT}}(|X|)$ for $X \in \mathcal{X}_3^{\mathrm{CT}}$ can be formulated as

$$\Phi_{\mathrm{CT}}(|X|) = \left\{ \left[\frac{-Q\left(\frac{|X|}{\sigma_x}\right) + Q\left(\frac{\varepsilon_o}{\sigma_X}\right)}{\alpha_3} + \left(\sqrt{\varepsilon_o + \alpha_2} + \frac{1}{\alpha_3\sqrt{\alpha_1}} \right)^2 \right]^{\frac{1}{2}} - \frac{1}{\alpha_3\sqrt{\alpha_1}} \right\}^2 - \alpha_2. \tag{4.42}$$

From (4.42), it can be readily shown that the compander is determined by the parameters α_1, α_2 and α_3. When either ε_o or ε_X is unknown, the problem of designing the NLPsDF based CT becomes undetermined. Hence, for the sake of both implementation and comparison, the values of ε_o and ε_X are assumed to be fixed in the case of NLPsDF. Specifically, we let $\varepsilon_X = \varepsilon_X^{\mathcal{L}_{\mathrm{C}}}$. Thus, to meet (4.23) and (4.24), α_1 and α_3 can be formulated in terms of α_2, while the value of α_2 is chosen by minimising the average power-loss function $\mathcal{L}_{\mathrm{Po}}$ given in (4.27). Finally, upon substituting the values of α_1, α_2 and α_3 into (4.42), we can obtain the desired NLPsDF based compander.

Finally, the CPsDF, LPsDF and NLPsDF based expanders can be simply obtained by calculating the related inverse functions of (4.19), respectively.

4.4 Performance Analysis

Generally, the nonlinear distortion of TD OFDM signals results in loss of orthogonality, yielding ICI, which may degrade the attainable system performance. In this section, we analyse the nonlinear effect of both CO-OFDM and of our proposed CTO-OFDM systems. For notational brevity, the definitions given in (4.12a) and (4.12b) are also used in the following analysis.

4.4.1 Generalised Analytical Model for O-OFDM Systems

Let us commence by introducing a generalised analytical model for the O-OFDM systems considered in this chapter. Firstly, as mentioned in Section 4.2.1, when M is sufficiently large, the TD symbols $x_{\mathrm{T}}(l)$ (i.e., X) approximately follow the Gaussian distribution with a mean of zero and a variance of σ_X^2. In this case, the Bussgang theorem [184] can be invoked for analysing the effects of nonlinear distortion. Since the nonlinearity considered in this paper is memoryless, the nonlinearity of the transmitter processor expressed as $S = f_{\mathrm{Tx}}(X)$ can be modelled as [184]

$$S = \rho_{\mathrm{a}} X + W, \tag{4.43}$$

where ρ_{a} is the attenuation factor that can be obtained as

$$\begin{aligned}\rho_{\mathrm{a}} =& \frac{\mathbb{E}[SX]}{\mathbb{E}[X^2]} \\ =& \frac{1}{\sigma_X^2}\mathbb{E}\left[f_{\mathrm{Tx}}(X)X\right] \\ =& \frac{1}{\sigma_X^2}\int\limits_{-\infty}^{\infty} x f_{\mathrm{Tx}}(x) p_X(x) \mathrm{d}x. \end{aligned} \tag{4.44}$$

Based on [184], the distortion term W in (4.43) is uncorrelated with X, i.e. we have $\mathbb{E}[WX] = 0$. The mean and variance of the distortion term W can be derived as

$$\begin{aligned}\mu_w \triangleq& \mathbb{E}[W] \\ =& \mathbb{E}[S - \rho_{\mathrm{a}} X] = \mathbb{E}[S] - \rho_{\mathrm{a}}\mathbb{E}[X] \\ =& \mathbb{E}[S] - 0 \\ =& \int\limits_{-\infty}^{\infty} s p_S(s) \mathrm{d}s \end{aligned} \tag{4.45}$$

and

$$\begin{aligned}\sigma_w^2 \triangleq& \mathbb{E}\left[W^2\right] - (\mathbb{E}[W])^2 \\ =& \mathbb{E}[(S - \rho_{\mathrm{a}} X)^2] - \mu_w^2 \\ =& \mathbb{E}[S^2] - \rho_{\mathrm{a}}^2 \mathbb{E}[X^2] - \mu_w^2 \\ =& \int\limits_{-\infty}^{\infty} s^2 p_S(s) \mathrm{d}s - \rho_{\mathrm{a}}^2 \sigma_x^2 - \mu_w^2, \end{aligned} \tag{4.46}$$

respectively.

Next, similarly to the TD modelling shown in (4.12), let the FD symbol of each subchannel shown in (4.4) and (4.5) be modelled as

$$\left\{\mathsf{X} : \mathsf{X}_i \triangleq x_{\mathrm{F}}(i) \in \mathbb{C}\right\}; \tag{4.47a}$$

$$\left\{\mathsf{Y} : \mathsf{Y}_i \triangleq y_{\mathrm{F}}(i) \in \mathbb{C}\right\}; \tag{4.47b}$$

$$\left\{\mathsf{N} : \mathsf{N}_i \triangleq n_{\mathrm{F}}(i) \in \mathbb{C}\right\}; \tag{4.47c}$$

$$\left\{\mathsf{W} : \mathsf{W}_i \triangleq w_{\mathrm{F}}(i) \in \mathbb{C}\right\}, \tag{4.47d}$$

where $w_{\mathrm{F}}(i)$ represents the interference experienced by the ith subchannel, which is engendered by the distortion W given in (4.43). Then, based on (4.43), we can readily model the received FD symbol shown in (4.5) as

$$\mathsf{Y} = \rho_{\mathrm{a}} h_{\mathrm{F}} \mathsf{X} + h_{\mathrm{F}} \mathsf{W} + \mathsf{N}. \tag{4.48}$$

4.4.2 SINR Analysis

Based on (4.48), the received instantaneous Signal-to-Interference-plus-Noise power Ratio (SINR) of the ith subchannel can be expressed as

$$\begin{aligned}\gamma_{\mathrm{d}}(i) =& \frac{\rho_{\mathrm{a}}^2 \left|h_{\mathrm{F}}(i)\right|^2 \mathbb{E}[|\mathsf{X}|^2]}{\left|h_{\mathrm{F}}(i)\right|^2 \mathbb{E}[|\mathsf{W}|^2] + \mathbb{E}[|\mathsf{N}|^2]} \\ =& \frac{\rho_{\mathrm{a}}^2 \sigma_X^2}{\sigma_w^2 + \mu_w^2 + \frac{\sigma_{\mathrm{n}}^2}{|h_{\mathrm{F}}(i)|^2}}.\end{aligned} \tag{4.49}$$

According to Section 4.2, only the subchannels indexed with $i = 1, \ldots, N_{\mathrm{d}}$ are used for data transmission. Hence, the nonlinear effect induced by the transmitter processor $f_{\mathrm{Tx}}(X)$ on the data symbols can be quantified in terms of the average SINR of

$$\bar{\gamma}_{\mathrm{d}} = \frac{1}{N_{\mathrm{d}}} \sum_{i=1}^{N_{\mathrm{d}}} \gamma_{\mathrm{d}}(i), \tag{4.50}$$

where, upon substituting (4.49) into (4.50), we can show that for the time-invariant VLC channels, the parameters that determine the nonlinear effects are ρ_{a}, σ_w^2 and μ_w^2. Furthermore, it can be readily shown that the higher $\bar{\gamma}_{\mathrm{d}}$, the lower the nonlinear effects experienced by the O-OFDM systems becomes. Hence the better the performance becomes. Below, the SINRs of the various O-OFDM systems considered in this chapter are derived.

DCO-OFDM

First, for the DCO-OFDM system, let us rewrite (4.43) as

$$S = \rho_{\mathrm{a,DC}} X + W_{\mathrm{DC}}, \tag{4.51}$$

where, upon substituting (4.13) and (4.17) into (4.44), the attenuation factor $\rho_{\mathrm{a,DC}}$ is given by

$$\rho_{\mathrm{a,DC}} = Q\left(\frac{\varepsilon_{\min}}{\sigma_X}\right) - Q\left(\frac{\varepsilon_{\max}}{\sigma_X}\right). \tag{4.52}$$

Moreover, upon substituting (4.18) into (4.45) and (4.46), the mean and variance of the distortion term can be derived as

$$\begin{aligned}\mu_{w_{\mathrm{DC}}} =& \varepsilon_{\min} Q\left(-\frac{\varepsilon_{\min}}{\sigma_X}\right) + \varepsilon_{\max} Q\left(\frac{\varepsilon_{\max}}{\sigma_X}\right) \\ &+ \frac{\sigma_X}{\sqrt{2\pi}}\left[Q_1\left(0, \frac{\varepsilon_{\min}}{\sigma_X}\right) - Q_1\left(0, \frac{\varepsilon_{\max}}{\sigma_X}\right)\right] \end{aligned} \tag{4.53}$$

and

$$\begin{aligned}\sigma^2_{w_{\mathrm{DC}}} =& \varepsilon^2_{\min} + (\sigma^2_X - \varepsilon^2_{\min}) Q\left(\frac{\varepsilon_{\min}}{\sigma_X}\right) + \varepsilon_{\min} \frac{\sigma_X Q_1\left(0, \frac{\varepsilon_{\min}}{\sigma_X}\right)}{\sqrt{2\pi}} \\ &- (\sigma^2_X - \varepsilon^2_{\max}) Q\left(\frac{\varepsilon_{\max}}{\sigma_X}\right) - \varepsilon_{\max} \frac{\sigma_X Q_1\left(0, \frac{\varepsilon_{\max}}{\sigma_X}\right)}{\sqrt{2\pi}} \\ &- \rho^2_{\mathrm{a,DC}} \sigma^2_x - \mu^2_{w_{\mathrm{DC}}}, \end{aligned} \tag{4.54}$$

respectively. Finally, upon substituting (4.52), (4.53) and (4.54) into (4.49), we obtain the SINR for the DCO-OFDM system.

Discussions Recall for Section 4.2.1 that the constellation energy of a given QAM scheme is normalised to unity, so that the sensitivity to nonlinear distortions is the same for different CO-OFDM systems. In this case, as shown in Section 4.3.1, the signal variance of the DCO-OFDM system using CSIM is much lower than that of the DCO-OFDM system employing QAM. Note that the lower-bounded clipping level $\varepsilon_{\min}$ is restricted to be non-positive values, as defined in Section 4.3.2. Since the Q-function is a monotonically decreasing function, we can readily show that the lower the signal variance σ^2_X, the higher the value of $\rho_{\mathrm{a,DC}}$ given in (4.52) becomes, while, the smaller the value of $\mu_{w_{\mathrm{DC}}}$ given in (4.53) and $\sigma^2_{w_{\mathrm{DC}}}$ given in (4.54) become. Upon substituting these parameters into (4.49), we can readily see that the lower the signal variance, the higher the SINR becomes, yielding a better overall system performance. Therefore, we can show that at the same sensitivity to nonlinear clipping, the CSIM scheme is capable of attaining a better performance than that of the QAM scheme for the DCO-OFDM systems, as it will be shown in Section 4.5.

CTO-OFDM Here, we consider two specific cases for the CTO-OFDM systems.

In the first case, we assume that the expander is not invoked at the receiver, i.e. the scheme shown in the upper dashed box of Fig. 4.2 is used. In this case, both the CT and the HC components are analysed as follows. Firstly, we can express (4.43) as

$$S = \rho_{\mathrm{a,CT}} X + W_{\mathrm{CT}}. \tag{4.55}$$

Upon substituting (4.13) and (4.19) into (4.44), the attenuation factor $\rho_{\text{a,CT}}$ can be expressed as

$$\begin{aligned}\rho_{\text{a,CT}} =& \frac{1}{\sigma_X^2}\int\limits_{-\infty}^{\infty} x f_{\text{CT}}(x) p_X(x)\mathrm{d}x \\ =& \frac{2}{\sigma_X^2}\left\{\int\limits_{0}^{\varepsilon_o} x^2 p_X(x)\mathrm{d}x + \varepsilon_S \int\limits_{\varepsilon_X}^{\infty} x p_X(x)\mathrm{d}x + \int\limits_{\varepsilon_o}^{\varepsilon_X} x f_{\text{CT}}(x) p_X(x)\mathrm{d}x\right\} \\ =& 1 - 2Q\left(\frac{\varepsilon_o}{\sigma_X}\right) + \frac{1}{\sigma_X}\sqrt{\frac{2}{\pi}}\left[\varepsilon_S Q_1\left(0, \frac{\varepsilon_X}{\sigma_X}\right) - \varepsilon_o Q_1\left(0, \frac{\varepsilon_o}{\sigma_X}\right)\right] \\ &+ \frac{2}{\sigma_x^2}\mathbb{E}\left[SX|X \in \mathcal{X}_{3,+}^{\text{CT}}\right],\end{aligned} \tag{4.56}$$

where the last term is defined as $\mathbb{E}\left[SX|X \in \mathcal{X}_{3,+}^{\text{CT}}\right] \triangleq \int\limits_{\varepsilon_o}^{\varepsilon_X} x f_{\text{CT}}(x) p_X(x)\mathrm{d}x$, for which closed-form formulas can be derived, when the implementations of the CPsDF, LPsDF as well as NLPsDF based CTs given in Section 4.3.5 are assumed. However, for the sake of simplicity, in this paper, Monte Carlo simulations are applied for calculating the term $\mathbb{E}\left[SX|X \in \mathcal{X}_{3,+}^{\text{CT}}\right]$ for each of the above-mentioned implementations. Next, the mean of the distortion term W_{CT} can be obtained by substituting (4.21) into (4.45), yielding

$$\mu_{w_{\text{CT}}} = 0. \tag{4.57}$$

Furthermore, based on (4.27), we can express the variance of the distortion term W_{CT} in term of the average power-loss function as

$$\begin{aligned}\sigma_{w_{\text{CT}}}^2 =& \mathbb{E}[S^2] - \rho_{\text{a,CT}}^2\sigma_x^2 - \mu_{w_{\text{CT}}}^2 \\ =& \mathbb{E}[X^2] - \mathcal{L}_{\text{Po}} - \rho_{\text{a,CT}}^2\sigma_x^2 \\ =& \sigma_X^2 - \mathcal{L}_{\text{Po}} - \rho_{\text{a,CT}}^2\sigma_x^2.\end{aligned} \tag{4.58}$$

Consequently, the SINR of this case can be obtained by substituting (4.56), (4.57) and (4.58) into (4.49).

In the second case, we assume that the CT components are perfectly restored without amplifying the noise at the receiver side. However, no processing is assumed by the HC components. It can be readily shown that this is actually equivalent to the case of DCO-OFDM. But, the detailed expressions are omitted here since they can be obtained from those of the DCO-OFDM by substituting $\varepsilon_{\min}$ and $\varepsilon_{\max}$ into $-\varepsilon_X$ and ε_X, respectively. Thus, when the HC of DCO-OFDM is assumed to be symmetric in conjunction with $\varepsilon_{\min} = -\varepsilon_S$ and $\varepsilon_{\max} = \varepsilon_S$, we can readily show that our CTO-OFDM is capable of outperforming DCO-OFDM, since we have $\varepsilon_X > \varepsilon_S$ implying a higher SINR for our CTO-OFDM than that of DCO-OFDM. However, it should be noted that this is achieved at the cost of an increased complexity.

Table 4.1: Parameters for All Simulations

	Q	M	N_d	N_d/M	L_cp
ACO-OFDM	$4, 16, 64, 256$	256	64	25%	5 or 13
DCO-OFDM			127	49.61%	
CTO-OFDM			127	49.61%	

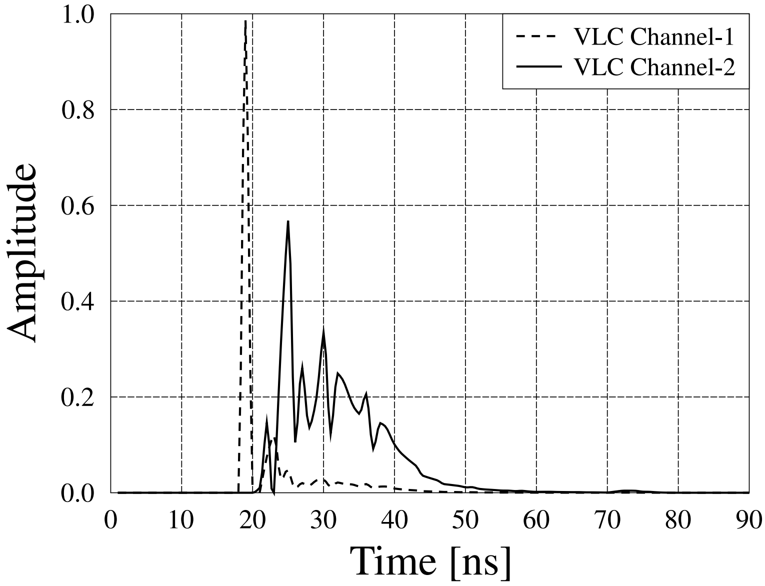

Figure 4.5: Two indoor VLC channels generated according to [183] used in the simulations.

4.5 Performance Results

In this section, simulation results are provided for investigating the performance of the CO-OFDM and CTO-OFDM systems. The system setup and the parameters used in our simulations are summarised in Table 4.1. We consider the communication scenario, where the transmitter and receiver are placed in a room with dimensions of [length=4 m, width=4 m, height=8 m]. Correspondingly, the transmitter LED is placed at the position of [0.06 m, 0.06 m, 6 m], while the PD is placed at the position of [1.5 m, 2.5 m, 1 m]. The other parameters for the transmitter, receiver, as well as the reflectance of building material are assumed to be the same as those stated in [183]. Specifically, three bounces are considered for calculating the impulse response of the VLC channels expressed in (4.3). In our simulations, the pair of indoor VLC multipath channels shown in Fig. 4.5 are considered. As seen in Fig. 4.5, the second channel model is more dispersive than the first channel model. Furthermore, we consider O-OFDM systems using QPSK, 16QAM, 64QAM or 256QAM in conjunction with $M = 256$ subcarriers, among which N_d subcarriers are used for data transmission. According to the principles of the O-OFDM systems considered, we have $N_\mathrm{d} = (M-2)/2$ for both the DCO-OFDM and CTO-OFDM systems, while $N_\mathrm{d} = M/4$ for the ACO-OFDM system. Therefore, it can be shown that about $N_\mathrm{d}/M = 49.61\%$ of the subchannels are actively used for data transmission in both the DCO-OFDM and the CTO-OFDM systems. By contrast, only $N_\mathrm{d}/M = 25\%$ subchannels are employed by the ACO-OFDM system. In all the O-OFDM systems, the CP length is chosen to be $L_\mathrm{cp} = 5$ and 13 samples for the first and second VLC channel models, respectively. For the sake of comparison, three dynamic ranges are considered, namely $2\varepsilon_S = (\varepsilon_\mathrm{max} - \varepsilon_\mathrm{min}) = 4$, 5 and 6.

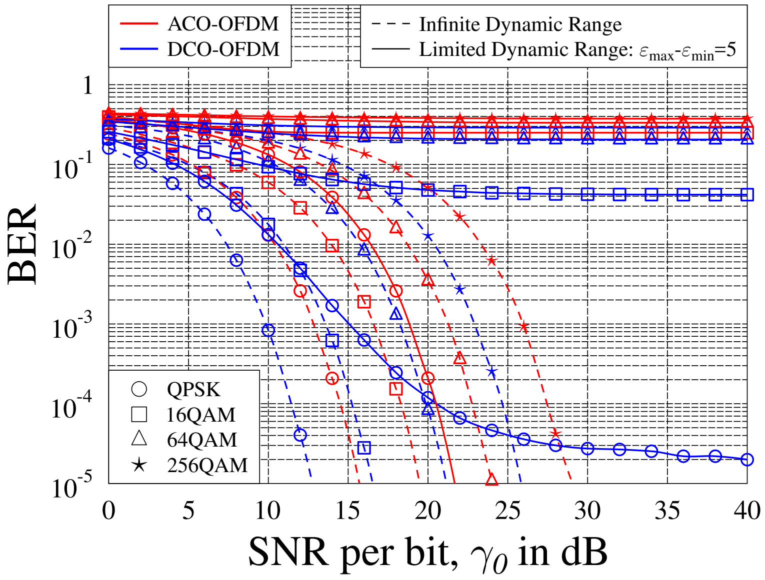

Figure 4.6: Performance comparison between the DCO-OFDM and ACO-OFDM systems using QPSK, 16QAM and 256QAM, when communicating over AWGN channels. All other system parameters are summarised in Table 4.1.

In Fig. 4.6, the BER performance of the ACO-OFDM and DCO-OFDM systems is compared, when communicating over non-dispersive AWGN channels. In this figure, QPSK, 16QAM, 64QAM and 256QAM are considered. Correspondingly, a CP length of $L_\mathrm{cp} = 0$ is set for both the systems. For the dynamic range, in addition to $\varepsilon_\mathrm{max} - \varepsilon_\mathrm{min} = 5$, we also consider the ideal scenario of having an infinite dynamic range. Specifically, the dynamic range set for the DCO-OFDM system is $[\varepsilon_\mathrm{min}, \varepsilon_\mathrm{max}] = [-1, 4]$. From the results of Fig. 4.6, we infer the following observations. First, for a given CO-OFDM system operating with a limited dynamic range, as the constellation size Q increases, the BER becomes more and more sensitive to the nonlinear distortion imposed by the hard clipping. This trend is the same as that observed in the classic OFDM system in RF communications, experiencing nonlinear distortion, as shown in [91, 92]. Finally, as seen in Fig. 4.6, an error floor occurs for the CO-OFDM systems associated with large constellation sizes for a limited dynamic range. This is because the nonlinear distortion generated by hard clipping usually results in ICI, as detailed in Section 4.4. Hence, when the SNR is sufficiently high, the SINR is dominated by the ICI, as seen in (4.49). As a result, the system exhibits an error floor.

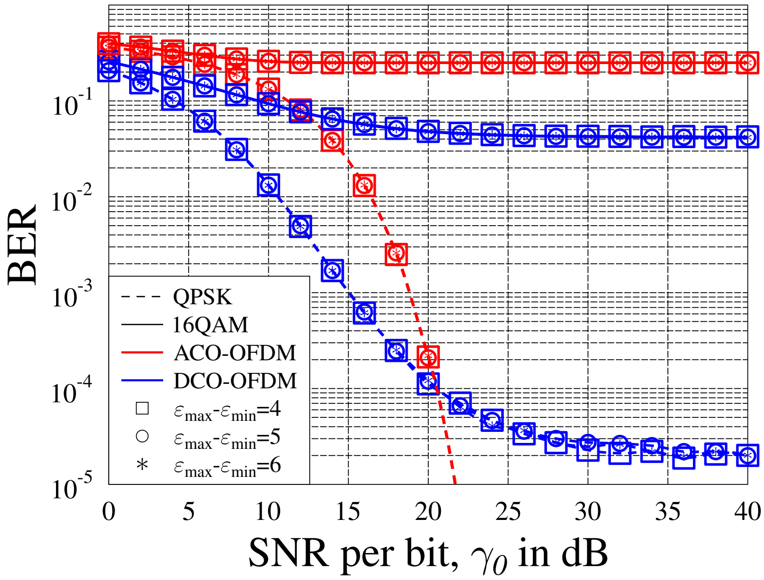

Figure 4.7: BER performance of both the DCO-OFDM and ACO-OFDM systems operated with different dynamic ranges, when communicating over AWGN channels. All other system parameters are summarised in Table 4.1.

In Fig. 4.7, we study the BER performance of the DCO-OFDM and ACO-OFDM systems for different dynamic ranges of $\varepsilon_{\max} - \varepsilon_{\min} = 4$, 5 and 6, when communicating over AWGN channels. Both QPSK and 16QAM are characterised. Again, due to the AWGN channels considered, a CP length of $L_{\mathrm{cp}} = 0$ is assumed. Specifically, the dynamic ranges of the DCO-OFDM system are set to $[-1, 3]$, $[-1, 4]$ and $[-1, 5]$. Observe from Fig. 4.7 that there is no significant difference among the BER curves of a given CO-OFDM system for a given constellation scheme, when different dynamic ranges are used. This observation can be explained as follows. According to our analytical results given in Section 4.4.2, the achievable SINR of both CO-OFDM systems is mainly dependent on the lower clipping limit $\varepsilon_{\min}$, as shown in (4.49). In other words, given a sufficiently wide dynamic range, the upper clipping limit $\varepsilon_{\max}$ has little impact on the resultant parameters of ρ_{a}, μ_w and σ_w^2, as indicated by (4.52)-(4.54). In this case, when the hard clipping scheme is employed, the system performance can be hardly improved by further increasing the dynamic range by increasing the upper clipping limit $\varepsilon_{\max}$.

Table 4.2: Analytical Results of System Complexity

Rate in bits/s/Hz	VLC System	Parameters (m, N, k, Q)	Complexity order of system in dB
0.9922	DCO-OFDM-QPSK	$(1, 1, 1, 4)$	28.0277
	DCO-OFDM-CSIM	$(4, 16, 1, 16)$	39.0998
	DCO-OFDM-CSIM	$(4, 64, 1, 4)$	39.0998
1.2344	DCO-OFDM-CSIM	$(4, 256, 1, 4)$	45.1204

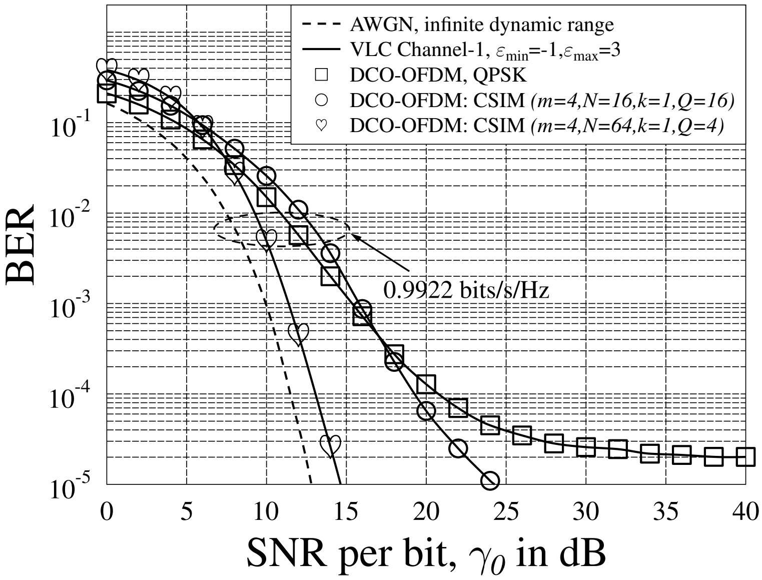

Figure 4.8: BER performance of the DCO-OFDM system using QPSK and CSIM, when communicating over the VLC channel-1. The dynamic range is set to [-1,3]. All other system parameters are summarised in Table 4.1 and Table 4.2.

In Fig. 4.8-4.12, we investigate the BER performance of the DCO-OFDM system using QPSK and CSIM, when communicating over the VLC channels. In these figures, The dynamic ranges of $[-1, 3]$ and $[-2, 2]$ are considered. For the DCO-OFDM system using QPSK, the MAR is 0.9922 bits/s/Hz. By contrast, the same MAR is attained by the CSIM schemes associated with $(m = 4, N = 16, k = 1, Q =$

16) and $(m = 4, N = 64, k = 1, Q = 4)$. To elaborate further, the CSIM scheme associated with $(m = 4, N = 256, k = 1, Q = 4)$ and characterised in Fig. 4.12 yields the MAR of 1.2344 bits/s/Hz. In particular, for the DCO-OFDM system using all the three CSIM schemes, a total of $G = 31$ groups of CSIM symbols are transmitted within each O-OFDM symbol block. For the sake of comparison, the remaining $(N_{\rm d} - mG) = 3$ FD subcarriers convey QPSK symbols. Furthermore, when CSIM is employed, the low-complexity receiver scheme shown in the upper dashed box of Fig. 4.2 is used, while the ML detector of Section 3.3.1 is employed. The corresponding analytical results of systems' complexity order, which are obtained based on (4.9) and (4.10), are given in Table 4.2, From the simulation results of Fig. 4.8-4.12, we can infer the following observations.

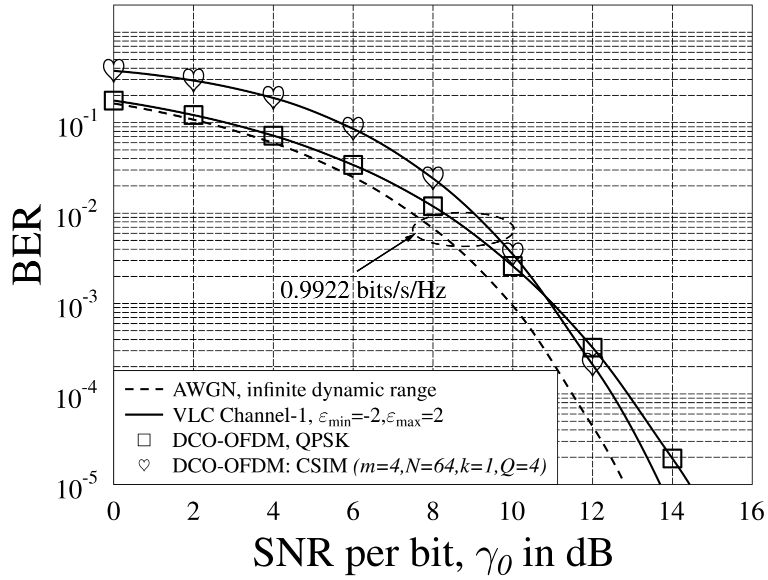

Figure 4.9: BER performance of the DCO-OFDM system using QPSK and CSIM, when communicating over the VLC channel-1. The dynamic range is set to [-2,2]. All other system parameters are summarised in Table 4.1 and Table 4.2.

Firstly, we can observe from Fig. 4.8 that for a given MAR of 0.9922 bits/s/Hz, the BER performance of the DCO-OFDM system using CSIM is severely degraded, when a higher-order QAM constellation is employed for modulating the activated symbols. This observation highlights that it is important to compare the performance of different O-OFDM systems under the same sensitivity to nonlinear distortions. Otherwise, the corresponding system comparisons may not be objective. Secondly, as shown in Fig. 4.8-4.11, the DCO-OFDM system using CSIM outperforms the DCO-OFDM system using QPSK for the same sensitivity to nonlinear distortions, as well as for the same MAR of 0.9922 bits/s/Hz. However, as seen in Table 4.2, the complexity order of the DCO-OFDM system using CSIM is higher than that of the DCO-OFDM

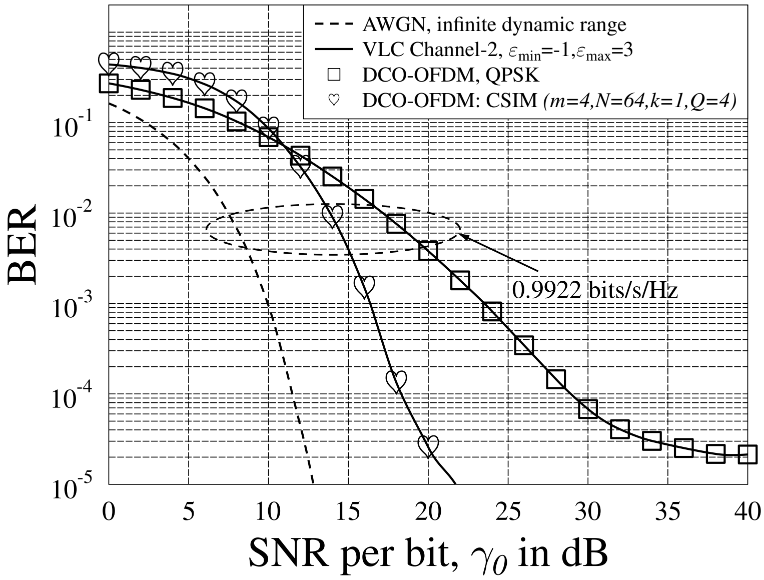

Figure 4.10: BER performance of the DCO-OFDM system using QPSK and CSIM, when communicating over the VLC channel-2. The dynamic range is set to [-1,3]. All other system parameters are summarised in Table 4.1 and Table 4.2.

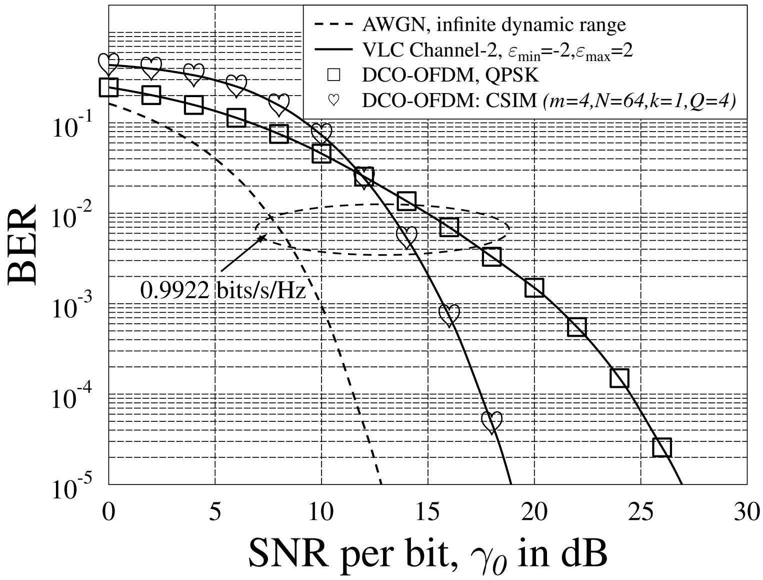

Figure 4.11: BER performance of the DCO-OFDM system using QPSK and CSIM, when communicating over the VLC channel-2. The dynamic range is set to [-2,2]. All other system parameters are summarised in Table 4.1 and Table 4.2.

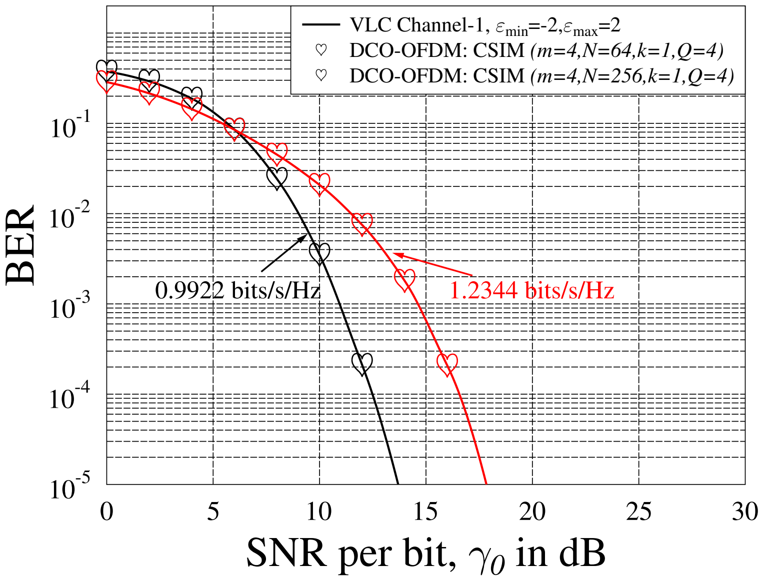

Figure 4.12: BER performance of the DCO-OFDM system using CSIM schemes, when communicating over the VLC channel-1. The dynamic range is set to [-2,2]. All other system parameters are summarised in Table 4.1 and Table 4.2.

system using QPSK. This observation confirms our analytical results discussed in Section 4.4.2, where the SINR attained by the CSIM scheme is higher than that attained by the QAM scheme. Furthermore, an additional diversity gain and coding gain can be achieved by the CSIM scheme, as analysed in Chapter 3. Hence, in comparison to the DCO-OFDM system using QAM, a substantially improved BER performance can be achieved by the DCO-OFDM system using CSIM. The diversity performance of the CSIM scheme can be further characterised by the simulation results of Fig. 4.10. When the optical signals propagate over the dispersive multipath VLC channel-2 of Fig. 4.5, the attainable BER performance of the CSIM scheme associated with the diversity order of $m = 4$ becomes limited in comparison to the BER performance shown in Fig. 4.8 for the less dispersive multipath VLC channel-1. Hence, a higher-diversity CSIM codebook can be designed to further improve the system performance. However, in this case more symbols have to be activated for maintaining the same MAR, hence imposing a higher complexity, as analysed in Chapter 3. Finally, we can observe from Fig. 4.12 that for a given constellation size $Q = 4$, the DCO-OFDM system using our CSIM scheme is capable of attaining a higher MAR, which is 1.2344 bits/s/Hz for our CSIM associated with $(m = 4, N = 256, k = 1, Q = 4)$. However, as shown in Table 4.2, this is achieved at the cost of complexity. We shall emphasise that the DCO-OFDM system using QPSK can only attain a MAR of 0.9922 bits/s/Hz. This observation confirms our discussions of Chapter 3, suggesting that our CSIM is a spectrally efficient scheme. The above-mentioned striking features of the CSIM scheme suggest that it is eminently suitable for O-OFDM systems.

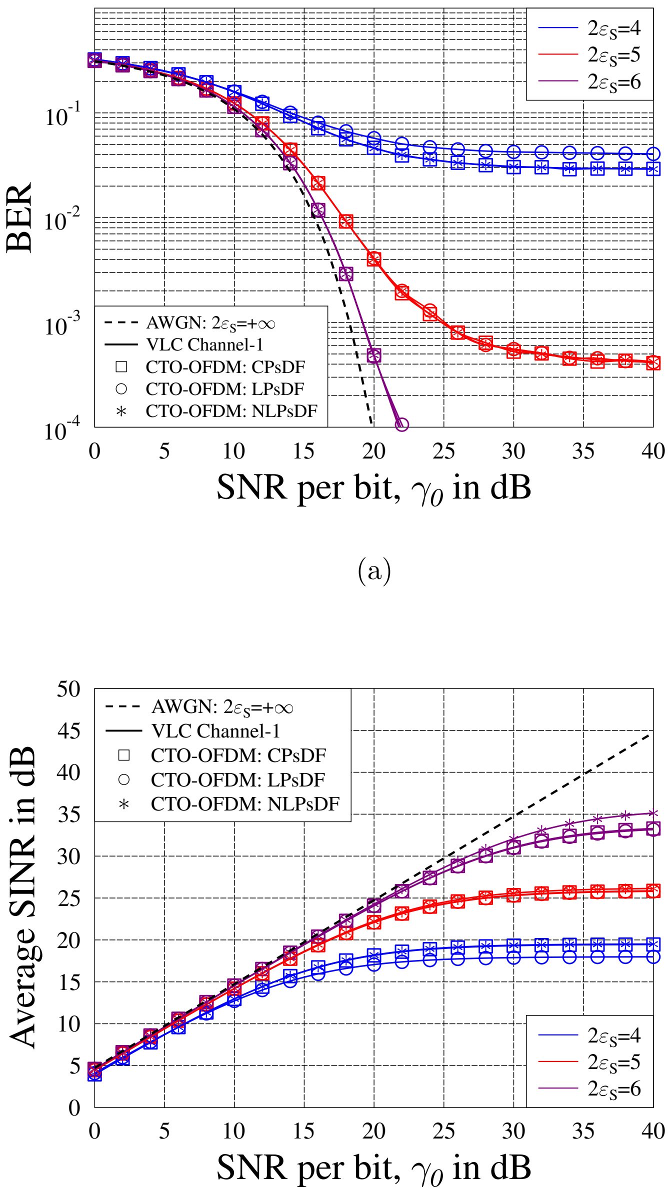

(a)

(b)

Figure 4.13: Performance comparison of CPsDF, LPsDF and NLPsDF based CTO-OFDM systems using 64QAM, when communicating over VLC channel-1. The expander is not employed at the receiver side. All other system parameters are summarised in Table 4.1.

In Fig. 4.13, we study the performance of CTO-OFDM systems employing CPsDF, LPsDF or NLPsDF based CTs, when communicating over multipath indoor VLC channels. For the sake of comparison, the VLC channel-1 associated with a CP length of $L_{\text{cp}} = 5$ and a 64QAM scheme are employed. It should be noted that the performance of other modulation schemes and channel scenarios will obey similar trends, as inferred from our theoretical analysis provided in Section 4.4.2. The dynamic ranges are set to $[-2, 2]$, $[-2.5, 2.5]$ and $[-3, 3]$. Furthermore, in order to investigate the inherent nonlinear distortion of each CT scheme, no expanders are employed in these simulations. Observe from the results of Fig. 4.13 (a) that the BER performance of the CPsDF-based CT is competitive in comparison to that of the NLPsDF-based CT, both of which slightly outperform the LPsDF-based CT. This observation can in fact be explained with the aid of the analytical SINR results of Fig. 4.13 (b). As seen in these figures, the average SINR of the CPsDF-based CT is almost the same as that of the NLPsDF-based CT. However, the LPsDF-based CT suffers from a higher interference than both the CPsDF and NLPsDF based CTs. Correspondingly, the BER performance of the LPsDF-based CT is worse than that of the CPsDF and NLPsDF based CTs.

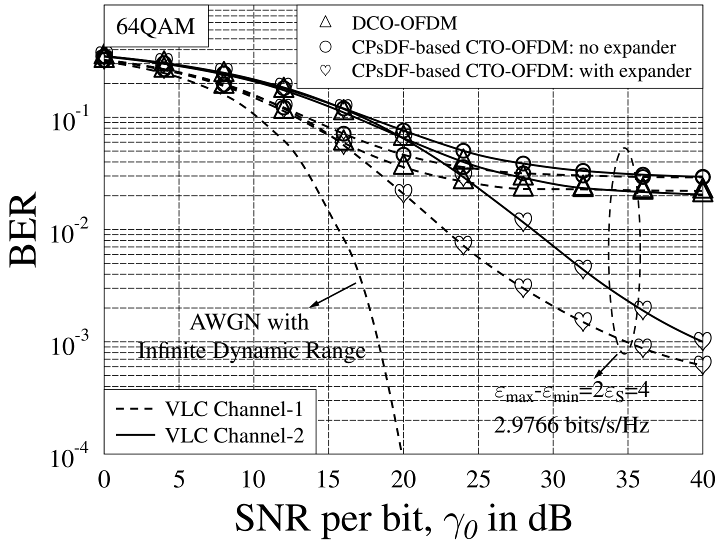

Figure 4.14: Performance comparison between the DCO-OFDM and CTO-OFDM systems using 64QAM, when communicating over indoor VLC channels. The dynamic ranges of both systems are set to $[-2, 2]$. All other system parameters are summarised in Table 4.1.

In Fig. 4.14-4.17, we investigate the performance of the DCO-OFDM and CTO-OFDM system using 64QAM or 256QAM, when communicating over indoor VLC multipath channels. Specifically, the VLC channel-1 associated with a CP length of $L_{\text{cp}} = 5$ and the VLC channel-2 with a CP length of $L_{\text{cp}} = 13$ are employed.

For the sake of comparison, the dynamic ranges of both systems are set to $[-2, 2]$ or $[-2.5, 2.5]$. As inferred from Fig. 4.13, the CPsDF-based CT is employed by the CTO-OFDM system, where the pair of receiver processing schemes shown in Fig. 4.2 are used. From the results of Fig. 4.14-4.17 we infer the following observations.

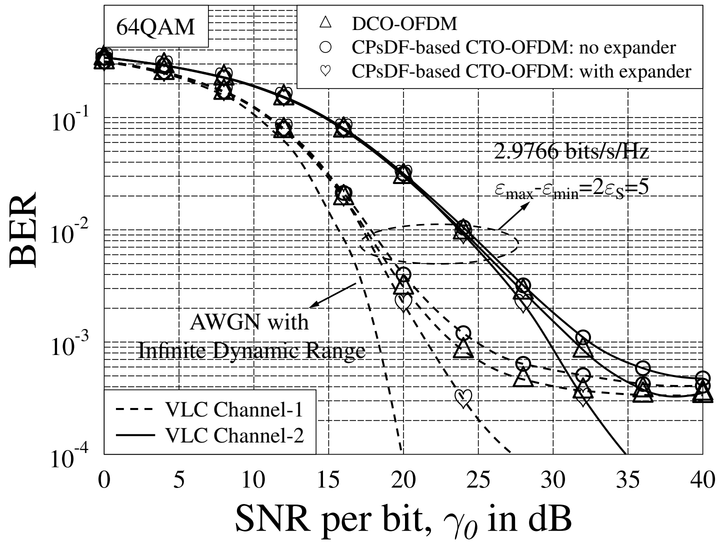

Figure 4.15: Performance comparison between the DCO-OFDM and CTO-OFDM systems using 64QAM, when communicating over indoor VLC channels. The dynamic ranges of both systems are set to $[-2.5, 2.5]$. All other system parameters are summarised in Table 4.1.

Firstly, as observed from Fig. 4.14-4.17, the CTO-OFDM system using the expander always outperforms the DCO-OFDM system. This observation confirms our analysis of CTO-OFDM carried out in Section 4.4.2, where we have shown that if the CT components can be recovered at the receiver side, our CTO-OFDM becomes capable of outperforming DCO-OFDM. Secondly, as seen in Fig. 4.14 -4.17, as the operational range increases, the performance gain attained by CTO-OFDM becomes less attractive in the light of the corresponding receiver complexity. This implies that a tradeoff has to be struck between the performance gain and complexity cost for designing efficient CTO-OFDM systems. Finally, as inferred from Fig. 4.14 and Fig. 4.17, if DCO-OFDM fails to support reliable communications, CTO-OFDM may be activated. This becomes more evident, when error correction codes are employ. Therefore, the flexibility of our CTO-OFDM system is higher than that of the CO-OFDM system.

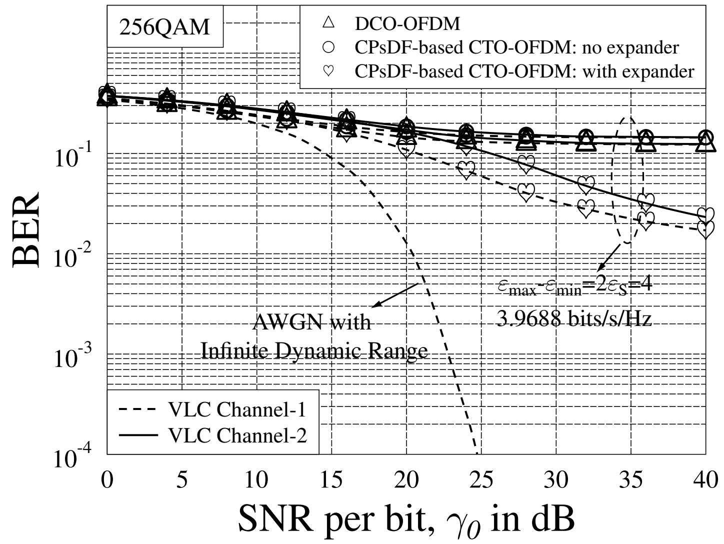

Figure 4.16: Performance comparison between the DCO-OFDM and CTO-OFDM systems using 256QAM, when communicating over indoor VLC channels. The dynamic ranges of both systems are set to $[-2, 2]$. All other system parameters are summarised in Table 4.1.

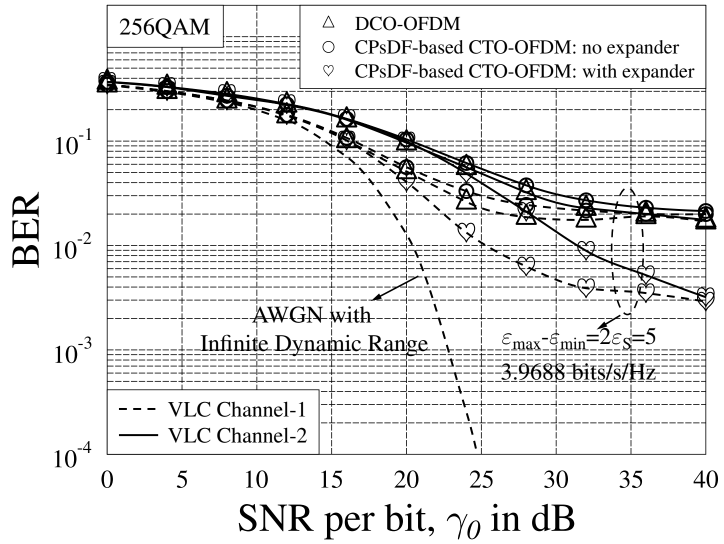

Figure 4.17: Performance comparison between the DCO-OFDM and CTO-OFDM systems using 256QAM, when communicating over indoor VLC channels. The dynamic ranges of both systems are set to $[-2.5, 2.5]$. All other system parameters are summarised in Table 4.1.

4.6 Conclusions

In this chapter, the CSIM scheme has been applied to a DCO-OFDM system. We have demonstrated that in comparison to the classic QAM signalling, the CSIM signalling is capable of attaining a better BER performance in VLCs, albeit at a slightly higher complexity. Furthermore, we have shown that our CSIM scheme is able to attain a higher rate than that achieved by classic QAM signalling, when the same constellation is used. As a further improvement, piecewise CT schemes have been conceived for O-OFDM systems, in order to constrain the transmitted signals within the limited dynamic range of LEDs. We have outlined the general principles and design criteria of piecewise CT schemes operated in different optical propagation scenarios. Three types of piecewise companders have been designed for the O-OFDM systems, which are the CPsDF, LPsDF and NLPsDF based CTs. Furthermore, the nonlinear effect of both the hard clipping and CT on the performance of the O-OFDM systems has been investigated in the context of different scenarios by both analysis and simulations. Our studies show that in comparison to the ACO-OFDM system, both the DCO-OFDM and CTO-OFDM systems are capable of attaining a higher bandwidth efficiency. Moreover, the CTO-OFDM system is shown to exhibit a high flexibility, as well as a capability to support high data-rate transmissions in the face of nonlinear effects. We also point out that a tradeoff has to be struck between the performance gain and the complexity cost for designing efficient CTO-OFDM systems.

Chapter 5

Conclusions and Future Work

5.1 Conclusions

In this thesis, we have conceived CS-assisted designs for enhancing the performance of indoor attocells. In particular, the key challenges of deploying indoor attocells, which are asynchronous impulsive noise, bandwidth efficiency and LED nonlinearity, have been tackled by our proposed CS-assisted systems, which are summarised below.

Chapter 1: In Section 1.1 and Section 1.2, we have detailed our motivation and introduced the integrated PLC/VLC system concept. Our studies have shown that the integrated PLC/VLC system, which has the advantages of cost-efficiency and a substantial unlicensed bandwidth without inflicting interference upon the existing RF communications, constitutes a compelling complement to the near-future wireless communication networks. Then, for the sake of convenience, the integrated PLC/VLC system has been decomposed into the PLC system and

Table 5.1: Summary of System Tradeoffs

Scheme	vs	Scheme	Rate in bits/s/Hz	SNR gain at BER of 10^{-4} in dB	Complexity ratio
IDFFT-CIS	vs	OFDM-MLD	1.67	15.05	$10^{3.2}$
LPIM-MLD	vs	QAM-MLD	1.50	19.50	$10^{3.6}$
CSIM-MLD	vs	QAM-MLD	1.50	16.00	$10^{1.8}$
LPIM-MLD	vs	LPIM-GIRCD	1.50	0.50	$10^{0.6}$
CSIM-MLD	vs	CSIM-GIRCD	1.50	1.00	$10^{1.0}$
DCO-OFDM-CSIM	vs	DCO-OFDM-QAM	0.99	11.00	$10^{1.1}$

the VLC system. Specifically, we have discussed some of the challenges tackled, which striking an attractive performance versus complexity tradeoff. Finally, in Section 1.3, we have presented an overview of CS, which is applied as our pervasive tool. We have shown that CS constitutes an attractive low-complexity estimation or detection tool in the context of high-dimension search problems.

Chapter 2: In Section 2.2, CIS-assisted IDFFT aided systems have been proposed for broadband indoor PLCs in order to mitigate the deleterious effects of the multipath fading and the asynchronous impulsive noise. Specifically, we have detailed the conceptual framework of our CIS in Section 2.4, where a 2D interleaver was conceived in Section 2.4.1 for dispersing the asynchronous impulsive bursts. Then, the received pilots have been modelled in Section 2.4.2 relying on the mathematical formulation of CS with the aid of our IDFFT system. In Section 2.4.3, we have proposed a computationally efficient search algorithm for approaching the optimal at a modest pilot design complexity. Based on our studies of this chapter, the basic design guidelines of our CIS-assisted IDFFT aided system may be summarised as follows. The 2D interleaver of the proposed CIS-assisted IDFFT aided system has to be carefully designed in order to efficiently randomise the impulsive noise bursts at the cost of the lowest possible time delay. The design of pilot symbols also commands special attention in order to facilitate the accurate estimation and efficient mitigation of asynchronous impulsive noise, because both the specific position and the number of pilots critically affects the CS-based estimation performance. Hence, we recommended a search algorithm for finding the most appropriate positions of the pilots in an offline manner. The number of pilots also has to be optimised for striking a flexible tradeoff between the performance gain attained and the effective transmission rate reduction imposed by the pilot-overhead. Finally, based on the 2D interleaver and pilot design, we proposed a CIS-assisted symbol detector, which has been shown to be capable of significantly improving the attainable system performance in comparison to the conventional OFDM system. Upon following these design guidelines, the computational complexity of the proposed CIS-assisted symbol detector remains moderates, where the extra complexity is mainly contributed by the additional FFT and IFFT operations. Specifically, as summarised in Table 5.1, at the BER of 10^{-4}, our CIS-assisted IDFFT system achieves about 15 dB SNR performance gain as well as requires about an order of $10^{3.2}$ increased complexity, in comparison to the classic OFDM system.

Chapter 3: In Section 3.2, the bit-to-symbol mapping rule was incorporated into a codebook. Then, its unified performance analysis was provided in Section 3.3.

Based on our theoretical analysis, the relevant codebook design criteria have been formulated in terms of the diversity gain, the coding gain, as well as the maximum achievable rate. Then, based on the diversity gain and the coding gain design criteria, a LPIM codebook has been proposed in Section 3.4. Both the analytical and the simulation results have confirmed that the LPIM scheme is capable of attaining a compelling BER performance. In Section 3.5, a generalised CSIM codebook has been proposed based on the maximum diversity gain and the maximum achievable rate design criteria. Moreover, in Section 3.5.3, we have proposed a novel design for our CSIM codebook in order to simultaneously satisfy the maximum diversity gain criterion as well as the MIP. Finally, the GIRCD has been proposed in Section 3.6 for both the LPIM and the CSIM in order to reduce the corresponding detection complexity. In Section 3.7, simulation results have been provided for characterising the overall system performance. Our investigations demonstrated that both OFDM-LPIM and OFDM-CSIM is capable of achieving a better BER performance than the classic OFDM scheme and the conventional OFDM-SIM arrangement. In particular, as summarised in Table 5.1, at the BER of 10^{-4} and the rate of 1.5 bits/s/Hz, the LPIM achieves about 20 dB SNR performance gain at the cost of about an order of $10^{3.6}$ increased complexity, whilst the CSIM achieves about 16 dB SNR performance gain at about an order of $10^{1.8}$ increased complexity, both in comparison to the classic OFDM system. Then, in comparison to the conventional SIM and LPIM schemes, the CSIM scheme strikes an appealing tradeoff between the SE and the EE. Furthermore, for a given maximum achievable rate and JMLD, the LPIM scheme is capable of achieving a better BER performance than the CSIM scheme, albeit at a much higher complexity. The GIRCD can be invoked for significantly reducing the complexity of both the LPIM and CSIM schemes. At a high rate, the LPIM scheme using GIRCD has been shown to be capable of attaining a good BER performance at a reduced complexity. An even lower complexity is imposed by the CSIM scheme using GIRCD, albeit a slight performance loss. As summarised in Table 5.1, in comparison to the MLD, our GIRCD reduces the complexity by a factor of about $10^{0.6}$ at the cost of 0.5 dB SNR performance loss at the BER of 10^{-4} for the LPIM scheme, while for the CSIM scheme, about an order of $10^{1.0}$ complexity reduction at the cost of about 1 dB SNR performance loss is observed.

Chapter 4: In Section 4.2, the CSIM scheme of Chapter 3 has been applied to a DCO-OFDM system. We have demonstrated that in comparison to the classic QAM signalling, the CSIM signalling is capable of attaining a better BER performance in VLC, albeit at a slightly increased complexity. Specifically, as summarised in Table 5.1, in comparison to the classic OFDM system, the DCO-OFDM system using CSIM achieves about 11 dB SNR performance gain at about an order of $10^{1.1}$ higher complexity, for the VLC scenario of Fig. 4.10. Furthermore, we have shown that our CSIM scheme is capable of attaining a higher rate than that achieved by classic QAM signalling, when the same constellation is used. In particular, about 24% improvement of the maximum achievable rate is observed in Fig. 4.12 for our CSIM using the QPSK constellation at about four times the complexity, in comparison to the conventional QPSK scheme dispensing with CSIM. As a further improvement, piecewise CT schemes have been conceived in Section 4.3 for O-OFDM systems, in order to constrain the transmitted signals to the limited dynamic range of LEDs. In Section 4.3.5, we have outlined the general principles and design criteria of piecewise CT schemes operated in different optical propagation scenarios. Moreover, three types of piecewise companders have been designed for the O-OFDM systems, which are the CPsDF, LPsDF and NLPsDF based CTs. Furthermore, the nonlinear effect of hard clipping and CT on the performance of the O-OFDM systems has been investigated in the context of different scenarios by both analysis and simulations. Our studies show that in comparison to the ACO-OFDM system, both the DCO-OFDM and CTO-OFDM systems are capable of attaining a higher bandwidth efficiency. Moreover, the CTO-OFDM system has been shown to exhibit a high flexibility, as well as a capability to support high data-rate transmissions in the face of nonlinear effects. We also point out that a tradeoff has to be struck between the performance gain and the complexity cost of designing efficient CTO-OFDM systems.

5.2 Future Work

Our future work is summarised as follows.

- Firstly, channel coding will be employed in our CIS-assisted IDFFT system of Chapter 2, OFDM-LPIM/CSIM systems of Chapter 3, as well as O-OFDM-CSIM system of Chapter 4, in order to further improve the attainable system performance.
- Secondly, in order to enhance the performance of O-OFDM systems, our future work will be focused on modifying our CSIM signalling scheme, so that the nonlinear effects can be mitigated at the transmitter side. Furthermore, advanced

ICI mitigation schemes will be conceived for our CTO-OFDM at the receiver side.

- Thirdly, we will design and characterise an integrated PLC/VLC system for both uplink and downlink multiuser transmissions.
- Finally, in a nutshell, CS is capable of tackling numerous technical issues at an appealingly low complexity. Therefore, it will be continuously used for our future research.

Appendix **A**

Derivation of Spectral Efficiency

According to Section 3.3, the Channel State Information (CSI) is assumed to be perfectly known at the receiver. Hence, based on the modelling of (3.4c), the mutual information $I(\boldsymbol{s}_g;\boldsymbol{y}_g)$ can be expressed as [150]

$$\begin{aligned} I\left(\boldsymbol{s}_g;\boldsymbol{y}_g\right) =&\mathbb{E}_{\bar{\boldsymbol{H}}_g}[I(\boldsymbol{s}_g;\boldsymbol{y}_g|\bar{\boldsymbol{H}}_g)] \\ =&\mathbb{E}_{\bar{\boldsymbol{H}}_g}[\mathcal{H}(\boldsymbol{y}_g|\bar{\boldsymbol{H}}_g)-\mathcal{H}(\boldsymbol{y}_g|\boldsymbol{s}_g,\bar{\boldsymbol{H}}_g)] \\ =&\mathbb{E}_{\bar{\boldsymbol{H}}_g}[\mathcal{H}(\boldsymbol{y}_g|\bar{\boldsymbol{H}}_g)]-\mathcal{H}(\bar{\boldsymbol{n}}_g), \end{aligned} \tag{A.1}$$

where the differential entropy of the m-dimensional complex Gaussian vector with a mean vector $\mathbf{0}$ and a covariance matrix of $N_0\boldsymbol{I}_m$ is given by [150]

$$\begin{aligned} \mathcal{H}(\bar{\boldsymbol{n}}_g) =& \log_2(\pi e N_0)^m = m\log_2(\pi e N_0) \\ =& m\log_2\left(\frac{\pi e k}{m\gamma_s}\right). \end{aligned} \tag{A.2}$$

On the other hand, the conditional entropy $\mathcal{H}(\boldsymbol{y}_g|\bar{\boldsymbol{H}}_g)$ can be formulated as [150]

$$\begin{aligned} \mathcal{H}(\boldsymbol{y}_g|\bar{\boldsymbol{H}}_g) =& -\int_{\boldsymbol{y}_g} p(\boldsymbol{y}_g|\bar{\boldsymbol{H}}_g)\log_2 p(\boldsymbol{y}_g|\bar{\boldsymbol{H}}_g)\mathrm{d}\boldsymbol{y}_g \\ =&\mathbb{E}_{\boldsymbol{y}_g}[-\log_2 p(\boldsymbol{y}_g|\bar{\boldsymbol{H}}_g)]. \end{aligned} \tag{A.3}$$

According to (3.1), the codebook $\mathcal{V}$ is defined so that each group of L data bits can be regarded as being directly mapped into a symbol vector in $\mathcal{V}$. Since the input data bits are i.i.d., it is reasonable to assume that the candidates in $\mathcal{V}$ are equiprobable, i.e. we have $p(\boldsymbol{v}_i) = 1/2^L$ for $i = 1,\ldots,2^L$. Hence, with the aid of (3.7) and by invoking Bayes' rule, the conditional probability $p(\boldsymbol{y}_g|\bar{\boldsymbol{H}}_g)$ can be expressed as

$$\begin{aligned}
p(\boldsymbol{y}_g|\bar{\boldsymbol{H}}_g) &= \sum_{i=1}^{2^L} p(\boldsymbol{y}_g|\boldsymbol{v}_i, \bar{\boldsymbol{H}}_g)p(\boldsymbol{v}_i) = \frac{1}{2^L}\sum_{i=1}^{2^L} p(\boldsymbol{y}_g|\boldsymbol{v}_i, \bar{\boldsymbol{H}}_g) \\
&= \frac{1}{2^L}\sum_{i=1}^{2^L} \frac{1}{(\pi N_0)^m} \exp\left\{-\frac{\|\boldsymbol{y}_g - \bar{\boldsymbol{H}}_g\boldsymbol{v}_i\|_2^2}{N_0}\right\} \\
&= \frac{1}{2^L}\sum_{i=1}^{2^L} \frac{1}{(\pi N_0)^m} \exp\left\{-\frac{\|\bar{\boldsymbol{H}}_g(\boldsymbol{s}_g - \boldsymbol{v}_i) + \bar{\boldsymbol{n}}_g\|_2^2}{N_0}\right\}.
\end{aligned} \tag{A.4}$$

Additionally, let us define a set of

$$\mathcal{E} \triangleq \{\boldsymbol{e} = \boldsymbol{v}_j - \boldsymbol{v}_i : \boldsymbol{v}_i \neq \boldsymbol{v}_j, \forall \boldsymbol{v}_i, \boldsymbol{v}_j \in \mathcal{V}\}. \tag{A.5}$$

Then, with the aid of (A.5), Eq. (A.4) can be formulated as

$$\begin{aligned}
p(\boldsymbol{y}_g|\bar{\boldsymbol{H}}_g) =& \frac{1}{2^L}\left(\frac{1}{(\pi N_0)^m}\exp\left\{-\frac{\|\bar{\boldsymbol{n}}_g\|_2^2}{N_0}\right\}\right. \\
&\left. + \mathbb{E}_{\boldsymbol{e}}\left[\frac{1}{(\pi N_0)^m}\exp\left\{-\frac{\|\bar{\boldsymbol{H}}_g\boldsymbol{e} + \bar{\boldsymbol{n}}_g\|_2^2}{N_0}\right\}\right]\right) \\
=& \frac{1}{2^L}\left(\frac{m\gamma_s}{\pi k}\right)^m \left(\exp\left\{-\frac{\|\bar{\boldsymbol{n}}_g\|_2^2}{k} m\gamma_s\right\}\right. \\
&\left. + \mathbb{E}_{\boldsymbol{e}}\left[\exp\left\{-\frac{\|\bar{\boldsymbol{H}}_g\boldsymbol{e} + \bar{\boldsymbol{n}}_g\|_2^2}{k} m\gamma_s\right\}\right]\right),
\end{aligned} \tag{A.6}$$

which is dependent on $\bar{\boldsymbol{n}}_g$ given $\bar{\boldsymbol{H}}_g$ and γ_s. Hence, for the sake of convenience, we define the implementation function of

$$\epsilon(\bar{\boldsymbol{n}}_g, \bar{\boldsymbol{H}}_g, \gamma_s) \triangleq p(\boldsymbol{y}_g|\bar{\boldsymbol{H}}_g) \tag{A.7}$$

to explicitly emphasize the dependence on the channel parameters. Then, Eq.(A.3) can be alternatively expressed as

$$\mathcal{H}(\boldsymbol{y}_g|\bar{\boldsymbol{H}}_g) = \mathbb{E}_{\bar{\boldsymbol{n}}_g}[-\log_2 \epsilon(\bar{\boldsymbol{n}}_g, \bar{\boldsymbol{H}}_g, \gamma_s)]. \tag{A.8}$$

Finally, upon substituting (A.2) and (A.8) into (A.1), we arrive at

$$I\left(\boldsymbol{x}_g; \boldsymbol{y}_g\right) = \mathbb{E}_{\bar{\boldsymbol{H}}_g, \bar{\boldsymbol{n}}_g}[-\log_2 \epsilon(\bar{\boldsymbol{n}}_g, \bar{\boldsymbol{H}}_g, \gamma_s)] - m\log_2\left(\frac{\pi e k}{m\gamma_s}\right). \tag{A.9}$$

It should be noted that the upper bound of $I(\boldsymbol{x}_g; \boldsymbol{y}_g)$ in our scenario can be derived as

$$\begin{aligned}
I\left(\boldsymbol{x}_g;\boldsymbol{y}_g\right) =&\mathbb{E}_{\bar{\boldsymbol{H}}_g}[I(\boldsymbol{x}_g;\boldsymbol{y}_g|\bar{\boldsymbol{H}}_g)]\\
=&\mathbb{E}_{\bar{\boldsymbol{H}}_g}[\mathcal{H}(\boldsymbol{x}_g|\bar{\boldsymbol{H}}_g)-\mathcal{H}(\boldsymbol{x}_g|\boldsymbol{y}_g,\bar{\boldsymbol{H}}_g)]\\
=&\mathcal{H}(\boldsymbol{x}_g)-\mathbb{E}_{\bar{\boldsymbol{H}}_g}[\mathcal{H}(\boldsymbol{x}_g|\boldsymbol{y}_g,\bar{\boldsymbol{H}}_g)]\\
\leq&\mathcal{H}(\boldsymbol{x}_g)=-\sum_{i=1}^{2^L}p(\boldsymbol{v}_i)\log_2 p(\boldsymbol{v}_i)\\
&\qquad\quad=-\sum_{i=1}^{2^L}\frac{1}{2^L}\log_2\frac{1}{2^L}=L,
\end{aligned}\tag{A.10}$$

where the upper bound is achieved, when γ_s is sufficiently high.

Appendix B

Find the bound of ε_o

Firstly, let us define the LHS of (4.31) as

$$f(\varepsilon_o) \triangleq Q\left(\frac{\varepsilon_o}{\sigma_X}\right) - \frac{\varepsilon_S - \varepsilon_o}{\sigma_X\sqrt{2\pi}} Q_1\left(0, \frac{\varepsilon_o}{\sigma_X}\right), \tag{B.1}$$

which has the first derivative of

$$\frac{\mathrm{d}f(\varepsilon_o)}{\mathrm{d}\varepsilon_o} = \frac{\varepsilon_o(\varepsilon_S - \varepsilon_o)}{\sigma_X^2\sqrt{2\pi}} Q_1\left(0, \frac{\varepsilon_o}{\sigma_X}\right) \geq 0, \tag{B.2}$$

showing that $f(\varepsilon_o)$ is a non-decreasing function. Hence, for a given $\varepsilon_S \leq \sigma_X\sqrt{2/\pi}$, we can readily show that

$$f(\varepsilon_o) \geq f(0) = \frac{1}{2} - \frac{\varepsilon_S}{\sigma_X\sqrt{2\pi}} \geq 0, \tag{B.3}$$

implying that for any $0 \leq \varepsilon_{\mathrm{o}} < \varepsilon_S$, Eq.(4.31) is always satisfied. On the other hand, for a given $\varepsilon_S > \sigma_X\sqrt{2/\pi}$, there exists a lower bound of ε_o to meet the condition of (4.31), i.e., we have

$$\begin{cases} f(\varepsilon_o) \geq 0, & \text{if } \varepsilon_{o,\min} \leq \varepsilon_o < \varepsilon_S \\ f(\varepsilon_o) < 0, & \text{if } 0 \leq \varepsilon_o < \varepsilon_{o,\min}. \end{cases} \tag{B.4}$$

Bibliography

[1] L. Hanzo, H. Haas, S. Imre, D. O'Brien, M. Rupp, and L. Gyongyosi, "Wireless myths, realities, and futures: From 3G/4G to optical and quantum wireless," *Proceedings of the IEEE*, vol. 100, pp. 1853–1888, May 2012.

[2] ITU-R Report M.2243, "ITU-R Report M.2243: Assessment of the global mobile broadband deployments and forecasts for international mobile telecommunications," Tech. Rep. M.2243, ITU-R, 2011.

[3] C. E. Shannon, "A mathematical theory of communication," *The Bell System Technical Journal*, vol. 27, pp. 379–423, July 1948.

[4] D. J. Costello and G. D. Forney, "Channel coding: The road to channel capacity," *Proceedings of the IEEE*, vol. 95, pp. 1150–1177, June 2007.

[5] L. Hanzo, M. El-Hajjar and O. Alamri, "Near-capacity wireless transceivers and cooperative communications in the MIMO era: Evolution of standards, waveform design, and future perspectives," *Proceedings of the IEEE*, vol. 99, pp. 1343–1385, Aug. 2011.

[6] A. Goldsmith, *Wireless communications.* Cambridge university press, 2005.

[7] L. Hanzo, J. Akhtman, M. Jiang, and L. Wang, *MIMO-OFDM for LTE, Wi-Fi and WiMAX.* John Wiley & Sons, 2011.

[8] Xiaoxin Wu, B. Murherjee and D. Ghosal, "Hierarchical architectures in the third-generation cellular network," *IEEE Wireless Communications*, vol. 11, pp. 62–71, June 2004.

[9] A. Ghosh *et al.*, "Heterogeneous cellular networks: From theory to practice," *IEEE Communications Magazine*, vol. 50, pp. 54–64, June 2012.

[10] R. Q. Hu and Y. Qian, *Heterogeneous cellular networks.* John Wiley & Sons, 2013.

[11] G. Mansfield, "Femtocells in the us market-business drivers and consumer propositions," *FemtoCells Europe*, vol. 19271948, 2008.

[12] J. G. Andrews, H. Claussen, M. Dohler, S. Rangan, and M. C. Reed, "Femtocells: Past, present, and future," *IEEE Journal on Selected Areas in Communications*, vol. 30, pp. 497–508, April 2012.

[13] T. Komine and M. Nakagawa, "Integrated system of white LED visible-light communication and power-line communication," *IEEE Transactions on Consumer Electronics*, vol. 49, pp. 71–79, Feb. 2003.

[14] M. Nakagawa, "CLEO 07 Invited paper visible light communications," *Lasers and Electro-Optics*, vol. 1, pp. 6–11, May 2007.

[15] J. M. Kahn and J. R. Barry, "Wireless infrared communications," *Proceedings of the IEEE*, vol. 85, pp. 265–298, Feb. 1997.

[16] T. Komine and M. Nakagawa, "Fundamental analysis for visible-light communication system using LED lights," *IEEE Transactions on Consumer Electronics*, vol. 50, no. 1, pp. 100–107, 2004.

[17] H. Haas, *Harald Haas: Wireless data from every light bulb*, July 2011. Available at `www.ted.com/talks/harald_haas_wireless_data_from_every_light_bulb`.

[18] *IEEE Standard for Local and Metropolitan Area Networks–Part 15.7: Short-Range Wireless Optical Communication Using Visible Light*, Sept 2011. IEEE Std. 802.15.7-2011.

[19] A. Jovicic, *Qualcomm Lumicast: A high accuracy indoor positioning system based on visible light communication*, April 2016. Available at `www.qualcomm.com/documents/lumicast-whitepaper`.

[20] J. Routin and C. E. L. Brown, "Improvements in and relating to electricity meters," tech. rep., British Patent 24,833, Oct. 1898.

[21] *IEEE Standard for Broadband over Power Line Networks: Medium Access Control and Physical Layer Specifications*, 2010. IEEE Std. 1901-2010.

[22] *Unified high-speed wireline-based home networking transceivers-System architecture and physical layer specification*, 2011. ITU-T Rec. G.9960.

[23] HomePlug Powerline Alliance, *HomePlug AV2 White Paper*, 2013. Available at `http://www.homeplug.org/`.

[24] F. Canete, J. Cortes, L. Diez, and J. Entrambasaguas, "Modeling and evaluation of the indoor power line transmission medium," *IEEE Communications Mag.*, vol. 41, pp. 41–47, April 2003.

[25] M. Zimmermann and K. Dostert, “Analysis and modeling of impulsive noise in broad-band powerline communications,” *IEEE Transactions on Electromagnetic Compatibility*, vol. 44, no. 1, pp. 249–258, 2002.

[26] J. Vucic *et al.*, “White light wireless transmission at 200Mb/s net data rate by use of discrete-multitone modulation,” *IEEE Photonics Technology Letters*, vol. 21, no. 20, pp. 1511–1513, 2009.

[27] J. Vucic *et al.*, “513 Mbit/s visible light communications link based on DMT-modulation of a white LED,” *Journal of Lightwave Technology*, vol. 28, no. 24, pp. 3512–3518, 2010.

[28] A. M. Khalid *et al.*, “1-Gb/s transmission over a phosphorescent white LED by using rate-adaptive discrete multitone modulation,” *IEEE Photonics Journal*, vol. 4, no. 5, pp. 1465–1473, 2012.

[29] Z. Ghassemlooy, W. Popoola, and S. Rajbhandari, *Optical wireless communications.* CRC Press Boca Raton, FL, 2012.

[30] J. Neter, M. H. Kutner, C. J. Nachtsheim, and W. Wasserman, *Applied linear statistical models*, vol. 4. Irwin Chicago, 1996.

[31] A. Neumaier, “Solving ill-conditioned and singular linear systems: A tutorial on regularization,” *SIAM review*, vol. 40, no. 3, pp. 636–666, 1998.

[32] A. Tikhonov, “Solution of incorrectly formulated problems and the regularization method,” in *Soviet Math. Dokl.*, vol. 5, pp. 1035–1038, 1963.

[33] R. Tibshirani, “Regression shrinkage and selection via the Lasso,” *Journal of the Royal Statistical Society. Series B (Methodological)*, vol. 58, no. 1, pp. 267–288, 1996.

[34] S. S. Chen, D. L. Donoho, and M. A. Saunders, “Atomic decomposition by basis pursuit,” *SIAM Review*, vol. 43, no. 1, pp. 129–159, 2001.

[35] K. P. Murphy, *Machine learning: a probabilistic perspective.* MIT press, 2012.

[36] lldiko E. Frank and J. H. Friedman, “A statistical view of some chemometrics regression tools,” *Technometrics*, vol. 35, no. 2, pp. 109–135, 1993.

[37] S. Theodoridis and R. Chellappa, *Academic Press Library in Signal Processing: Signal Processing Theory and Machine Learning.* Academic Press Library in Signal Processing, Elsevier Science, 2013.

[38] S. Arlot, A. Celisse, *et al.*, “A survey of cross-validation procedures for model selection,” *Statistics surveys*, vol. 4, pp. 40–79, 2010.

[39] S. Boyd and L. Vandenberghe, *Convex Optimization.* New York, NY, USA: Cambridge University Press, 2004.

[40] K. Knight and W. Fu, "Asymptotics for lasso-type estimators," *The Annals of Statistics*, vol. 28, no. 5, pp. 1356–1378, 2000.

[41] E. Candes and T. Tao, "The dantzig selector: Statistical estimation when p is much larger than n," *The Annals of Statistics*, vol. 35, no. 6, pp. 2313–2351, 2007.

[42] S. G. Mallat and Z. Zhang, "Matching pursuits with time-frequency dictionaries," *IEEE Transactions on Signal Processing*, vol. 41, pp. 3397–3415, Dec. 1993.

[43] D. L. Donoho and X. Huo, "Uncertainty principles and ideal atomic decomposition," *IEEE Transactions on Information Theory*, vol. 47, pp. 2845–2862, Nov. 2001.

[44] M. Elad and A. M. Bruckstein, "A generalized uncertainty principle and sparse representation in pairs of bases," *IEEE Transactions on Information Theory*, vol. 48, pp. 2558–2567, Sept. 2002.

[45] D. L. Donoho and M. Elad, "Optimally sparse representation in general (nonorthogonal) dictionaries via ℓ_1 minimization," *Proceedings of the National Academy of Sciences*, vol. 100, no. 5, pp. 2197–2202, 2003.

[46] D. L. Donoho, M. Elad and V. N. Temlyakov, "Stable recovery of sparse overcomplete representations in the presence of noise," *IEEE Transactions on Information Theory*, vol. 52, pp. 6–18, Jan 2006.

[47] E. J. Candes and T. Tao, "Decoding by linear programming," *IEEE Transactions on Information Theory*, vol. 51, pp. 4203–4215, Dec. 2005.

[48] R. G. Baraniuk, M. Davenport, R. DeVore, and M. B. Wakin, "A simple proof of the restricted isometry property for random matrices," *Constructive Approximation*, vol. 28, no. 3, pp. 253–263, 2008.

[49] S. Foucart and H. Rauhut, *A mathematical introduction to compressive sensing*, vol. 1. Birkhäuser Basel, 2013.

[50] W. B. Johnson and J. Lindenstrauss, "Extensions of lipschitz mappings into a hilbert space," *Contemporary mathematics*, vol. 26, no. 189-206, p. 1, 1984.

[51] R. G. Baraniuk, V. Cevher, and M. B. Wakin, "Low-dimensional models for dimensionality reduction and signal recovery: A geometric perspective," *Proceedings of the IEEE*, vol. 98, pp. 959–971, June 2010.

[52] T. T. Cai, G. Xu and J. Zhang, "On recovery of sparse signals via ℓ_1 minimization," *IEEE Transactions on Information Theory*, vol. 55, pp. 3388–3397, July 2009.

[53] A. M. Tillmann and M. E. Pfetsch, "The computational complexity of the restricted isometry property, the nullspace property, and related concepts in compressed sensing," *IEEE Transactions on Information Theory*, vol. 60, pp. 1248–1259, Feb. 2014.

[54] D. L. Donoho, "Compressed sensing," *IEEE Transactions on Information Theory*, vol. 52, pp. 1289–1306, April 2006.

[55] E. J. Candès *et al.*, "Compressive sampling," in *Proceedings of the international congress of mathematicians*, vol. 3, pp. 1433–1452, Madrid, Spain, 2006.

[56] R. G. Baraniuk, "Compressive sensing [lecture notes]," *IEEE Signal Processing Magazine*, vol. 24, pp. 118–121, July 2007.

[57] E. J. Candes and M. B. Wakin, "An introduction to compressive sampling," *IEEE Signal Processing Magazine*, vol. 25, pp. 21–30, March 2008.

[58] A. M. Bruckstein, D. L. Donoho, and M. Elad, "From sparse solutions of systems of equations to sparse modeling of signals and images," *SIAM review*, vol. 51, no. 1, pp. 34–81, 2009.

[59] M. F. Duarte and Y. C. Eldar, "Structured compressed sensing: From theory to applications," *IEEE Transactions on Signal Processing*, vol. 59, no. 9, pp. 4053–4085, 2011.

[60] D. Takhar *et al.*, "A new compressive imaging camera architecture using optical-domain compression," in *Proc. SPIE*, vol. 6065, pp. 606509–606509–10, 2006.

[61] M. Lustig, D. L. Donoho, J. M. Santos, and J. M. Pauly, "Compressed sensing MRI," *IEEE Signal Processing Magazine*, vol. 25, pp. 72–82, March 2008.

[62] J. Haupt, W. U. Bajwa, M. Rabbat, and R. Nowak, "Compressed sensing for networked data," *IEEE Signal Processing Magazine*, vol. 25, pp. 92–101, March 2008.

[63] W. U. Bajwa, J. Haupt, A. M. Sayeed, and R. Nowak, "Compressed channel sensing: A new approach to estimating sparse multipath channels," *Proceedings of the IEEE*, vol. 98, pp. 1058–1076, June 2010.

[64] A. Gomaa and N. Al-Dhahir, "A sparsity-aware approach for NBI estimation in MIMO-OFDM," *IEEE Transactions on Wireless Communications*, vol. 10, pp. 1854–1862, June 2011.

[65] Z. Tian and G. B. Giannakis, "Compressed sensing for wideband cognitive radios," in *IEEE International Conference on Acoustics, Speech and Signal Processing, 2007. ICASSP 2007.*, vol. 4, pp. IV–1357–IV–1360, April 2007.

[66] G. Caire, and T. Y. Al-Naffouri, and A. K. Narayanan,, "Impulse noise cancellation in OFDM: an application of compressed sensing," in *IEEE International Symposium on Information Theory, 2008. ISIT 2008.*, pp. 1293–1297, July 2008.

[67] L. Lampe, "Bursty impulse noise detection by compressed sensing," in *2011 IEEE International Symposium on Power Line Communications and Its Applications (ISPLC),*, pp. 29–34, April 2011.

[68] H. Zhang, L. L. Yang, and L. Hanzo, "Compressed impairment sensing-assisted and interleaved-double-FFT-aided modulation improves broadband power line communications subjected to asynchronous impulsive noise," *IEEE Access*, vol. 4, pp. 81–96, 2016.

[69] H. Zhang, L. L. Yang, and L. Hanzo, "Compressed sensing improves the performance of subcarrier index-modulation-assisted OFDM," *IEEE Access*, vol. 4, pp. 7859–7873, 2016.

[70] R. G. Gallager, *Principles of digital communication*, vol. 1. Cambridge University Press Cambridge, UK, 2008.

[71] G. M. Davis, S. G. Mallat, and Z. Zhang, "Adaptive time-frequency decompositions," *Optical Engineering*, vol. 33, no. 7, pp. 2183–2191, 1994.

[72] S. Chen and J. Wigger, "Fast orthogonal least squares algorithm for efficient subset model selection," *IEEE Transactions on Signal Processing*, vol. 43, pp. 1713–1715, July 1995.

[73] T. Blumensath and M. E. Davies, *On the difference between orthogonal matching pursuit and orthogonal least squares*, 2007. unpublished.

[74] D. Needell and J. A. Tropp, "Cosamp: Iterative signal recovery from incomplete and inaccurate samples," *Applied and Computational Harmonic Analysis*, vol. 26, no. 3, pp. 301–321, 2009.

[75] T. Blumensath and M. E. Davies, "Iterative hard thresholding for compressed sensing," *Applied and computational harmonic analysis*, vol. 27, no. 3, pp. 265–274, 2009.

[76] J. A. Tropp, "Greed is good: algorithmic results for sparse approximation," *IEEE Transactions on Information Theory*, vol. 50, pp. 2231–2242, Oct. 2004.

[77] M. A. Davenport and M. B. Wakin, “Analysis of orthogonal matching pursuit using the restricted isometry property,” *IEEE Transactions on Information Theory*, vol. 56, no. 9, pp. 4395–4401, 2010.

[78] Q. Mo and Y. Shen, “A remark on the restricted isometry property in orthogonal matching pursuit,” *IEEE Transactions on Information Theory*, vol. 58, pp. 3654–3656, June 2012.

[79] J. Wang and B. Shim, “On the recovery limit of sparse signals using orthogonal matching pursuit,” *IEEE Transactions on Signal Processing*, vol. 60, no. 9, pp. 4973–4976, 2012.

[80] E. Liu and V. N. Temlyakov, “The orthogonal super greedy algorithm and applications in compressed sensing,” *IEEE Transactions on Information Theory*, vol. 58, pp. 2040–2047, April 2012.

[81] Z. Ben-Haim, Y. C. Eldar and M. Elad, “Coherence-based performance guarantees for estimating a sparse vector under random noise,” *IEEE Transactions on Signal Processing*, vol. 58, pp. 5030–5043, Oct. 2010.

[82] T. T. Cai and Lie Wang, “Orthogonal matching pursuit for sparse signal recovery with noise,” *IEEE Transactions on Information Theory*, vol. 57, pp. 4680–4688, July 2011.

[83] L.-H. Chang and J.-Y. Wu, “An improved RIP-based performance guarantee for sparse signal recovery via orthogonal matching pursuit,” *IEEE Transactions on Information Theory*, vol. 60, no. 9, pp. 5702–5715, 2014.

[84] H. Hrasnica, A. Haidine, and R. Lehnert, *Broadband powerline communications: network design.* John Wiley & Sons, 2005.

[85] M. Zimmermann and K. Dostert, “A multipath model for the powerline channel,” *IEEE Transactions on Communications*, vol. 50, no. 4, pp. 553–559, 2002.

[86] F. J. C. Corripio, J. A. C. Arrabal, L. D. del Rio, and J. T. E. Munoz, “Analysis of the cyclic short-term variation of indoor power line channels,” *IEEE Journal on Selected Areas in Communications*, vol. 24, pp. 1327–1338, July 2006.

[87] A. M. Tonello, F. Versolatto, and A. Pittolo, “In-home power line communication channel: Statistical characterization,” *IEEE Transactions on Communications*, vol. 62, pp. 2096–2106, June 2014.

[88] H. Meng, Y. L. Guanand, and S. Chen, “Modeling and analysis of noise effects on broadband power-line communications,” *IEEE Transactions on Power Delivery*, vol. 20, no. 2, pp. 630–637, 2005.

[89] J. A. Cortés *et al.*, "Analysis of the indoor broadband power-line noise scenario," *IEEE Transactions on Electromagnetic Compatibility*, vol. 52, no. 4, pp. 849–858, 2010.

[90] K. L. Blackard, T. S. Rappaport, and C. W. Bostian, "Measurements and models of radio frequency impulsive noise for indoor wireless communications," *IEEE Journal on Selected Areas in Communications*, vol. 11, pp. 991–1001, Sept. 1993.

[91] L. Hanzo, M. Münster, B. Choi, and T. Keller, *OFDM and MC-CDMA for Broadband Multi-user Communications, WLANs and Broadcasting.* John Wiley & Sons, May 2003.

[92] L.-L. Yang, *Multicarrier communications.* John Wiley & Sons, 2009.

[93] H. A. Suraweera, C. Chai, J. Shentu, and J. Armstrong, "Analysis of impulse noise mitigation techniques for digital television systems," in *Proc. 8th International OFDM Workshop*, Sept. 2003.

[94] S. V. Zhidkov, "Analysis and comparison of several simple impulsive noise mitigation schemes for OFDM receivers," *IEEE Transactions on Communications*, vol. 56, pp. 5–9, January 2008.

[95] Chi-Hsiao Yih, "Iterative interference cancellation for OFDM signals with blanking nonlinearity in impulsive noise channels," *IEEE Signal Processing Letters*, vol. 19, pp. 147–150, March 2012.

[96] N. Andreadou and A. M. Tonello, "On the mitigation of impulsive noise in power-line communications with LT codes," *IEEE Transactions on Power Delivery*, vol. 28, pp. 1483–1490, July 2013.

[97] N. Andreadou and F.-N. Pavlidou, "Mitigation of impulsive noise effect on the PLC channel with QC-LDPC codes as the outer coding scheme," *IEEE Transactions on Power Delivery*, vol. 25, pp. 1440–1449, July 2010.

[98] Jurgen Haring and A. Vinck, "Iterative decoding of codes over complex numbers for impulsive noise channels," *IEEE Transactions on Information Theory*, vol. 49, pp. 1251–1260, May 2003.

[99] Jing Lin and M. Nassar, and B. L. Evans, "Impulsive noise mitigation in power-line communications using sparse bayesian learning," *IEEE Journal on Selected Areas in Communications*, vol. 31, pp. 1172–1183, July 2013.

[100] U. Sorger, I. D. Broeck, and M. Schnell, "Interleaved FDMA-a new spread-spectrum multiple-access scheme," in *1998 IEEE International Conference on*

Communications, 1998. ICC 98. Conference Record., vol. 2, pp. 1013–1017 vol.2, 1998.

[101] Z. Liu, "Maximum diversity in single-carrier frequency-domain equalization," *IEEE Transactions on Information Theory*, vol. 51, pp. 2937–2940, Aug. 2005.

[102] D. Anastasiadou and T. Antonakopoulos, "Multipath characterization of indoor power-line networks," *IEEE Transactions on Power Delivery*, vol. 20, pp. 90–99, Jan. 2005.

[103] J. M. Cioffi, G. P. Dudevoir, M. V. Eyuboglu, and G. D. Forney, "MMSE decision-feedback equalizers and coding. I. Equalization results," *IEEE Transactions on Communications*, vol. 43, pp. 2582–2594, Oct. 1995.

[104] D. Divsalar and F. Pollara, "Turbo codes for PCS applications," in *1995 IEEE International Conference on Communications, 1995. ICC '95 Seattle, 'Gateway to Globalization',*, vol. 1, pp. 54–59 vol.1, June 1995.

[105] S. Dolinar and D. Divsalar, "Weight distributions for turbo codes using random and nonrandom permutations," TDA Progr. Rep. 42-122, Jet Propulsion Lab., Pasadena, CA, USA, Aug. 1995.

[106] H. R. Sadjadpour, N. Sloaneand, M. Salehiand and G. Nebe, "Interleaver design for turbo codes," *IEEE Journal on Selected Areas in Communications*, vol. 19, pp. 831–837, May 2001.

[107] J. Sun and O. Y. Takeshita, "Interleavers for turbo codes using permutation polynomials over integer rings," *IEEE Transactions on Information Theory*, vol. 51, pp. 101–119, Jan. 2005.

[108] L. Welch, "Lower bounds on the maximum cross correlation of signals (corresp.)," *IEEE Transactions on Information Theory*, vol. 20, pp. 397–399, May 1974.

[109] M. A. Sustik, J. A. Tropp, I. S. Dhillon, and R. W. Heath, "On the existence of equiangular tight frames," *Linear Algebra and its applications*, vol. 426, no. 2-3, pp. 619–635, 2007.

[110] N. Y. Yu, "A construction of codebooks associated with binary sequences," *IEEE Transactions on Information Theory*, vol. 58, pp. 5522–5533, Aug. 2012.

[111] D. J. Love, R. W. Heath, and T. Strohmer, "Grassmannian beamforming for multiple-input multiple-output wireless systems," *IEEE Transactions on Information Theory*, vol. 49, pp. 2735–2747, Oct. 2003.

[112] P. Xia, S. Zhou, and G. B. Giannakis, "Achieving the welch bound with difference sets," *IEEE Transactions on Information Theory*, vol. 51, pp. 1900–1907, May 2005.

[113] A. Medra and T. N. Davidson, "Flexible codebook design for limited feedback systems via sequential smooth optimization on the Grassmannian manifold," *IEEE Transactions on Signal Processing*, vol. 62, pp. 1305–1318, March 2014.

[114] B. K. Natarajan, "Sparse approximate solutions to linear systems," *SIAM journal on computing*, vol. 24, no. 2, pp. 227–234, 1995.

[115] J. Akhtman and L. Hanzo, "Power versus bandwidth-efficiency in wireless communications: The economic perspective," in *2009 IEEE 70th Vehicular Technology Conference Fall (VTC 2009-Fall)*, pp. 1–5, Sept. 2009.

[116] M. Di Renzo, H. Haas, A. Ghrayeb, S. Sugiura and L. Hanzo, "Spatial modulation for generalized MIMO: Challenges, opportunities, and implementation," *Proceedings of the IEEE*, vol. 102, pp. 56–103, Jan. 2014.

[117] Y. Chen, S. Zhang, S. Xu, and G. Y. Li, "Fundamental trade-offs on green wireless networks," *IEEE Communications Magazine*, vol. 49, pp. 30–37, June 2011.

[118] G. Y. Li *et al.*, "Energy-efficient wireless communications: tutorial, survey, and open issues," *IEEE Wireless Communications*, vol. 18, pp. 28–35, December 2011.

[119] C.-L. I *et al.*, "Toward green and soft: a 5G perspective," *IEEE Communications Magazine*, vol. 52, pp. 66–73, February 2014.

[120] Y. Wu *et al.*, "Green transmission technologies for balancing the energy efficiency and spectrum efficiency trade-off," *IEEE Communications Magazine*, vol. 52, pp. 112–120, Nov. 2014.

[121] R. Abu-alhiga and H. Haas, "Subcarrier-index modulation OFDM," in *2009 IEEE 20th International Symposium on Personal, Indoor and Mobile Radio Communications*, pp. 177–181, Sept 2009.

[122] D. Tsonev, S. Sinanovic and H. Haas, "Enhanced subcarrier index modulation (SIM) OFDM," in *2011 IEEE GLOBECOM Workshops*, pp. 728–732, Dec. 2011.

[123] E. Basar, U. Aygolu, E. Panayirci and H. V. Poor, "Orthogonal frequency division multiplexing with index modulation," *IEEE Transactions on Signal Processing*, vol. 61, pp. 5536–5549, Nov. 2013.

[124] S. Sugiura, S. Chen, and L. Hanzo, “Coherent and differential space-time shift keying: A dispersion matrix approach,” *IEEE Transactions on Communications*, vol. 58, pp. 3219–3230, November 2010.

[125] R. Zhang, L. L. Yang, and L. Hanzo, “Generalised pre-coding aided spatial modulation,” *IEEE Transactions on Wireless Communications*, vol. 12, pp. 5434–5443, November 2013.

[126] P. Yang, M. D. Renzo, Y. Xiao, S. Li, and L. Hanzo, “Design guidelines for spatial modulation,” *IEEE Communications Surveys Tutorials*, vol. 17, pp. 6–26, Firstquarter 2015.

[127] N. Ishikawa, S. Sugiura, and L. Hanzo, “Subcarrier-index modulation aided OFDM - will it work?,” *IEEE Access*, vol. 4, pp. 2580–2593, 2016.

[128] E. Basar, “Index modulation techniques for 5G wireless networks,” *IEEE Communications Magazine*, vol. 54, pp. 168–175, July 2016.

[129] M. Wen, X. Cheng, and L. Yang, *Index Modulation for 5G Wireless Communications*. Springer, 2016.

[130] M. Wen, X. Cheng and L. Yang, “Optimizing the energy efficiency of OFDM with index modulation,” in *2014 IEEE International Conference on Communication Systems (ICCS)*, pp. 31–35, Nov. 2014.

[131] M. Wen, X. Cheng, M. Ma, B. Jiao, and H. V. Poor, “On the achievable rate of OFDM with index modulation,” *IEEE Transactions on Signal Processing*, vol. 64, pp. 1919–1932, April 2016.

[132] H. Zhang, L. L. Yang, and L. Hanzo, “LDPC-coded index-modulation aided OFDM for in-vehicle power line communications,” in *2016 IEEE 83rd Vehicular Technology Conference (VTC Spring)*, pp. 1–5, May 2016.

[133] R. Fan, Y. Yu and Y. Guan, “Orthogonal frequency division multiplexing with generalized index modulation,” in *2014 IEEE Global Communications Conference (GLOBECOM)*, pp. 3880–3885, Dec. 2014.

[134] E. Basar, “OFDM with index modulation using coordinate interleaving,” *IEEE Wireless Communications Letters*, vol. 4, pp. 381–384, Aug. 2015.

[135] Y. Xiao *et al.*, “OFDM with interleaved subcarrier-index modulation,” *IEEE Communications Letters*, vol. 18, pp. 1447–1450, Aug. 2014.

[136] M. Z. A. Khan and B. S. Rajan, “Single-symbol maximum likelihood decodable linear STBCs,” *IEEE Transactions on Information Theory*, vol. 52, pp. 2062–2091, May 2006.

[137] V. Tarokh, N. Seshadri and A. R. Calderbank, “Space-time codes for high data rate wireless communication: performance criterion and code construction,” *IEEE Transactions on Information Theory*, vol. 44, pp. 744–765, March 1998.

[138] J. Boutros and E. Viterbo, “Signal space diversity: a power- and bandwidth-efficient diversity technique for the Rayleigh fading channel,” *IEEE Transactions on Information Theory*, vol. 44, pp. 1453–1467, July 1998.

[139] Y. Xin, Z. Wang, and G. B. Giannakis, “Space-time diversity systems based on linear constellation precoding,” *IEEE Transactions on Wireless Communications*, vol. 2, pp. 294–309, March 2003.

[140] G. Wang, H. Liao, H. Wang, and X.-G. Xia, “Systematic and optimal cyclotomic lattices and diagonal space-time block code designs,” *IEEE Transactions on Information Theory*, vol. 50, pp. 3348–3360, Dec. 2004.

[141] W. Su, Z. Safar, and K. J. R. Liu, “Full-rate full-diversity space-frequency codes with optimum coding advantage,” *IEEE Transactions on Information Theory*, vol. 51, pp. 229–249, Jan. 2005.

[142] Lie-Liang Yang, “Signal detection in antenna-hopping space-division multiple-access systems with space-shift keying modulation,” *IEEE Transactions on Signal Processing*, vol. 60, pp. 351–366, Jan. 2012.

[143] J. Boutros, E. Viterbo, C. Rastello, and J. C. Belfiore, “Good lattice constellations for both Rayleigh fading and Gaussian channels,” *IEEE Transactions on Information Theory*, vol. 42, pp. 502–518, March 1996.

[144] Z. Liu, Y. Xin and G. B. Giannakis, “Linear constellation precoding for OFDM with maximum multipath diversity and coding gains,” *IEEE Transactions on Communications*, vol. 51, pp. 416–427, March 2003.

[145] N. H. Tran, H. H. Nguyen, and T. Le-Ngoc, “Bit-interleaved coded OFDM with signal space diversity: Subcarrier grouping and rotation matrix design,” *IEEE Transactions on Signal Processing*, vol. 55, pp. 1137–1149, March 2007.

[146] N. Prasad, L. Venturino, and X. Wang, “Diversity-multiplexing tradeoff analysis for OFDM systems with subcarrier grouping, linear precoding, and linear detection,” *IEEE Transactions on Information Theory*, vol. 56, pp. 6078–6096, Dec. 2010.

[147] J. Zhang, L. L. Yang, L. Hanzo, and H. Gharavi, “Advances in cooperative single-carrier FDMA communications: Beyond LTE-advanced,” *IEEE Communications Surveys Tutorials*, vol. 17, pp. 730–756, Secondquarter 2015.

[148] L.-L. Yang, “Receiver multiuser diversity aided multi-stage minimum mean-square error detection for heavily loaded DS-CDMA and SDMA systems,” *IEEE Transactions on Communications*, vol. 58, pp. 3397–3404, December 2010.

[149] S. Verdu, “Spectral efficiency in the wideband regime,” *IEEE Transactions on Information Theory*, vol. 48, pp. 1319–1343, Jun 2002.

[150] T. M. Cover and J. A. Thomas, *Elements of information theory.* John Wiley & Sons, 2012.

[151] J. Joung, C. K. Ho, and S. Sun, “Spectral efficiency and energy efficiency of OFDM systems: Impact of power amplifiers and countermeasures,” *IEEE Journal on Selected Areas in Communications*, vol. 32, pp. 208–220, February 2014.

[152] X. Giraud, E. Boutillon, and J. C. Belfiore, “Algebraic tools to build modulation schemes for fading channels,” *IEEE Transactions on Information Theory*, vol. 43, pp. 938–952, May 1997.

[153] D. V. Sarwate, “Meeting the welch bound with equality,” in *Sequences and their Applications*, pp. 79–102, Springer, 1999.

[154] A. Jovicic, J. Li and T. Richardson, “Visible light communication: opportunities, challenges and the path to market,” *IEEE Communications Magazine*, vol. 51, pp. 26–32, December 2013.

[155] H. Burchardt, N. Serafimovski, D. Tsonev, S. Videv and H. Haas, “VLC: Beyond point-to-point communication,” *IEEE Communications Magazine*, vol. 52, pp. 98–105, July 2014.

[156] R. Zhang and L. Hanzo, “Multi-layer modulation for intensity-modulated direct-detection optical OFDM,” *IEEE/OSA Journal of Optical Communications and Networking*, vol. 5, pp. 1402–1412, Dec. 2013.

[157] J. Jiang, P. Zhang, R. Zhang, S. Chen, and L. Hanzo, “Aperture selection for ACO-OFDM in free-space optical turbulence channel,” *IEEE Transactions on Vehicular Technology*, vol. 65, pp. 6089–6100, Aug. 2016.

[158] J. Jiang *et al.*, “Video streaming in the multiuser indoor visible light downlink,” *IEEE Access*, vol. 3, pp. 2959–2986, 2015.

[159] T. Keller and L. Hanzo, “Adaptive multicarrier modulation: a convenient framework for time-frequency processing in wireless communications,” *Proceedings of the IEEE*, vol. 88, pp. 611–640, May 2000.

[160] J. Armstrong, "OFDM for optical communications," *Journal of Lightwave Technology*, vol. 27, pp. 189–204, Feb. 2009.

[161] J. Carruthers and J. Kahn, "Multiple-subcarrier modulation for nondirected wireless infrared communication," *IEEE Journal on Selected Areas in Communications*, vol. 14, pp. 538–546, April 1996.

[162] J. Armstrong and A. J. Lowery, "Power efficient optical OFDM," *Electronics Letters*, vol. 42, pp. 370–372, March 2006.

[163] S. D. Dissanayake and J. Armstrong, "Comparison of ACO-OFDM, DCO-OFDM and ADO-OFDM in IM/DD systems," *Journal of Lightwave Technology*, vol. 31, pp. 1063–1072, April 2013.

[164] J. Armstrong and B. J. C. Schmidt, "Comparison of asymmetrically clipped optical OFDM and DC-biased optical OFDM in AWGN," *IEEE Communications Letters*, vol. 12, pp. 343–345, May 2008.

[165] D. Barros, S. Wilson and J. Kahn, "Comparison of orthogonal frequency-division multiplexing and pulse-amplitude modulation in indoor optical wireless links," *IEEE Transactions on Communications*, vol. 60, pp. 153–163, January 2012.

[166] S. Dimitrov, S. Sinanovic and H. Haas, "Clipping noise in OFDM-based optical wireless communication systems," *IEEE Transactions on Communications*, vol. 60, pp. 1072–1081, April 2012.

[167] X. Ling, J. Wang, X. Liang, Z. Ding and C. Zhao, "Offset and power optimization for DCO-OFDM in visible light communication systems," *IEEE Transactions on Signal Processing*, vol. 64, pp. 349–363, Jan. 2016.

[168] L. Chen, B. Krongold, and J. Evans, "Theoretical characterization of nonlinear clipping effects in IM/DD optical OFDM systems," *IEEE Transactions on Communications*, vol. 60, pp. 2304–2312, August 2012.

[169] S. H. Han and J. H. Lee, "An overview of peak-to-average power ratio reduction techniques for multicarrier transmission," *IEEE Wireless Communications*, vol. 12, no. 2, 2005.

[170] T. Jiang and Y. Wu, "An overview: Peak-to-average power ratio reduction techniques for OFDM signals," *IEEE Transactions on Broadcasting*, vol. 54, pp. 257–268, June 2008.

[171] Y. Rahmatallah and S. Mohan, "Peak-to-average power ratio reduction in OFDM systems: A survey and taxonomy," *IEEE Communications Surveys Tutorials*, vol. 15, pp. 1567–1592, Fourth 2013.

[172] X. Wang, T. T. Tjhung and C. S. Ng, “Reduction of peak-to-average power ratio of OFDM system using a companding technique,” *IEEE Transactions on Broadcasting*, vol. 45, pp. 303–307, Sept. 1999.

[173] X. Wang, T. T. Tjhung, C. S. Ng and A. A. Kassim, “On the SER analysis of A-law companded OFDM system,” in *IEEE Global Telecommunications Conference, 2000. GLOBECOM ’00*, vol. 2, pp. 756–760, 2000.

[174] X. Huang, J. Lu, J. Zheng, K. B. Letaief and J. Gu, “Companding transform for reduction in peak-to-average power ratio of OFDM signals,” *IEEE Transactions on Wireless Communications*, vol. 3, pp. 2030–2039, Nov. 2004.

[175] T. Jiang, Y. Yang and Y.-H. Song, “Exponential companding technique for PAPR reduction in OFDM systems,” *IEEE Transactions on Broadcasting*, vol. 51, pp. 244–248, June 2005.

[176] J. Hou, J. H. Ge and J. Li, “Trapezoidal companding scheme for peak-to-average power ratio reduction of OFDM signals,” *Electronics Letters*, vol. 45, pp. 1349–1351, December 2009.

[177] J. Hou, J. Ge, D. Zhai and J. Li, “Peak-to-average power ratio reduction of OFDM signals with nonlinear companding scheme,” *IEEE Transactions on Broadcasting*, vol. 56, pp. 258–262, June 2010.

[178] Y. Wang, L. H. Wang, J. H. Ge and B. Ai, “An efficient nonlinear companding transform for reducing PAPR of OFDM signals,” *IEEE Transactions on Broadcasting*, vol. 58, pp. 677–684, Dec. 2012.

[179] S. P. DelMarco, “General closed-form family of companders for PAPR reduction in OFDM signals using amplitude distribution modification,” *IEEE Transactions on Broadcasting*, vol. 60, pp. 102–109, March 2014.

[180] M. Hu, Y. Li, W. Wang and H. Zhang, “A piecewise linear companding transform for PAPR reduction of OFDM signals with companding distortion mitigation,” *IEEE Transactions on Broadcasting*, vol. 60, pp. 532–539, Sept. 2014.

[181] H. Elgala, R. Mesleh and H. Haas, “Predistortion in optical wireless transmission using OFDM,” in *Ninth International Conference on Hybrid Intelligent Systems, 2009. HIS ’09.*, vol. 2, pp. 184–189, Aug. 2009.

[182] H. Qian, S. J. Yao, S. Z. Cai and T. Zhou, “Adaptive postdistortion for nonlinear LEDs in visible light communications,” *IEEE Photonics Journal*, vol. 6, pp. 1–8, Aug. 2014.

[183] K. Lee, H. Park and J. R. Barry, “Indoor channel characteristics for visible light communications,” *IEEE Communications Letters*, vol. 15, pp. 217–219, February 2011.

[184] J. Bussgang, “Cross correlation function of amplitude-distorted Gaussian signals,” tech. rep., Research Laboratory of Electronics, Massachusetts Institute of Technology, 1952.

Subject Index